ulm university universität ulm

Investigation of localized electrochemical interfaces with advanced microscopic techniques:

AFM-SECM and FIB/SEM tomography

Zur Erlangung des Doktorgrades Dr. rer. nat.

der Fakultät für Naturwissenschaften der Universität Ulm

vorgelegt von

Angelika Holzinger

aus Heilbronn

Ulm, 2019

Amtierender Dekan: Prof. Dr. Peter Dürre

Erstgutachter: apl. Prof. Dr. Christine Kranz

Zweitgutachter: Prof. Dr. Jürgen R. Behm

Tag der Promotion: 16. Juli 2019

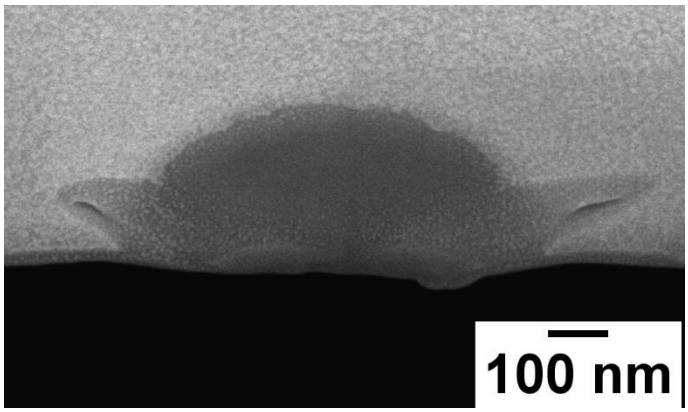

Much to learn you still have.

- Yoda

I. Content

II. Abbreviations

ACT	-	Aqueous complexation followed by transfer
AFM	-	Atomic force microscopy
Ag/AgCl	-	Silver/silver chloride reference electrode
AIROF	-	Anodic iridium oxide film
ATR FTIR	-	Attenuated total reflection FTIR
BSE	-	Backscattered electron(s)
CE	-	Counter electrode
CV	-	Cyclic voltammetry
DPA	-	Differential pulse amperometry
DRIE	-	Deep reactive ion etching
EDX	-	Energy dispersive X-ray
EIROF	-	Electrochemically deposited iridium oxide film
ETD	-	Everhart-Thornley detector
FIB	-	Focused ion beam
FTIR	-	Fourier-transform infrared spectroscopy
HOPG	-	Highly oriented pyrolytic graphite
IBID	-	Ion beam induced deposition
ISE	-	Ion selective electrode
ISFET	-	Ion sensitive field effect transistor
ITIES	-	Interface between two immiscible electrolyte solutions
Mt/AFM-SECM	-	Molecule touching/ AFM-SECM
NHE	-	Normal hydrogen electrode
NiHCF	-	Nickel hexacyanoferrate
NMR	-	Nuclear magnetic resonance spectroscopy
NPP model	-	Nernst-Planck, Poisson model
OCP	-	Open circuit potential
ORR	-	Oxygen reduction reaction
PECVD	-	Plasma-enhanced chemical vapor deposition

PB	-	Prussian blue
RE	-	Reference electrode
ROS	-	Reactive oxygen species
SE	-	Secondary electron(s)
SECM	-	Scanning electrochemical microscopy
SEM	-	Scanning electron microscopy
SG/TC mode	-	Substrate generation / tip collection mode
SHE	-	Standard hydrogen electrode
SiN	-	Silicon nitride
SIROF	-	Sputtered iridium oxide film
SNOM	-	Scanning near-field microscopy
SPM	-	Scanning probe microscopy
STEM	-	Scanning transmission electron microscopy
STM	-	Scanning tunneling microscopy
SVET	-	Scanning vibrating electrode technique
TARM –AFM-SECM	-	Tip-attached redox mediator – AFM-SECM
TATB	-	Tetraphenylarsonium tetraphenylborate
TEM	-	Transmission electron microscopy
TIC	-	Transfer by interfacial complexation
TID	-	Transfer by interfacial decomplexation
TLD	-	Through-the-lens detector
TOC	-	Transfer followed by organic-phase complexation
TOIROF	-	Thermal oxidation of iridium oxide film
UME	-	Ultramicroelectrode
XRD	-	X-ray diffraction

III. Abstract

Comprehensive knowledge about interfacial processes is essential for the development of innovative miniaturized sensors or the investigation of biological samples. Miniaturization of sensors with sub-micron and nanoscale dimensions and sensor arrays is accompanied by challenges, such as changes in the efficiency of the sensor, changes in the general behavior at small sensor dimensions, or difficulties in handling of such devices. Therefore, a detailed evaluation of possible factors influencing the performance of miniaturized sensors has to be done prior to applications. Studying processes at surfaces, ranging from e.g., single cells[1] to corroding materials[2] and investigations of nanoscale 3D and 2D materials, e.g. nanotubes[3] and graphene[4], got accessible with high-resolution microscopic techniques with improved resolution down to the sub-nanoscale[5–7]. Especially combined scanning probe techniques (SPM)[2,8–10] enable the investigation of localized surface properties. Amongst other hybrid methods, atomic force - scanning electrochemical microscopy (AFM-SECM) is highly attractive for studying processes at the solid/liquid interface, and also for investigations of liquid/liquid interfaces[11]. In order to enhance the field of applications, AFM-SECM probes may be modified facilitating the requirements for biomedical applications and for usage with electroanalytical techniques. Whereas AFM-SECM provides predominantly information of surface processes, the combination of focused ion beam (FIB) and scanning electron microscopy (SEM)[12,13] enables the detection and reconstruction of the inner structure of (nano)porous materials. This was already reported for several materials, ranging from nanoparticles in dye-sensitive solar cells[14] to investigations of biological[15,16] and geological[16] samples.

Within the first part of this thesis, the focus of research is targeted towards modification of AFM-SECM probes facilitating biomedically relevant measurements, such as sensing hydrogen peroxide (H_2O_2) release or generation in close proximity to a sample surface (chapter 4), and localized pH sensing with associated surface changes (chapter 5).

In chapter 4, the surface modification of AFM tip-integrated electrodes with electrocatalytically active layers is presented, namely Prussian Blue (PB) for H_2O_2 sensing. In contrast to a relatively high potential (0.5 – 0.8 V vs. normal hydrogen electrode

(NHE)[17]) for H_2O_2 oxidation at platinum electrodes, modification with PB provides moderate electrochemical reduction potentials (-0.05 V vs. standard reference electrode (SHE)[18]) and improved selectivity[19]. The disadvantage of the limited stability of PB particular in higher H_2O_2 concentration can be attenuated by co-deposition of PB and nickel-hexacyanoferrate (NiHCF)[20]. Prior to AFM-SECM investigations, different electrode materials and conditions, e.g. vacuum conditions and drying processes, which are necessary for AFM-SECM probe fabrication, are evaluated on modified ultramicroelectrodes (UME). Besides a thorough characterization, the stability and sensitivity of the H_2O_2 sensors are investigated, and first results towards localized H_2O_2 detection by AFM-SECM are presented in 4.3.3.

In chapter 5, solid-state pH sensors integrated into AFM tips are evaluated since local pH changes play an important role, for example in corrosion science or investigation of living cells[21,22]. Antimony/antimony oxide[23,24], anodic iridium oxide film (AIROF)[25,26] and electrochemical iridium oxide film (EIROF)[27] were investigated as AFM tip-integrated pH sensor materials. The most suitable modification with respect to stability and sensitivity in pH calibrations is evaluated (5.3.1 and 5.3.3) and first AFM-SECM measurements of the dissolution of calcite crystals as a model sample mapping surface changes along with a pH change to more alkaline pH values[28,29] are presented in 5.3.2.

In chapter 6, detailed investigations of FIB-milled nanoporous arrays in silicon nitride (SiN) membranes are presented, which were used as solid-state support for electrochemistry at the interface between two immiscible electrolyte solutions (ITIES)[30,31]. FIB can be used for mask-less prototyping of arrays with readily adjustable dimensions[32–34]. Since this fabrication process may change the performance of such micro- and nanoporous solid-state materials due to implantation of positively charged Ga ions[35] or due to a varying pore shape resulting from re-deposition during the FIB milling process[32,36,37], a comprehensive analysis of these devices is essential. The suitability of AFM-SECM in the investigation of micro- and nanoscale interfaces is shown by the performance of AFM-SECM with a conductive AFM tip, which was used to visualize the different diffusion behavior at these nanoporous arrays, as the ratio between the pore size and the distance between single pores within an array are affecting the diffusion behavior at these devices (6.3.1). The detailed investigations on the location of the nano-interfaces at the

nanoporous SiN membranes are shown in 6.3.3 and 6.3.4. In addition, the localized electrochemical deposition of silica at the nanoITIES was used to visualize the location of the interface within the nanopores. For the first time, FIB/SEM tomography was performed for the investigations of the location of this interface at such silica deposits.

IV. Zusammenfassung

Zur Entwicklung innovativer miniaturisierter Sensoren, sowie zur Untersuchung biologischer Vorgänge, ist ein detailliertes Verständnis der zugrundeliegenden Prozesse notwendig, die an Grenzflächen ablaufen. Mögliche Einflüsse, die das Verhalten und die Anwendbarkeit solcher Mikrosensoren beeinträchtigen können, müssen im Vorfeld detailliert untersucht werden. Untersuchungen an Grenzflächen in der Größenordnung weniger Mikro- oder Nanometer profitieren von den Weiterentwicklungen im Bereich der hochauflösenden Mikroskopie-Techniken[5–7] und insbesondere kombinierter Rastersondentechniken[2,8–10], da hier ortsaufgelöste Messungen von elektrochemischen Oberflächenprozessen ermöglicht werden. Die Kombinationstechnik von Rasterkraft- und elektrochemischer Rastersondenmikroskopie (*atomic force - scanning electrochemical microscopy*, AFM-SECM), welche hochauflösende Abbildungen einer Oberfläche bei gleichzeitiger Bestimmung elektrochemischer Oberflächenprozesse vereint, ist ein Beispiel einer solchen Hybridtechnik. Eine weitere Mikroskopie-Technik stellt die Kombination aus fokussiertem Ionenstrahl (FIB) und Rasterelektronenmikroskopie (SEM) dar, die es ermöglicht Proben hinsichtlich ihrer mikro- und nanoporösen Strukturen[12,13] zu untersuchen. Dabei erstreckt sich das Anwendungsgebiet der FIB/SEM Tomographie von der Untersuchung von Nanopartikeln, die in Solarzellen genutzt werden[14], bis hin zu Untersuchungen von biologischen[15,16] und geologischen[16] Proben.

Der erste Abschnitt der zugrundeliegenden Arbeit umfasst die Modifikation von AFM-SECM Sensoren, die biomedizinisch relevante Untersuchungen ermöglicht, wie zum Beispiel die Detektion von Wasserstoffperoxid (H_2O_2, Kapitel 4) oder ortsaufgelöste pH Änderungen (Kapitel 5).

In Kapitel 4 wird die elektrochemische Modifikation der elektroaktiven Fläche von AFM-SECM Spitzen mit Preußisch Blau (PB) gezeigt. Im Gegensatz zu Platinelektroden, die hohe Oxidationspotentiale (0.5 – 0.8V vs. NHE[17]) zur H_2O_2 Bestimmung benötigen, kann mittels PB-modifizierten Elektroden unter milden Bedingungen (-0.05 V vs. SHE[18]) gemessen werden. Gleichzeitig wurde eine erhöhte Selektivität beobachtet[19]. Ein Nachteil von PB ist die begrenzte Stabilität, besonders bei hohen H_2O_2 Konzentrationen, welche jedoch durch

zusätzliche Abscheidung von NiHCF[20] verbessert werden kann. Unterschiedliche Elektrodenmaterialien und Messbedingungen, die während der Herstellung von AFM-SECM Sensoren erforderlich sind, wurden anhand modifizierter Ultramikroelektroden (UME) untersucht. Neben einer detaillierten Untersuchung und Charakterisierung der modifizierten Spitzen, wurde die H_2O_2 Sensitivität und das lineare Ansprechverhalten der Sensoren untersucht. Erste AFM-SECM Messungen von lokalisiert erzeugtem Peroxid werden in Abschnitt 4.3.3 diskutiert.

In Kapitel 5 wird die Modifikation von AFM-SECM Proben mit einem pH Sensor präsentiert, da die Änderung des pH-Wertes sowohl in Korrosion, aber auch in biologischen Zellen eine wichtige Rolle spielt, um nur zwei Beispiele zu nennen[21,22]. Unterschiedliche Modifikationen von pH-sensitiven AFM-SECM Spitzen wurden untersucht, und zwar Antimon/Antimonoxid[23,24], anodischer Iridiumoxid-Film (AIROF)[25,26] und elektrochemisch abgeschiedene Iridiumoxid-Filme (EIROF)[27] als pH-sensitives Elektrodenmaterial. Dabei wurden diese unterschiedlichen pH Sensoren auf ihre Stabilität und Sensitivität in pH Messungen untersucht und verglichen (5.3.1 und 5.3.3). Erste Untersuchungen mittels AFM-SECM werden in Abschnitt 5.3.2 gezeigt. Dabei wurden Calcit-Kristalle abgebildet, die beim Lösen in wässriger Lösung eine lokale pH Änderung zu basischen pH erzeugen[28,29].

In Kapitel 6 wird die genaue Untersuchung von nanoporösen Siliziumnitrid Membranen dargestellt, die als Supportmaterial für nanoITIES (*nano-interface between two immiscible electrolyte solutions*) verwendet werden[30,31]. Unter anderem wurde AFM-SECM dazu genutzt, um das Diffusionsverhalten an diesen nanoporösen Strukturen zu untersuchen, da dieses maßgeblich von dem Verhältnis zwischen dem Porenradius und dem Abstand zwischen den Poren abhängt (6.3.1). Neben dem Einfluss der Herstellungsart dieser nanoporösen Membranen durch FIB, wie in Abschnitt 6.3.2 gezeigt, wird eine genaue Untersuchung der Lage der Grenzfläche von ITIES in diesen Nanoporen beschrieben und anhand der elektrochemischen Abscheidung von Silikapartikeln an der Phasengrenze zweier nichtmischbaren Flüssigkeiten innerhalb des nanoporösen Netzwerkes gezeigt (Abschnitt 6.3.3 und 6.3.4) Des Weiteren ermöglicht die genaue Untersuchung der Nanoporen mittels FIB/SEM Tomographie eine Rekonstruktion der porösen Struktur und der lokalen Abscheidung der Silikapartikel.

V. Experimental background

The following section gives a comprehensive overview of the theoretical background, which is the basis of the research presented within this thesis: fundamental principles of electrochemistry at UMEs and at ITIES, AFM, SECM, the combination of AFM-SECM and FIB/SEM tomography.

1 Fundamentals in electrochemistry

Electrochemistry includes all processes related to electric reactions that can be traced to chemical processes. In case of potentiometry, no measurable current flow is involved. In case that the process induces a current flow, one can distinguish between galvanic or electrolytic processes. Thereby, galvanic reactions are spontaneous by connecting two systems by a conductive media, which is important for energy storage and production. If a reaction is forced by an applied external potential larger than the eigenpotential of the system, it is called electrolytic. In electrolytic cells, different types of reactions are possible with the concordance that every system strives for the equilibrium state with minimized molar free energy $\Delta_r G$, resulting in the chemical potential μ_i of component i within an electrochemical process described as[38]:

$$\mu_i = \mu_i^0 + RT\ln a_i \quad (1)$$

$$\mu_i = \left(\frac{\partial G}{\partial n_i}\right)_{T,P,n_{j\neq i}} \quad (2)$$

With the standard chemical potential (μ_i^0) of component i, the activity of the component i (a_i), the molar gas constant (R) and the temperature (T), the pressure (P) and the amount of substance (n_i).

The equilibrium is dynamic, which means that both, oxidation and reduction, are taking place at the same rate in the equilibrium state. The chemical potential leads to the Nernst equation, which describes the Galvani potential in equilibrium in dependence of the activity of the participating compounds. If the Galvani potential difference $\Delta\varphi$ is measured against the SHE, it can be replaced by the electrode potential E[39]:

$$E = E^0 + \frac{RT}{nF}\left(\frac{\prod_{ox} a_{ox}^{v}}{\prod_{red} a_{red}^{v}}\right) \quad (3)$$

With the number of participating electrons (n), the Faraday constant (F), the potential at standard conditions (E^0) and a stoichiometric factor (v).

To reach the equilibrium state within a certain time (dt), a charge (dQ) is transferred within the system resulting in a faradaic current (i)[38]:

$$i = \frac{dQ}{dt} \quad (4)$$

The Nernst equation applies therefore for reversible reactions. Reversible electrochemical processes are governed by the concentrations at the surface, by fast electron transfer, and lack of additional homogenous reactions in solution of the produced species forming side product when a reduced species is oxidized and vice versa. Whereas for irreversible reactions, the back reaction is kinetically hindered or additional side products inhibit the conversion of all reduced species back to oxidized species (and vice versa). Quasi-reversible reactions are governed by kinetic and mass transport. The Nernst equation describes the electrochemical reaction from a thermodynamic point of view. If kinetic processes are affecting the electrochemical reaction, an additional potential, the so-called overpotential (η), has to be applied to overcome the activation energy and to drive the reaction. The Tafel equation describes this overpotential in relation to the decadic logarithm of the current and of the exchange current, which describes the resulting faradaic activity in the equilibrium state with a zero current[38]. The kinetics of a redox reaction can be expressed by the standard rate constant k_0 with high values (1 – 10 cm/s)[38] for reactions reaching the equilibrium state in a short time. The rate constant is used to describe the kinetics of the cathodic reaction $k_{cathodic}$ (or anodic as k_{anodic}) by:

$$k_{cathodic} = k_0 \cdot e^{-\alpha f \cdot (E - E^{0'})} \quad (5)$$

$$k_{anodic} = k_0 \cdot e^{(1-\alpha) f \cdot (E - E^{0'})} \quad (6)$$

$E^{0'}$ is the formal potential and E the relative energy of the electron participating in the redox reaction. The Butler-Volmer[40] describes the anodic (i_+) and the cathodic (i_-) current depending on the exchange current(i_0) in dependence of the overpotential by:

$$i = i_+ + i_- = i_0\left[e^{-\alpha f \eta} - e^{(1-\alpha) f \eta}\right] \quad (7)$$

Nonfaradaic current contributions to the overall recorded current are based especially on the growth of a capacitance layer, namely the electrical double layer. The double layer can be described as a capacitor, resulting in a current flow by applying an external voltage. The current i_C is described by the differential capacitance (C_d), the potential (E) and time (t) and is dependent on the electrodes' surface and the electrolyte solution[39]:

$$i_C = C_d \cdot \frac{dE}{dt} \quad (8)$$

The double layer consists of different regions described by the Stern model. This theory combines the former models of Helmholtz and of Gouy and Chapman. In close proximity to the electrode, an oriented ion layer is formed, which is termed the inner Helmholtz layer with adsorbed ions on the surface of the electrodes due to Van der Waals forces, and the outer Helmholtz layer with the ions surrounded by solvent molecules and described by the Poisson equation[39]:

$$\frac{d^2\varphi}{dx^2} = -\frac{\rho}{\varepsilon_r \varepsilon_0} \quad (9)$$

The second derivative of the potential (φ) to the perpendicular direction to the electrode (x) is thereby dependent on the charge density (ρ) and the relative (index r) and absolute (index 0) permittivity (ε).

The Gouy-Chapman model describes an adjoining diffuse region considering the thermal motion of the ions near the electrode surface and includes the presence of counter ions within the diffusive layer, This layer is described by the so-called zeta potential, which drops exponentially with distance[39].

1.1 Potentiometry

Potentiometric measurements are based on the detection of changes in the eigenpotential of a system due to concentration changes with respect to the potential of a reference electrode. This is the basic principle of ion-selective electrodes (ISE), in which an inner reference electrode located in an inner electrolyte solution is separated from the analyte solution by a semipermeable membrane. Diffusion and exchange of selective ions within this membrane leads to a potential difference at the membrane. The membrane can be either made of glass, as used in the pH glass electrode, or by a solid or liquid crystalline membrane. This membrane is doped with either charged ions enabling the detection of analytes of opposite polarity, or with ionophores enabling the selective interaction of ions. This ionophores within the membrane can be both, neutral or charged, depending on the analyte species[41]. The potential gradient according to the exchange of the analyte ions within this membrane is measured via the open circuit potential (OCP) and is described by the Nernst equation (1-3). Exemplarily, for detecting pH changes, the Nernst equation can be re-written as:

$$E = E^0 + \frac{RT}{nF} \cdot \log\left(a_{H_3O^+}\right) \rightarrow \quad E = E^0 - \frac{59.2\ mV}{n} \cdot pH \tag{10}$$

With the gas constant (R), the temperature (T), the Faraday constant (F), the number of electrons (n) and the activity of H_3O^+ ions (a).

Hence, this approach just represents the potential in the case of thermodynamic equilibrium. Diffusional, kinetic or migration processes are not taken into account. In case, the solution contains a mixture of ions, interferences have to be considered. A semi-empirical extension of the Nernst equation for the potential (E) of ISEs is described by the Nikolsky-Eisenman equation[41].

$$E = E_i^0 + \frac{RT}{z_i F} \cdot \ln\left(a_i + \sum_{i \neq j} k_{ij}^{pot} \cdot a_j^{z_i/z_j}\right) \tag{11}$$

With the constant potential (E_i^0), ion charge (z), gas constant (R), temperature (T), Faraday constant (F), activity a and the selectivity constant (k_{ij}^{pot}) for two ions i and j. The

interfering ion contributing to the measured potential is represented by the index j. The equation is based on the equilibrium state and any kinetic effects of ion transfer are neglected. An extension to the general assumption of the equilibrium state is given by the diffusion-layer-model, which takes into account the steady-state and local equilibrium conditions at the membrane surface. The diffusion and the ion concentration at or within the membrane are thereby time dependent. The most detailed description of potentiometric measurements is given by an advanced non-equilibrium model considering both, variations in time and in distance. This model is based on the Nernst-Planck equation, describing the ion flux dependent on time and space and the Poisson equation, defining the current density[42]. The graphs in Figure 1 represent the potentials described by the Nernst-Planck and Poisson (NPP) model (Figure 1 A) in comparison to the phase boundary model (Figure 1 B), which is a classical model assuming equilibrium conditions and neglecting migration and kinetic effects. The variation in the membrane potential changes in the range of mV for the NPP model compared to the phase boundary model (B).

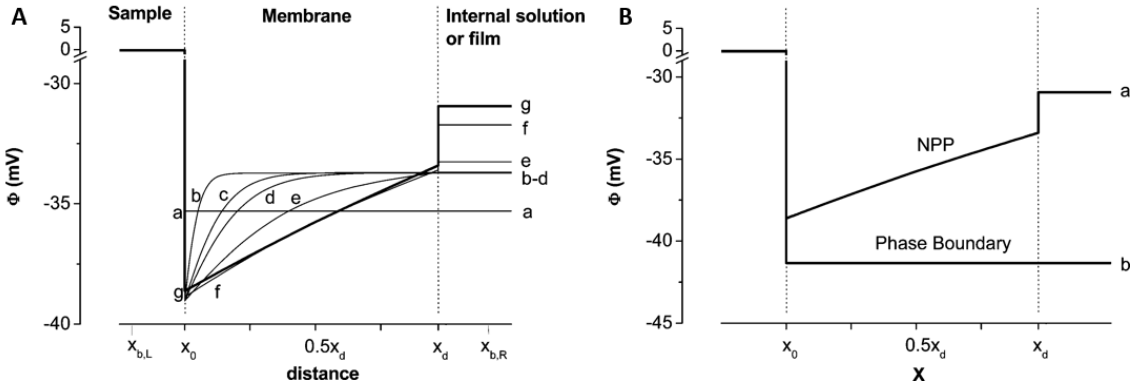

Figure 1 Schemes of the time- and space-dependent potentials described by the NPP model (A) and compared to the classical phase boundary model (B). The membrane potential in (A) is defined as the integral over the distance between a point in the bulk solution $x_{b,L}$ and a point in the internal solution $x_{b,R}$ at different times: 4 x 10^{-4} s (a), 1.64 s (b), 13.1 s (c), 26.2 s (d), 104.8 s (e), 420 s (f) and at steady-state conditions (13440 s, g).[42] Reprinted with permission from Bobacka, J., Ivaska, A. Lewenstam, A. *Chem. Rev.* **2008**, *108*, 329-351. Copyright 2019 American Chemical Society. https://doi.org/10.1021/cr068100w.

ISEs are used for the detection of a large variety of ions, as a standard analytical method in water analysis or food control, and are also used for characterization of pharmaceutical or biological samples[43]. The most used ISE is for the determination of pH using a hydronium-sensitive glass electrode developed over a century ago and based on the exchange of ions within the glass as the semipermeable membrane[44]. Next to ion-selective electrodes, ion-selective sensing can be performed with solid-state electrodes, such as conductive polymers, metals or ion-sensitive field-effect transistors (ISFETs). This is especially favorable for miniaturized sensors. The capability of pH sensing using metals as solid electrode materials is based on the equilibrium between the metal and its oxide, or between two oxidation states of the metal/material. A variation in pH leads to changes in the equilibrium state and, therefore, to a change in the eigenpotential of the material. Thereby, the composition of the metal and its oxide (or of two different oxides) varies leading to an electron transfer towards the electrode and the detection of the changed pH value by the electronic setup. Because there is a limited amount of the metal and its oxide (or of both metaloxides), especially for miniaturized sensors, also the capacitance of the material is reduced. This results in a higher material resistance, which affects the potential stability in potentiometric measurements[42]. Competing site-reactions may lead to false interpretations or to potential drifts during the measurements. Many metal/metal oxides can be used for pH sensing, whereas stability and/or linearity vary dependent on the different metal/metal oxides, conditions, and complexity of sample mixtures[45,46]. Suitable metal/metal oxides have to be stable in solution, but also soluble enough that the ratio of metal and corresponding oxide may vary to achieve equilibrium depending on pH changes. The pH response has to be fast, just depending on the diffusion of the H_3O^+ ions towards the pH sensor, and reproducible over a wide pH range. Response times determined by an electrochemical time-of-flight technique were up to a tenth of seconds for AIROF[25,26] electrodes, dependent on the film thickness[47]. Dependent on the underlying redox reaction of the pH-sensitive materials, the sensitivity varies as shown in Table 1 for a selection of metal/metal oxides. The underlying redox process during pH detection is shown exemplarily for the AIROF and the antimony/antimony oxide electrode[23,24], which were used in experiments presented within this thesis. The potential determining equilibrium for the AIROF and the antimony electrode may be written as follows:

$$2\ \mathrm{IrO_2(0H)_{(2-x)}}(H_2O)_{(2+x)}^{(2-x)-} + (3-2x)\mathrm{H^+} + 2\mathrm{e^-} \leftrightarrow \mathrm{Ir_2O_3(OH)_3(H_20)_3^{3-}} + 3\ \mathrm{H_2O}$$

$$\mathrm{Sb_2O_3} + 6\ \mathrm{H^+} + 6\ \mathrm{e^-} \leftrightarrow 2\ \mathrm{Sb} + 3\ \mathrm{H_2O}$$

metal/metal oxide or metal oxides as pH sensor	pH response	pH range
monocrystalline Sb/SbO_2	52 mV/pH	pH 2-10
Ir/IrO_2	63 mV/pH	pH 2-9
Pd/PdO (thermal)	59.6 mV/pH	pH 2.5 – 8.5
Pd/PdO (electrochemical)	71.4 mV/pH	pH 3 - 8[48]
AIROF (electrochemical)	65 – 80 mV/pH	pH 2.5 – 8.5
AIROF (thermal)	59 mV/pH	pH 2 - 12[49]
AIROF (sputtered)	59.5 mV/pH	pH 2 – 8.5
PtO_2	46.7 mV/pH	pH 5 – 10
RuO_2	61.8 mV/pH	pH 2 – 12
RhO_2 x H_2O	62.8 mV/pH	pH 2 – 12
OsO_2 x H_2O	51.2 mV/pH	pH 2 – 11

Table 1 pH response and linear pH range for some metal/metal oxides suitable as pH sensors[45].

Different fabrication strategies have been reported with respect to crystallographic properties[50–52], stability[53], and efficiency in pH sensing[54,55]. Especially, the response of iridium oxide electrodes varies depending on the fabrication process, namely, the sputtered iridium oxide film (SIROF)[56,57], thermal oxidation of Ir salts (TOIROF)[58,59] or

electrochemically deposited films like EIROF[27], and AIROF[60–62]. The slope for the pH response for AIROF electrodes can also be expressed by 59·(3 - 2x)/2 mV/pH[45]. Additionally, the influence of oxidation state[27] and of the substrate for the pH-sensitive film with respect to stability[63] has been investigated. All pH sensors have to be calibrated prior to usage.

1.2 Diffusion-limited currents at UMEs

In voltammetric measurements, the faradaic current related to a redox reaction is recorded. The current signal is influenced by transport processes in the electrolytic cell, namely diffusion, migration and convection. In a system with no additional steering and no temperature or density gradient, convection can be neglected. In electrolyte solution with high electrolyte concentrations in the range of 0.1 – 1 M, the migration of charged particles from the bulk solution to the electrode surface is mostly suppressed and can also be neglected because the electrolyte ions are carrying 97 % of the current in bulk solution[38]. In case of fast electron transfer kinetics, the faradaic current can then be described by the diffusion processes towards the electrode's surface. The diffusion-limited current I(t) is described for a spherical electrode by a semi-infinite approach via the Cottrell equation[38]:

$$I(t) = \frac{nFA\sqrt{D_0}c_0^*}{\sqrt{\pi t}} + \frac{nFAD_0c_0^*}{r_0} \qquad (12)$$

Thereby, the current consists of a time-dependent and a time-independent term, respectively, defined by the electrode area (A) and radius (r_0), Faraday constant (F), the number of electrons (n), the bulk concentration (c_0*) and diffusion coefficient (D_0) of the electroactive species (labelled with the index 0). In case, the diffusion layer, which is rather a region than a layer, is much smaller than the electrode area, the current signal becomes time-dependent. In the case of ultramicroelectrodes defined by the critical radius of 25 µm[38], this relation changes and the diffusion layer is in the same dimension or even larger than the electrode size. The current signal becomes time-independent and is termed steady-state current I_{ss}[38]:

$$I_{ss} = \frac{nFAD_0c_0^*}{r_0} \tag{13}$$

At short time scales, however, the time-depending term cannot be neglected. Calculated by Shoup and Szabo[64], the time-dependence can be expressed for a planar disk microelectrode as:

$$f(\tau) = 0.7854 + 0.8862\tau^{-1/2} + 0.2146e^{(-0.7823\tau^{-1/2})} \tag{14}$$

With τ as a dimensionless variable for the time defined as

$$\tau = \frac{4D_0t}{r_0^2} \tag{15}$$

According to equation (15), the time dependence is strongly related to the size of the electrode and results either in a linear or radial diffusion. For UMEs, the diffusion is linear to the surface within nano- to microseconds, but this merges within milliseconds into a radial diffusion and a resulting steady-state current. Due to this fast response at UMEs, fast electrochemical processes can be investigated under steady-state conditions.

1.2.1 *Surface and geometry of UMEs*

The current response depends on the electrode's geometry and surface roughness, defined by the relation between the microscopic area (A_m) and the geometric area (A_g), which can be interpreted as the projection of the surface boundary. For polished electrodes, the surface roughness is low, with[38]:

$$2 - 3 > \frac{A_m}{A_g} \tag{16}$$

In case that the diffusion layer is larger than the actual electrode size, which is the case for time scales above some seconds at UMEs, just the so-called geometric area of the surface is relevant. In case that the roughness is within the dimension of the diffusion

field, which is the case for fast time scales (nano or milliseconds) or unpolished surfaces, the actual electrode area is relevant. Clearly apparent from equation (12) and (13), the current is related to the area A of the electrode and different geometries, such as frame, disk, band, cylindrical, or conical electrodes result in different current responses[65]. An overview of the steady-state current responses with respect to the geometrical parameter is summarized in Table 2.

electrode geometry	**steady-state current**[66]
disc microelectrode	$I_{ss} = 4nFaDc_0^*$ (17)
ring microelectrode	$I_{ss} = nFl_oDc_0^*$ with $l_0 = \frac{[\pi^2(b+c)]}{\ln[16(b+c)/(c-b)]}, \quad \frac{c}{b} < 1.25$ (18)
conical microelectrode	$I_{ss} = 4nFDc_0a(1+qH^p)$ with $H = h/a$, $q = 0.3661$ and $p = 1.14466$ (19)

Table 2 Overview of the steady-state current at nano/micro-electrodes with respect to different electrode geometries.

For SECM measurements (see section 2.2), which allows mapping of local heterogeneity of electrochemical properties, the dimensions of the insulating sheath of the UME are crucial, because the current flow, when the UME is in close proximity to the sample surface, is not only influenced by the nature of the sample but also by the insulating sheath of the UME. An optimal ratio (RG value) of the radius of the electrode (r_{UME}) and the insulating sheath ($r_{insulating\ sheath}$) was derived from numerical simulations[67] as

$$10 \geq \frac{r_{insulating\ sheath}}{r_{UME}} \qquad (20)$$

1.3 Electrochemistry at the ITIES

Besides electrochemistry at the interface between a solid electrode and a liquid electrolyte solution, a polarized interface between two immiscible electrolyte solutions (ITIES) is highly interesting for electroanalysis. Thereby, electrochemical processes within the liquid/liquid system are described by different mechanisms, summarized in Figure 2.

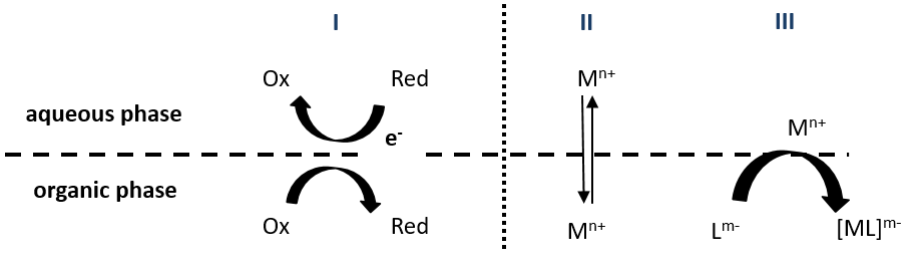

Figure 2 Scheme of different electrochemically induced processes at ITIES: electron transfer by two redox reactions in both phases (I), ion transfer (II) and facilitated ion transfer in the presence of a ligand molecule in one of the phases (III).

The charge transfer at ITIES can be based on electron transfer, but also on ion transfer, which can be either a direct transfer of a molecule soluble in both phases or a facilitated transfer in the presence of a ligand molecule in one of the phases. The facilitated transfer can be grouped into different types of transfer, as summarized in Table 3.

types of facilitated ion transfer	**ACT** – aqueous complexation followed by transfer	**TIC** – transfer by interfacial complexation	**TID** – transfer by interfacial decomplexation	**TOC** – transfer followed by organic-phase complexation
schemes	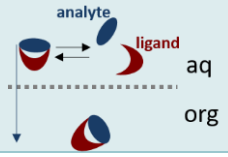	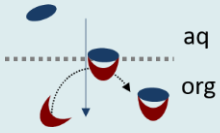	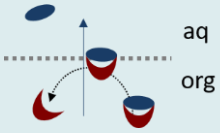	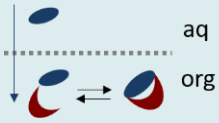

Table 3 Overview of facilitated ion transport[68].

Additionally, adsorption and desorption processes at the interface can be analyzed by impedance measurements and electrocapillary curves. Thereby, the kinetics of layer formation can be investigated, and new materials can be formed at a defect-free interface between two liquids. The thermodynamics of charge transfer at the liquid/liquid interface are described by the Nernst equation like in the case of a liquid/solid interface (see equations 1-3) and the Galvani potential of the transfer can be described by the solvation potentials in the aqueous and the organic phase, respectively. For the electron transfer, two redox reactions, one in each liquid, are taking place at the same time. In most cases, the charge transfer is coupled with multiple reactions and additional transfer due to charge balance within the system has to be taken into account. The current is expressed by the Butler-Volmer equation (see equation 7) with the flux of charge J_i or J_{el}, which is

described by first-order kinetics in case of ion transfer and by second-order kinetics for electron transfer at ITIES. The kinetics of the transfer can be expressed by the rate constants of the forward (k_f) and backward (k_b) transfer of an ion i with a concentration c_i as[69]

$$J_i = k_f c_i(w) - k_b c_i(o) \quad (21)$$

$$J_{el} = k_f c_{R1}(w) c_{O2}(o) - k_b c_{O1}(w) c_{R2}(o) \quad (22)$$

The indices R and O in equation (22) represent the reduced and oxidized species in the water and organic phase, respectively. The current within the liquid/liquid system is defined as positive with the transport of a positive charge from the water to the organic phase, and vice versa[69].

1.3.1 *The interface between two liquids*

Compared to electrochemistry at a solid/liquid interface, for which the charge distribution is described by the electrical double layer at the compact interface of a solid electrode, the interface between two liquids can be interpreted as two mirrored, diffusive layers, the so-called back-to-back double layer, each of them facing one of the electrolyte solutions. The two diffusive layers can be described by the Gouy-Chapman model. The charge distribution at the liquid/liquid interface is described by the modified Verwey-Niessen model[70], whereas in early publications, both diffusive layers are separated by a compact inner layer similar to the inner Helmholtz layer with a negligible potential drop[71]. An extension to first assumptions was the description of this inner layer as a sandwich structure of alternating solvent molecules from the aqueous and organic phase, respectively[72], or as a mixture of both solvents[73,74]. Girault and Schiffrin described additionally interfacial ion pairs of both electrolytes as a kind of specific adsorption at the interface[75]. The potential difference ($\Delta_o^w \phi$) at the interface can be expressed as the sum of these three layers, the interfacial potential drop within the inner layer ($\Delta_o^w \phi_{in}$) and the potential of the diffusive layers ϕ_2 in both phases as[69]:

$$\Delta_o^w \phi = \Delta_o^w \phi_{in} + \phi_2^o - \phi_2^w \quad (23)$$

1.3.2 *Electrochemistry at ITIES*

For electrochemical experiments at liquid/liquid interfaces, four electrodes are necessary, where one counter (CE) and one reference electrode (RE) are placed in each electrolyte solution (SY as organic and RX as aqueous electrolyte), respectively. For miniaturized electrochemical interfaces, the detected current is low (in the range of pA to nA) and a two electrode setup can be used, with one reference electrode in each phase. The polarized interface itself acts as the working electrode within the non-polarizable system. The electrochemical cell is expressed by the following notation[69]:

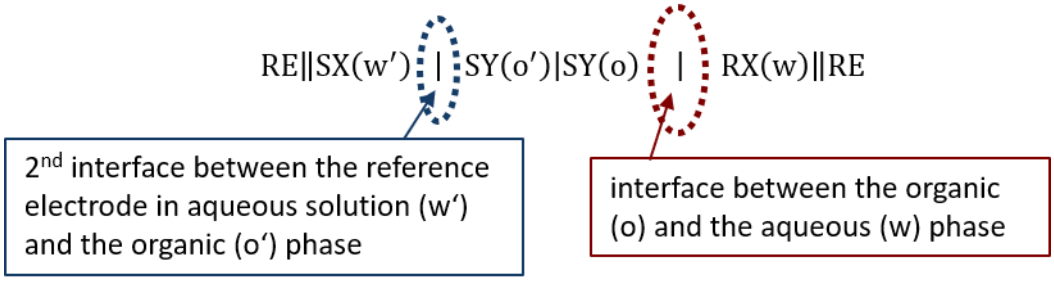

For the detection of standard potentials of a redox couple using a conventional three-electrode system, only the potential of the reference electrode has to be taken into account. In liquid/liquid interface measurements, the potentials of both reference electrodes, as well as the potential at the second liquid/liquid interface (represented as SX(w´)|SY(o´) in the notation, marked in blue) necessary for the reference electrode of the organic phase solution, are influencing the overall potential and the standard potential of the ion/electron transfer. The cell potential (E_{cell}) can be described as the difference between the potentials at the reference electrode in the aqueous phase (E_{aq}) and in the organic phase (E_{org})[69]:

$$E_{cell} = E_{org} - E_{aq} = \Delta_o^w\phi - \Delta_{o'}^{w'}\phi + E_j \qquad (24)$$

The term $(\Delta_{o'}^{w'}\phi + E_j)$ represents the potential difference at the interface of the organic electrolyte solution and the reference electrode of the organic phase with an aqueous reference solution. An aqueous (quasi-) reference electrode is used in most cases, due to the limited number of available non-aqueous reference electrodes. The reference electrode of the organic phase can be considered as an ion-selective-type electrode with the liquid junction (E_j) at the interface between the reference electrode (aq) and the

organic electrolyte solution. The potential window is defined or limited by the transfer of the electrolyte ions. In the electrochemical cell given above, the limit at positive potentials is the transfer of the R^+ ion from the aqueous to the organic electrolyte solution or the transfer of the Y^- ion from the organic to the aqueous solution. The limit at negative potentials is vice versa, the positive ion (S^+) of the organic electrolyte solution is transferred to the aqueous phase or the X^- (aq) ion to the organic electrolyte solution. Similar to the standard hydrogen electrode, the organic electrolyte tetraphenylarsonium tetraphenylborate (TATB) is defined as the zero potential[69] by

$$\Delta_o^w \phi = 0 \qquad (25)$$

within the system, which is used to determine the half-wave potential of an analyte. The center of the current-potential curve is defined as zero, because the ion size, the diffusion coefficients in water and the potential for the transfer towards the aqueous solution are equal for TA^+ and TB^- (or at least very similar that they can be assumed to be equal). This is also called the TATB assumption[76]. Hence, adsorption phenomena at the interface, the energy of the transfer back to the organic solvent or the solvation of the ions in both phases are not taken into account in the TATB assumption[77].

1.4 Electrochemistry at nano-interfaces

Electrochemistry at micro- and nanometer-sized interfaces using nanopipettes[78,79] and solid-state supports such as membranes[80–86] is a promising tool for analytical applications as the miniaturization of interfaces results in an enhanced signal showing increased charge and mass transfer compared to any macroscopic approach, which is also the case for electrochemical reactions at the ITIES[11]. Additionally, miniaturization reduces the ohmic drop and leads to a reduced capacitive current[87,88]. With nanoporous arrays, a large number of single interfaces can be achieved, leading to an enlarged electrochemical signal by multiple interfaces. A detailed understanding of the kinetics of ion transport can be investigated at small scale interfaces, which was reported first by the groups of Girault[89,90] and Mirkin[78], and for electron transport by Bard and co-workers[91]. The diffusional behavior at micro- and nanopores or -pipettes depends on the location of the interface

(see Figure 3) resulting in either a linear diffusion profile within the pore or pipette, or in a radial diffusion at the orifice of the pore/pipette[92,93]. For ITIES, diffusion occurs in both directions from the interface facing the aqueous and the organic electrolyte, respectively[68].

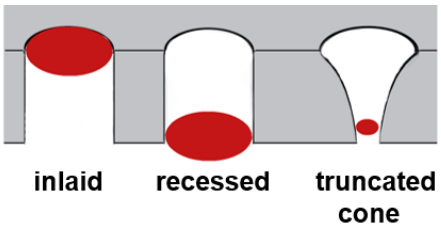

Figure 3 Scheme of three different pores with interfaces (marked in red) located at different positions within the pores, namely inlaid and recessed for pores with parallel pore walls, and a recessed interface for a truncated cone-shaped geometry.

The current I_i at micro- and nano-ITIES for the transfer of an ion i is described by the modified Cottrell equation (see equation 13) for radial diffusion towards an inlaid interface located at a pore/pipette orifice with radius r_o[94]:

$$I_i = 4nFDc_i r_o \tag{26}$$

With the bulk concentration of the ion i (c_i), the Faraday constant (F), the diffusion coefficient (D) and the number of participating electrons (n). For a recessed interface at the position (L) within the pore (which can be also seen as the length of the pore/pipette), the limiting current is described by[94]

$$I_i = \frac{4\pi nFDc_i r_o^2}{4L + \pi r_o} \tag{27}$$

For a truncated cone-shaped pore or pipette, both radii of the orifices have to be considered with $r_o < r_L$ resulting in the following equation[37].

$$I_i = \frac{4\pi nFDc_i r_o r_L}{4L + \pi r_o} \tag{28}$$

Single pores within a solid material can be arranged either ordered within an array with defined distances between single pores or randomly distributed in an ensemble[82]. The distance or pore-to-pore separation influences the diffusion profiles of the array/ensemble, resulting in either overlapped diffusion regions for pores in close proximity to each other (see Figure 4 A), or in individual diffusion at each pore (see Figure 4 B)[30].

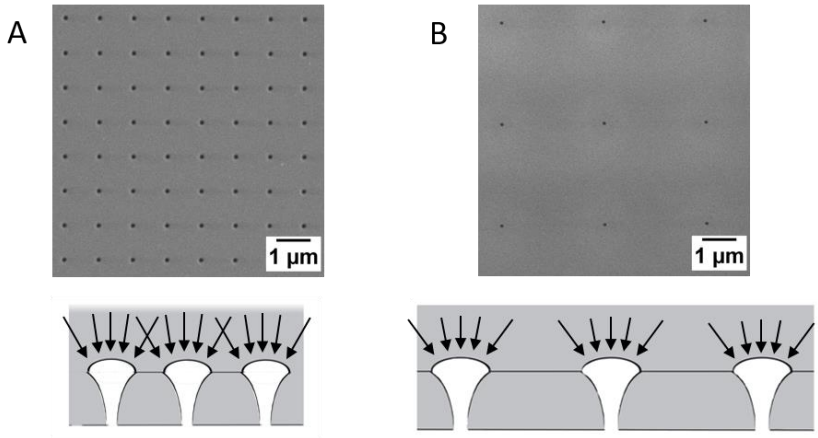

Figure 4 Influence of the pore-to-pore separation ratio within a pore array. For closely arranged pores as shown in the SEM image in A, the radial diffusion at a single pore results in an overlaid diffusion profile for the overall array as schematically represented below. Whereas for a large pore-to-pore separation as shown in the SEM image in B, the diffusion profiles are not overlapping and individual hemispherical diffusion at the pores, as indicated in the corresponding schemes, is governing the overall response.

Numerical simulations compared to experimentally obtained cyclic voltammograms at nano-ITIES within pores[95,96] or pore arrays[97–99] were used to localize the interfaces. Also, simulations were performed to identify individual radial diffusion at the pores with determining a separation ratio between the pore radius (r_a) and the distance between single nanopores (r_c)[97,100] with a critical value for individual diffusion of[30]:

$$\frac{r_c}{r_a} > 56. \tag{29}$$

2 Scanning probe techniques

2.1 Atomic force microscopy

Since the introduction in 1986 by Binnig, Quate, and Gerber[101], AFM developed into an important tool in surface characterization, ranging from material science to biology[102]. In AFM, the force interaction between a surface and a sharp tip located at the end of a cantilever is detected. These forces can be described by the Lennard-Jones potential and can be divided into attractive or repulsive forces. The electric double layer interactions or interactions resulting from overlapping atomic orbitals are repulsive, whereas capillary, electrostatic and Van der Waals forces are attractive. Other forces such as chemical, hydrophobic, steric or magnetic forces may be attractive or repulsive. The tip is located at the end of a flexible cantilever, typically made of silicon nitride or Si. The AFM tip can be additionally modified with e.g. nanotubes[103], nanowires[104], microneedles[105], colloids[106] or single molecules[107] for imaging high aspect ratio features or for single-molecule force spectroscopy experiments. Critical for AFM probes is their resonance frequency (f_0), spring constant (k) and the quality factor (Q), which should be chosen carefully in respect to the targeted application and investigated sample, respectively. The parameters describe the stiffness of the AFM cantilever and with this the ability to react on external forces. With high resonance frequencies in the range of 1 – 500 kHz and with small spring constants (0.07 - 100 N/m), forces of 10^{-6} to 10^{-12} N can be measured, without issues that the cantilever is influenced by external vibrations. Different operation modes are available with respect to the characteristics of the substrate under investigation. The contact mode is preferably used for hard surfaces due to strong force interaction between tip and substrate. The surface can be scanned in either constant height or constant force mode (also called topographical mode). The tip is either kept in a defined position in the z-axis, recording the variations in force, or a defined force is kept constant and the height is adjusted when the force interaction between tip and sample varies while scanning in x,y -direction. In the dynamic mode, the tip oscillates in a defined distance above the surface. This mode can be either frequency-modulated or amplitude-modulated[108]. For the investigation of soft samples, the tapping mode[109] (or intermittent mode) is used that results from the amplitude-modulated mode but additionally strikes the sample surface

on every oscillation[109]. The tip is oscillating close to its resonance frequency and the change in the amplitude due to tip-sample interaction is detected. Additionally, a phase shift indicates a varying adhesion or viscosity of the surface material. In all operation modes, the interaction results in a bending of the cantilever, which is detected - in most cases - via a laser focused at the backside of the cantilever and reflected to a split photodiode. The detected photocurrent signal is then converted into an output voltage, which is used via an electronic feedback system to maintain a fixed force, or amplitude or resonance frequency of the AFM probe by the z-piezo when the cantilever is bent due to the force interactions. Due to these interactions, the topography of a sample can be mapped and additional information about mechanical properties of the sample can be obtained and different materials can be distinguished due to varying adhesion between the tip and the sample surface.

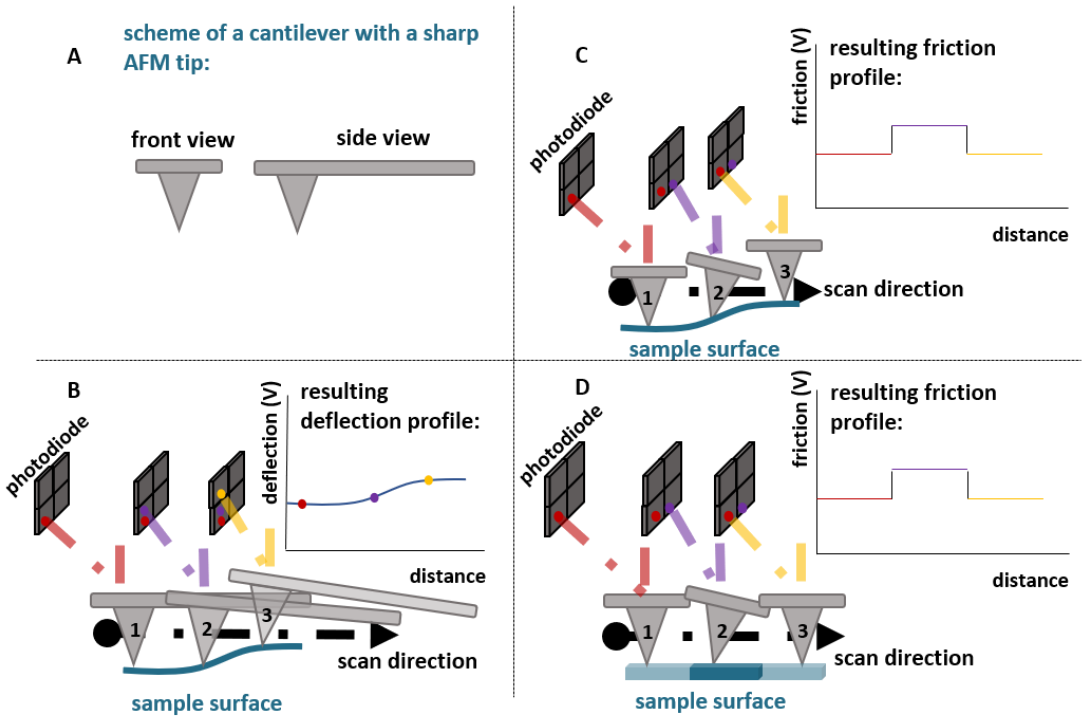

Figure 5 Scheme of an AFM probe in front and side view (A); the detection of the deflection and friction signal in AFM contact mode with corresponding signals shown as profile (B-D). The AFM probes in (C-D) labeled with 1-3 show the AFM probe at three different positions representing the movement of the tip in the scan direction.

AFM measurements can be performed in air, liquid and under vacuum condition, whereas the latter is most sensitive and atomic resolution can be achieved under optimized conditions[110]. Tip artifacts, as shown in Figure 6, can be minimized or avoided by suitable experimental conditions and a careful adjustment of scan parameters. Nevertheless, the results have to be interpreted carefully. So far, a variety of advanced AFM modes were developed e.g., peak force tapping™ AFM[111] gaining additional information on adhesion, and Young modulus, force volume mode[112], enabling the mapping of interactive forces by recording a set of force curves, scanning Kelvin probe microscopy[113] recording the contact potential difference between the tip and a surface, and especially AFM-SECM, which is discussed in detail in 2.3.

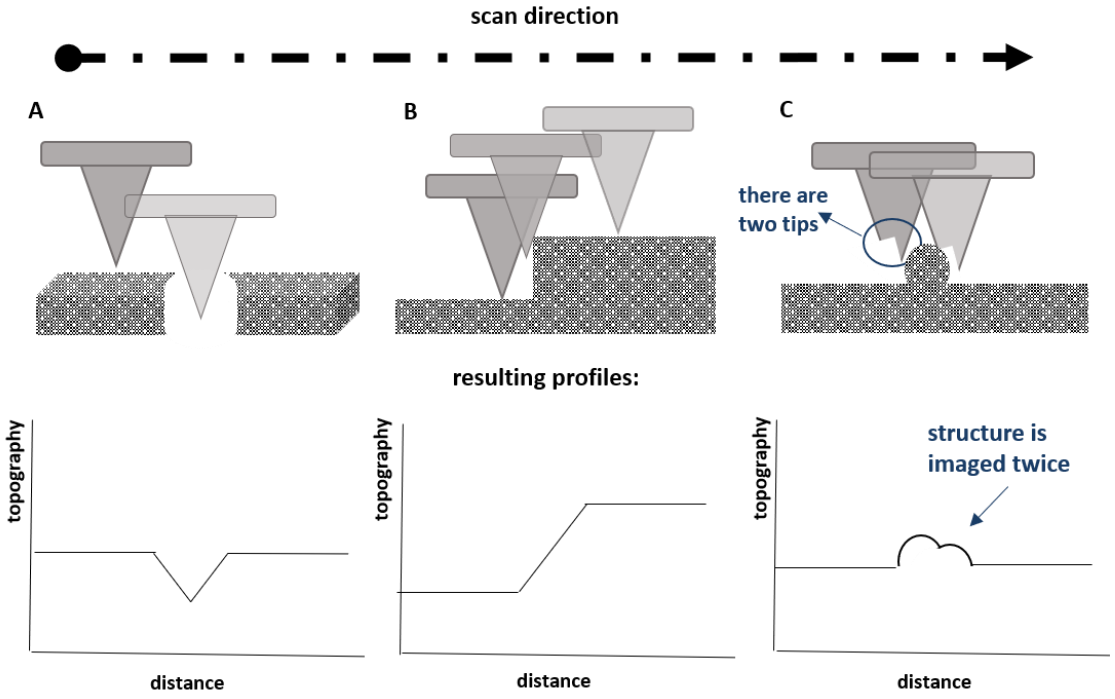

Figure 6 Scheme of possible artifacts in AFM measurements. The topography image may reflect the shape of the AFM tip, in case that the structure of the sample has smaller dimensions than the tip (A), edges might be also imaged not correctly (B). Contaminated AFM probes may result in double or multiple imaging of the actual sample structure (C). The displayed tips in A-C represents one tip at different times moving in the scan direction.

2.2 Scanning electrochemical microscopy

In SECM, which was first reported in 1989 by Bard and coworkers[114], a nano- or microelectrode is scanned across a sample surface of interest mapping local electrochemical processes. SECM can be applied in many fields research fields including life sciences[115] or corrosion studies[116], and investigations of amperometric, potentiometric or conductive signals at homogeneous and heterogeneous samples can be monitored[117]. A comprehensive description of SECM instrumentation, SECM tips, and applications in various fields is given elsewhere[117]. Briefly summarized, the positioning and movement of the SECM tip is realized - in most cases – by stepper motors and piezoelectric devices. A three- or four-electrode set-up is used consisting of the scanning UME as working electrode, a counter, and a reference electrode and if required, the substrate as the second working electrode. In a first step, the SECM tip is brought in close proximity to the substrate's surface, which is realized by recording approach curves (Figure 7 A, B). In the presence of a redox active species with fast electron transfer characteristic, the current is measured at the tip, which is biased at the required potential while approaching to the surface. In bulk solution, the conversion of the redox active species results in a steady-state current signal. When the tip is in a distance of several radii of the electroactive radius of the SECM tip to the surface, the current signal is influenced depending on the nature of the substrate. At insulating substrates, the current decreases due to hindered diffusion of the redox mediator to the SECM tip, which is termed 'negative feedback'. In the presence of a conductive substrate, the converted redox species can be regenerated at the sample surface resulting in an increased current signal, called 'positive feedback'. To determine the distance between the SECM tip and the surface, the resulting approach curves are compared to theoretical curves obtained via numerical simulation. While imaging, the distance between tip and substrate plays a crucial role. For relatively flat samples, the scanning can be performed in constant height, whereas for rough surfaces (influence of roughness corresponds to the size of the SECM tip), approaches have been introduced to keep a constant distance between the sample and the SECM tip (Figure 7 D). This can be realized by applying a horizontal vibration to the SECM tip, which results in damping in the oscillation with varying distances. This damping can be measured either by optical[118] or piezoelectric detectors[119] as published by Schuhmann and co-workers, or by the integration of a tuning fork, as presented by

James et al.[120]. The damping is used as the signal for a feedback loop to keep the distance constant – this mode is adapted from scanning nearfield microscopy (SNOM) and termed shear force mode. A constant distance can be further detected in the constant current[121] or constant impedance mode[122]. A similar approach keeping the electrode area in a defined distance is given by SECM with soft-stylus probes[123], whereas the insulating material is in contact with the sample surface. The SECM tip is bent due to the flexible insulating material. Next to different positioning modes, the imaging of a sample can be also divided into different modes. In the generation/collection mode[124], the electrochemical species is generated at the SECM tip and then detected at the substrate's surface or vice versa (Figure 7 C). A variation of the generation/collection mode is the redox competition mode[125], in which the same electrochemical reaction is detected by both, SECM tip and substrate.

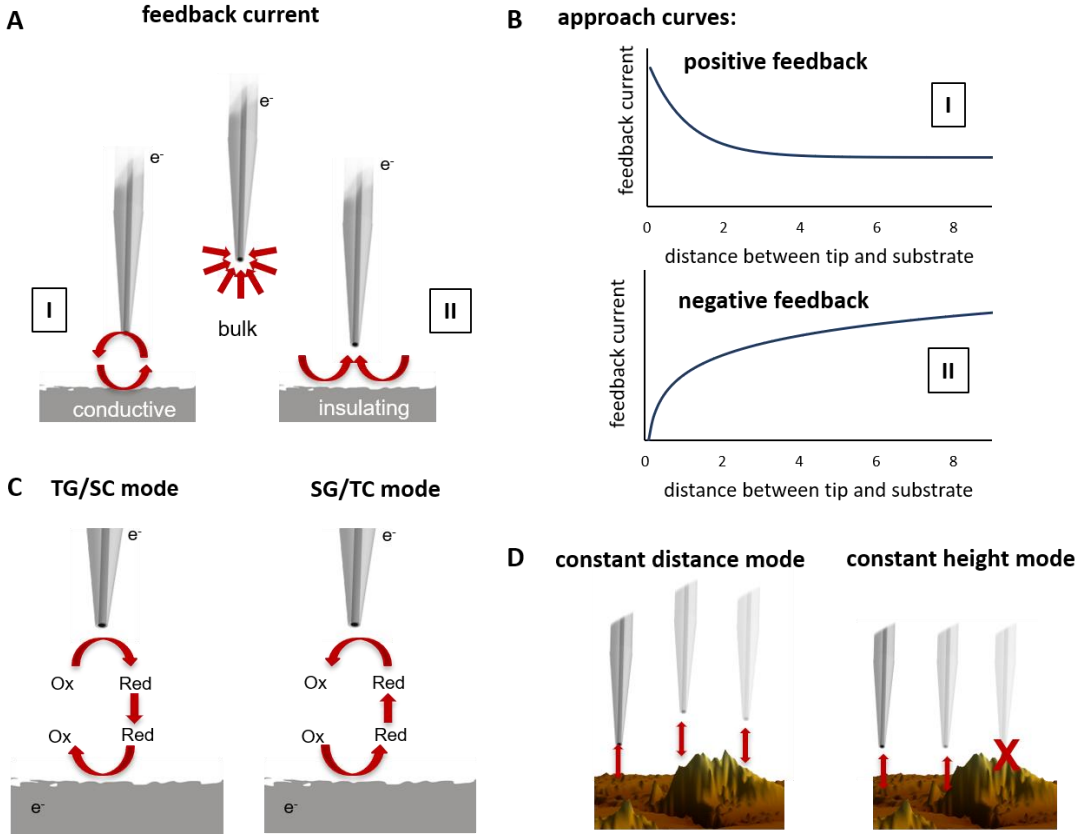

Figure 7 Schemes of different operation modes used in SECM: The feedback mode (A) with corresponding approach curves (B), tip generation/ substrate collection (TG/SC) and substrate generation/ tip collection (SG/TC) mode (C) and modes related to the detection in either constant distance or constant height (D).

In the so-called direct mode[126], the applied potential between the tip and a substrate can be used for localized modification of the sample, by deposition[126] or by generating localized pit corrosion[127]. SECM has also been combined with a number of analytical methods, e.g. optical microscopy[128], IR spectroscopy[129], surface plasmon resonance[130], and other scanning probe techniques. For example, by replacing the SECM electrode with a micropipette, which is known as scanning ion conductance microscopy (SICM), the conductance between a reference electrode located in an electrolyte solution within the pipette and the reference electrode in the bath solution is detected[131]. SICM is frequently used to map the topography of soft samples given a non-invasive approach. By combining both SECM and SICM, the topographical information detected by SICM can be directly correlated to electrochemical processes at the sample surface detected by SECM. A miniaturized electrode can be either integrated into the pipette as a ring electrode surrounding the orifice of the pipette or in a double (or multiple) channel arrangement, using one barrel of the pipette filled with electrolyte solution for SICM and another barrel filled with the electrode material for SECM (Figure 8 A). The combination with AFM is described in detail in the following section.

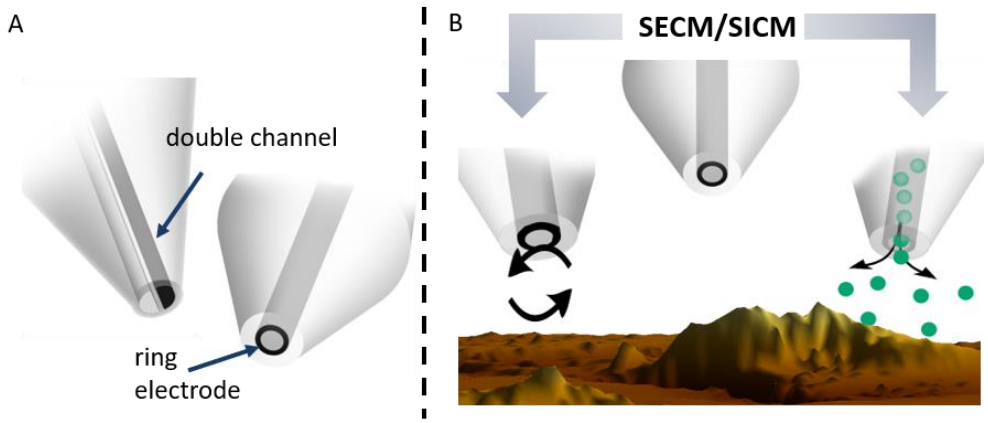

Figure 8 Scheme of combined SECM/SICM tips with varying geometries (A); the black area shows the electrode material, scheme for the different imaging principles (B): the SECM ring-electrode is detecting electrochemical processes, whereas the conductance between two reference electrodes (indicated as green dots) is used to determine the topography. A. Holzinger, C. Steinbach, C. Kranz, „Chapter 4: Scanning Electrochemical Microscopy (SECM): Fundamentals and Applications in Life Sciences“, in Electrochemical Strategies in Detection Science (Ed. Damien W. M. Arrigan), RSC Detection Science, 2015. *Adapted from Ref. [115] with permission from the Royal Society of Chemistry.* https://doi.org/10.1039/9781782622529-00125.

2.3 AFM-SECM

First published by Macpherson and Unwin in 2000[132], the combination of AFM and SECM enables imaging of high-resolution topography and electrochemical processes by detection of force interaction between a conical tip and a surface (AFM) and the electrochemical signal related to surface properties (SECM). Whereas in this publication, a cantilever-shaped conical electrode served as the AFM tip and simultaneously as the SECM electrode, the independent detection of an electrochemical signal by a recessed AFM tip-integrated electrode was first realized by Kranz et al.[133]. First imaging of soft biological samples was reported for the investigations of the activity of glucose oxidase[134] or horseradish peroxidase[135] by AFM in tapping or contact mode, respectively, and SECM generation/collection mode. Modification of AFM-SECM probes by immobilization of redox mediators, namely, tip-attached redox mediator (TARM)-AFM-SECM[136] and investigation of immobilized macromolecules or DNA in the so-called molecule touching (Mt)/AFM-SECM[137] was shown by Demaille and co-workers. For example, the detection of proteins by measurements in AFM tapping mode and SECM feedback mode with a lateral resolution in the topography of a few 100 nm[138] was reported. The immobilization of DNA sensors to AFM/SECM probes was also realized by modification of the tip-integrated electrode with polypyrrole[139]. Further investigations of biological samples were realized by Hirata et al.[140], mapping glucose oxidase immobilized on highly oriented pyrolytic graphite (HOPG) in tapping mode, and by Kranz and co-workers with the localized mapping of enzymatic consumption of glucose by detection of H_2O_2 with a horseradish peroxidase-modified AFM-SECM probe in AFM contact mode[141]. Besides investigations of biological samples, AFM-SECM can be used for visualizing corrosion processes and the electrochemical behavior of metal compositions. Macpherson and co-workers investigated the behavior of metal anodes by AFM-SECM[142] and Davoodi et al. detected active pitting and local corrosion of mixed Al alloys by an L-shaped AFM tip with an integrated Pt wire as SECM electrode[143–145]. The localized corrosion of copper in acidic solution was reported by Izquierdo et al.[146,147]. The dissolution of calcite was detected by AFM-SECM[148], whereby the tip-integrated Pt electrode was used for water oxidation by an applied anodic potential and afterward used for detecting pits within the calcite in the acidic region by the generated protons. Investigations of diffusional transport at

nanopores by AFM-SECM was reported for the transport of glucose[149], of redox-active species[150], as well as for electrode arrays within closely-spaced microdiscs[150,151].

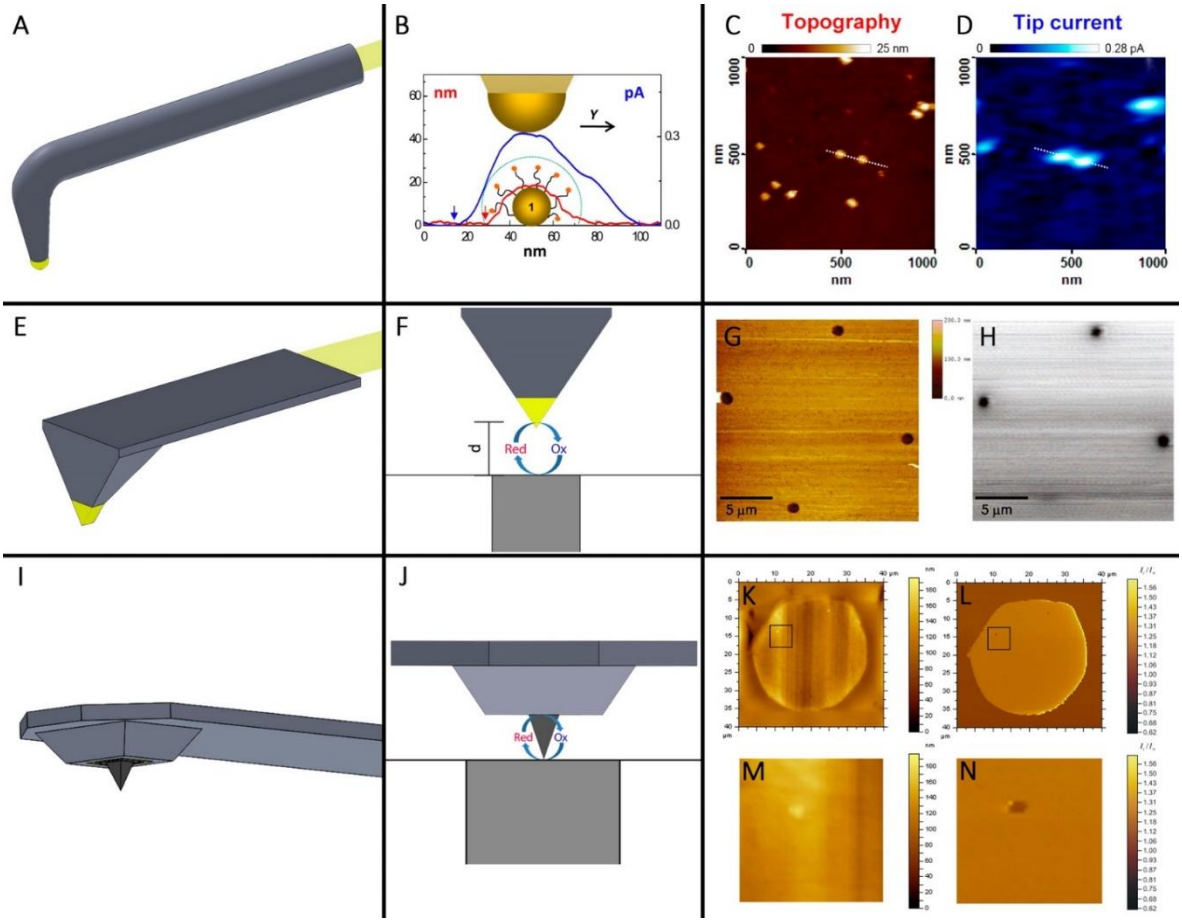

Figure 9 Overview on different AFM-SECM probe geometries: Schemes of a hand-made AFM-SECM probe with a conical microelectrode with a spherical apex[152] (A); batch-fabricated AFM-SECM probe with a triangular, conductive AFM tip[153] (E) and commercial AFM probe modified by a conductive layer conductive BDD layer and insulated, followed by the exposure of a recessed frame electrode by FIB-milling[154] (I). The detection principle of the electrochemical signal is depicted in B, F and J and corresponding results of AFM-SECM measurements are shown for the detection of Au particles in Mt/AFM-SECM[152] (C), individual recorded topography (G) and current signal (H) with a conductive AFM tip[153] and simultaneously detected topography (K, M) and current signal (L, N) of an UME with an AFM-SECM probe with a recessed conductive BDD electrode; magnified view of the results (M, N) show the blocked current signal of the UME due to a diamond particle at the UME surface [154]. Reprint with permission from Eifert, A., Kranz, C. *Anal. Chem.* **2014**, *86*, 5190−5200. Copyright 2019 American Chemical Society. https://doi.org/10.1021/ac5008128.

Different geometries and fabrication procedures of AFM-SECM probes have been published so far, for example, hand-made[155,156], batch-fabrication[153,157,158] and modification of commercially available probes[140,159–161], of which some examples are depicted in Figure 9. According to the fabrication process, different electrode shapes and sizes are possible, namely ring shaped[162], square[163], frame[133,159], disk[164], cone-shaped[132] or spherical[165]. Especially, FIB processing enables manufacturing a wide range of different geometries, electrode shapes, and sizes, or different arrangements of the electrode area within the AFM-SECM probe[133,161,166]. This contribution is based on the fabrication of recessed frame electrodes as first reported by Kranz et al.[133]. This method implies the modification of a commercially available AFM probe with a thin adhesive layer of Ti and a conductive gold layer, followed by insulation with Si_xN_y, Si_xN_y/SiO_2 mixed layers or Parylene C.

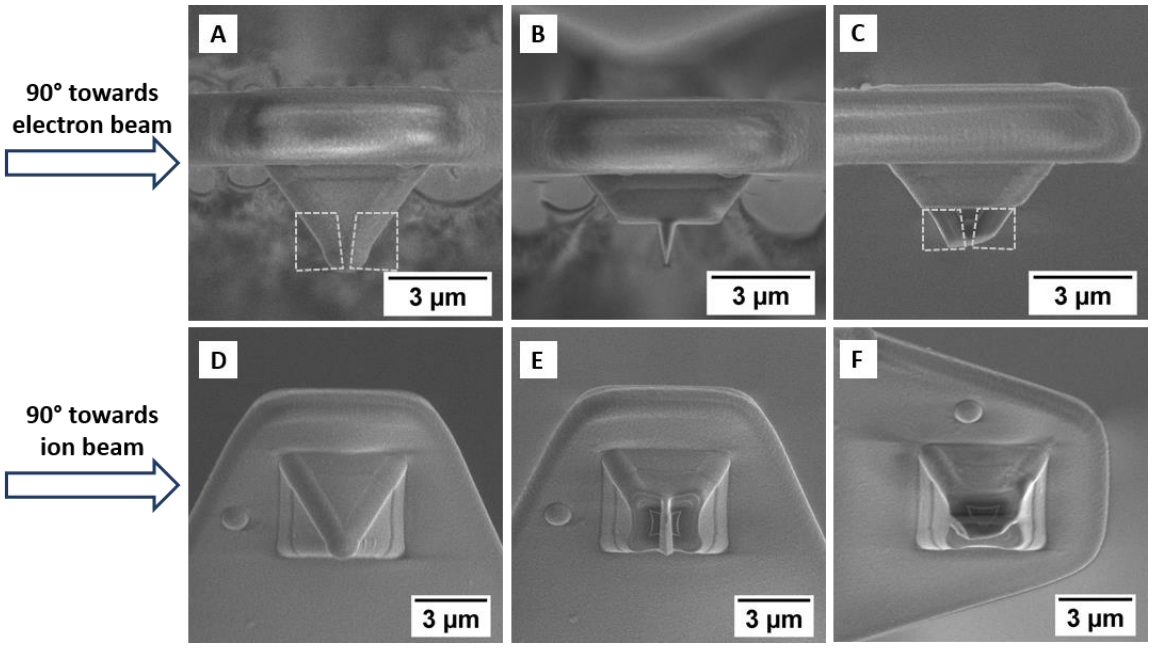

Figure 10 SEM images of an AFM-SECM probe during FIB-milling in two different perspectives, either perpendicular towards the electron or ion beam, indicated on the left side: an insulated AFM-SECM probe with mark-ups of the area, which is removed by FIB (A) and after FIB-milling (B). By mounting the AFM-SECM probe in 90° to the original position and removing the marked region in (C) by FIB-milling, the electrode is exposed with a thorn located in the center. The SEM images depicted in D-F show the Au and the insulation layers during the single fabrication steps, 90° towards the ion beam and 52° towards the e-beam, respectively. Acceleration voltage: 3 kV and beam current: 36 pA.

The exposure of the recessed electrode area is done by FIB-milling, which is also used for the preparation of a new AFM tip located in the center of the square formed by the frame-shaped electrode. The individual fabrication FIB-milling steps are summarized in Figure 10. The resulting Au frame electrode with a frame width of about 100 nm, depending on the thickness of the deposited Au layer, can be varied in size according to the desired application. Additional modifications of the tip-integrated electrode result in advanced probes suitable for detection of specific analytes. The AFM tip produced by FIB-milling is located in the center of the Au frame. In this case, the tip is reshaped from the original Si AFM probe, but variations in position are also possible and L-shaped AFM-SECM probes made of insulating material (Parylene C) and located next to the electrode area were reported and used for the mapping of carbon nanotubes[159].

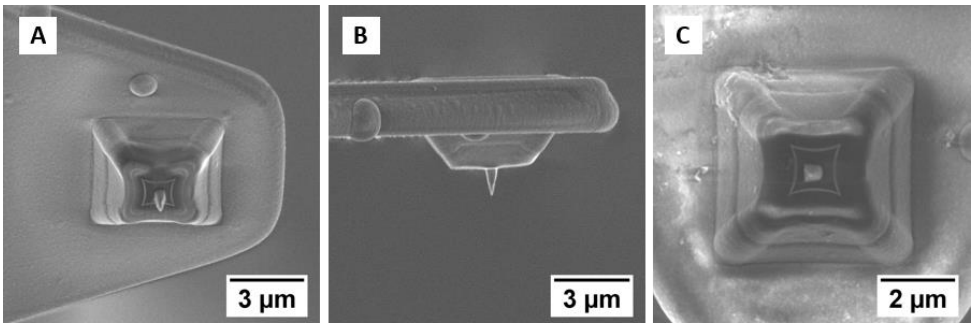

Figure 11 SEM images of the final AFM-SECM probe imaged in different perspectives as shown in Figure 10 (A, B) and top view of the final Au frame (C); Acceleration voltage: 3 kV and beam current: 36 pA.

A precise characterization of the actual geometry of AFM-SECM probes is essential and small variations, the RG values, artifacts within the AFM-SECM probe and the position of the tip at or within the AFM-SECM probe[167,168] show an impact on the current signal, which was shown by simulations for AFM-SECM probes with the AFM tip as conical electrode. Additionally, the effect at the border between insulating and conductive regions of a sample has been shown by simulations for AFM-SECM probes with a recessed electrode geometry predicting an overlapped current signal of the insulating and conductive region, respectively[169].

Different electrode materials can be used for AFM-SECM. Gold[133,156,170,171] or platinum[132,159] are most commonly utilized, but also boron-doped diamond[154,172], carbon nanotubes[164] or conductive colloids[165] have been reported so far. Additionally, modification of gold electrodes with a Pt/C composite deposited via IBID[173,174] enables an easily tunable electrode area, adjustable to the requirements of the targeted AFM-SECM measurements.

3 FIB/SEM tomography

In scanning electron microscopy (SEM)[175], a high energy electron beam is generated by a thermionic or field emission emitter, focused and de-magnified by a set of electromagnetic lenses and is finally scanned over a defined area of the sample surface. When the energetic electrons penetrate the sample, elastic and inelastic scattering occurs at atoms of the sample, whereby the trajectories of the electrons are changed and energy is transferred during scattering events. This interaction with the sample causes the emission of secondary electrons (SE), as well as characteristic X-rays and bremsstrahlung. The actual trajectories of the primary electrons within the sample volume can be described by Monte-Carlo simulations[176]. Incident electrons, which are able to leave the sample after scattering are called backscattered electrons (BSE). The interaction between the primary electron beam and the sample thereby depends on the acceleration voltage of the electron beam, as a higher acceleration voltage results in a higher penetration depth within the sample (Figure 12). Additionally, the yield of detectable electrons is dependent on the composition and density of the sample material and the incident angle of the electron beam towards the sample surface.

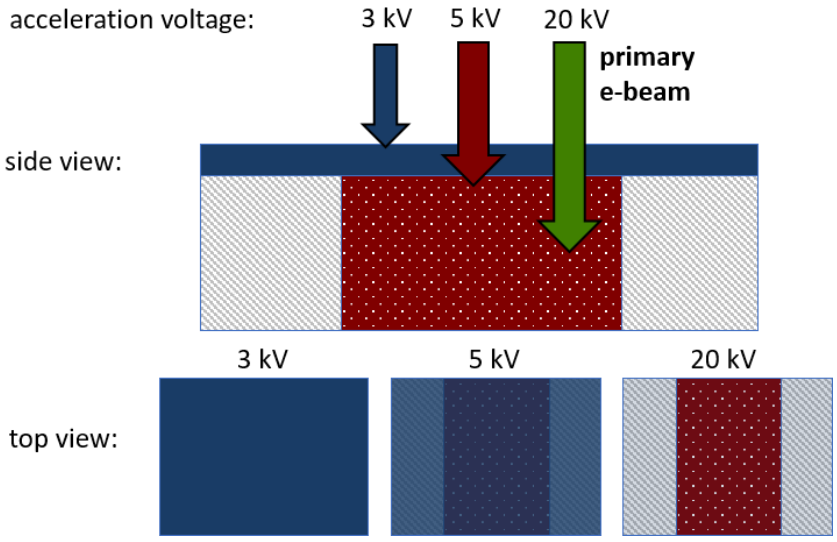

Figure 12 Scheme of a model sample and the influence of the acceleration voltage of the primary e-beam (represented by three arrows for three different acceleration voltages) in the detected SEM (top view): the higher the applied voltage, the more of the inner structure of a sample is visible in the SEM image.

Therefore, as they originate from a certain depth of the sample, the amount of BSE able to leave the sample depends strongly on density and composition, as well as crystal orientation. SE are sensitive for surface relief, due to their lower energy content (50 eV and less). Only SE emitted near the sample surface are able to leave the sample and be collected by a detector. The contrast in SEM images results from varying amounts of detected electrons per pixel. SEM gives, therefore, information on the localized structure of materials of known composition within the sample and the surface structure. In SEM, conductive samples can be easily imaged, whereas imaging of insulating materials may cause distortions due to charging effects. The most commonly used detector in SEM is the Everhart-Thornley detector (ETD)[177] based on the conversion of electrons into photons by a scintillator, enhancing the signal by $10^5 – 10^6$ times within a photomultiplier and signal collection by a computational read-out system. The ETD is located perpendicular to the optical axis of the primary electron beam within the chamber of the SEM. State-of-the-art microscopes provide an enhanced resolution by using an electron detector placed above the objective lens pole pieces within the electron column, which are referred to as through-the-lens detector (TLD). The use of the so-called immersion mode, in which the magnetic field from the objective lens pole piece is extended to the sample surface, attracts SE to travel towards the TLD. SEM is used primarily as an imaging method, but modification and structuring of samples are also possible with a focused electron beam[178]. A beam of accelerated ions instead of electrons is preferred for nano- and microstructuring of materials. FIB is highly suitable for mask-less tunable fabrication steps compared to other microfabrication processes, e.g. e-beam lithography[179] or deep reactive ion etching (DRIE)[83]. For FIB, mostly a gallium ion source is used[180]. FIB plays a significant role, ranging from microfabrication, investigation of materials perpendicular to the surface by cross-sectioning, TEM sample preparation, up to deposition of metals and insulator materials by ion beam induced deposition (IBID) either as protection layer or for surface modification. Examples for FIB applications relevant to the research presented within this thesis are the exposure of the electroactive area in AFM-SECM probes[133,160,161], fabrication of nanoporous arrays in solid-state materials[31–34], cross-sectioning of nanopores for investigation of electron or ion beam-induced variations in pore shapes[36] and fabrication of high-aspect AFM probes for investigation of such nanopores by FIB-milling considering e.g. the surface tilt or other parameters[181]. With the availability of

FIB/SEM dual-beam instruments[182], the investigation and reconstruction of materials by FIB/SEM tomography[183] becomes possible and structures of several nanometers can be resolved[184,185]. By an automated successive FIB milling and SEM imaging of the freshly exposed faces, a whole sample volume can be investigated with an axial resolution of 3 – 30 nm[10]. The acquired image stack, which represents the sampled volume, is processed by a 3D software, whereby sample drifts or variations in contrast during FIB/SEM image acquisition can be corrected. The 3D reconstruction of the actual morphology of the sample gives access to the porosity and inner structure with nanometer resolution. Figure 13 gives an overview of FIB/SEM tomography and 3D reconstruction of a nanoporous structure, which is discussed in detail in section 6. FIB/SEM tomography can be applied to a large variety of scientific questions, such as the investigations of nanoparticles in dye-sensitive solar cells[14] and of nanotube arrays[3]. Investigations of the inner structure of micro- and nanoporous materials[12,13] or Al-Si alloys[186], but also the investigation of biological[15,16] and geological[16] samples have been reported.

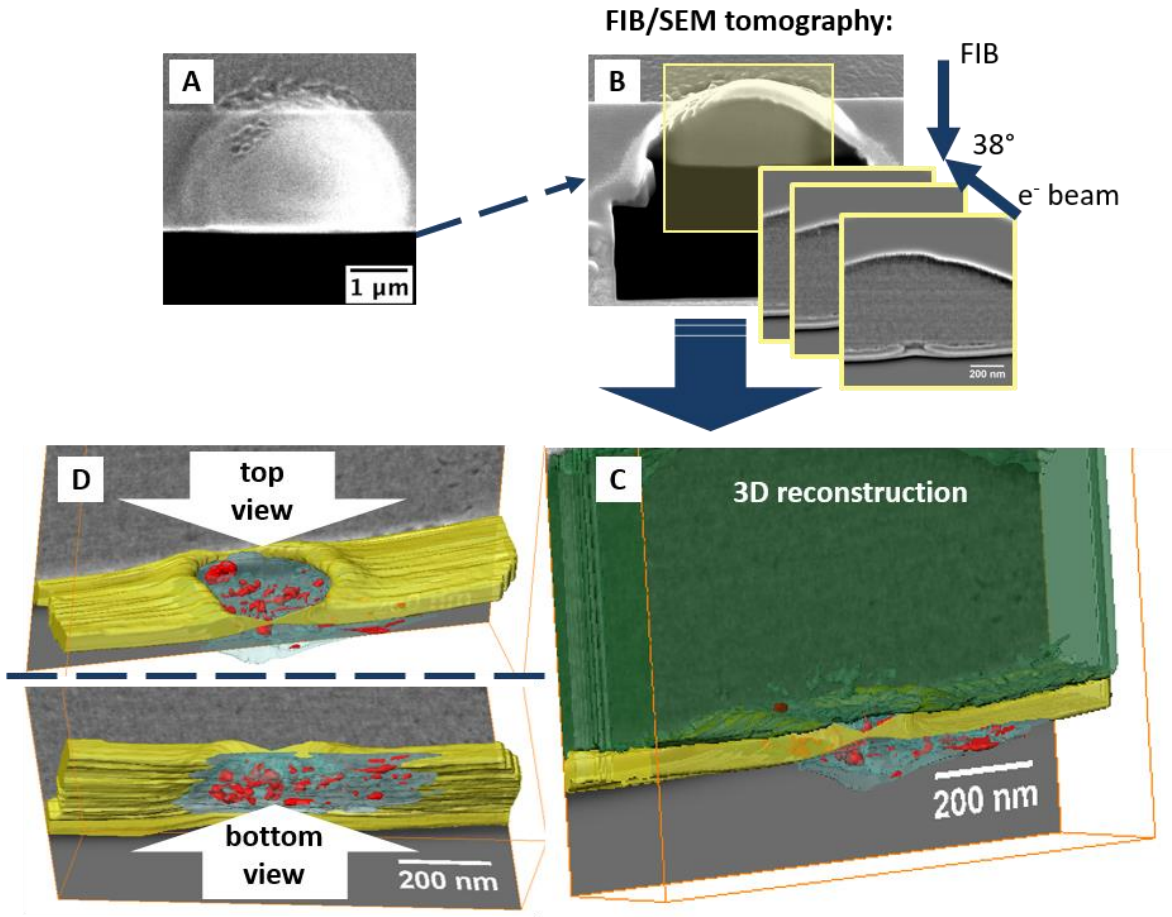

Figure 13 FIB/SEM tomography: For 3D tomography, the sample of interest is stabilized with a Pt/C protection-layer and a cross-section is milled by FIB. The FIB-induced SE image in A shows the perspective of the ion beam, whereas in B the perspective of the SEM with a tilt correction of 38° towards the ion beam is shown (the actual angle between ion and electron beam is 52° and defined by the spatial arrangement of the e-beam and ion-beam columns). The yellow-framed SEM images represent single slices after consecutive FIB milling. After drift and contrast correction, the slices can be reconstructed as a 3D image (C). The structure can be presented in different perspectives (D). A. Holzinger, G. Neusser, B. J. J. Austen, A. Gamero-Quijano, G. Herzog, D. W. M. Arrigan, A. Ziegler, P. Walther, and C. Kranz, *Faraday Discuss.*, 2018, **210**, 113. *Adapted from Ref.* [187]. *Distributed under the license Creative Commons Attribution-NonCommercial 3.0 Unported (CC-BY-NC 3.0),* https://creativecommons.org/licenses/by-nc/3.0/.

VI. Results and discussion

In the following, the results obtained by modifications of AFM-SECM probes are presented. In chapter 4, the influence of the individual pretreatment steps necessary for the mounting of the AFM tip-integrated PB/NIHCF bilayers as H_2O_2 -sensitive material into the experimental setup is evaluated in respect to sensitivity and stability. First results for the detection of localized H_2O_2 generation at an UME is presented in 4.3.3. In contrast, to the modification of AFM-SECM probes with the active sensor material, in chapter 5, the modification of AFM-SECM probes with an additional metal layer for tip-integrated pH sensors is evaluated. First measurements have already been reported by Jong Seok Moon[188], who fabricated the Ir and Sb integrated AFM tips, respectively, used in chapter 5. Within this thesis, the performance in pH sensing of these modified AFM-SECM probes is presented and first AFM-SECM measurements of localized surface changes together with ongoing pH changes during the dissolution of calcite crystals are detected (5.3.2).

In chapter 6, the diffusion at nanoporous membranes is presented visualizing the diffusion behavior dependent on the pore-to-pore separation of individual nanopores within an array and showing the capability of AFM-SECM with a conductive AFM tip for the detection of localized electrochemical processes[181]. The nanoporous solid-state materials, which are presented in this thesis, were fabricated by FIB milling enabling readily tunable geometries of nanopore arrays. Although, FIB fabricated nanoporous membranes were already investigated for electrochemical processes at the liquid/liquid interface[30,31], the actual location of the interface between both liquids within these nanopores is not verified yet. The actual pore shape and implantation of Ga^+ ions during FIB milling might change the hydrophilicity of these nanopores and with this change the behavior of these devices used as support material for electrochemistry at liquid/liquid interfaces. This was not considered so far in previous publications and will be evaluated in chapter 6, among other investigations, by FIB/SEM tomography.

4 H_2O_2 sensing with AFM tip-integrated electrodes

4.1 Introduction

Hydrogen peroxide (H_2O_2) plays a crucial role in biological systems as reactive oxygen species (ROS)[189], as a product of the oxygen reduction reaction (ORR) in acidic media[190], and thus, H_2O_2 is important for developing new catalytic materials in energy storage[191]. It is also an important species in environmental water and atmospheric samples indicating phototoxic effects and environmental pollutions[192]. Next to others, like fluorometric[193] or spectrophotometric[194] methods, H_2O_2 can be determined by electrochemical approaches[195]. First detection approaches with solid metal electrodes were reported for the oxidation of H_2O_2 at potentials of + 0.5 – 0.8V vs. NHE[17] in acidic or neutral solutions depending on the electrode material, or H_2O_2 reduction at 1.76 vs. NHE[196]. Hence, reduction of O_2 and other electroactive compounds present in samples, such as ascorbic acid in biological samples, might interfere with the electrochemical detection of H_2O_2[197]. Additionally, the H_2O_2 conversion shows large overpotentials at metal electrodes[196]. Therefore, electrode modifications have been investigated enabling the conversion of H_2O_2 at moderate potentials with enhanced sensitivity for H_2O_2[195]. Examples for such sensors are electrodes modified with enzymes embedded e.g. in redox polymers[198] or nano-sized materials, such as multi-walled carbon nanotubes with nanoparticles[199]. Metal hexacyanoferrates and especially Prussian Blue (PB)[19] show also a promising response in H_2O_2 detection via the Fenton reaction[200]. PB, with $KFe(II)[Fe(III)(CN)_6]$as the soluble and $Fe(III)_4[Fe(II)(CN)_6]_3$ the insoluble salt, and analogues metal hexacyanoferrates form a face-center-cubic structure with iron(II) and iron(III) ions in the network of the complex[201]. The electrocatalytic activity of PB is related to the FeN_x units in the crystal framework determined by x-ray diffraction (XRD) and Fourier-transform infrared spectroscopy (FT-IR)[202]. The reduction of H_2O_2 occurs at a potential of - 0.05V vs. SCE and is catalyzed by Fe(II) ions[18], whereas O_2 does not interfere, because the reduction of O_2 to H_2O occurs at a potential of 0.2V vs. SCE[18]. Additionally, PB is insensitive to other reductants interfering in H_2O_2 sensing in biological samples[203]. For metal hexacyanoferrates other than PB, the electrocatalytic activity for H_2O_2 is due to defects of PB crystals in the salt lattice[19,204]. The oxidation and reduction of iron hexacyanoferrate leads to the formation of Berlin Green (or Prussian Yellow, $Fe(III)[Fe(III)(CN)_6]$)[201] and the Everitt's salt (or Prussian White, Berlin White, $K_2Fe(II)[Fe(II)(CN)_6]$) with structures comparable to PB[205].

$$Fe[Fe(CN)_6] + K^+ + e^- \rightleftharpoons KFe[Fe(CN)_6] + K^+ + e^- \rightleftharpoons K_2Fe[Fe(CN)_6]$$

Prussian Yellow ↔ PB ↔ Prussian White

$$Fe_4[Fe(CN)_6]_3 + 3K^+ \rightleftharpoons 3\ KFe[Fe(CN)_6] + Fe^{3+}$$

insoluble ↔ soluble

Thereby, the role of potassium ions is significant for the redox reaction, because the electrochemical processes are related to the transport of K^+ rather than the transfer of electrons within the PB lattice[206]. The amount of K^+ within the PB crystal structure also affects the sensitivity for H_2O_2 detection. The influence of the used electrolyte solution, containing K^+ cations during electrochemical PB deposition was shown by Zhang et al.[207]. A potential shift in the open circuit potential of PB was obtained in dependence to the used electrolyte. K^+ ions within the crystal lattice also guarantee the electro-neutrality. The ability for K^+ (de-)insertion during oxidation and reduction, respectively, enables also the use of PB for insertion electrochemistry in e.g. energy storage due to its capability to store K^+ ions[208,209]. PB is frequently used for H_2O_2 sensing, especially in biosensors[203] and even the synonym "artificial peroxidase" was established in literature[210].

The first deposition of PB on electrode materials by dipping the electrodes into a ferric ferricyanide solution was published in 1978 and the redox behavior was shown by single sweep voltammograms[211]. The first electrochemical deposition was presented by Itaya et al.[212,213]. Since then, different approaches for the electrochemical synthesis of PB has been reported resulting in a variation of the structure and the stoichiometric composition of PB depending on the electrochemical conditions. Epitaxial growth of PB on gold was realized by electrochemical deposition at a constant potential[214]. PB was deposited on gold nanoparticles to enhance the sensitivity (10.6 µA/(µM·cm^2))[215] towards H_2O_2 compared to bulk gold electrodes, and even the simultaneous formation of gold nanoparticles and PB on gold or glassy carbon electrodes was reported by Kumar et al. with H_2O_2 sensitivities up to 5 nA/nM[216]. Other materials used as supporting electrode materials for PB deposition are Pt and carbon paste using a ferricyanide solution for the electrochemical

deposition by cyclic voltammetry[217], or Pt/C composite deposited via IBID showing enhanced stability and H_2O_2 sensitivity compared to gold as electrode material[218]. A drawback of PB for H_2O_2 sensing is its reduced long-term stability. The stability of PB is influenced by the pH value of the analyte solution and a loss of stability can be seen in alkaline solutions due to the possible formation of $Fe(OH)_3$[219]. Because the conversion of H_2O_2 results in the production of OH^- ions in neutral and alkaline media, the long-term stability of PB is limited to a few minutes in the presence of higher amounts (tenths of mM) of H_2O_2[220]. PB can be stabilized by co-deposition of conductive polymers[221] enabling additionally the embedding of enzymes in biosensors[203]. An alternative modification to overcome this limitation is the co-deposition with other metal hexacyanoferrates showing no sensitivity to H_2O_2, but exhibit enhanced stability in neutral and alkaline media[204,222]. Komkova et al. examined an optimal ratio for mixed metal hexacyanoferrates of three bilayers of PB and nickel hexacyanoferrate (NiHCF) with reduced sensitivity compared to PB films but enhanced long-term stability for several hours[20]. PB-modified electrodes were already used for the localized detection of H_2O_2 evolution by SECM in the generation/collection mode[218] and used as a lactate biosensor in soft-stylus SECM[223]. A H_2O_2 sensitivity of 1.6 $A/(M \cdot cm^2)$[223] could be achieved for the lactate biosensor. Additionally, the dissolution and corresponding loss in H_2O_2 sensitivity for mixed PB/NiHCF bilayers[20,224] were investigated via SECM.

4.2 Experimental

The modification of electrodes with H_2O_2 sensitive PB/NiHCF was done according to the procedure published by Komkova et al.[20]. Three bilayers of PB/NiHCF were electrochemically deposited by alternating deposition of PB and NiHCF. All electrochemical measurements were performed with a (bi)potentiostat (660A or 660C, CH Instruments). All solutions were diluted with ultrapure water (18.2 MΩ, ELGA LabWater, Veolia Water Solutions & Technologies). PB as first layer was deposited in a solution containing 4 mM $FeCl_3 \cdot 6\ H_2O$ (pro analysi, Merck KGaA) and 4 mM $K_3[Fe(CN)_6]$ (Honeywell, Fluka) in 0.1 M HCl (from 32% HCl Normapure, VWR Chemicals) and 0.1 M KCl (pro analysi, Merck KGaA) by cyclic voltammetry within a potential range of 0.4 to 0.75 V vs. Ag/AgCl reference electrode (sat. KCl, RE-1CP, ALS Co) at a scan rate of 20 mV/s. The electrodes were rinsed after deposition with ultrapure water and the first layer was dried at 80°C for 15 min. NiHCF was deposited at a potential range of 0 – 0.8 V at 100 mV/s in a mixture of 1 mM $NiCl_2$ (pro analysi, Merck KGaA) and 0.5 mM $K_3[Fe(CN)_6]$ in 0.1 M HCl and 0.5 M KCl. Subsequent depositions were done without additional tempering by alternating deposition of PB and NiHCF up to 6 depositions of 2 CV cycles for each compound resulting in three bilayers of mixed films.

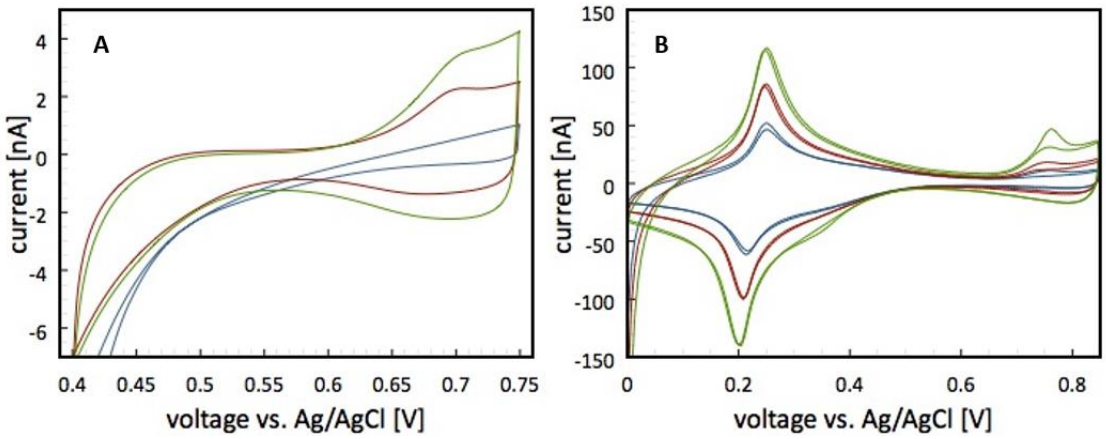

Figure 14 Electrochemical deposition of PB (A) and NiHCF (B) by cyclic voltammetry: PB: 1st (blue), 3rd (red) and 5th (green) layer were deposited at 0.4 - 0.75 V vs. Ag/AgCl reference electrode; scan speed: 20 mV/s. NiHCF: 2nd (blue), 4th (red) and 6th (green) layer were deposited at 0 - 0.8 V vs. Ag/AgCl reference electrode; scan speed: 100 mV/s.

After deposition, the film was activated by cycling at a potential range of 0 – 0.85 V vs. Ag/AgCl reference electrode at 40 mV/s in 0.1 M HCl/ 0.1 M KCl with varying numbers of scans. After activation, the electroactive PB/NiHCF film was dried at 80°C for at least 30 min. Before and after electrochemical modification of the UMEs, the electrode surface was investigated by optical microscopy (AXIO Imager.M1m, Zeiss) and by SEM (Quanta 3D FEG, ThermoFisher Scientific), if not stated otherwise. The sensitivity and response of the modified electrodes towards H_2O_2 were tested by calibration at a constant potential of 0 V vs. Ag/AgCl reference electrode with subsequent addition of equimolar aliquots of H_2O_2 (40 µL (50 µL) of 10 mM H_2O_2 (from 30 % H_2O_2, EMSURE, Merck)) to 0.05 M phosphate buffer (4 mL (5 mL), pH 6-7, consisting of $Na_2HPO_4 \cdot 12\ H_2O$ (NORMAPUR, VWR Chemicals)/$NaH_2PO_4 \cdot H_2O$ (pro analysi, Merck KGaA) in 0.1 M KCl electrolyte solution within a concentration range of 99 – 476 µM. For evaluation of the results, the averaged steady-state currents after current leveling were used. High concentrations of H_2O_2 (1 – 2 mM) were used next to calibrations to test the stability of the sensors. The activation in 0.1 M HCl/ 0.1 M KCl was used to determine the amount of active PB film on the electrodes after being exposed to H_2O_2 solution.

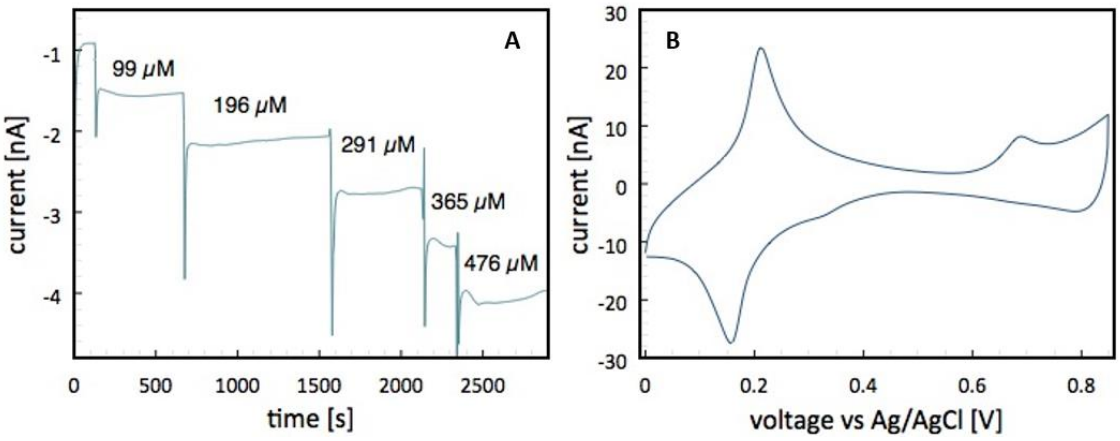

Figure 15 H_2O_2 calibration in 0.05 M phosphate buffer of a PB/NiHCF-modified Pt UME (diameter: 25 µm) with successive addition of equimolar aliquots of 10 mM H_2O_2 (A) and corresponding CV in 0.1 M HCl/ 0.1 M KCl recorded prior to calibration; scan rate: 0.02 mV/s (B).

Additionally, the dissolution of PB/NiHCF bilayers was investigated in solution by contact AFM-SECM (5500 AFM/SPM microscope, Keysight Technologies). All AFM images and correlating height and current profiles were processed by Pico View (Keysight Technologies) or Gwyddion[225]. The electrochemical liquid cell consisted of the AFM-SECM probe as working electrode, an Ag/AgCl quasi-reference electrode (Goodfellows) and a Pt wire (Goodfellows) as counter electrode. Different conditions were evaluated with respect on the stability and response of the PB/NiHCF film for H_2O_2 sensing. Details of the AFM-SECM probe fabrication is based on the procedures described elsewhere[133]. Briefly summarized, the modification of an AFM tip-integrated electrode is comparable to the modification of UMEs. It has to be ensured that the sharp AFM tip remains unmodified. Therefore, the AFM-SECM probe was investigated by SEM after modification with PB/NiHCF bilayers and the AFM tip had to be reshaped in case of deposited particles located on the AFM tip, because NiHCF is known to deposit spontaneously, also without applied potentials during electrochemical deposition and thus, the deposition of PB/NiHCF bilayers is not just occurring at the electrode surface. Additionally, the electrode area of tip-integrated electrodes was enlarged by IBID (precursor: methyl-cyclopentadienyl-trimethyl platinum, ThermoFisher Scientific) of a Pt/C composite[174] and the PB/NiHCF films deposited on this electrode material were evaluated for stability, H_2O_2 response and sensitivity. The modification of the AFM-SECM probes with Pt/C was done by consecutive deposition of rectangular patterns surrounding the AFM tip (Figure 16). To guarantee that the AFM tip remains free of the conductive material, a circular pattern was used removing possible Pt/C deposition at or close to the AFM tip. Thereby, the AFM tip was reshaped after the final deposition of the PB/NiHCF film to obtain a sharp and clean AFM tip. Single steps of the Pt/C deposition and cleaning by FIB milling are summarized in Figure 16.

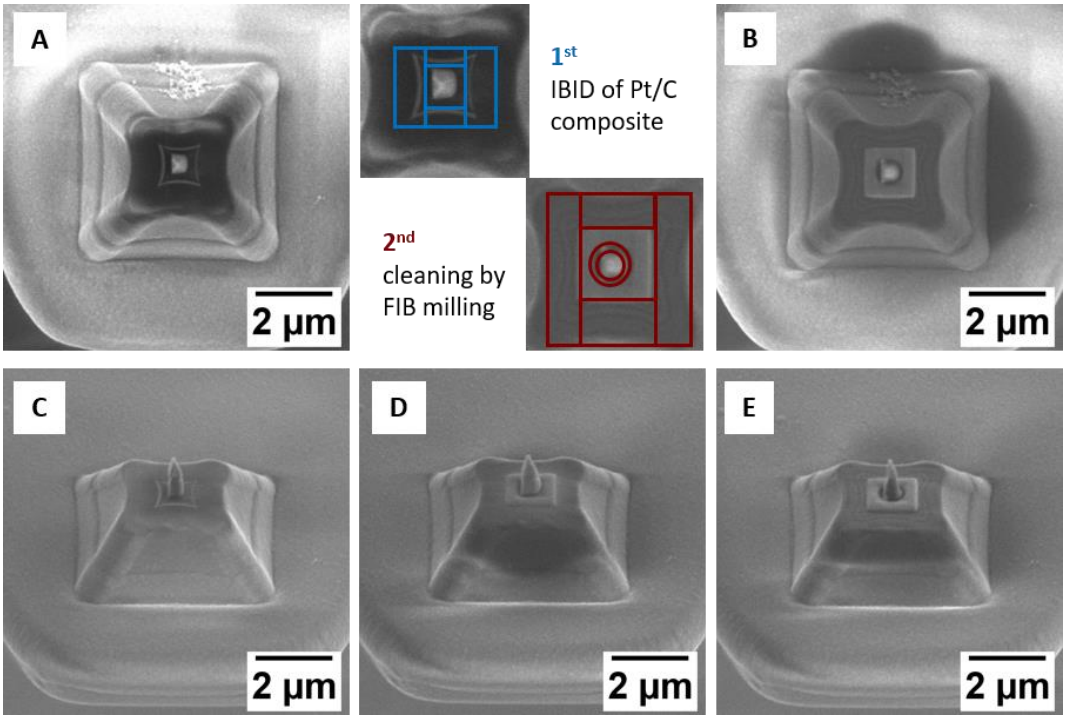

Figure 16 SEM images showing the modification of AFM-SECM probes with Pt/C composite by IBID: The exposed Au frame electrode (shown in A) is modified by IBID (rectangular blue area), followed by circular cleaning around the AFM tip and rectangular cleaning patterns next to the actual electrode area (marked in red) by FIB milling prior to electrochemical modification with PB/NiHCF (B). Single fabrication steps are shown 54° tilted, before (C) and after (D) Pt/C deposition and after FIB cleaning-(E). Acceleration voltage: 3kV and beam current: 35.5 pA.

The AFM-SECM probes have to be glued onto the AFM mount (nosecone) and the electrical contact of the electrode was insulated afterward by UV glue (Dymax 9001-E-V3.1 or DYMAX 425, Dymax Europe GmbH). The influence of UV light (UV light: λ= 320 - 395 nm, 9 W/cm^2, Dymax UV lamp 75 Blue Wave, Dymax Corp.), which is required for curing the glue, on the stability of PB/NiHCF films was also examined. Preliminary measurements were done with UMEs being less time consuming to modify and enabling simplified handling compared to AFM-SECM probes. The Pt and Au UMEs used for these measurements were fabricated as described elsewhere[65,226].

4.3 Results and discussion

This first section summarizes and discusses the results obtained with PB/NiHCF-modified UMEs, followed by the modification and optimization for the electrochemical deposition of PB/NiHCF onto AFM-tip-integrated electrodes. First results in AFM-SECM measurements are presented in section 4.3.3.

4.3.1 *PB/NiHCF-modified UMEs*

The modification of UMEs with three PB/NiHCF bilayers resulted in an inhomogeneous film with different structures and colors as visible in SEM and optical images (Figure 17), respectively. Thereby, the varying colors indicate different oxidation states of the PB and varying stoichiometry of the PB structure. No correlation between the color or the shape of the deposited film and the electrochemical deposition could be drawn.

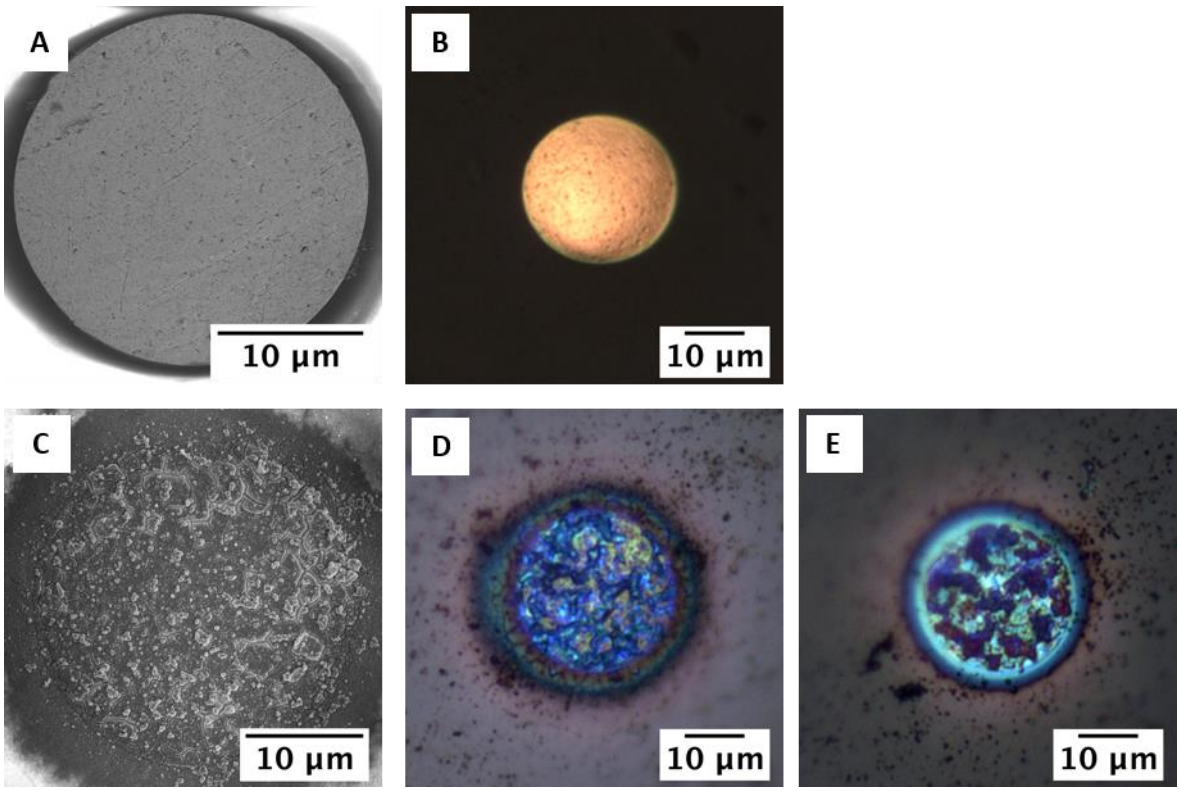

Figure 17 SEM (A, C) and optical images (B, D, E) of UMEs (diameter: 25 µm) before (A, B) and after (C-E) electrochemical deposition of PB/NiHCF bilayers.

The inhomogeneous structure might be also related to an inhomogeneous mixture of the PB and the NiHCF at the surfaces of the modified electrodes. To exclude changes in morphology and correlating loss of H_2O_2 sensitivity during the measurement due to an irregular composition of the PB/NiHCF-mixed bilayers, the elemental composition of the film was investigated via EDX mapping as shown in Figure 18. The counts for Ni are homogeneously distributed over the entire film and the Fe map in Figure 18 shows additionally an enhanced intensity for Fe compared to Ni as a consequence of the presence of Fe ions in both, iron and nickel hexacyanoferrates. The intensity distribution of the Pt signal originating from the electrode material beneath the PB/NiHCF bilayers reveals an inhomogeneous thickness of the PB/NiHCF film with less deposit on the areas with high Pt counts (white labeled in Figure 18, Pt). The excitation volume according to the penetration depth of the electron beam into the sample volume is, of course, larger than the actual thickness of the PB/NiHCF bilayers, which is apparent in the detected Pt intensities.

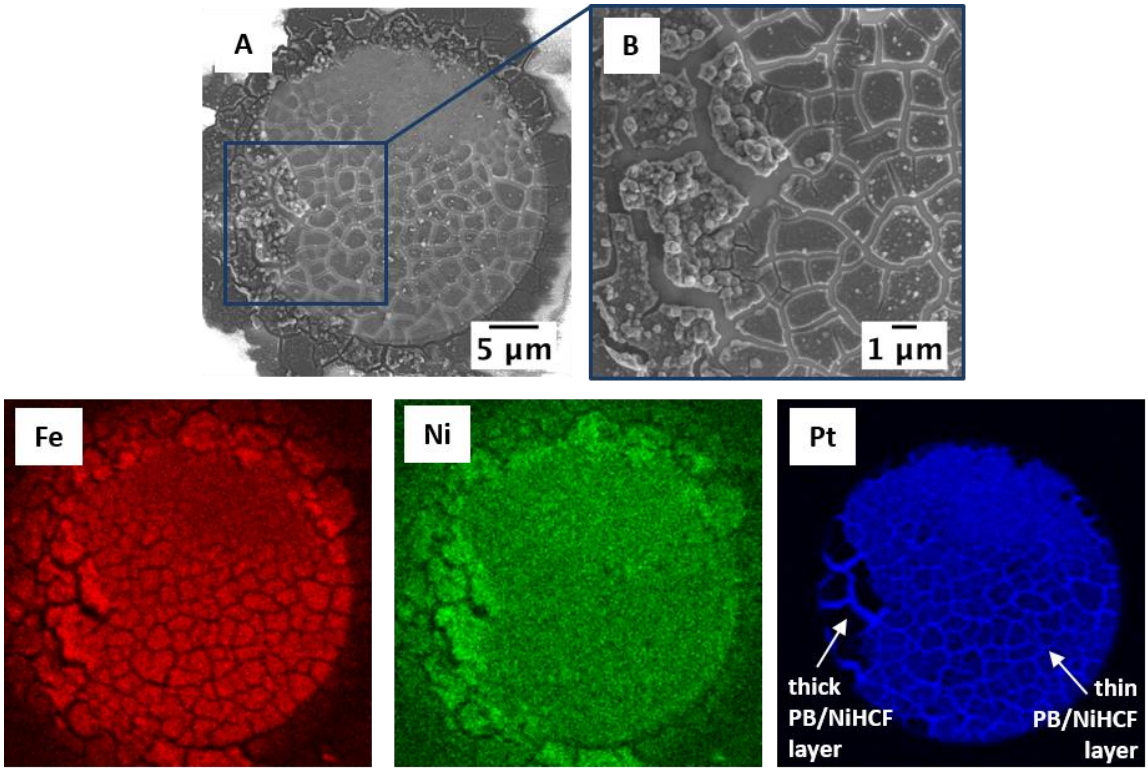

Figure 18 SEM (A, B) and EDX mapping (colored images showing the distribution of the elements: red (Fe), green (Ni) and blue (Pt)) of an UME (diameter: 25 µm) modified with PB/NiHCF-mixed film. Acceleration voltage: 5 kV. EDX mapping represents the average elemental distribution of in sum 512 frames (resolution: 256 x 200 pixels).

A penetration depth of up to at least a µm has to be assumed in PB/NiHCF layers at an acceleration voltage of 5 kV as used in the following EDX mappings, depending on the local material composition and density. This varying thickness cannot be related to the composition of the mixed film and higher Fe and Ni intensities in the EDX maps are likely related to an increased thickness of the PB/NiHCF bilayers. The observed cracks may be associated with the vacuum conditions. Because the precise stoichiometry of PB[227] and NiHCF[228] is not known due to varying composition and oxidation states of PB and varying K^+ content in both salt structures, quantification is not possible. The homogeneous distribution of Ni is clearly visible in Figure 18. In case of an irregular composition of the mixed PB/NiHCF film, the distribution of the intensity for Ni should be irregular as well. Another approach for the investigation of the composition of the mixed film of PB/NiHCF is the dissolution of single PB particles in the presence of H_2O_2 detectable by changes in the morphology of the film. The dissolution of the PB/NiHCF was measured in-situ by AFM-SECM and the results are depicted in Figure 19. Next to the dissolution of these particles, the change in topography can be also explained by mechanical removal of surface structures due to the scanning AFM tip. Thereby, resulting artifacts within the topographical image are visible and marked by white arrows (see Figure 19). While imaging of the modified UME as depicted in the images in Figure 19 A and B, no H_2O_2 was present in the solution and no potential was applied to the AFM-SECM probe. Hence, the observed changes in topography could be addressed to mechanical removal of the PB/NiHCF bilayers. The AFM topography shown in Figure 19 C is the last scan recorded after a duration of in total 7.5 h showing the PB/NiHCF film that was not removed during this measurement. Between the results shown in B and C, a potential was applied to the AFM-SECM tip sufficient for generating H_2O_2 (- 0.5 V vs. quasi-Ag/AgCl reference electrode) and the surface changes during consecutive AFM scans were detected. For improved visualization of the morphological changes, just a small section of the PB/NiHCF-modified UME was investigated in detail (white square in Figure 19 B). The results for three consecutive AFM scans are depicted in the AFM topography images in Figure 19 D-F. The morphology of the PB/NiHCF-modified UME changed within approximately 12 min in the presence of H_2O_2 generated at the AFM-SECM probe. The dissolution of a large particle is visible, which is also partially removed by the scanning AFM tip.

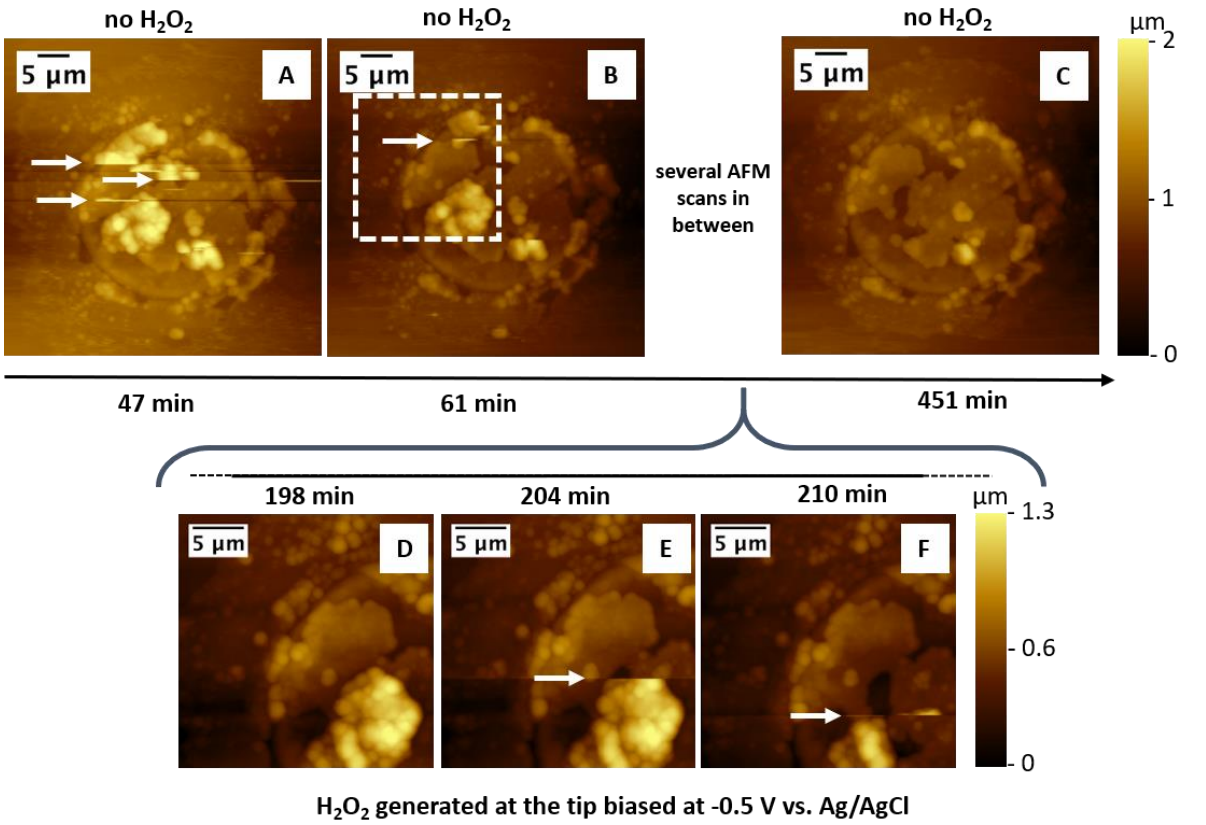

Figure 19 Investigation of the stability and surface changes of a modified UME while H_2O_2 is generated at the AFM-SECM probe, by contact AFM in liquid. During imaging the surface depicted in A-C, no potential was applied to the AFM-SECM probe. Original size: 50 x 50 µm^2(A, B), 60 x 60 µm^2 (C), scan speed: 0.6 ln/s (60 µm/s) (A,B), 0.8 ln/s (96 µm/s) (C). The timeline (not to scale) depicted in the figure shows the times (min) when the images were recorded during a total duration of the experiment of 7.5 h. For the small area of the PB/NiHCF-modified UME depicted in D-F, the AFM-SECM probe was biased at -0.5 V vs. quasi-Ag/AgCl reference electrode and H_2O_2 was generated in close proximity to the surface. Scan direction: down (D), up (E) and down (F),original size: 25 x 25 µm^2, scan speed: 1.5 ln/s (37 µm/s). The AFM topography in D-F shows single scans recorded in between the scans shown in B and C, after a duration of 198, 204 and 210 min, respectively.

But the reduced size of the particle and shrinkage of its structure visible in the morphological changes in image E to F can be associated with the dilution in the presence of H_2O_2 generated at the AFM-SECM probe. Thereby, the volume of this particle is reduced by approximately 62%. Following scans at different scan areas in the presence of H_2O_2, however, showed no further changes in the AFM topography (results are not shown). The AFM-SECM investigation in Figure 19 shows that higher regions of the PB/NiHCF bilayers or particles located on top of the 'main' PB/NiHCF bilayers are predominantly removed in the presence of H_2O_2. In SEM

images, these regions are also visible and changes in surface morphology after exposure of the PB/NiHCF-modified electrodes to varying concentration of H_2O_2 were observed. The sensitivity loss in H_2O_2 detection observed in the recorded electrochemical i-t curves may be correlated to the morphology changes visible in the consecutively recorded SEM images. H_2O_2 sensitivity and response of the modified electrodes were determined by calibration measurements before and after the exposure of modified electrodes to H_2O_2, whereas in between the single SEM images shown in Figure 20, the UME was exposed to solutions of 0.7, 0.8 and 1 mM H_2O_2, respectively, and an i-t-curve was recorded over a period of 25 min for each H_2O_2 concentration. Comparing the SEM data to the topographical changes observed in the AFM-SECM investigation shown in Figure 19, a change or dissolution of these particles on top of the 'main' PB/NiHCF film would be expected.

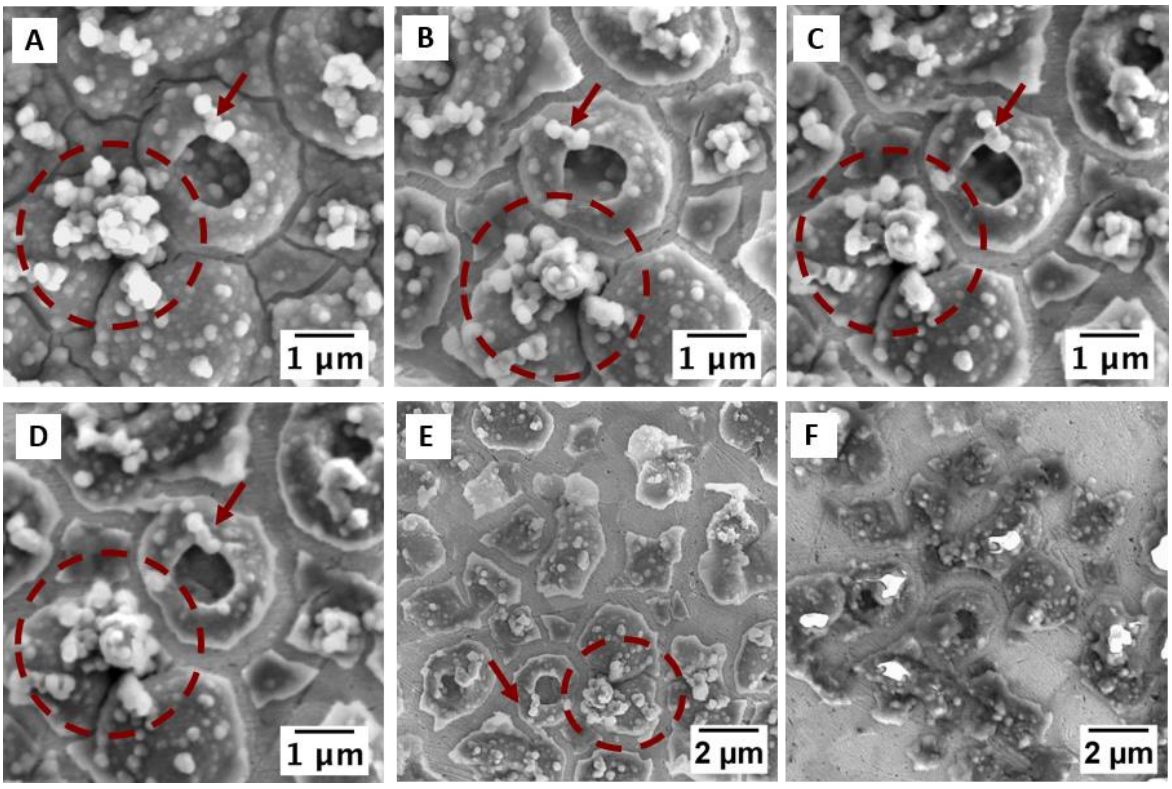

Figure 20 SEM investigation of a PB/NiHCF-modified UME after electrochemical deposition (A) and after exposure to different H_2O_2 concentrations: 0.7 mM (B), 0.8 mM (C, D) and 1 mM (E, F). Regions of the PB/NiHCF bilayers labeled by red arrows and circles are stable in the presence of H_2O_2. Acceleration voltage: 5 kV; 53 pA (A,B) and 852 pA (C - F).

These particles are marked by a red arrow and circle in Figure 20 and showed however almost no changes during the consecutive H_2O_2 exposures in between recording the individual SE images. In contrast to AFM investigations, the main characteristic of the PB/NiHCF bilayers is a plate-structured deposit on the UME, which showed a reduction in surface coverage with consecutive H_2O_2 detection. The changes in the surface coverage are more obvious with additional H_2O_2 exposure, especially visible in the SEM images displayed in E and F showing a larger area of the PB/NiHCF-modified UME. The dissolution of the PB/NiHCF film seems to be homogeneous and along the edges of the visible structures, which is energetically favorable. Whereas the particles on top of these main characteristic plate-structured deposits were dissolved during AFM investigations, these structures observed in the SEM images as bright single particles, appear to be not affected by the H_2O_2 exposure. Hence, these particles might consist either of NiHCF as a stable component of the mixed film insensitive to H_2O_2 or these particles and structures consist of mixed components of PB/NiHCF. The results obtained by EDX mapping shown in Figure 18 indicate that a homogeneous mixture of PB and NiHCF is most likely. The localized change and dissolution of a pure PB film in the presence of H_2O_2 were detected in consecutive AFM scans as shown in Figure 21. Thereby, a Pt UME modified only with PB was investigated at a constant H_2O_2 concentration (1 mM) similar to the concentrations used in the SEM studies (as shown in Figure 20).

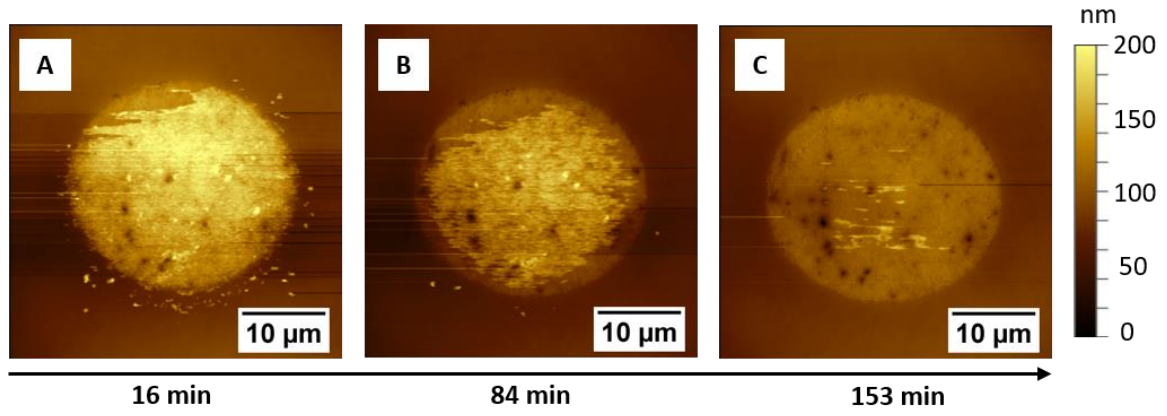

Figure 21 AFM topography of a PB-modified Pt UME (diameter: 25 µm) in the presence of 1 mM H_2O_2 in 0.05 M phosphate buffer. The depicted AFM images are recorded at 16, 84 and 153 min, respectively, of in total 2.5 h, showing the changes in the surface coverage during this AFM investigation. Original size: 60 x 60 µm^2, scan speed: 0.5 ln/s. Electrochemical deposition of PB was done with 20 cycles according to the experimental conditions described in 4.2.

Within approximately 2.5 h, the whole PB film was removed. A possible influence of the vacuum conditions during SEM imaging was also investigated. A H_2O_2 calibration curve and corresponding loss of PB at a modified electrode with consecutive H_2O_2 exposure is exemplarily shown in Figure 22. In between the deposition of PB and NiHCF, the electrodes were exposed to vacuum (chamber vacuum of the SEM, in the range of 10^{-6} mbar), namely after the 1st (PB), 2nd (NiHCF) and 3rd (PB) layer. After the deposition of in sum 6 layers in accordance with 3 PB/NiHCF-mixed bilayers, the electrode was investigated by SEM.

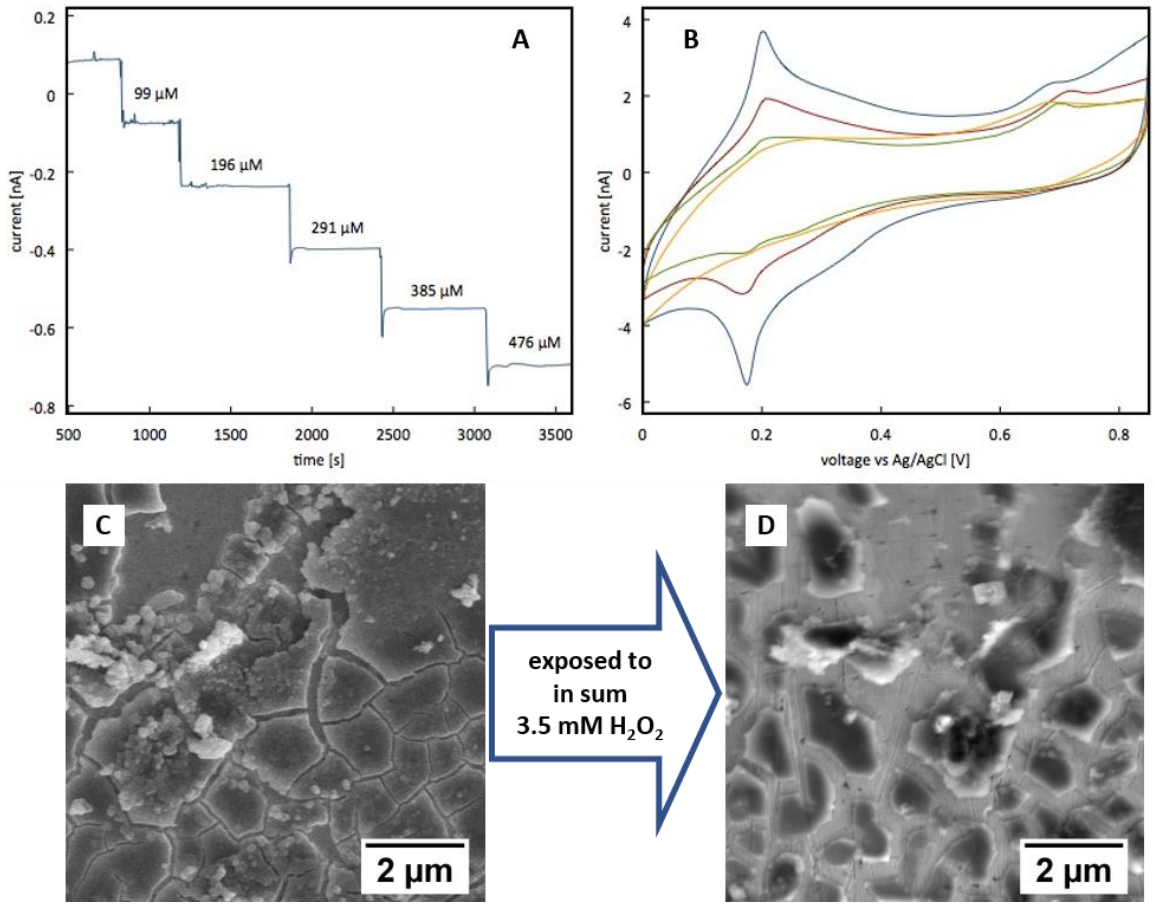

Figure 22 1st H_2O_2 calibration in 0.05 M phosphate buffer of a PB/NiHCF-modified Pt UME (diameter: 25 µm) and corresponding CV in 0.1 M HCl/KCl (scan rate: 0.02 mV/s) after 1st calibration (blue) and after successive exposure to 1 mM H_2O_2 for 25 min, respectively (running order: red, green, yellow). SEM images after PB/NiHCF deposition (C) and after H_2O_2 detection (D) of in total of 3.5 mM H_2O_2 over a period of approximately 2 h; acceleration voltage: 5kV, 7pA (C) and 8 nA (D).

In between the single H_2O_2 calibrations, the PB/NiHCF-modified UME was only characterized by CV in 0.1 M HCl/KCl and the change in the morphology was detected by optical microscopy avoiding any influence of additional vacuum conditions in between consecutive H_2O_2

exposures. In the optical images depicted in Figure 23, a clear change in the composition of the mixed bilayers is visible, indicated by a change in color. Thereby, PB is reduced to Prussian Yellow, visible as a yellow-brown region on the modified UME, and Prussian White, which is insensitive to H_2O_2. Single spots of the PB/NiHCF film were removed during H_2O_2 exposure that is visible in Figure 23 B and C at the bright regions within the film showing the underlying Pt electrode surface.

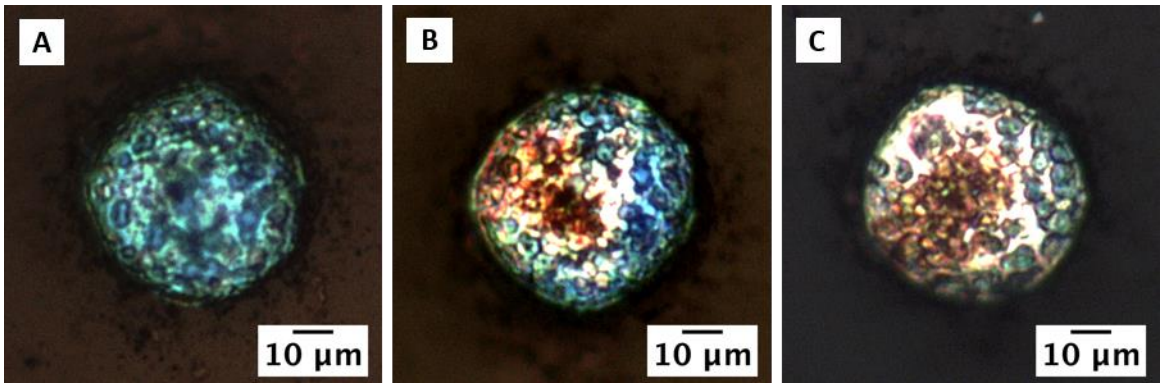

Figure 23 Optical images of a PB/NiHCF-modified UME after electrochemical deposition of PB/NiHCF bilayers (A), after the 1st H_2O_2 calibration (B) and after 2nd exposure to 1 mM H_2O_2 for 25 min (C).

Comparable results obtained by optical images of a PB/NiHCF-modified Pt UME without vacuum conditions in between the single layer depositions showed enhanced removal of the active bilayers without any distinctive color changes. The change in the surface of the modified electrode with successive H_2O_2 calibrations is shown in Figure 24.

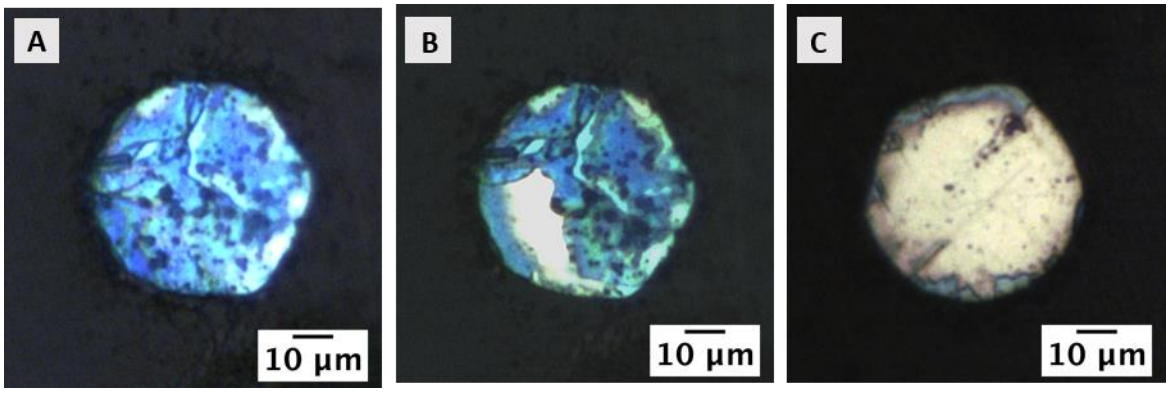

Figure 24 Optical images of a PB/NiHCF-modified UME after electrochemical deposition of PB/NiHCF bilayers (A), after the 1st H_2O_2 calibration (B) and after 5th calibration, which equals an exposure to approx. 2 mM H_2O_2 (C).

In Figure 25, the comparison between two H_2O_2 calibrations with PB/NiHCF-modified UMEs with and without vacuum conditions, respectively, shows enhanced stability for the bilayers exposed to vacuum, which is in accordance to the observation via optical microscopy.

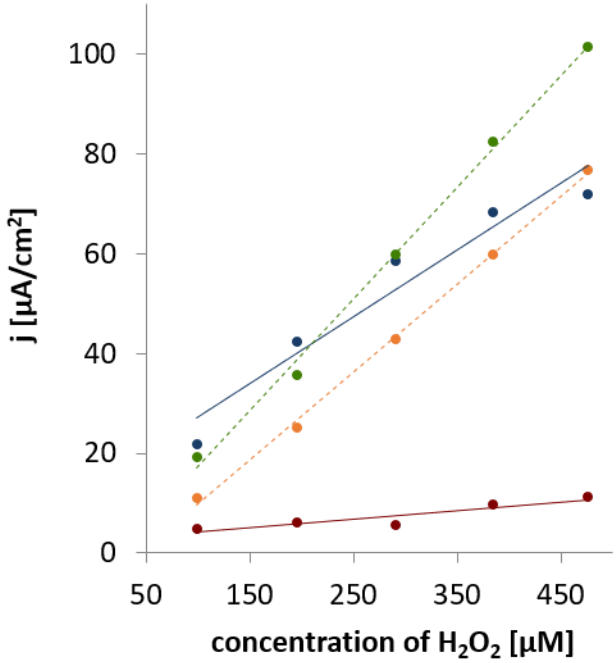

Figure 25 H_2O_2 calibration of PB/NiHCF-modified Pt UMEs (diameter: 25 µm) with (dashed lines; 1st: orange and 2nd: green) and without exposure to vacuum conditions between layer deposition (solid lines; 1st: blue and 2nd: red).

The enhanced stability of the modified UMEs, which were exposed to vacuum, might be related to the removal of water ('drying processes') in the crystal lattice. The location of water molecules in the PB lattice has been determined by attenuated total reflection FTIR (ATR-FTIR)[229] and powder neutron diffraction revealing both, coordinated and uncoordinated regions of water molecules within the crystal lattice of PB[230]. Investigations of PB by ^1H nuclear magnetic resonance spectroscopy (NMR) showed that the water molecules are bound to the high-spin Fe(III) ions in the crystal lattice influencing the conductivity of the material[231]. On the other hand, coordinated water molecules occupy space in the PB lattice, which might be filled with K^+ ions that enable charge transport during electrochemical processes[227] as described in the introduction. Water molecules after electrochemical deposition from aqueous solution might also be located in between PB particles and the removal of incorporated water from pores within the PB film by vacuum might lead to enhanced stability

of the PB layers. A simple explanation for the reported enhanced sensitivity might by the fact that rapid drying under vacuum conditions induces fractures within the PB film, which leads to an enlargement of the surface area. Thereby, the film might be more sensitive to H_2O_2 but, on the other side, PB dilution preferentially occurs at these edges, which reduces the stability. This was not observed during the course of these investigations.

In the next step, Pt/C composite as electrode material for the electrochemical deposition of PB/NiHCF-mixed films was investigated. The activation of the PB/NiHCF-modified UME by cycling in 0.1 M HCl/KCl shows an enlarged amount of PB deposited on the UME with Pt/C composite as electrode material (Figure 26). The electrode area modified by Pt/C deposition was determined by CV using $[Ru(NH_3)_6]Cl_3$ as outer sphere redox species resulting in an active electrode area of 755 μm^2, whereas a bare Pt electrode used for comparison had an active electrode area of 825 μm^2. In contrast to the smaller active electrode area, the current of the PB redox signal is approximately 5 times higher for Pt/C composites as electrode material compared to the PB/NiHCF modification of bare Pt UMEs.

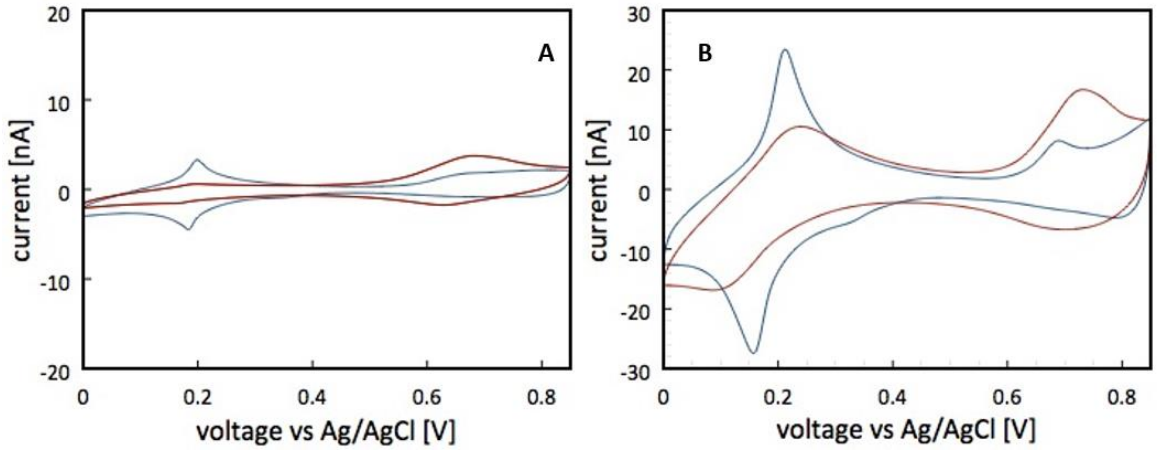

Figure 26 CV in 0.1 M HCl/ 0.1 M KCl of PB/NiHCF-modified Pt UME (diameter: 25 µm, A) and on a Pt UME (diameter: 25 µm) modified with Pt/C composite prior to layer deposition (B), scan rate: 0.02 V/s. Blue CVs were recorded after deposition of PB/NiHCF bilayers and red CVs were recorded after H_2O_2 calibration, respectively. After 4 consecutive calibrations (99 - 476 µM H_2O_2 for each calibration) at the UME, where data are shown in (A), and after 5 consecutive calibrations (99 - 476 µM H_2O_2 for each calibration) for the Pt/C modified UME shown in (B).

In Figure 27, the optical image of an UME is shown after the deposition of Pt/C composite by IBID, whereas the optical images in B and C show the electrodes after electrochemical deposition of the PB/NiHCF bilayers. In Figure 27 C, a large overspread of the PB/NiHCF film is visible, which might be also the explanation for the enhanced amount of PB located on the UME.

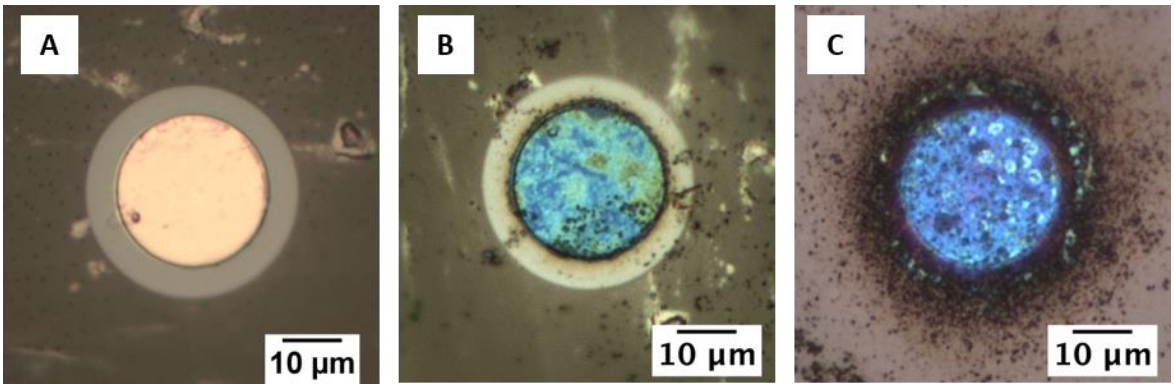

Figure 27 Optical images of UMEs (diameter: 25 µm) with additional deposition of a Pt/C composite by IBID; before (A) and after (B, C) the electrochemical deposition of PB/NiHCF bilayers. The overspread of deposited PB/NiHCF depicted in C is reduced by additional FIB milling prior to layer deposition (A) as depicted in (B).

This overspread should be avoided in the modification of AFM-SECM probes due to the loss of the lateral resolution in localized H_2O_2 detection. It was assumed that this overspread is related to additional deposition of Pt/C next to the actual electrode area. To confirm this assumption and to avoid this overspread, the region surrounding the actual electrode area was cleaned by FIB milling after deposition of the Pt/C composite, but prior to the electrochemical deposition of the PB/NiHCF film (Figure 27 A). The resulting PB/NiHCF modification of the UME is shown in Figure 27 B with a negligible overspread around the actual electrode surface. Thereby, it can be concluded that this overspread was actually based on the additional deposition of Pt/C composite. A direct comparison of the H_2O_2 sensitivity of PB/NiHCF-modified UMEs with bare Pt or Pt/C composite as supporting electrode material is shown in Figure 28. Additionally, the effect of the FIB cleaning after deposition of the Pt/C composite to reduce the overspread of PB/NiHCF is taken into account.

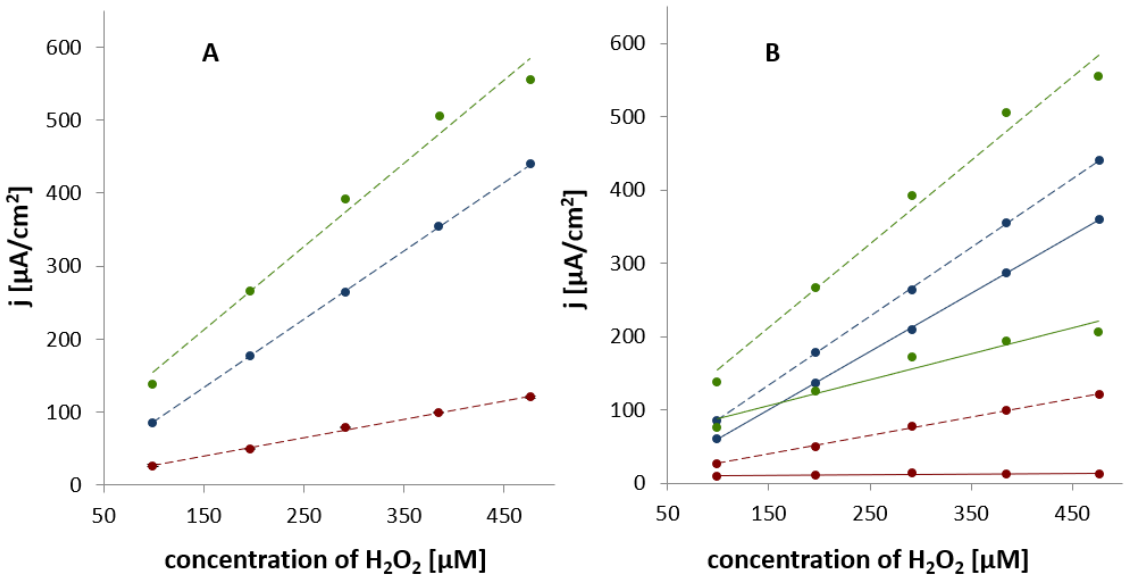

Figure 28 Comparison of H_2O_2 sensitivity and stability of a PB/NiHCF-modified UME at different supporting electrode materials: Pt/C composite (blue), Pt/C composite with additional FIB cleaning (green) and bare Pt UME with no additional treatment prior to electrochemical deposition of PB/NiHCF (red) (A). The stability in consecutive calibrations of PB/NiHCF-modified UMEs is compared in (B) whereas dashed lines represent the first and solid lines the second calibration, respectively (colors are same as in (A)).

The measured current response at the 5 consecutive H_2O_2 additions of the compared three UMEs vary with a factor of 3.5 ± 0.2 (Pt/C without FIB milling) and 5.0 ± 0.3 (Pt/C with FIB milling), respectively, within the data sets for Pt supporting electrode material and Pt/C-modified Pt (or Au) UMEs with or without additional FIB milling (Figure 28). A loss of sensitivity is observable for consecutive calibrations for all electrodes, but for Pt/C-modified UMEs improved stability compared to bare Pt as supporting electrode material is observed. The enhanced H_2O_2 sensitivity may be related to an increased amount of PB within the PB/NiHCF bilayers, whereas this is not necessarily related to an enlarged electrode surface, but to the different supporting electrode materials, namely Pt and Pt/C composite. The stability of the PB/NiHCF bilayers within consecutive calibrations (up to 5 calibrations) of H_2O_2 in phosphate buffer was investigated on different supporting electrode materials and for UMEs exposed to vacuum.

The results are compared in Figure 29. The loss in sensitivity is clearly recognizable for all investigated electrodes, but increased stability for the electrodes exposed to vacuum between single H_2O_2 calibrations is visible compared to UMEs with no additional treatment. The Pt/C modification of the UMEs prior to the deposition of PB/NiHCF bilayers resulting in enhanced sensitivity for H_2O_2, shows also enhanced stability in H_2O_2 detection.

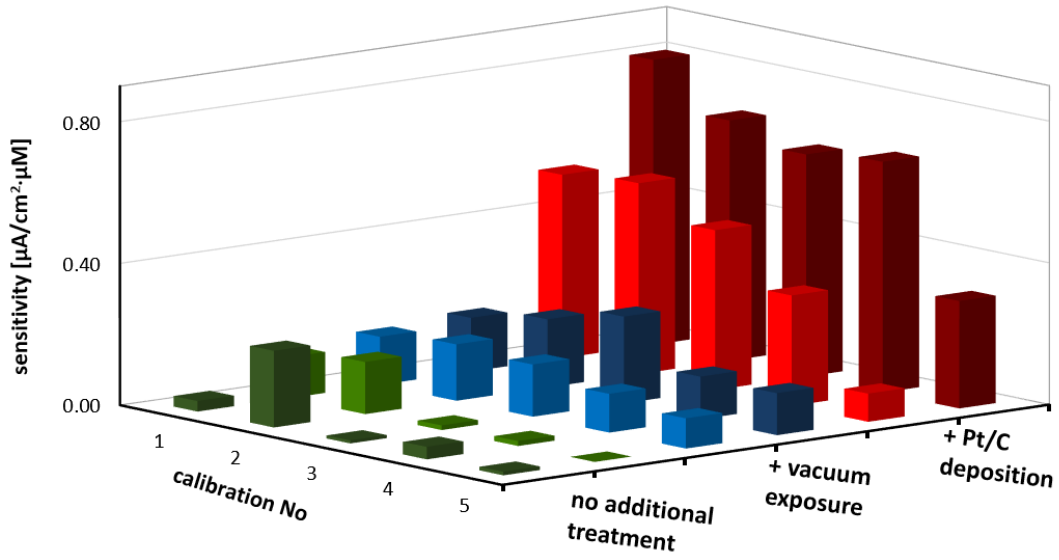

Figure 29 Comparison of the H_2O_2 sensitivity for 5 successive calibrations of two PB/NiHCF-modified UMEs with no additional treatment (green), two PB/NiHCF-modified UMEs additionally exposed to vacuum conditions (blue) and two PB/NiHCF-modified UMEs with Pt/C as supporting electrode material (red).

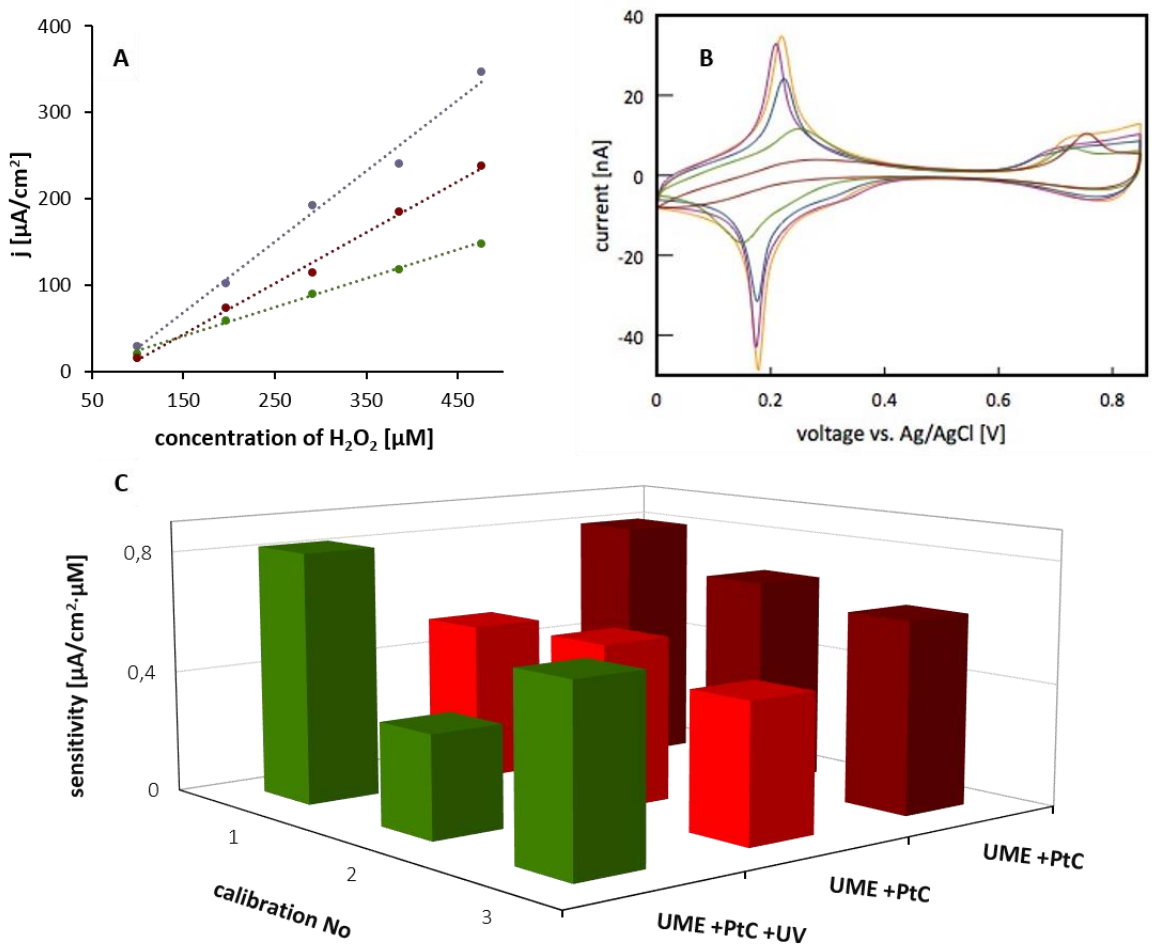

Figure 30 Investigation of H_2O_2 stability after the exposure of the PB/NiHCF-modified electrodes to UV light: consecutive H_2O_2 calibrations in 0.05 M phosphate buffer of a PB/NiHCF-modified UME (diameter: 25 µm) with Pt/C composite as supporting electrode material (A), colors: 1st (blue), 2nd green) and 3rd (red) calibration, and corresponding CVs in 0.1 M HCl/ 0.1 M KCl (B) after deposition (yellow), exposure to UV light (purple) and after consecutive H_2O_2 calibrations (running order: blue, green, red), scan rate: 0.02 mV/s. The sensitivity of three consecutive H_2O_2 calibrations recorded at three individual UMEs modified with Pt/C (red) and additionally exposed to UV light (green), is compared in C.

Also, the influence of UV light towards the performance of PB/NiHCF-modified UMEs in respect to H_2O_2 sensitivity and stability was investigated. Therefore, a PB/NiHCF-modified Au UME with Pt/C composite as supporting electrode material was exposed to UV light for 120 s after electrochemical deposition of PB/NiHCF bilayers and after their activation by cycling in 0.1 M HCl/0.1 M KCl (Figure 30). The H_2O_2 calibration in phosphate buffer showed good linearity within the concentration range of 99 – 909 µM H_2O_2 and a sensitivity of 0.82 µA/(cm²·µM) for the first calibration (Figure 30 A), which is comparable to the results obtained

by modified Pt/C-UMEs without UV light exposure. Between recording the calibrations, the PB/NiHCF bilayers were characterized by CV in HCl/KCl (Figure 30 B). Additionally, the influence of the UV light in respect to the H_2O_2 response was compared in the CVs recorded prior and after the exposure of the modified UME to UV light (see yellow and purple CVs in Figure 30 B). No significant change in the amount of PB could be detected and no negative effect within the following consecutive calibrations was observed. Both treatments, namely the vacuum and the UV exposure of the modified electrodes, might result in a loss of hydrate water and an enhanced drying of the H_2O_2-active film. In literature, the exposure of PB to light of different wavelength has been reported and an increase in the formation of PB could be associated to the photo-reduction of the iron(III) in the $[Fe(III)(CN)_6]^{3-}$ anion[232]. The transfer of ferricyanide to ferrocyanide was shown for UV light (λ= 365 m)[232,233]. The photo-reduction is not linked to the wavelength of the used light source, but to the energy transferred by irradiation. Therefore, it is possible that residues of $FeCl_3$ and $[Fe(III)(CN)_6]^{3-}$ within the freshly prepared PB films are reduced to Fe(II) and PB is additionally formed. However, the redox signal of PB shown in Figure 30 B doesn't show significant differences between the CVs recorded prior and after the exposure of the modified UMEs to UV light. Also, IR investigations indicated no change of the vibration bands within the film (data not shown). Thereby, a change of the PB structure can be excluded and the enhanced stability of the PB/NiHCF-modified films is probably related to the fast drying of the film and additional PB formation for both, vacuum and UV conditions. In conclusion, vacuum conditions and UV light, which are necessary for the preparation of modified AFM-SECM probes, seem to have a positive effect on the performance of the electrodes. Improved stability is observed under both conditions. Pt/C composite as supporting electrode material is also suitable and showed enhanced stability and sensitivity compared to bare Pt UMEs as supporting electrode material.

4.3.2 *PB/NiHCF-modified AFM-SECM probes*

Modification of AFM tip-integrated electrodes with PB/NiHCF bilayers, which has been investigated within this thesis for the first time, was obtained using the same conditions as described for UMEs with concentrations of the solutions for PB and NiHCF deposition adopted from Komkova et al.[20] (4 mM $FeCl_3$/$K_3[Fe(CN)_6]$ and 1 mM $NiCl_2$/ 0.5 mM $K_3[Fe(CN)_6]$). Thereby, the electrode area was exposed by FIB milling and increased with a Pt/C composite by IBID[174]. First measurements with these modified AFM-SECM probes were performed in H_2O_2

calibration experiments to investigate their H_2O_2 sensitivity and stability (Figure 31 C). In Figure 31 A and B, an AFM-SECM probe after the deposition of 3 PB/NiHCF bilayers is shown. The SEM images reveal a complete coverage of the whole pyramidal AFM tip. Because the deposition of NiHCF is known to be spontaneous, this might be reasonable for the observed deposition of the H_2O_2-sensitive PB/NiHCF layer onto the whole AFM tip. This should be avoided to ensure localized measurements of H_2O_2.

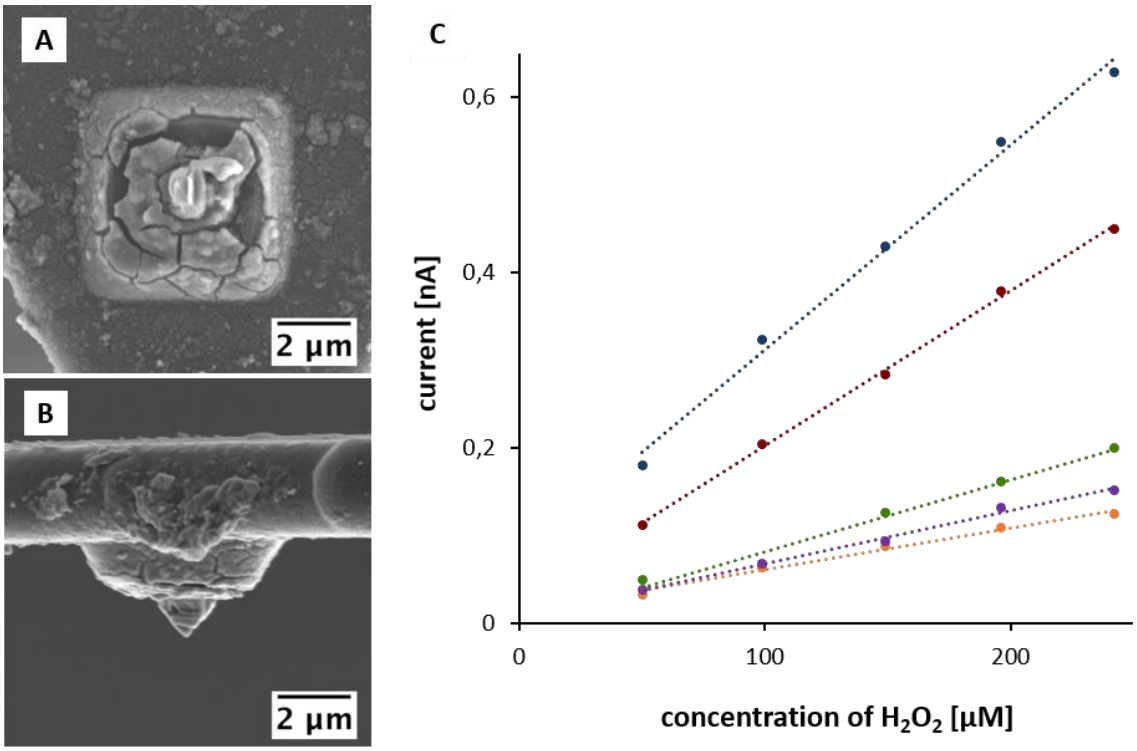

Figure 31 SEM image of a PB/NiHCF-modified, tip-integrated: top view (A) and side view (B) of the pyramidal AFM tip. Linearity and H_2O_2 sensitivity of 5 successive calibrations (C; running order: blue, red, green, orange, purple). Because of the huge overspread of the PB/NiHCF bilayers, the electrode area was not taken into account and the absolute current signal is correlated to the H_2O_2 concentration (C).

Therefore, the deposition of PB/NiHCF bilayers has been optimized with tip-less AFM-SECM probes and tested in H_2O_2 calibration experiments. In Figure 32, the deposition of PB/NiHCF following the procedure of Komkova et al.[20] is depicted in A, whereas the deposition of two PB/NiHCF bilayers using a reduced concentration of the original deposition solutions by 66% is shown in B. It is obvious that the optimization of the PB/NiHCF layer deposition resulted in

the localized deposition of H_2O_2-sensitive material located at the original electrode area with an overspread due to a radial diffusion at the microelectrode during the electrochemical deposition. In Figure 32 C, the PB/NiHCF deposition occurred additionally at the area surrounding the actual microelectrode as a result of the Pt/C deposition by IBID and/or the spontaneous deposition of NiHCF.

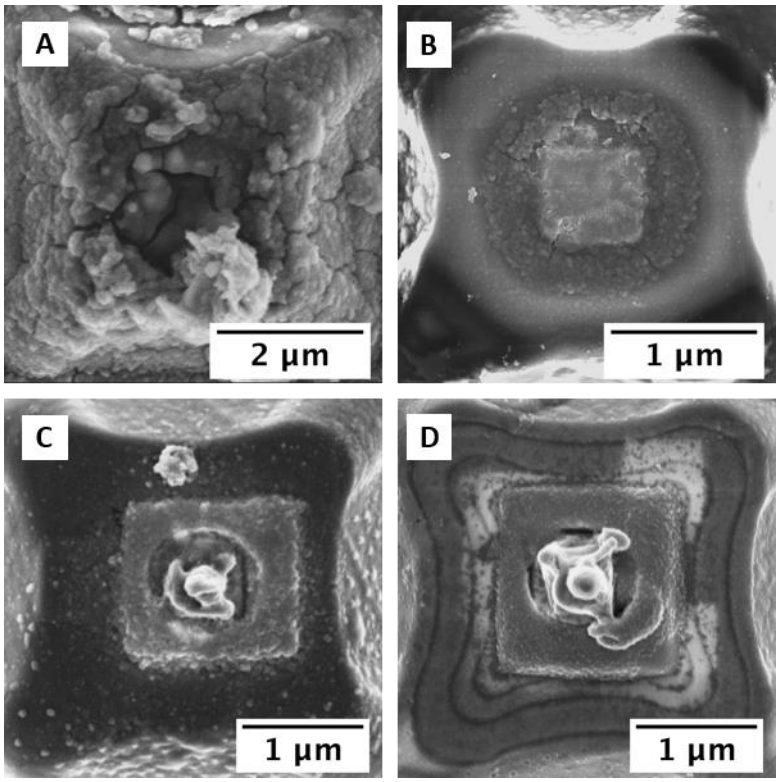

Figure 32 SEM images of PB/NiHCF-modified, tip-integrated electrodes, with 4 mM $FeCl_3$/$K_3[Fe(CN)_6]$ and 1 mM $NiCl_2$/ 0.5 mM $K_3[Fe(CN)_6]$ concentrations for the electrochemical deposition of 3 PB/NiHCF bilayers (A) and reduced concentrations of the used solutions of 1.33 mM $FeCl_3$/$K_3[Fe(CN)_6]$ and 0.33 mM $NiCl_2$/ 0.17 mM $K_3[Fe(CN)_6]$) during electrochemical deposition of 2 PB/NiHCF bilayers (B-D); without (C) and with (D) additional FIB cleaning after IBID of the Pt/C composite. Acceleration voltage: 5 kV (A) and 3 kV (B-D)/ 24 pA (A), 43 pA (B) and 86 pA (C, D). The SEM images in (B – D) are recorded in the immersion mode.

This increased deposition of a thin Pt/C layer next to the actual microelectrode area was reduced by subsequent FIB milling as depicted in Figure 32 D. The sensitivity and stability of the PB/NiHCF-modified AFM-SECM probes with a reduced concentration of the deposition solutions were tested in consecutive H_2O_2 calibrations. In the following graph (Figure 33), the H_2O_2 sensitivity of a PB/NiHCF-modified, tip-integrated electrode (in blue) is compared to results obtained with modified UMEs. The reduction of the amount of PB and NiHCF during

electrochemical deposition didn't show a reduced sensitivity, in contrast even an enhanced sensitivity for the first 3 H_2O_2 calibrations with the PB/NiHCF-modified, tip-integrated electrode was observed. The influence of UV light exposure on the behavior of the PB/NiHCF bilayers was also investigated as the mounting of the AFM-SECM probes requires the exposure to UV light.

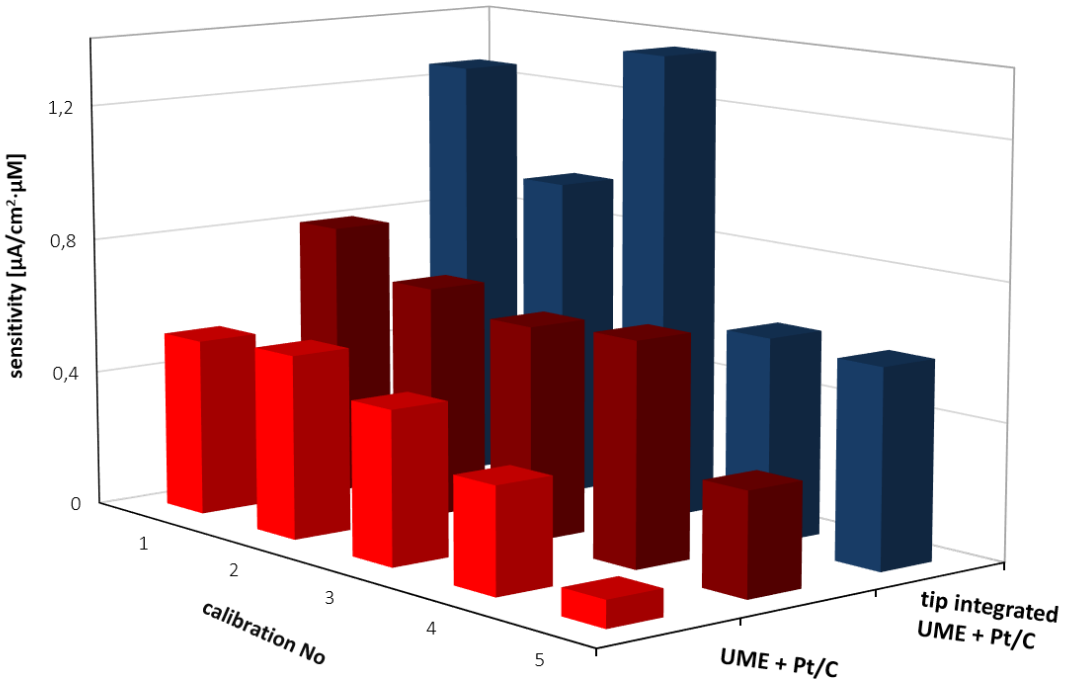

Figure 33 Comparison of the H_2O_2 sensitivity for 5 successive calibrations of a PB/NiHCF-modified tip-integrated electrode (blue) to PB/NiHCF-modified UMEs modified with Pt/C (light and dark red).

The investigation of the influence of the UV light was already tested with modified UMEs (see 4.3.1), resulting in enhanced stability of PB/NiHCF bilayers. The AFM-SECM probes were exposed to UV light after the deposition of the 1st and the 3rd layer corresponding to the deposition of PB, whereas the 2nd and 4th layer correspond to the deposition of NiHCF resulting in two PB/NiHCF bilayers. In the following section, individual AFM-SECM probes are compared showing good H_2O_2 sensitivity in consecutive calibrations. Using a reduced concentration of the deposition solutions, for the modification of AFM-SECM probes with PB/NiHCF bilayers resulted in rather limited reproducibility. In fact, only the 4 (13 %) presented probes showed a response to H_2O_2 and 27 (87 %) tested AFM-SECM probes showed either no signal in the

'activation' CV in HCl/KCl or no H_2O_2 sensitivity at all. In the following, the different responses of the presented probes are evaluated in detail to identify the reason for this good H_2O_2 sensitivity. The H_2O_2 sensitivity of different AFM-SECM probes with slightly different electrode sizes and geometries are compared in Figure 34 A. The compared probes are named according to the colors in the graphs, namely purple, blue, red and black.

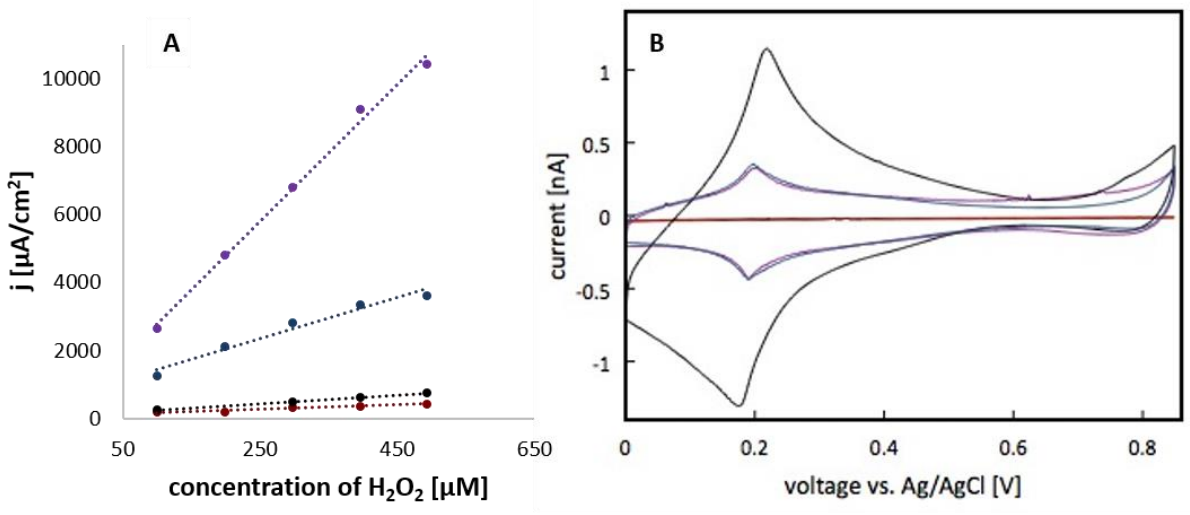

Figure 34 Comparison of H_2O_2 sensitivity and linearity of PB/NiHCF-modified AFM-SECM probes with UV exposure (purple, blue, red) and without (black) UV exposure during electrochemical layer deposition (A). CV in 0.1 M HCl/ 0.1 M KCl of PB/NiHCF-modified AFM-SECM probes (B) recorded prior to calibrations depicted in (A), scan rate: 0.02 V/s. Corresponding data are of the same color.

A summary of the sensitivities and electrode area is given in Table 4. The 1st H_2O_2 calibrations obtained with PB/NiHCF-modified AFM-SECM probes are shown in Figure 34 A, being exposed to UV light (purple, blue and red dashed lines; results correspond to three individual AFM-SECM probes), and without being exposed to UV light (black dashed line). It is clearly visible that the sensitivity of the probes exposed to UV light is strongly enhanced by a factor of 4.9 up to 16.3 in relation to the results labeled in black. Just one PB/NiHCF-modified AFM-SECM probe with additional UV exposure (red dashed line in Figure 34 A) shows a reduced sensitivity by a factor of 0.5. Although the same conditions for the electrochemical deposition of PB/NiHCF bilayers were applied to all samples, the deviation in the resulting sensitivities is huge. A comparison of the 'activation' CVs of the H_2O_2-active bilayers in 0.1 M HCl/ 0.1 M KCl

	black	red	blue	purple
exposed to UV light	No	Yes		
FIB cleaning after PB/NiHCF bilayer deposition	No	No	Yes	
H_2O_2 sensitivity [µA/(cm² · µM)]	1.24	0.65	6.10	20.17
ratio	-	0.5	4.9	16.3
electrode geometry	square, no AFM tip	Pt/C frame electrode + AFM tip		
electrode surface [µm²]	13.8	12.7	1.1	1.8

Table 4 Comparison of H_2O_2 sensitivity and corresponding ratio of AFM-SECM probes exposed to UV light in respect to the AFM-SECM probe not exposed to UV light (black), electrode surface as determined by CV in 1,1'-ferrocenedimethanole and H_2O_2 sensitivity regardless of the active electrode surface of PB/NiHCF-modified AFM-SECM probes as depicted in Figure 34.

(the amount of PB can be estimated by its redox signal at approximately 0.2 V vs. Ag/AgCl reference electrode (Figure 34 B)) doesn't explain these enhanced sensitivities. Only the data obtained for one AFM-SECM probe exposed to UV light during electrochemical layer deposition (displayed in red colors in Figure 34 and Table 4) shows a reduced sensitivity and a low concentration of PB, according to the redox signal for PB in the CV displayed in Figure 34 B. Indeed, the electrode revealing the highest signal (black CV in Figure 34 B) shows for the 1st calibration the worst sensitivity (not exposed to UV light). The comparison of the active electrode surface as determined by CV in 5 mM 1,1'-ferrocenedimethanole shows deviations for the respective AFM-SECM probes as summarized in Table 4. The differences in electrode size and H_2O_2 sensitivity are shown in Figure 34 B and in Table 4, respectively. The individual samples are named according to the colors in Figure 34. The data in Table 4 show significant deviations in the H_2O_2 sensitivities, which does not correlate with the actual electrode surface. Whereas for the probe 'black' (no UV exposure), a square electrode was used without an AFM tip (as depicted in Figure 32 B), the AFM-SECM probes with an electrode area (named as blue and purple) reflect Pt/C frame electrodes surrounding the AFM tip (SEM image of the 'blue'

AFM-SECM probe is shown in Figure 32 D). The AFM-SECM probe labeled as 'red' is shown in the SEM image in Figure 32 C, without additional FIB cleaning after Pt/C deposition, but also with an AFM tip surrounded by the active Pt/C-modified electrode area. Because the 'red' AFM-SECM probe shows complete coverage of the pyramidal AFM probe in the SEM image in Figure 32 C, the actual electrode area before the deposition of PB/NiHCF-bilayers is larger (see values listed in Table 4). The detection of H_2O_2 correlates with the amount of PB as the H_2O_2-sensitive material. The amount of PB is dependent on the concentration of $FeCl_3$ and $K_3[Fe(CN)_6]$ during electrochemical deposition and the actual electrode area, on which the PB is deposited. Because the concentration during the electrochemical deposition for all AFM-SECM probes in the compared results was kept the same, the differences in sensitivity are either related to the electrode surface or to the positive influence of the exposure to UV light in between the deposition of the individual layers. Indeed, the AFM-SECM probe ('red'), exposed to UV light and with the highest electrode area (see CV recorded in 1,1'-ferrocenedimethanole) and a PB/NiHCF coverage of the whole pyramidal AFM probe visible in the SEM image in Figure 32 C, shows the worst sensitivity with the lowest amount of PB according to the results shown in Figure 34. The difference between this AFM-SECM probe and the other probes is the additional FIB cleaning next to the actual electrode area, which guarantees a localized deposition of PB/NiHCF bilayers. This additional treatment doesn't have a direct influence on the H_2O_2 sensitivity but on the amount of deposited material. The amount of PB as estimated by the redox signal in the CVs shown in Figure 34 B is comparable for the 'purple' and 'blue' AFM probes, but lower for the 'red' AFM probe. Up to this point, no correlation could be found between the amount of PB/NiHCF bilayers, detected by the 'activation' of the bilayers by cycling in HCl/KCl solution and the coverage area observed in the SEM images, and the resulting H_2O_2 sensitivity of the modified AFM-SECM probes. All PB/NiHCF-modified AFM-SECM probes showed a sensitivity loss with consecutive H_2O_2 calibrations, which is in accordance with a diminishing concentration of PB during H_2O_2 detection due to more alkaline pH values of the solution induced by the H_2O_2 reduction.

The ‘blue’ AFM-SECM probe tested by two successive H_2O_2 calibrations showed a sensitivity loss of approximately 58 %, the ‘purple’ probe showed a sensitivity loss of 45 %, red probe of 31 % and black probe of 25 %. The PB/NiHCF electrochemical deposition of two bilayers with reduced concentration compared to the original deposition protocol was repeated. It would be favorable to reactivate used PB/NiHCF-modified AFM-SECM probes for further investigations.

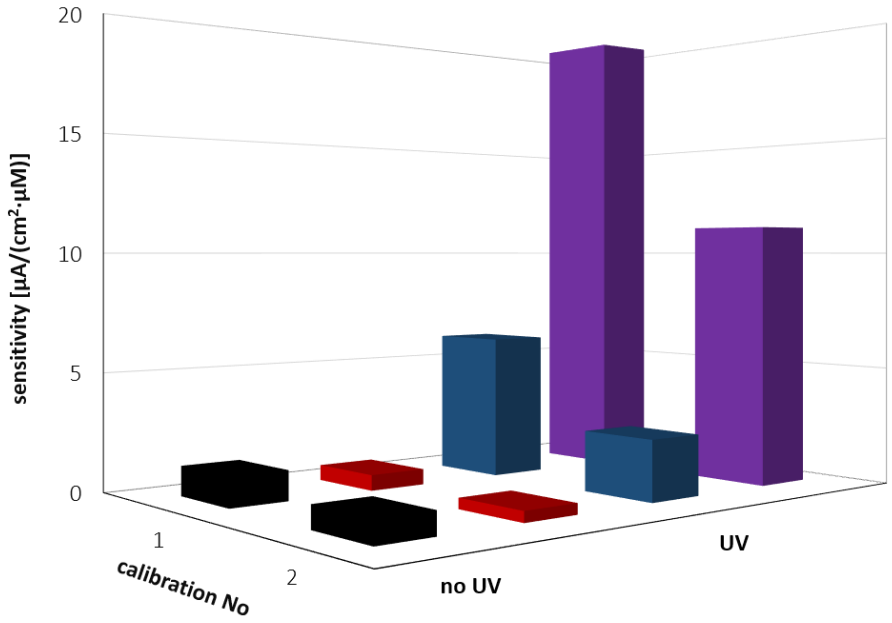

Figure 35 H_2O_2 sensitivities for two consecutive calibrations of the PB/NiHCF-modified AFM-SECM probes. The colors are in accordance with the modified AFM-SECM probes summarized in Table 4.

Additional deposition of PB and NiHCF should also result in an enlarged amount of PB on the AFM-SECM probe. Because the same probe is used, there are no differences in preliminary preparation steps (electrode size, additional FIB cleaning, etc.) of the AFM-SECM probe that showed already good behavior in H_2O_2 sensing. With the assumption that the electrochemical deposition results in PB/NiHCF-mixed bilayers as postulated by Karyakin and coworkers[222], the amount of PB/NiHCF-mixed material should be increased with additional deposition. Because the modified AFM-SECM probe was used in H_2O_2 calibration and according to the loss of sensitivity of the H_2O_2-active film during the 2nd calibration, the amount of PB and NiHCF still left on the electrode area is unknown. Nevertheless, an enhanced H_2O_2 sensitivity after the

2nd electrochemical deposition of mixed bilayers is expected. In Figure 36 A, the H_2O_2 calibration (green dashed line) actually shows an enhanced sensitivity, which is three times higher than the sensitivity of the 1st calibration after the 1st electrochemical deposition of

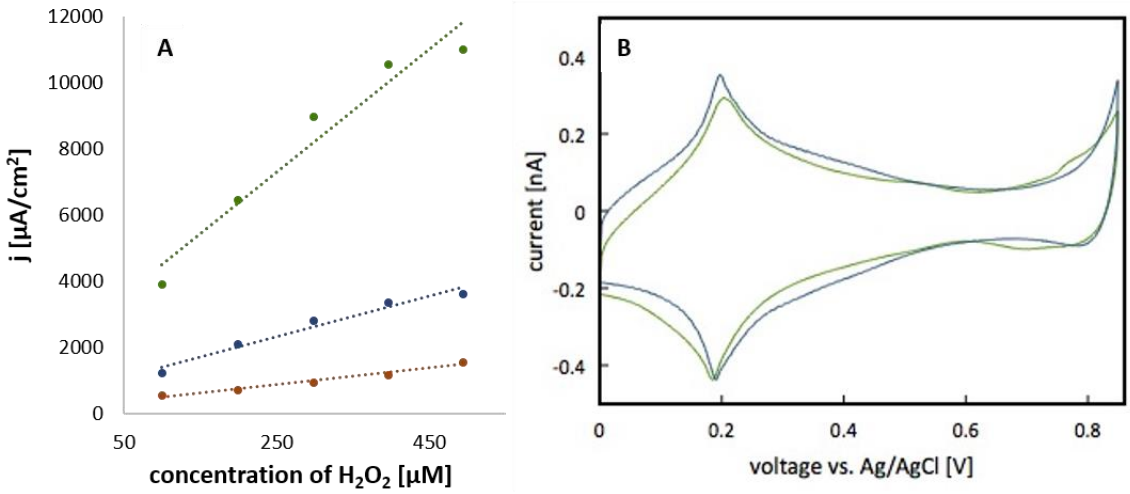

Figure 36 Comparison of H_2O_2 sensitivity and linearity of one PB/NiHCF-modified AFM-SECM probe with UV exposure during electrochemical layer deposition (A): 1st (blue) and 2nd (red) H_2O_2 calibration after 1st electrochemical layer deposition and H_2O_2 calibration (green) after 2nd electrochemical layer deposition. CV in 0.1 M HCl/ 0.1 M KCl of the PB/NiHCF-modified AFM-SECM probe (B) recorded after 1st (blue) and 2nd (green) electrochemical layer deposition and prior to calibrations depicted in (A), scan rate: 0.02 V/s.

PB/NiHCF (blue), but the amount of PB shows just a small deviation in the CVs recorded in 0.1M HCl/ 0.1 M KCl (Figure 36 B). In both electrochemical depositions, the AFM-SECM probe was exposed to UV light after the 1st and the 3rd layer deposition. The difference in sensitivity is therefore not associated with the exposure of the PB/NiHCF-modified AFM-SECM probe to UV light. The enhanced stability can be addressed neither to the exposure of the PB/NiHCF-modified AFM-SECM probes to UV light nor to the amount of PB. Because the same AFM-SECM probe was used in this comparison, there were no additional differences, namely the electrode area or geometry of the original Pt/C-modified electrode. Additionally, the hypothesis that alternating electrochemical deposition of PB and NiHCF results in the formation of bilayers is questionable. The presented results are reflecting individual AFM-SECM probes, at this stage, no quantitative conclusion could be drawn. The investigation of

27 of 31 PB/NiHCF-modified AFM-SECM probes showed no H_2O_2 sensitivity or any stable behavior in H_2O_2 detection if this is related to handling issues (e.g., electrical discharge, etc.) or insufficient stability of the deposited layers could not be clarified.

4.3.3 *Localized detection of H_2O_2 by AFM-SECM*

For the first AFM-SECM measurements, the original deposition protocol as published by Komkova et al.[20] was used resulting in a PB/NiHCF-modified AFM-SECM probe with complete coverage of the pyramidal AFM tip. In this investigation, no localized signal was expected to reflect the size of an electrode as a model sample during H_2O_2 generation by an applied potential. Therefore, the PB/NiHCF-modified AFM-SECM probe was used for imaging the H_2O_2 evolution at a Pt/C-modified Pt UME biased at – 0.5 V vs. quasi-Ag/AgCl reference electrode, which is sufficient to generate H_2O_2[234]. The morphology was detected in AFM contact mode and the generated H_2O_2 in SECM generation/collection mode (Figure 37 B, D, and F). Control experiments were performed at a sample bias of 0 V vs. Ag/AgCl quasi-reference electrode, which is not sufficient for H_2O_2 generation (Figure 37 A, C and E). The current signal in Figure 37 F recorded by the PB/NiHCF-modified, tip-integrated electrode clearly shows a response to H_2O_2 generated at the UME. Even a difference between the original electrode area and the overlapping Pt/C composite could be detected.

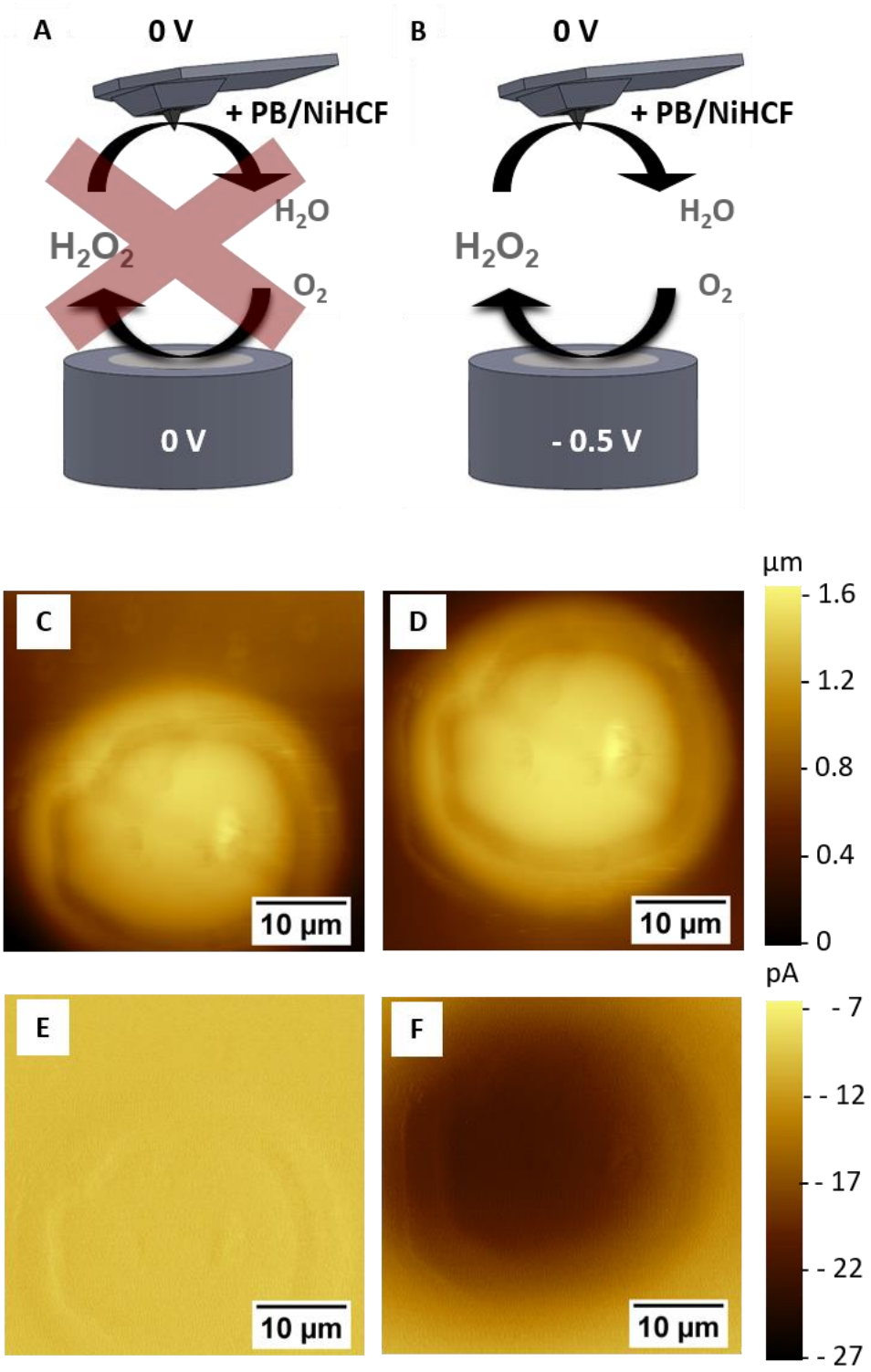

Figure 37 AFM-SECM images recorded at an UME with a PB/NiHCF-modified AFM-SECM probe; setup according to the schemes depicted in (A) and (B): topography (C, D) and corresponding tip current (E, F) recorded at the AFM-SECM probe with a sample bias of 0 V (E) and – 0.5 V (F) vs. Ag/AgCl quasi-reference electrode, respectively, and a tip bias at 0 V vs. Ag/AgCl quasi-reference electrode in both measurements. Original size: 54 x 54 µm^2, scan rate: 0.2 ln/s (10.9 µm/s).

Although the used AFM-SECM probe was completely covered with H_2O_2-active PB/NiHCF bilayers (as shown in Figure 31 A, B), still localized information could be obtained, as the signal of the H_2O_2 reduction mainly results from the film at or close to the AFM-integrated electrode surface. This becomes more obvious in the 3D representation of the AFM topography overlaid with the current signal as shown in Figure 38.

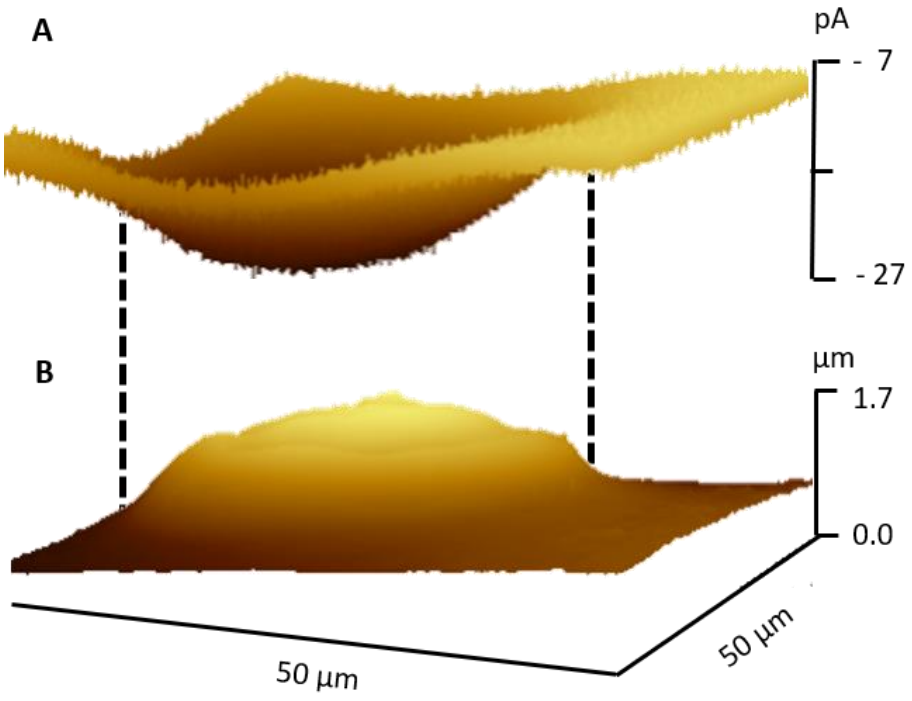

Figure 38 3D representation of the results shown in Figure 37. The current signal of H_2O_2 reduction detected at a PB/NiHCF-modified AFM-SECM probe (A) and AFM topography (B).

In addition, the H_2O_2-sensitive PB/NiHCF bilayers may also have been removed during previous scans or calibrations, which would also explain that there are no obvious artifacts in the topography visible. The H_2O_2 conversion is predominantly located at PB/NiHCF bilayers deposited onto the AFM tip-integrated microelectrode. Nevertheless, for investigations of unknown sample morphology and/or spatially heterogenous H_2O_2 release, the H_2O_2 sensing layer should be well defined and confined to the electrode surface. Although the current signal was stable during 5 consecutive AFM scans, partial dissolution of the PB/NiHCF film during measurements might lead to a false interpretation of the detected current signals for unknown samples.

To exclude electrochemical activity in the absence of the PB/NiHCF bilayers and any crosstalk between the current signal and the topography detected simultaneously by AFM-SECM, an unmodified AFM-SECM probe was used additionally as shown in Figure 39. As expected, no current response related to H_2O_2 consumption could be detected by the unmodified AFM-SECM probe.

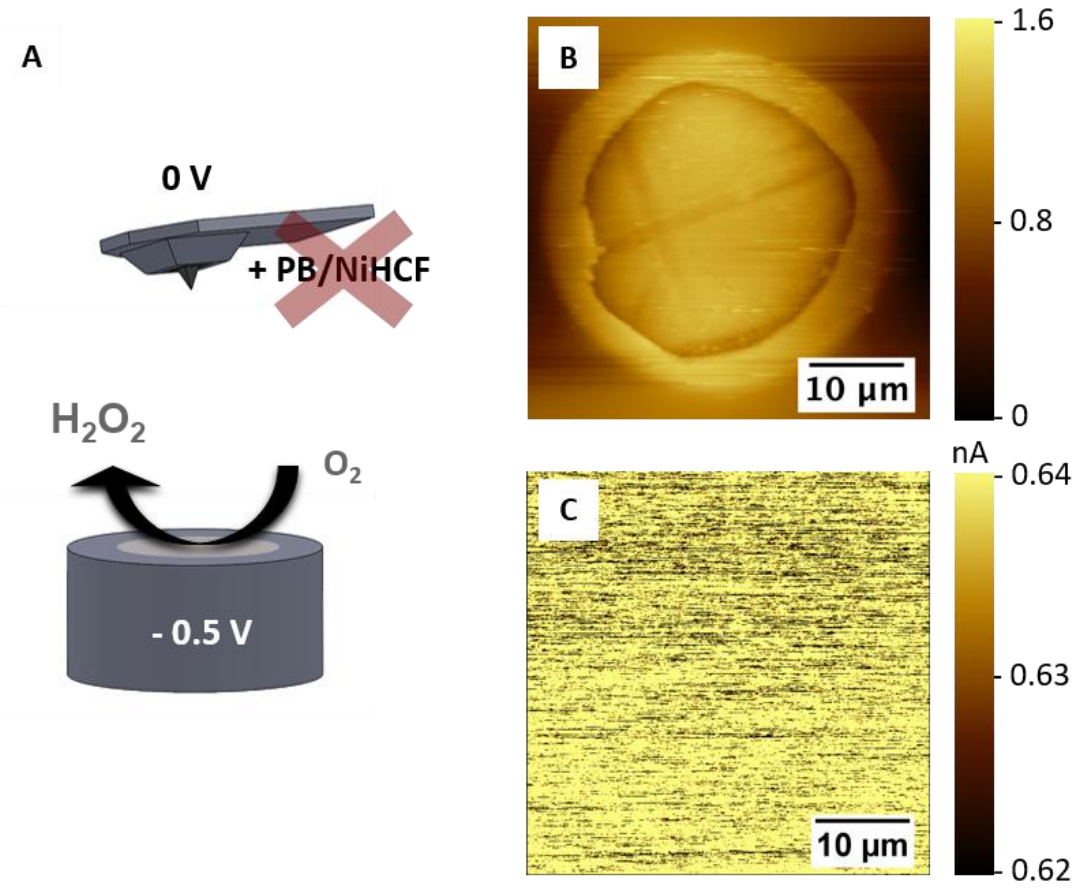

Figure 39 AFM-SECM image of an UME recorded with an unmodified AFM-SECM probe; set-up according to the scheme depicted in (A): Topography (B) and corresponding tip current (C) recorded at an unmodified AFM-SECM probe with the sample biased at – 0.5 V vs. Ag/AgCl quasi-reference electrode and with an AFM-SECM probe bias of 0 V vs. Ag/AgCl quasi-reference electrode. Original size: 46 x 46 µm^2, scan rate: 0.25 ln/s (11.4 µm/s).

4.4 Conclusion and outlook

Within this section, PB/NiHCF-modified UMEs and AFM-SECM probes for H_2O_2 detection have been investigated. Thereby, significant influences of parameters used for the fabrication of AFM-SECM probes have been identified, namely the influence of vacuum conditions, UV light and Pt/C composite as supporting electrode material. In general, no negative effect of all these parameters could be detected. In contrast, a significantly improved stability and sensitivity for the detection of H_2O_2 was achieved. Preliminary experiments for mapping localized H_2O_2 evolution at an UME using a PB/NiHCF-modified AFM-SECM probe are presented. Although the used AFM-SECM probe was completely covered with PB/NiHCF bilayers, a localized detection of H_2O_2 could be shown. This can be explained that only the PB/NiHCF-covered tip-integrated electrode area close to the sample surface contributed predominantly to the recorded signal. Additionally, a change in the morphology of the PB/NiHCF film, as shown in 4.3.1 for the modification of UMEs, might result in that the non-electrode areas covered by PB/NiHCF film are not significantly contributing to the overall signal. To avoid the coverage of the complete tip, AFM-SECM investigations have to be repeated with optimized parameters for the electrochemical deposition of PB/NiHCF bilayers reported within this section. The bilayer-modified probes, either UMEs or AFM tip-integrated electrodes, showed a good response to H_2O_2 with enhanced stability compared to PB as electrocatalytic layer for H_2O_2 reduction. A reduced concentration and number of deposited PB/NiHCF bilayers used for the modification of AFM tip-integrated electrodes showed a reduced amount of PB/NiHCF located on the AFM-SECM probe as detected by SEM, but H_2O_2 calibrations showed enhanced sensitivity for H_2O_2. However, the reproducibility with respect to AFM-SECM probe modification needs to be improved in future experiments. Characterization of individual PB/NiHCF-modified AFM-SECM probes showed additionally no comparable behavior and no correlation between the redox signals within cycling in 0.1 M HCl/ 0.1 M KCl for activation of the PB/NiHCF bilayers and the actual sensitivity towards H_2O_2. All investigations of the PB/NiHCF bilayers by AFM-SECM, SEM, EDX, optical microscopy and electrochemical measurements led to the conclusion that the formation of bilayers by alternating electrochemical deposition of PB and NiHCF could not be confirmed, but rather the formation of a homogeneous PB/NiHCF film with varying thicknesses in relation to the amount of deposited PB and NiHCF is most likely. Further investigations with respect to the actual composition of PB/NiHCF-mixed layers are needed in future. With a detailed investigation of

the mixed films, the modification of AFM-SECM probes can be optimized and a higher yield of PB/NiHCF-modified sensors with appropriate performance in H_2O_2 sensing can be gained.

5 AFM tip-integrated pH sensors

5.1 Introduction

The miniaturization of pH sensors is essential for localized pH measurements and enables research of metabolic or signaling processes in biomedical related research for example mapping changes of pH at the cell level[21], as well as the detection of localized corrosion processes[22]. Therefore, the sensor material has to be biocompatible, mechanically resistant and the pH sensor has to be miniaturized[45]. The most common pH sensor is the pH-sensitive glass electrode. Carter et al.[235] used a glass microelectrode for the study of corrosion processes. For the investigation of biological samples, P. C. Caldwell used a glass microelectrode for intracellular pH sensing at muscle fibers of crabs[236] and at a giant squid axon[237]. Next to pH-sensitive glass electrodes, metal/metal oxides were widely used for pH detection during the last century[45,238]. A range of suitable metal/metal oxides, such as RuO_2[239], WO_3[240], and most important iridium oxide[62] and the antimony/antimony oxide[23,24] electrode, have been investigated so far and successfully applied for pH monitoring in biological research. For example, intracellular investigation of the giant squid axon with a 1 µm antimony electrode[241] and in extracellular investigations of endothelial cells[242] and carbonic anhydrase located at the brain[243] have been demonstrated. SECM is highly suitable for the localized detection of changes in electrochemical signals at a surface and potentiometric measurements combined with SECM were also successfully shown[244–246]. Mirkin and co-workers investigated pH changes around human breast epithelial cells with a 7 µm Sb UME[247]. The investigation of corrosion processes by SECM has been reviewed by Niu et al.[248]. For the detection of the oxygen reduction reaction and corresponding pH changes due to corrosion of metal or metal alloy surfaces, Sb[22], Ir oxide particles[249] or hydrogen ionophore liquid membranes[250] in combination with SECM have been used so far. Although SECM is highly suitable for mapping local changes in electrochemical signals, typically it is challenging to obtain simultaneously topographical information of the investigated sample. This gap can be closed by the combination of SECM with other surface sensitive techniques, e.g. with scanning vibrating electrode technique (SVET)[251,252] and SICM[253] for pH mapping. pH measurements in close vicinity to the area of interest with high spatial resolution may

further provide information on the reaction mechanism, the rate of reaction or the involved species itself. The combination of a pH-sensitive electrode integrated into an AFM probe may enable the local detection of pH changes simultaneous with changes in topography. Although the metal/metal oxide pH sensors have been used in a broad variety of applications, insufficient stability was reported, e.g. for the iridium oxide electrodes, and different oxidation states of the iridium oxide or different fabrication schemes of the active films showed a distribution of pH sensitivities of 82 – 92 mV/pH[27], 62 – 74 mV/pH[61], or 59 - 77 mV/pH[45]. Additionally, decreasing pH sensitivity in consecutive calibrations was also observed for iridium oxide electrodes[49]. However, no statistical data are available in literature and most of the publications present investigations in respect to individual sensors, which will be also discussed in the following sections. Within this thesis, Ir and Sb–modified AFM-SECM probes are investigated as pH sensors and the performance of the modified AFM-SECM probes is investigated by monitoring the dissolution of calcite crystals. Unwin and co-workers investigated the dissolution of calcite using a platinized Si_xN_y AFM cantilever to reduce the pH value to more acidic pH values, which accelerates the crystal dissolution[148]. Furthermore, the electrochemical deposition of EIROF onto AFM tip–integrated Au and Pt/C–modified Au microelectrodes is evaluated within the following chapter and investigated at Au and Pt/C–modified Au UMEs.

5.2 Experimental

Ultrapure water (18.2 MΩ, ELGA LabWater, Veolia Water Solutions & Technologies) was used for the preparation of all solutions. For Ir-modified AFM probes and iridium oxide modified UMEs, CVs in de-aerated 0.5 M H_2SO_4 (from 98 %, VWR Chemicals) in a potential range of - 0.45 V to 0.75 vs. Hg/$HgSO_4$ reference electrode (sat. K_2SO_4, CH Instruments) at a scan rate of 1 V/s was used to activate the iridium oxide film (Figure 40 A) prior to pH calibration.

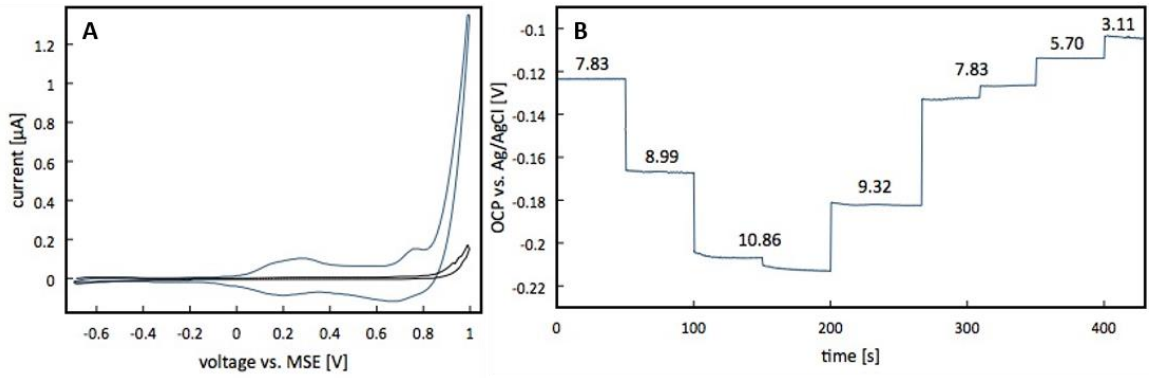

Figure 40 CV (A) in 0.5 M H_2SO_4 vs. Hg/$HgSO_4$ reference electrode, showing the 1st (black) and the last (blue) CV of in sum 500 cycles. Scan rate: 1 V/s. OCP measurement (B) in 0.05 M TRIS buffer with corresponding pH values determined by a pH glass electrode at room temperature after addition of HCl and NaOH, respectively.

OCP measurements (Figure 40 B) vs. Ag/AgCl reference electrode (sat. KCl, RE-1CP, ALS Co) were done in 0.05 M TRIS buffered solution (pH 6.96, tris(hydroxymethyl)-aminomethane, Merck KGaA) within a pH range of 2 – 11 using a (bi)potentiostat (CHI660A and CHI660C, CH Instruments). The pH values were adjusted by addition of 5 M HCl (from 30 % HCl, Normapure, VWR International GmbH) or 0.5 M NaOH (Merck KGaA), respectively. A complete exchange of different buffered solutions took several minutes, which impedes proper detection of the response time of the pH sensor towards pH changes. Therefore, the pH calibration was done by consecutive addition of aliquots of HCl or NaOH, respectively. After mixing the solution, a pH glass electrode (InLab® Expert pro, Mettler-Toledo Intl. Inc.) with an integrated temperature sensor was used to determine the pH values of the buffered solutions. The pH calibrations were done at room temperature with small fluctuations of 1 – 2 °C during measurements. A simultaneous detection of the pH with the pH glass electrode during OCP measurements in the same

solution was not possible due to strong interferences in the detected OCP signal by the glass electrode (see Figure 41).

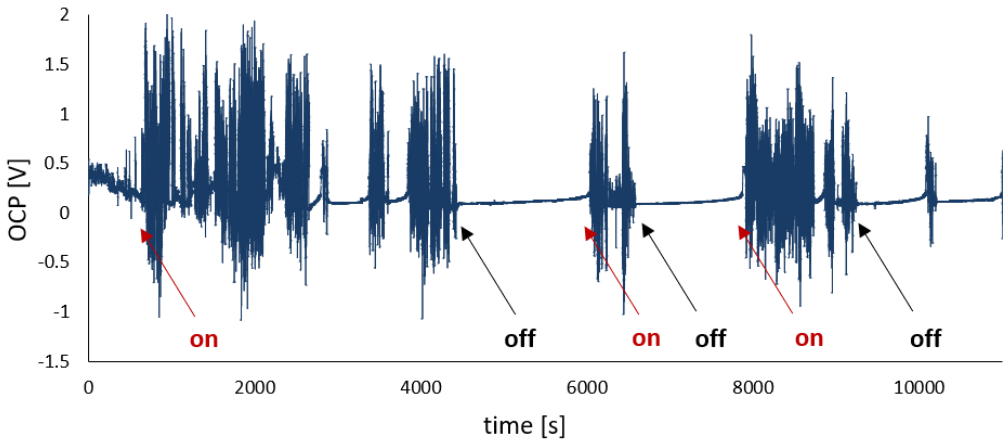

Figure 41 Influence of the pH glass electrode towards the OCP signal of an Ir/IrOx – modified AFM probe. OCP measurement in 0.05 M TRIS buffer at pH 2.5. The pH glass electrode was kept within the liquid cell in the Faraday cage and was turned on/off as labeled within the graph.

Different AFM tip- integrated pH sensors were investigated within this thesis, which were fabricated by former co-workers of Mizaikoff and Kranz. AFM probes modified with a pH-sensitive Sb layer were fabricated by Jong Seok Moon[188]. Briefly, a commercial Si_xN_y AFM cantilever was modified with a thin Ti adhesion layer and an Au layer (100 nm) with a DC sputter coater, followed by the deposition of Sb at the AFM tip with varying thicknesses (35 - 225 nm) by an RF sputter system. Afterward, the AFM-SECM probes were insulated by PECVD with Si_xN_y and SiO_2. An active pH-sensitive electrode and a defined AFM tip were exposed by FIB milling (Quanta 3D FEG, ThermoFisher Scientific) as reported in section 4.2. AFM-SECM probes were batch-fabricated by Heungjoo Shin[254] und modified with Ir. Silicon cantilevers were modified with a thin Pt layer and an Ir layer with a thickness of 300 - 400 nm. After the release of the cantilevers, additional deposition is required to compensate stress in order to use such probes for AFM measurements.

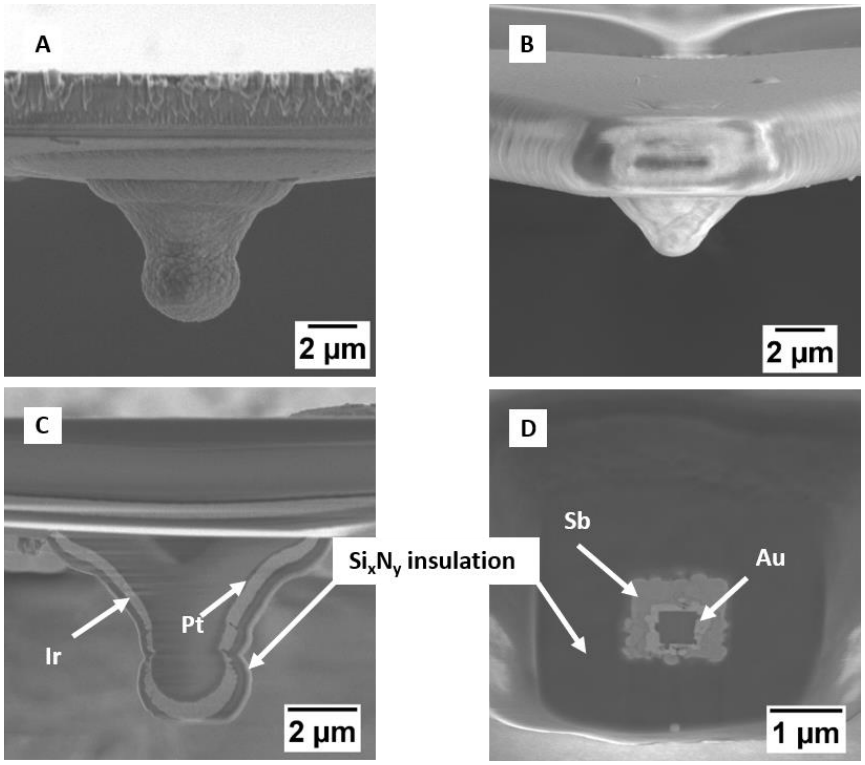

Figure 42 SEM of Ir (A, C) and Sb (B, D) modified AFM probes. The whole AFM tip shown in (A) was cut by FIB milling to expose all components of the Ir – modified AFM tip (labeled in C). The electrode area of an insulated Sb – modified AFM probe (B) was also exposed by FIB milling. The Sb layer deposited on Au is labeled in (D). Acceleration voltage: 3 kV,10 pA (Ir)/ 20 pA (Sb).

The different geometries of the AFM tip-integrated pH sensors are summarized in Figure 42. Prior to the calibration of the AFM tip- integrated pH sensors, the AFM-SECM probes were mounted onto an AFM nosecone or an insert using UV glue (Dymax 9001-E-V3.1 or DYMAX 425, Dymax Europe GmbH). Electrochemical deposition of iridium oxide film electrodes was done according to Yamanaka et al.[255]. 71.3 mg/50mL iridium(IV)oxide (Alfa Aesar GmbH & Co. KG) was stirred for 30 min, followed by the addition of 0.5 mL H_2O_2 (30%, Merck KGaA). After 10 min stirring, 208.2 mg anhydrous oxalic acid (Fluka Chemie GmbH) was added to the solution. The pH was adjusted to 10.5 by the addition of KCO_3 (Merck KGaA). After storing the solution for three days, the solution was purged with argon for 30 min prior to electrochemical deposition. Au wires (diameter: 10 µm, Goodfellows) were used as electrodes fabricated as described elsewhere[65,226]. Some Au electrodes were additionally modified with a Pt/C composite by IBID (precursor: methyl-cyclopentadienyl-trimethyl platinum, ThermoFisher Scientific) with respect to the EIROF

modification of AFM tip-integrated pH sensors. AFM-SECM probes were prepared based on the procedures as already reported[133] and described in section 4.2. The AFM tip–integrated Au electrode was modified with Pt/C via IBID. 5 mM $[Ru(NH_3)_6]Cl_3$ (98 %, Aldrich) in 0.1 M KCl (Merck KGaA) and 5 mM 1,1'-ferrocenedimethanole (98 %, Acros Organics) in 10% ethanol (from 96 %, VWR Chemicals) and 0.1 M KCl (Merck KGaA) were used to determine the electroactive electrode surface of the UMEs and the AFM-SECM probes prior to electrochemical modification with EIROF. pH-active iridium oxide films were deposited using a (bi)potentiostat. Different deposition techniques were evaluated as summarized in Table 5.

	deposition parameters
constant current	0.2 nA for 300 s
constant potential	0.75 V vs. Ag/AgCl for 300 s
CV	- 0.45 V - + 0.7 vs. Ag/AgCl, scan rates: 1- 10 V/s, 20 - 500 cycles
pulsed potential	E_1 = 0.75 V, E_2 = -0.45 V for 0.25 s, respectively; number of cycles: 25 -250

Table 5 Summary of deposition techniques with corresponding deposition parameters used for the EIROF formation, by CV, at a constant current, and at constant or pulsed potentials.

The modified UMEs were investigated after electrochemical deposition by optical microscopy (AXIO Imager.M1m, Zeiss), SEM (Quanta 3D FEG, ThermoFisher Scientific) and contact mode AFM (5500 AFM/SPM microscope, Keysight Technologies) with silicon nitride tips (OTR-P, Olympus). All AFM images and correlating height and current profiles were processed by Pico View (Keysight Technologies) or Gwyddion[225]. AFM-SECM measurements were done in contact mode AFM detecting the dissolution of calcite and the local associated pH changes by OCP measurements using a bipotentiostat (CHI842B, CH Instrument). The OCP output signal of the bipotentiostat was fed to an AD channel of the AFM controller for correlating the potentiometric data with the topographical image.

Prior to AFM-SECM investigations in TRIS buffered solution, the calcite sample was imaged in air in AFM contact mode to locate single calcite crystals. Calcite crystals were synthesized by the ammonia diffusion method from dissolved $CaCl_2$ (95 %, Carl Roth) and $(NH_4)_2CO_3$ (Merck KGaA) under NH_3 – saturated atmosphere[256]. The calcite crystals were embedded in Crystalbond (509, Plano) and partially polished with Al_2O_3 suspension (50 nm, MasterPrep, Buehler).

5.3 Results and discussion

In the following section, results of AFM-SECM probes modified with either an Ir or Sb metal layer are presented by pH calibrations in 5.3.1. Due to a limited number of available AFM-SECM probes modified with an Ir or Sb metal layer, respectively, the following results might be interpreted as first investigations showing the suitability of these AFM tip-integrated pH sensors, but also in detection of localized pH changes, exemplarily shown by AFM-SECM investigations of the dissolution of calcite crystals in 5.3.2. The fabrication of such modified AFM-SECM probes resulted in strong bending of the AFM cantilever due to intrinsic stress during sputtering of the e.g. Ir metal layer[254]. A limited number of Sb or Ir coated probes were available for combined measurements in the time frame of this thesis showing a cantilever bending of 1 – 2°. AFM cantilevers with more bending were used in OCP measurements for pH calibrations in bulk experiments. Additionally, EIROF-modified microelectrodes were tested in consecutive pH calibrations at UMEs (diameter: 10 µm), as presented in 5.3.3, as alternative fabrication strategy of a pH sensor integrated into AFM probes.

5.3.1 *AFM tip-integrated pH sensors*

After insulation of the AFM probes and exposure of an active electrode area by FIB milling as described in section 4.2, the pH sensitivity and linearity was investigated performing calibrations. The AFM probes with an integrated pH – sensitive AIROF electrode showed a stable pH response in long-term measurements (Figure 43) within consecutive calibrations. The pH response for the exemplarily presented pH sensor was 54.3 mV/pH, whereas a pH response of 65.4 mV/pH - also referred to as super-Nernstian behavior reported for AIROF electrodes[45] - could be determined in the buffered region shown in the zoomed graph in Figure 43. The linearity of the calibration graphs is in an acceptable range (inlaid table in Figure 43) to investigate qualitative pH changes, localized at a sample surface in following AFM-SECM investigations.

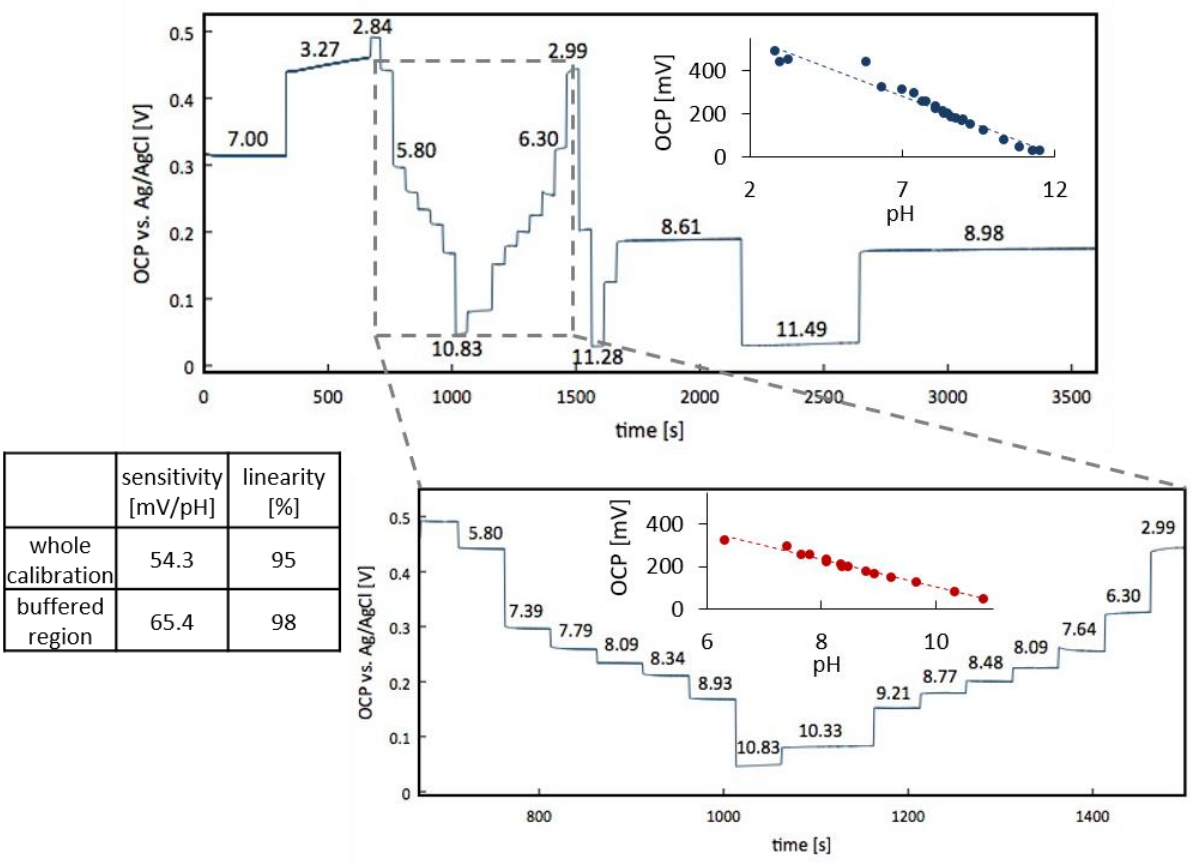

	sensitivity [mV/pH]	linearity [%]
whole calibration	54.3	95
buffered region	65.4	98

Figure 43 OCP vs. Ag/AgCl reference electrode of an AIROF-modified AFM probe in 0.05 M TRIS buffer detecting pH changes by addition of either 5 M HCl or 0.5 M NaOH, respectively. The table summarizes the sensitivity and linearity of the whole calibration experiment and the buffered region shown in the zoomed extract.

Exemplarily, the results for 4 consecutive calibrations of one Ir -modified AFM-SECM probe are shown in Figure 44, pH sensitivity and linearity are given in the implemented table for the different calibrations. The results reveal that the OCP signal showed a more linear behavior with a high recovery within consecutive calibrations for neutral to alkaline pH values, whereas the distribution of the detected potentials was increased in the acidic pH range. This has been already reported for AIROF electrodes showing a varying pH response with different pH sensitivities in correlation to the measured pH values[257].

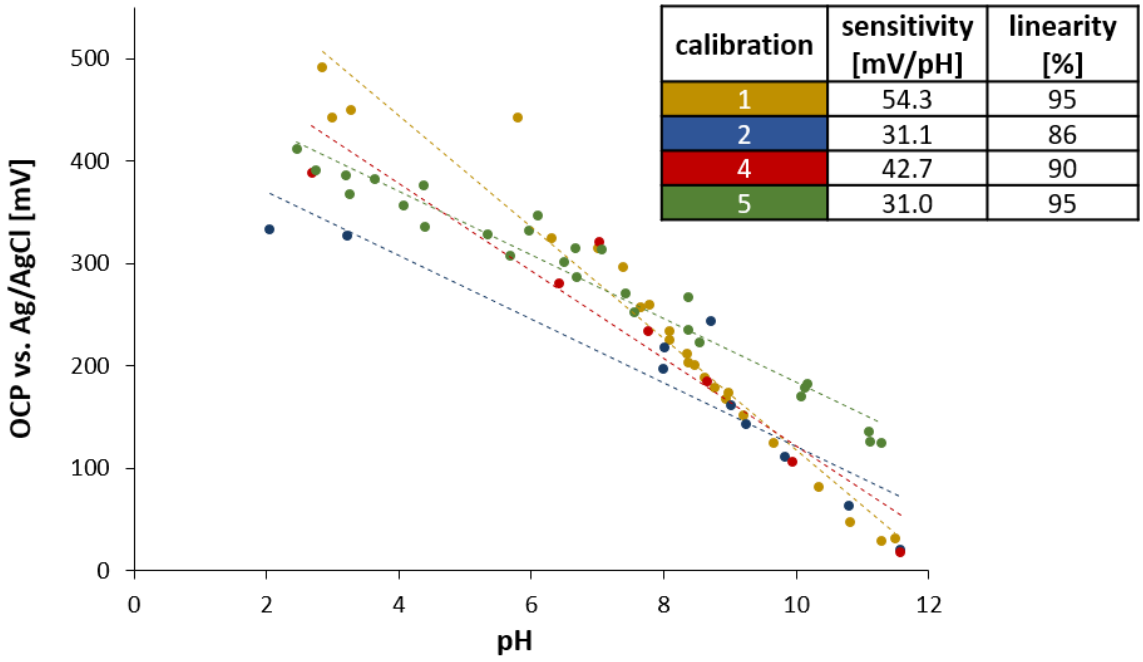

calibration	sensitivity [mV/pH]	linearity [%]
1	54.3	95
2	31.1	86
4	42.7	90
5	31.0	95

Figure 44 Calibration of an AIROF-modified AFM-SECM probe: Linear regressions of 4 consecutive pH calibrations with sensitivity and linearity given in the implemented table labeled by the respective colors. The 3rd calibration is not shown due to insufficient stability (see also Figure 45).

The OCP measurement for the third and the fourth calibration of this AIROF-modified AFM-SECM probe is presented in Figure 45. In contrast to Sb – modified electrodes, the iridium oxide film can be regenerated and pH sensitivity and linearity can be recovered by cycling in H_2SO_4. In Figure 45, the OCP measurements recorded with an AIROF-modified AFM probe are shown before and after the regeneration of the active iridium oxide film, demonstrating the great advantage of Ir over Sb. The presented results here correspond

to one AFM-SECM probe tested in consecutive pH calibrations due to a limited number of available AFM-SECM probes. Limitations according to available AFM-SECM probes were also a problem for Sb-modified AFM-SECM probes.

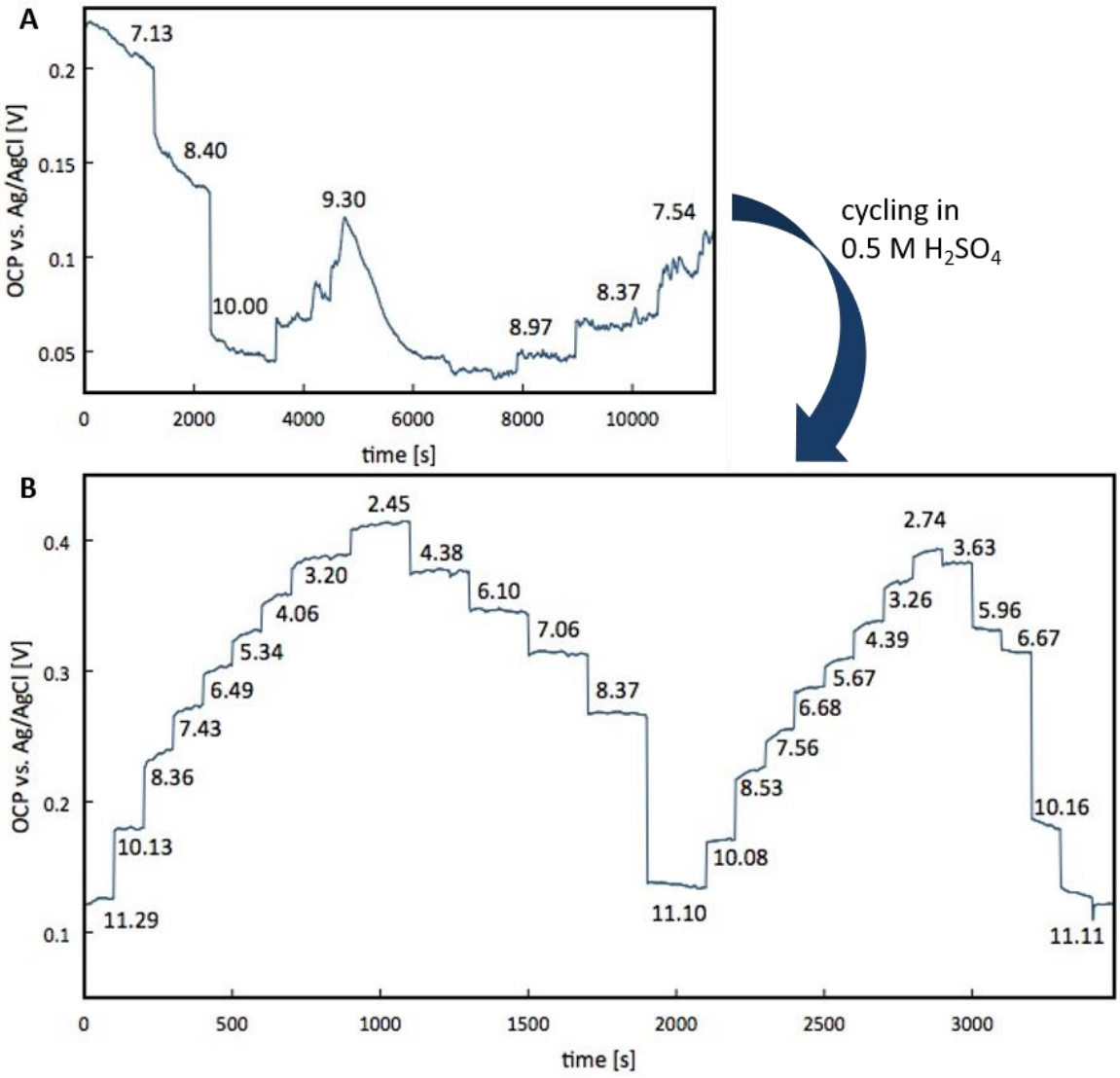

Figure 45 Regeneration of AIROF electrodes: OCP vs. Ag/AgCl reference electrode in 0.05 M TRIS buffer detecting pH changes by addition of either 5 M HCl or 0.5 M NaOH, respectively, before (A) and after (B) cycling in 0.5 M H_2SO_4. The linear regression of the results shown in (B) is depicted in Figure 44 as calibration 4 (red).

Individual probes could be tested in pH calibrations, as exemplarily depicted in Figure 46, showing two OCP measurements with correlating pH values of the buffered solution detected with a 100 nm Sb-modified AFM probe in a short (A) and a long-term (B) calibration, The results show a fast and stable pH response up to 300s (A) and being linear over several minutes at the same time (B). The pH sensitivity was 50.3 (A) and 55.9 (B) mV/pH, respectively, whereas the linearity in the OCP measurements was 99 % (A) and 97 % (B).

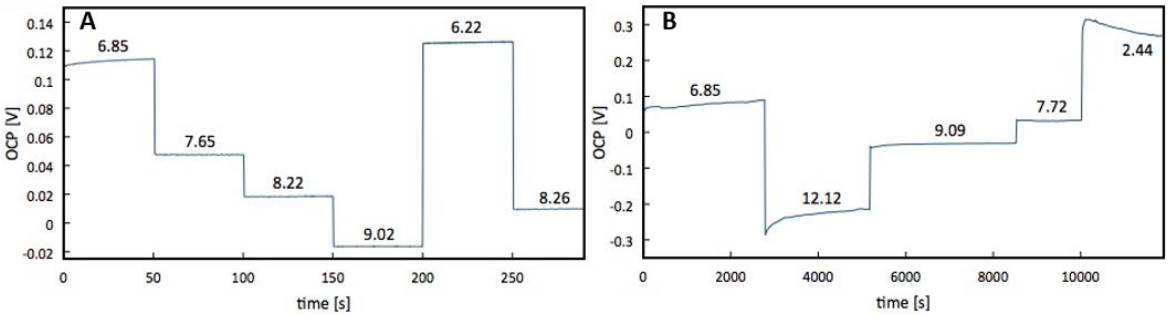

Figure 46 OCP vs. Ag/AgCl reference electrode in 0.05 M TRIS buffer detecting pH changes by addition of either 5 M HCl or 0.5 M NaOH, respectively. The change in short time scales (A) and stability within long time measurements (B) were investigated.

However, only a small percentage of available potentiometric Sb AFM-SECM sensors showed a measurable pH response, which may be associated with the long storage time (approx. 4 years) under ambient conditions. Additionally, some sensors showed a strong surface change after OCP measurements as depicted in Figure 47 B and C. It seems that the Sb layer undergoes some dissolution process and spread as small particles around the actual electrode area, which may be associated with the complete oxidation of the Sb layer during the long storage time. The Au layer is still visible and the in-plane area of the Au can be identified as the frame in the zoomed SE image in C, whereas the pyramidal shape of the Au modified AFM tip became visible in the surrounding region formerly covered by the Sb layer. In case of Sb – modified AFM-SECM probes, both metal layers (Au and Sb) are exposed and connected within an electrolyte solution resulting in a galvanic couple and, therefore, in the dissolution of Sb as the less noble metal. Localized corrosion and the adjoining removal of the Sb film because of impurities on the Sb electrodes was

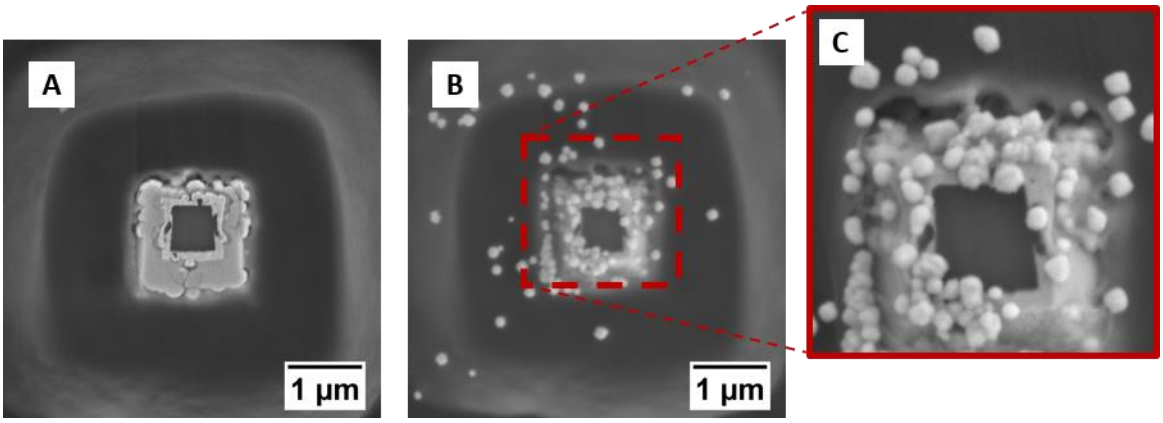

Figure 47 SEM images of a Sb-modified AFM-SECM probe before (A) and after (B) calibration. The zoomed region (C) shows the removal of the Sb layer. Acceleration voltage: 5 kV, 27 pA (A) /47 pA (B, C).

already reported, whereas these impurities were not specified[52]. However, prior studies using these Sb-modified AFM-SECM probes didn't show this behavior[188]. To eliminate any possible dissolution of the Sb metal layer by forming a galvanic couple, the deposition of Sb should be limited to the AFM tip and part of the cantilever, whereas Au as an electronic connection layer might be just deposited onto the AFM chip and cantilever[188]. Another possibility would be the exposure of an electrode area next to the pyramidal AFM tip, exposed by FIB milling in a top-down approach. Thereby, just the Sb metal deposited on top of Au is exposed. The SECM signal is then shifted towards the topographical information with respect on the distance between the AFM tip and the electrode area located close to the AFM tip. These investigations were not the focus of this thesis.

5.3.2 *Investigation of calcite dissolution by AFM-SECM*

First AFM-SECM measurements were conducted with Sb- and AlROF-modified AFM-SECM probes. Changes in the OCP detected by the AFM tip-integrated pH sensor were interpreted just qualitatively according to the obtained results in section 5.3.1. Prior to AFM-SECM investigations, the pH sensors were tested towards their pH sensitivity to guarantee a change in the OCP signal to more negative potentials for more alkaline pH values. As a model system, the dissolution of calcite was imaged with the AFM-SECM pH

sensors. Calcite is dissolved in aqueous solution by characteristic surface changes showing rhombohedral etch pits due to dissolution[28]. Additionally, the dissolution process results in a pH change to more alkaline pH values[29]. Thereby both, a surface change and a pH change should be detectable by the AFM-SECM probes. Similar investigations were published by Unwin and coworkers[253], detecting the dissolution of a calcite crystal with an edge length of approximately 25 µm by SECM-SICM revealing limited topographical information. In Figure 48, the results for the AFM-SECM investigations with an AFM tip-integrated Sb electrode are shown. The electrode area is located next to the actual AFM tip as depicted in the SE images in A - C. In the AFM deflection and topography images shown in D and E, the change in morphology of the calcite crystal is clearly visible revealing

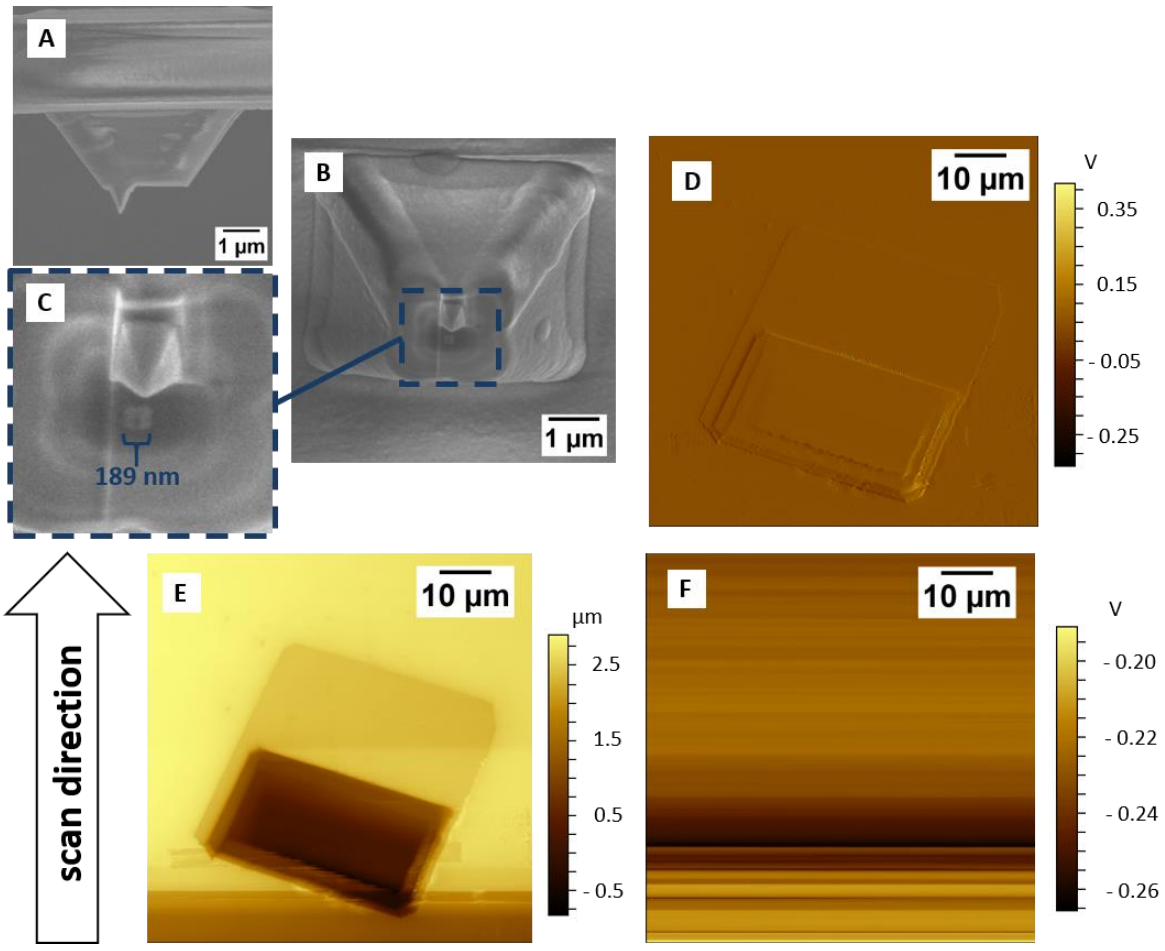

Figure 48 AFM-SECM measurement of the dissolution of calcite using an AFM tip-integrated Sb electrode: SEM images of the used AFM-SECM probe in side view (A) and 52° tilted (B), with a zoomed view to the actual electrode area with an edge length of 189 nm (C). Acceleration

voltage: 3 kV, 43 pA. AFM deflection (D) and topography (E) recorded in AFM contact mode and correlating potential changes detected by OCP vs. Ag/AgCl quasi-reference electrode (F). Original size: 80 x 80 µm^2, scan rate: 0.1 ln/s (16 µm/s).

the characteristic pit structures. The potential changes during AFM scanning are depicted in Figure 48 F showing lower potential values compared to regions without calcite, which correlate to a pH change towards more alkaline pH values. The lateral resolution in Figure 48 F is insufficient within the single line scans (x-direction), whereas a change in signals is localized with respect to the scan direction (marked by an arrow in Figure 48, y-direction). Same investigations were repeated with AFM-SECM probes with tip-integrated AIROF pH sensors. One AFM-SECM investigation is exemplarily shown in Figure 49. Thereby, a smaller calcite crystal (approx. 2-8 µm in length), compared to the one depicted in Figure 48, was mapped using the maximum scan range of the piezoelectric positioner in case the missing lateral resolution is correlated to convection effects of the moving tip. Although the Ir electrode area integrated into the AFM probe is large with an outer diameter of the ring electrode of 3.6 µm, the resolution in the scan direction (y-direction) was sufficient to detect localized pH changes related to the dissolution of calcite. However, no laterally resolved information on pH change in x-direction was observed. The height and potential profiles at the marked positions in E and D of Figure 49 are clearly showing a potential change towards lower potentials correlating with a higher pH value at the position of the calcite crystal with an elevated topography visible compared to the surrounding surface, in which the calcite crystal was embedded. Nevertheless, the change in the potential is still spread over the whole distance in x-direction lacking lateral information in the region of the calcite crystal. This broadening of the OCP signal seems to be absent in the y-direction, which indicates that the lack of resolution is not associated with the actual electrode size.

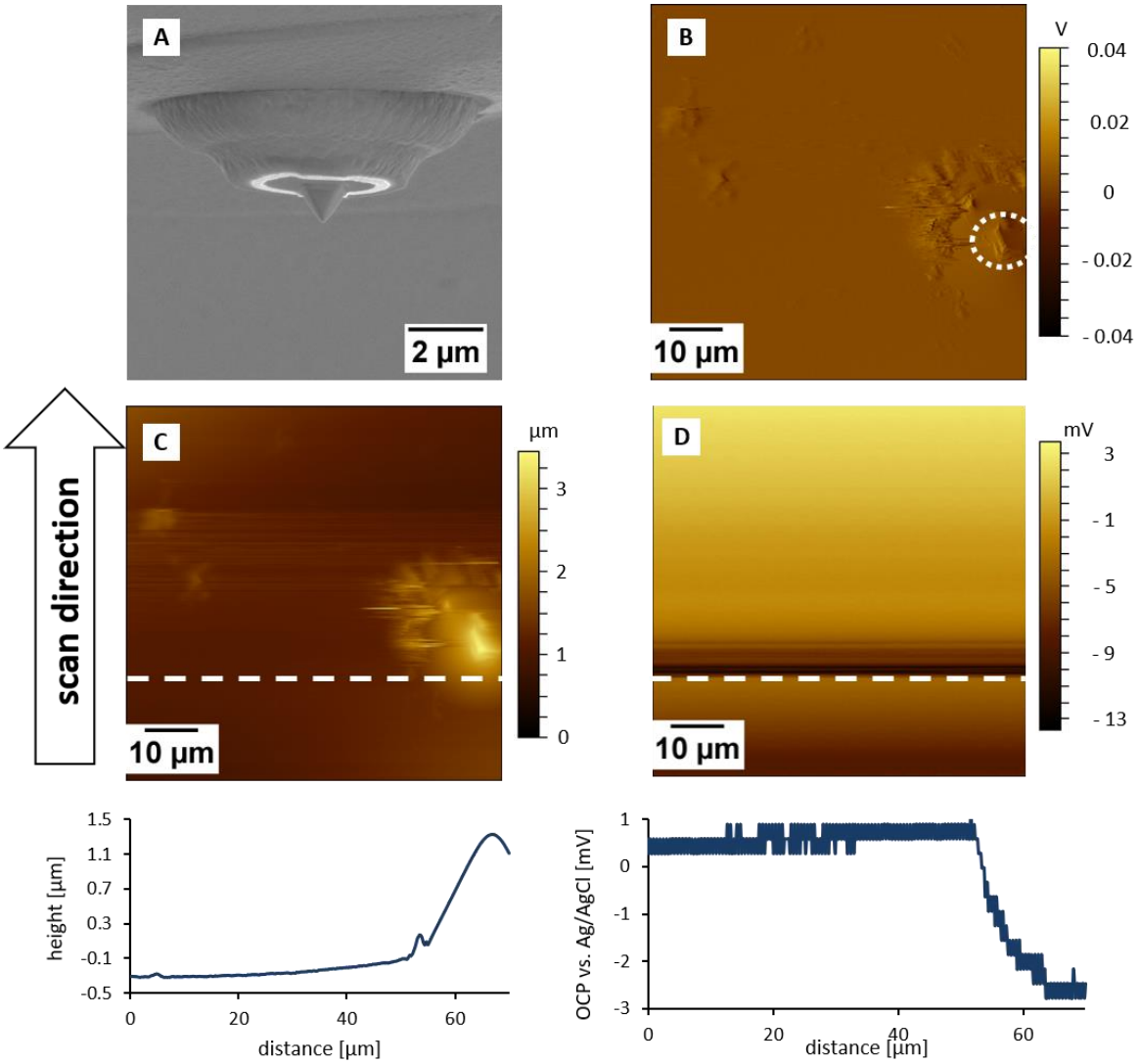

Figure 49 AFM-SECM imaging of the calcite dissolution with a tip-integrated AIROF electrode: SEM image of the used AFM-SECM probe with a ring electrode with an inner diameter of 2.97 µm (outer diameter = 3.64 µm, A). Acceleration voltage: 3 kV, 10 pA. AFM deflection (B) and topography (C) detected in AFM contact mode with correlating potential changes detected by OCP vs. Ag/AgCl quasi-reference electrode (D). The actual, exposed calcite crystal is marked by a white dotted circle in (B) embedded in crystal bond. The profiles of the topography and OCP at the marked region in (C) and (D), respectively, are given below. Original size: 90 x 79 µm^2, scan rate: 0.14 ln/s (25 µm/s).

The AFM-SECM measurement shown in Figure 49 is analyzed in detail in the following figures. In Figure 50, the change in the detected OCP signal extracted as single line scans (x-direction) is evaluated in detail. Thereby, the onset of a decreasing potential correlated

to the more alkaline pH value in close proximity to the calcite crystal can be seen in the first potential profile depicted in B and labeled with 1. This data corresponds to the dashed white line (1) in the AFM topography image shown in A. Line (2) corresponds to the last extracted profile as marked in Figure 50 A, indicating the actual location of the calcite crystal. This position is also marked in the corresponding heightprofile (labeled with an arrow, 2 in B). Thereby, the onset of the detectable potential change is shifted by approximately 7.3 µm, representing the distance between the dashed white lines 1 and 2 in (A). The minimum value for the OCP signal represents a change of approx. 3 mV in an area of 20 µm in the x-direction (dashed lines) shown in the profile in (C) corresponding to the OCP signal in the 3D representation in (B) as indicated by a blue arrow.

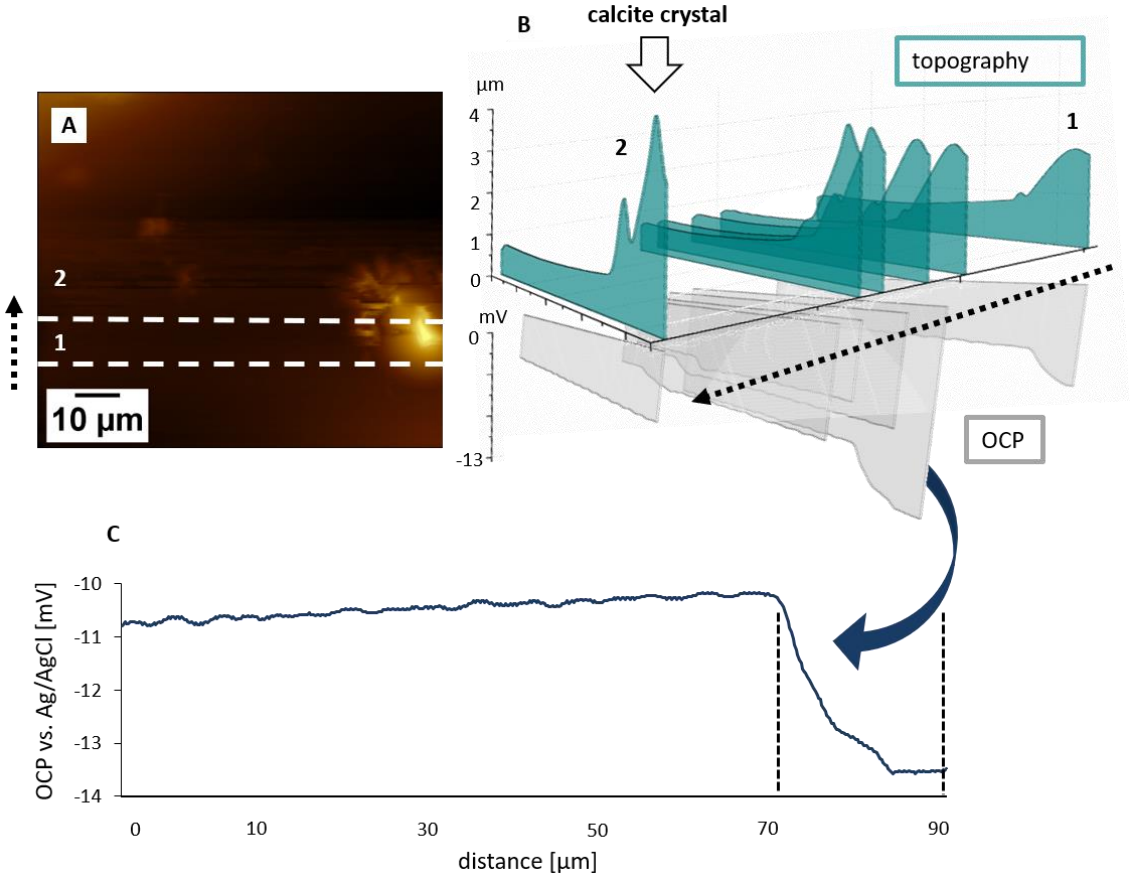

Figure 50 Response time of the OCP signal correlated to the location of the calcite crystal: Single height profiles as labeled by white dashed lines in the AFM topography (A) for the first (1) and the last (2) extracted profiles are compared to corresponding changes of the OCP at same positions (B). The scan direction (y-direction) is labeled by a black dashed arrow (in A and B) and the location of the crystal is indicated by an arrow in (B). Data correspond to the results shown in Figure 49.

The detailed evaluation of the response time with respect to the scan direction (y-direction) is shown in Figure 51. At the position marked by a white dotted line in the OCP image in A, the heightprofile in B and the OCP profile vs. distance shown in D are extracted. Additionally, the detected OCP signal vs. time as recorded by the external bipotentiostat is shown in C. Indeed, the profiles in C and D are almost identical, indicating no resolution in x-direction during the detected results. The onset of the changing potential towards more negative potentials correlating with a more alkaline pH is shifted towards the location of the calcite crystal by 7.3 µm. This largest potential change recorded during 2-3 µm (in y-direction) is approximately 10 mV followed by an increasing potential leveling to the background response in between a distance of 10 µm in the y-direction.

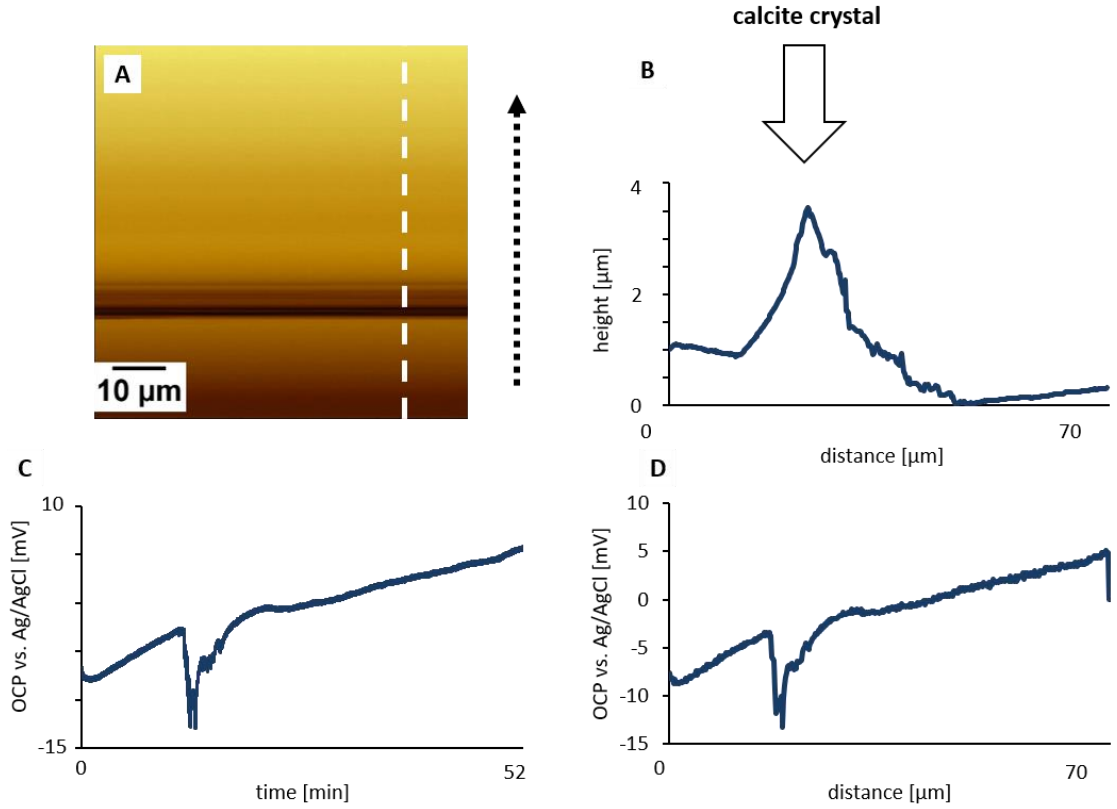

Figure 51 Evaluation of the response time in AFM scan direction (y-direction): Extracted profiles at the location marked by a dashed white line in the OCP signal (A) showing the potential changes in scan direction (indicated by a black, dashed arrow). The height profile (B) with the location of the actual calcite crystal marked by an arrow is compared to the OCP signal vs. time detected by the external bipotentiostat (C) and the OCP change vs. distance (D) as extracted from the OCP image in (A). Data correspond to the results shown in Figure 49.

In comparison, the obtained results reported by Unwin and coworkers[253] for SECM-SICM investigations using an AIROF-modified nanoelectrode, show that the detected OCP signal is increased compared to the actual size of the calcite crystal by the factor 2-3 or by a factor of 1.5 – 2 compared to a simulated potential shift according to the pH distribution above the calcite crystal. Whereas in this publication, the pH sensor had a dimension of 100 nm and additionally, the calcite dissolution was recorded in the SECM hopping mode recording single positions of the SECM-SICM probe along the x,y -direction without lateral scanning. The detected potential changes were recorded in a distance of approximately 100 nm towards the calcite crystal. Compared to this investigation, the obtained result shown in Figure 49 to Figure 51 is in a comparable range. The distance between the AIROF-modified electrode and the sample surface was in the range of 1 µm as defined by the length of the reshaped AFM tip, which also indicates a broadened signal due to enhanced diffusion. Indeed, the enlarged AIROF sensor used in the presented results in comparison to the nanoelectrode used by Unwin and coworkers[253] showed an enhanced resolution with respect to the scan direction (y-direction). This can be definitively interpreted as a positive trend for further investigations with AIROF-modified AFM-SECM probes. However, the resolution in the x-direction or the direction of single line scans has to be improved for future studies. In the AFM-SECM measurement shown in the previous figures, the resolution was 512 x 512 pixel, representing a line scan every 0.17 µm. With the scan speed of 0.14 ln/s (25 µm/s) one line was recorded in approximately 7 s and the area marked by the white dashed lines 1 and 2 in Figure 50 with the distance of 7.3 µm represent 43 lines, which were recorded in 5 min. This also correlates to the OCP signal detected by the external bipotentiostat showing a change in the potential in a duration of 7 min. Wipf and coworkers reported an optimal response time of < 10 s for AIROF microelectrodes[249], whereas for EIROF-modified electrodes, detected in a potentiometric time-of-flight experiment, the response time was determined as several tenths of seconds in relation to the thickness of deposited EIROF[258]. Thereby, the detected insufficient pH response in the x-direction of the single line scans might be indeed related to a scan speed, which is too fast for detecting an adequate pH change. Similar AFM-SECM measurements with comparable Ir and Sb- modified AFM-SECM probes with only small deviation in electrode size were used with varying AFM scan speed and scan size, resulting always in insufficient resolution in the x-direction (results are not shown). One explanation for the

lack in resolution may be additionally the mentioned convective effects of the scanning AFM probe. This effect should be strong for high scan speeds, whereas, during slow scanning, convection should be negligible.

5.3.3 *Electrochemical deposition of iridium oxide film electrodes*

Both, Ir- and Sb-derived pH active layers showed a broad distribution in pH sensitivity. In addition, bending of the cantilever might be an issue for the fabrication of such probes due to intrinsic stress during sputtering of Ir that requires additional microfabrication steps. Hence, the electrochemical deposition of pH-sensitive material onto the AFM tip integrated Au electrode was investigated. EIROF was deposited by different electrochemical techniques (see Table 5 in 5.2). The evaluation of optimized deposition parameters was tested with Au UMEs (diameter: 10 µm) prior to the modification of AFM-SECM probes. Additionally, the pH response of EIROF electrodes deposited to Pt/C-modified Au UMEs was evaluated. Pt/C composite was tested as the substrate material for EIROF pH sensors as the AFM tip-integrated Au frame electrodes can be increased by an additional Pt/C composite layer. This additional step results in an enhanced deposition of pH active iridium oxide, which is localized at a small electrode area but contains a sufficient amount of active pH material for stable pH response given the enlarged surface area by Pt/C deposition compared to the 100 nm thin Au frame electrode.

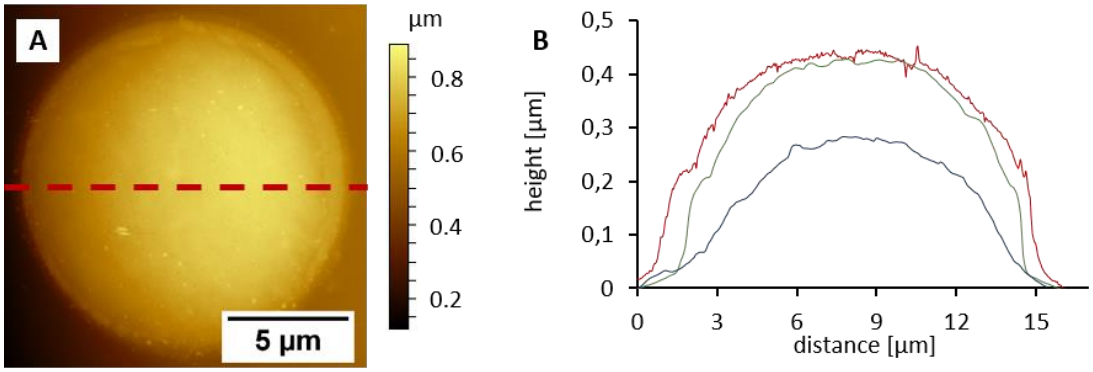

Figure 52 EIROF deposition on Au UMEs (diameter: 10 µm) modified with a 150 nm thin Pt/C composite by IBID: AFM topography of the modified UME (A) and corresponding height profiles (B) of the bare Au UME (blue), after modification via IBID (green) and after EIROF deposition by 100 pulse cycles (red), recorded in AFM contact mode. Original size: 17 x 17 µm², scan speed: 0.34 ln/s.

The first investigations of the modification of Au and Pt/C-modified Au UMEs were evaluated by imaging the electrode surface by optical microscopy, SEM and AFM to guarantee a homogeneous deposition on the whole electrode area by a thin EIROF layer. Figure 52 A shows the AFM topography of an Au UME (diameter: 10 µm) modified with 150 nm Pt/C layer via IBID, which is additionally modified with EIROF by applying 100 potential pulse cycles. The corresponding height profiles of the UME are shown in Figure 52 B after each modification of the surface with the final height profile showing the surface after deposition of a thin iridium oxide film (red). The EIROF depositions by CV and multiple pulses showed the most satisfactory results and both techniques were evaluated in more detail by changing deposition parameters. The pH response of the EIROF pH sensors was tested in consecutive pH calibrations (2 – 4 calibrations depending on the stability of the individual sensors) comparing different deposition cycles for both techniques. The results obtained for EIROF-modified UMEs with respect to the pH response in consecutive calibrations and the linearity of the obtained signals during these calibrations are presented in Figure 53. In A, the sensitivity is compared for sensors deposited via CV (shown in squares) and via multiple pulses (marked by crosses). The grey bar represents the sensitivity range for neutral to alkaline pH values (> pH 6) for EIROF-modified sensors as reported by Wipf et al.[257]. Only two out of 8 sensors, which are compared in Figure 53, showed a response to pH changes within 4 consecutive calibrations, whereas most of the others gave a stable response in two calibrations. Indeed, the linearity for all presented pH sensors as shown in Figure 53 B, was insufficient for quantitative pH detection. The black dotted line in B labels linearity of 90 % and the majority of the results are below this linearity.

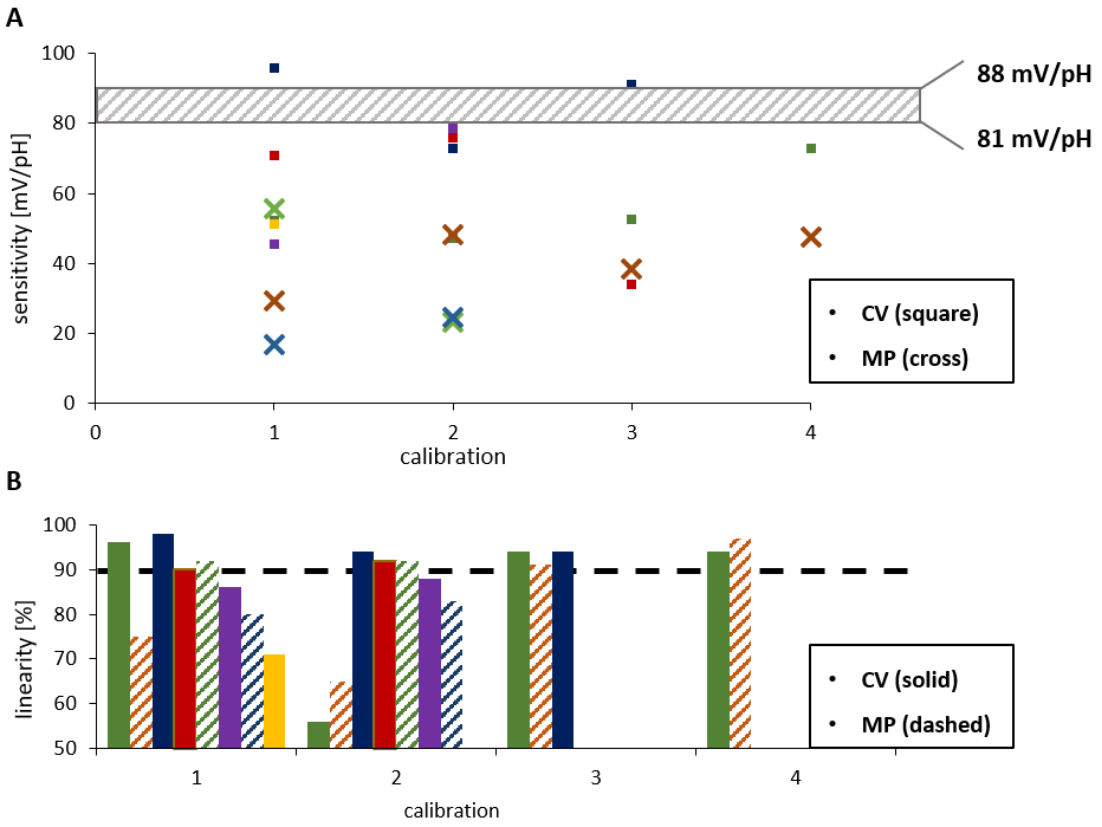

Figure 53 Sensitivity (A) and linearity (B) of pH calibrations for 8 EIROF-modified UMEs (diameter: 10 µm): The graphs represent results obtained with Au and Pt/C - modified UMEs by EIROF deposition via CV (squares in A and solid bars in B) and via MP (crosses in A and dashed bars in B) with varying numbers of cycles or pulses. The dashed bar in (A) shows the sensitivity range reported by Wipf et al.[257], the dashed line in (B) marks linearity of 90 %. Corresponding data is depicted in the same colors.

Similar to the results presented in section 5.3.1, the EIROF electrodes showed a broad distribution in pH sensitivity. The stability and the linearity in between consecutive calibrations, but also for different tested sensors, was unsatisfactory. The results of consecutive pH calibration of exemplarily two EIROF-modified Au UMEs are presented in Figure 54. These results correspond to the two pH sensors shown in Figure 53 with 4 consecutive calibrations. The quite large distribution measured with a single EIROF-modified sensor is for the obtained OCP values approximately 200 mV at pH values of 6 – 8 in consecutive pH calibrations, for both, EIROF deposited via CV (A) and multiple potential pulses (B).

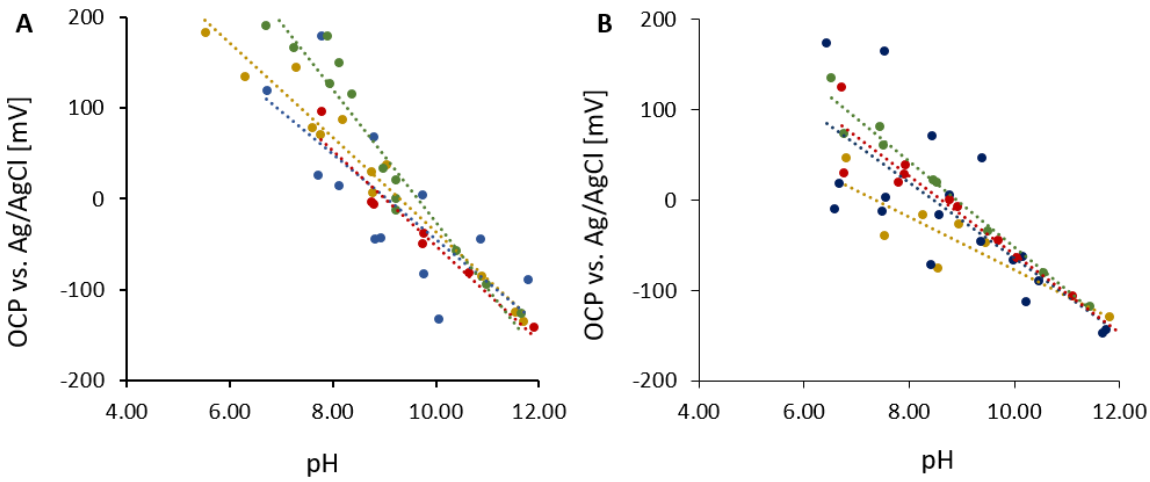

calibration	sensitivity [mV/pH]	linearity [%]
1	52.2	96
2	47.2	56
3	52.7	94
4	72.9	94

calibration	sensitivity [mV/pH]	linearity [%]
1	29.2	75
2	41.8	58
3	43.2	92
4	47.7	97

Figure 54 Calibration of EIROF-modified Au UMEs (diameter: 10 µm), electrochemically deposited by CV (A) or by multiple potential pulses (B): Linear regressions of 4 consecutive pH calibrations with sensitivity and linearity summarized in the tables below labeled in corresponding colors.

Similar results were also obtained by other researchers, e.g. by Wipf et al. with EIROF-modified carbon fiber microelectrodes[257], by Marzouk using different mm-sized substrates as supporting material for AEIROF sensors[63], or by Elsen et al., who investigated different deposition protocols for EIROF-modified gold microelectrodes[258]. In all of these reported investigations, individual pH sensors were reported also showing broad distributions in pH sensitivity between individual sensors and no information is given in respect to long-term stability of these pH sensors. Although different supporting electrode materials or different sizes of the modified electrodes are presented in the described examples above, a clear trend is recognizable. The results obtained in this thesis with the EIROF modification of either UMEs or AFM-SECM probes are in agreement with the reported findings. The electrochemical deposition of EIROF was initially investigated to overcome limitations of AFM-SECM probes with integrated Sb or Ir metal layers as pH sensor. But the results for EIROF-modified Au and Pt/C UMEs also showed a broad response in the range of 17 to 96 mV/pH with insufficient linearity (Figure 53Figure 53 B). Nonetheless, first EIROF modification of AFM-SECM probes with gold frame electrodes

and electrodes additionally modified with Pt/C composite via IBID were electrochemically modified by either CV or multiple potential pulses and characterized via calibration experiments. Thereby, the response time of the EIROF-modified AFM-SECM probes towards pH changes in TRIS buffered solution was investigated. The pH calibration curves obtained for 4 individual pH-sensitive AFM-SECM probes are summarized in the table shown in Figure 55. Again, a broad distribution ranging from 37 to 91 mV/pH in pH sensitivity for different probes, similar to the results of EIROF – modified UMEs was observed.

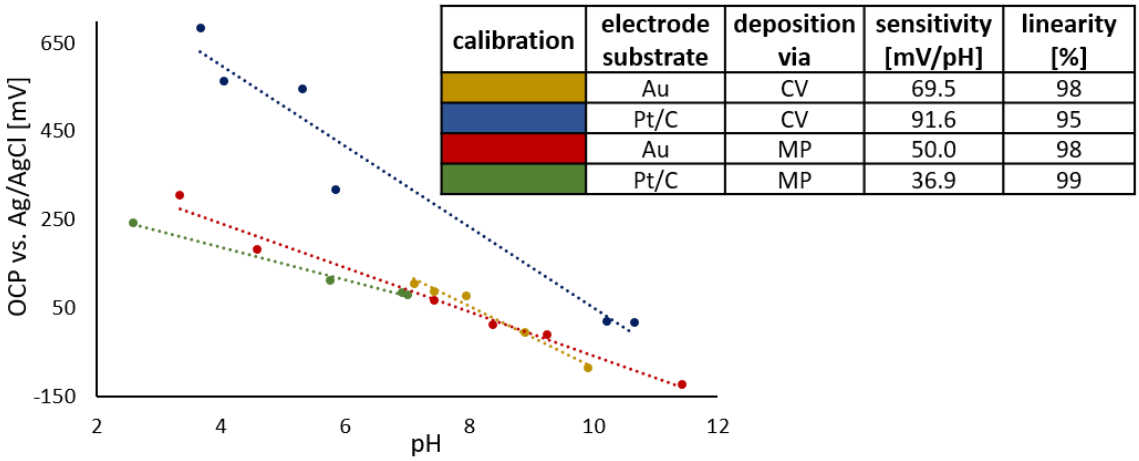

calibration	electrode substrate	deposition via	sensitivity [mV/pH]	linearity [%]
	Au	CV	69.5	98
	Pt/C	CV	91.6	95
	Au	MP	50.0	98
	Pt/C	MP	36.9	99

Figure 55 Calibration of EIROF-modified AFM-SECM probes, electrochemically deposited by multiple pulses (MP) or CV on Au or Pt/C - modified Au AFM-SECM probes: Linear regressions of 4 pH calibration graphs with sensitivity and linearity given in the table in respect to electrochemical deposition and substrate, are labeled in corresponding colors.

No differences between either the electrochemical deposition technique nor the underlying electrode material for the iridium oxide film showed preferable behavior in stability, pH sensitivity or linearity, in concordance with the results published elsewhere by Wipf et al.[257], Marzouk[63] or Elsen et al.[258]. Similar investigations for EIROF sensors at a macroscopic rotating ring-disk electrode as reported by Steegstra et al.[27] reported also a broad distribution in pH sensitivity according to the oxidation state of the iridium oxides. Indeed, they also address the results of individual EIROF electrodes and again no statistical data were presented. As the fabrication process is more time-consuming in respect to the modification of AFM-SECM probes, as every single AFM-SECM probe has to be modified

individually, further optimization of EIROF-modified AFM tip-integrated pH sensors was not further pursued within this thesis.

5.4 Conclusion and outlook

Within this section, AFM tip-integrated Sb and Ir pH sensors were investigated towards their pH response. The experiments performed within this thesis also show a limited reproducibility of the miniaturized pH electrodes as already reported in several publications (see introduction). For all different modification strategies, a broad distribution of pH sensitivity was observed. pH sensors prepared under the same conditions showed varying pH sensitivity for different pH electrodes but also for consecutive pH calibrations. The stability of the pH sensors was examined for approximately 1 h showing good pH sensitivity and recovery after several minutes. In case of EIROF pH sensors electrochemically deposited on Pt/C-modified Au electrodes, either in AFM-SECM probes or as UMEs, the pH sensitivity and linearity was insufficient, and the electrochemical deposition of iridium oxide seems to be unsuitable for tip-integrated pH sensors. Although the successful modification of carbon nanoelectrodes with electrochemical deposited iridium oxide used in combined SECM-SICM investigations of the calcite dissolution was reported by Unwin and co-workers[253], no information was provided for long-term stability of the presented pH sensors, nor multiple pH measurements were shown. Within this thesis, no clear improvement of the electrochemical modification in respect to reproducibility of the pH sensors could be observed. In section 5.3.2, Sb and Ir-modified AFM-SECM probes were used to detect the localized dissolution of calcite crystals with simultaneously recorded pH changes. No lateral resolution of pH changes could be observed. Variations in scan speed, scan size, the original pH of the electrolyte solutions or the used pH sensor, either Sb or Ir, always resulted in a change of the detected potential close to calcite particles, but without a clear correlation to the imaged morphology. However, compared to already reported investigations, e.g. by SECM-SICM[253], the resolution in the presented results of this thesis obtained for AIROF-modified AFM-SECM probes are in an acceptable range, especially in the scan direction (y-direction, see 5.3.2) of the measurements. Whereas a broad range in sensitivity was observed for both, Sb and Ir-modified AFM-SECM probes, the great

advantage of Ir-based pH sensors over Sb is its possibility to be 'reactivated' by anodic oxidation in H_2SO_4. AIROF electrodes were also investigated by Wipf and coworkers[249] towards their long-term stability in pH sensing. The size of the reported electrode was in the range of 10 µm in diameter consisting of Ir microparticles located in a microcapillary with an active electrode surface significantly larger than the here reported AFM-SECM sensors. Nevertheless, they reported the stability of individual sensors for over 2 months, also showing a reduced sensitivity in pH calibrations, but with linear behavior over several calibration experiments during these 2 months. Indeed, the results presented in this publication refer to one individual AIROF sensor showing good linearity during this period and just small deviations in sensitivity ranging from 66 – 74 mV/pH[249]. They also reported a yield of 30 – 50 % of in total 510 investigated AIROF sensors. Studies involving such a large number of miniaturized pH sensors is beyond the scope of this thesis. However, the reported long-term stability of the AIROF pH sensor seems to be promising also for AFM tip-integrated AIROF electrodes and further investigations should be focused on the optimization of the fabrication of these pH sensors.

6 Investigation of the ITIES at nanopore arrays

6.1 Introduction

The detailed characterization of nanoporous arrays used for electrochemistry at the ITIES is crucial for a comprehensive understanding and interpretation of transport phenomena taking place at the liquid/liquid interface. Especially, when changing the fabrication processes of such nanosized devices, the behavior, e.g. in diffusion or the location of the interface in these devices, might change dramatically. The direct visualization of diffusion phenomena at FIB-milled nanoporous arrays was shown by localized deposition of silica at the liquid/liquid interface in collaboration with Damien Arrigan's group at Curtin University (Li et al.[181]). The localized deposition showed different diffusional behavior for nanoporous arrays with varying pore-to-pore separation. However, it has to be noted that the final silica formation is realized by the hydrolyzation initialized by the electrochemical ion transfer of a precursor at the ITIES, followed by rinsing and drying processes, which may change or influence the actual or localized silica formation. For the in-situ observation of diffusion processes at nanoporous arrays, AFM-SECM is highly suitable. ITIES at nanoporous arrays profit from an enhanced charge transfer and are a promising interface for sensing applications[259]. The diffusion behavior at these micro- and nanoporous membranes are not just dependent on the dimensions (length and diameters) of the actual micro- or nanopores, but on the pore-to-pore separation resulting in an overlaid diffusion profile for short pore distances within the array (see also 1.4). Micro- and nanoporous membranes can be fabricated by standard microfabrication processes. For example, DRIE has been applied for membranes used in ITIES investigations[83], as well as e-beam lithography[98]. Especially, FIB enables the fabrication of arrays, without the need for shadow masks and with varying and easily adjustable pore-to-pore separations, as already reported for various materials[32–34]. The fabrication of nanosized geometries by FIB processing is favorable due to an easily tunable geometry within one fabrication step in varying materials, e.g. thin SiN membranes[31] or porous alumina[260]. Tong et al.[261] reported the fabrication of nanopores with diameters down to 10 nm by additional silica deposition using low-pressure chemical vapor deposition to FIB-milled nanopores within SiN membranes. Additional (cold) ion beam sculpting results in nanopores of just a few nanometers in diameter as reported by Li et al.[32] and Kuan et al.[34]. For investigations of the ITIES at nanoporous arrays, theoretical simulations and cyclic voltammetry showed

additionally that the separation of the individual interfaces plays a crucial role in the current signal and results in an overlapped diffusion profile for closely-spaced nanopores[30,97]. Local diffusion processes can be detected by scanning probe techniques as already reported for the diffusion at nanoporous membranes by SECM[262] or SICM[263–266]. AFM-SECM offers the advantage of simultaneous detection of the topography of nanoporous array by AFM and the localized detection of the electrochemical processes. The diffusional transport through pores by AFM-SECM has been shown by Kueng et al. for the transport of glucose[149], of redox-active species by Macpherson et al.[150] and for the diffusion at electrode arrays with closely-spaced microdiscs[150,151]. For the used nanoporous arrays in SiN membranes fabricated by e-beam lithography, an inlaid interface was predicted with the organic phase located within the nanopores due to the resulting electrochemical signals of the transfer of a model analyte at ITIES[267]. Investigations at similar nanostructured samples predicted the aqueous phase within the nanopores as shown by deposited nanoparticles located at the interface at nanoporous alumina membranes[86] or size exclusion of a ligand molecule at nanoporous silicalite membranes[268]. The hydrophilicity of the SiN membranes was characterized by contact angle[98,267] resulting in a hydrophobic back and a hydrophilic front side of the membrane. The pore walls were also assumed to be hydrophobic and therefore, the pores should be filled with the organic phase, which was supported by calculations[267]. The same geometry and location of the interface were assumed for FIB-milled nanoporous arrays and calculations of electrochemical transport at ITIES at these nanoporous arrays were based on an inlaid interface [31,267].

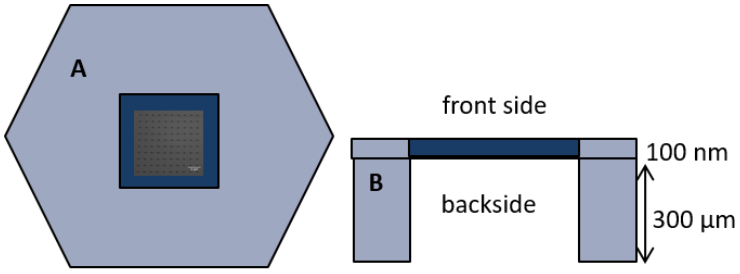

Figure 56 Scheme of the used SiN membranes with corresponding dimensions; top view (A) and side view (B).

FIB fabrication results in the implantation of Ga^+ ions[35] and results in a truncated cone-shaped geometry of the nanopores due to re-deposition of FIB-milled material[32,36,37]. Indeed, the implantation of charged ions in the SiN membranes should show an influence on the hydrophobicity of the surface. Contact angle measurements are not possible for the inner wall of nanoscale pores, hence the location of the interface has to be detected otherwise. With the truncated cone-shaped geometry resulting from FIB-milling, the nanopores have two varying orifices located at either the organic or aqueous facing side of the SiN membrane, respectively. This effect has not been taken into account yet for nanopore arrays used for ITIES investigations, only for solid-state electrodes recessed at the bottom of truncated pores[37]. Therefore, in the following section of this thesis, the nanopore arrays were fabricated by FIB-milling from either the front or the back of the SiN membrane resulting in varying pore diameters at each side of the membrane.

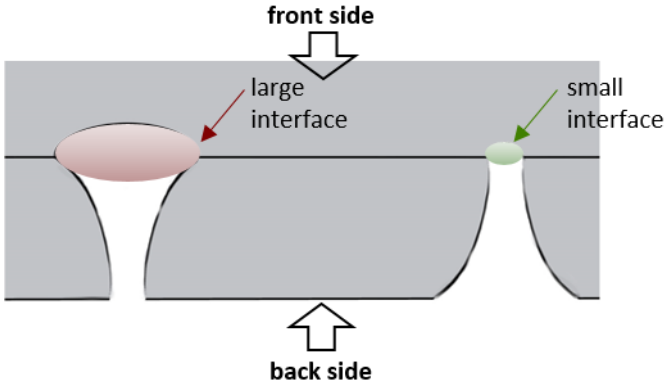

Figure 57 Scheme of front (left) and back (right) side FIB-milled nanopores and the varying pore diameters at one side of the membrane marked in red and green.

With the comparison of the resulting currents for the transfer of a model analyte, e.g. tetrapropylammonium chloride at the ITIES, the location of the interface at or within the nanopores can be predicted. This prediction is still based on theoretical assumption and the actual location of the interface can dramatically vary from these predictions, in particular when the inner side walls of the pore might be altered due to FIB milling. The interface between two liquids may be also of dynamic nature and a static interface, which is used for theoretical calculations, may not be suitable to characterize the location of these interfaces in detail. Different approaches for the investigation of the liquid/liquid

interface have been reported so far by spatial scanning spectroelectrochemistry and localized deposition of nanoparticles[269], by UV-VIS spectroscopy[270], and Raman confocal spectroscopy[271] with a spatial resolution in z-direction in the µm-range. Hence, the investigation of the interface between two immiscible liquids by spectroscopic approaches is lacking the required resolution essential to investigate nano-sized pores within membranes. The parallel displacement of the excitation light source as used in the mentioned techniques is not suitable for solid-state membranes. The visualization of the interior and shape of nanopores in SiN membranes has been demonstrated by high-resolution TEM tomography[272,273].

The first part of this section will show the visualization of different diffusional behavior in relation to the pore-to-pore separation by mapping the diffusion of a redox species at ITIES by AFM-SECM[181]. These measurements complete the investigations of the influence of the pore-to-pore separation by CV and corresponding theoretical calculations. Next to AFM-SECM, the localized deposition of silica deposits at ITIES was used for visualization of the diffusion profiles showing overlapped or individual diffusion in dependence of the pore-to-pore separation[181]. The formation of a solid phase directly at the interface due to an ion transfer at the ITIES may be used to identify the location of this interface within the nanopores. In section 6.3.2, different current responses of the transfer of tetrapropylammonium chloride (TPrACl) as a model analyte at the ITIES within FIB-milled nanopore arrays, fabricated either from the front or the back, are compared. Electrochemical silica deposition at the interface at the two different nanoporous arrays is used to visualize the differences between both approaches. Additionally, such silica deposits at ITIES were investigated by FIB/SEM tomography enabling the reconstruction of the pore shape, the morphology of the deposited silica directly located at the nanopores and especially within the nanopores. Additional EDX and STEM measurements were conducted to characterize the silica deposits.

The following results have been published partly by Liu et al.[181] and by Holzinger et al.[187].

6.2 Experimental

SiN membranes (SIMPore Inc. and DuraSiN Films, Protochips) with 50 and 100 nm thickness, respectively, were used as supporting material for nanoporous arrays fabricated by FIB milling (Zeiss Neon 40EsB, Carl Zeiss Nano Technology Systems for the arrays used for visualization of diffusion processes and FEI Helios Nanolab 600, ThermoFisher Scientific for electrochemical measurements and FIB/SEM tomography). The AFM-SECM probes used in part 6.3.2 of this chapter were produced as described elsewhere[133,160]. In brief, non-metalized silicon nitride probes (OTR-P, Olympus) were modified with a 5 nm Ti adhesion layer and a 100 nm gold layer prior to insulation by silicon nitride (PECVD). Then, the probes were additionally modified with a conical conductive tip of Pt/C composite by IBID (precursor: methyl-cyclopentadienyl-trimethyl platinum, ThermoFisher Scientific). The fabrication steps by FIB milling and IBID are displayed in Figure 58.

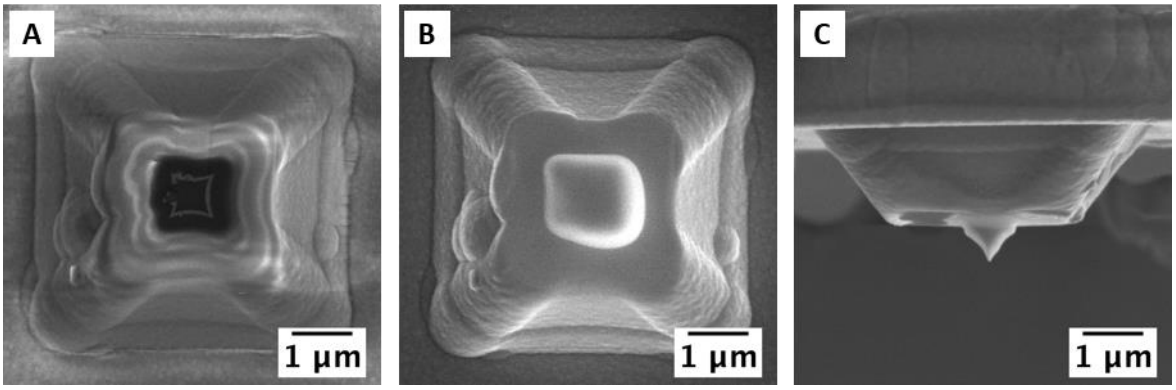

Figure 58 SEM images of the used AFM-SECM probe with a conductive Pt/C tip: the Au electrode frame (approximately 600 nm in diameter) was exposed by FIB milling (30 kV, A), Pt/C composite was deposited by IBID on top of the Au frame (square-shaped pattern with an edge length of 1 µm and an approximate height of 466 nm, B) and reshaped by FIB milling resulting in a curvature radii of 20-25 nm (C). *Adapted with permission from* Y. Liu, A. Holzinger, P. Knittel, L. Poltorak, A. Gamero-Quijano, W. D.A Rickard, A. Walcarius, G. Herzog, C. Kranz, and D.W.M. Arrigan. Visualization of diffusion within nanoarrays. *Anal. Chem.* **88,** 6689–6695 (2016). *Copyright 2019 American Chemical Society*. https://pubs.acs.org/doi/10.1021/acs.analchem.6b00513.

The AFM-SECM probe was characterized by CV in de-aerated 5 mM $Ru(NH_3)_6Cl_3$ / 0.1 M KCl (98 %, Aldrich/ pro analysi, Merck KGaA) at a scan rate of 0.1 V/s (Figure 59 B). For AFM-SECM measurements, AFM (5500 AFM/SPM microscope, Keysight Technologies) was used in contact mode and SECM was done in the generation-collection mode in 0.1 M KCl (pro analysi, Merck) detecting the reduction of $Ru(NH_3)_6^{3+}$ at - 0.3 V vs. Ag/AgCl in a three-electrode setup with the AFM-SECM probe as working electrode, a Ag/AgCl quasi-reference electrode (Goodfellows) and a Pt counter electrode (Goodfellows). All AFM images and correlating height and current profiles were processed by Pico View (Keysight Technologies). All solutions were prepared with ultrapure water (18.2 MΩ, ELGA LabWater, Veolia Water Solutions & Technologies). Dynamic mode AFM was additionally used to characterize the pore shapes of the nanopores used in section 6.3.2 and 6.3.3 with a FIB-sharpened NCL probe (k = 48 N/m, 190 kHz, Nano World). The electrochemical

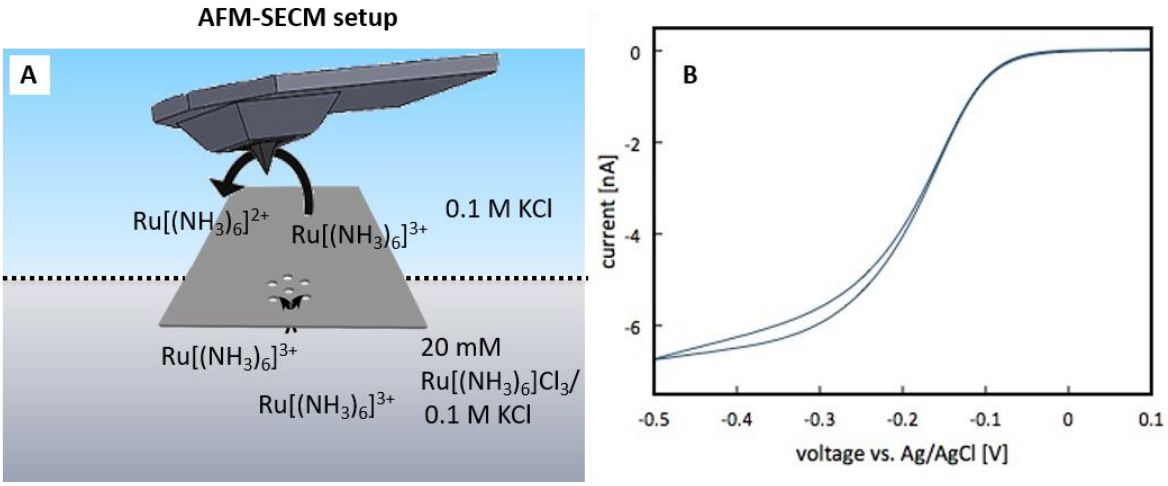

Figure 59 Scheme of the AFM-SECM setup used for detection of different diffusion behavior at nanoporous arrays within SiN membranes (A), with the upper reservoir filled with 0.1 M KCl (light blue) and the lower reservoir beneath the membrane filled with 20 mM $Ru(NH_3)_6Cl_3$ / 0.1 M KCl (grey-blue). CV of the conductive AFM tip recorded in 5 mM $Ru(NH_3)_6Cl_3$ / 0.1 M KCl, scan rate: 0.1 V/s (B). *Adapted with permission from* Y. Liu, A. Holzinger, P. Knittel, L. Poltorak, A. Gamero-Quijano, W. D.A Rickard, A. Walcarius, G. Herzog, C. Kranz, and D.W.M. Arrigan. Visualization of diffusion within nanoarrays. *Anal. Chem.* **88,** 6689–6695 (2016). *Copyright 2019 American Chemical Society*. https://pubs.acs.org/doi/10.1021/acs.analchem.6b00513.

investigations in 6.3.2 of ITIES at nanoporous arrays are based on the following electrochemical cell:

$$Ag/AgCl \mid x\ \mu M\ TPrACl,\ 10\ mM\ LiCl_{aq} \mid\mid 10\ mM\ BTPPATPBCl_{\ DCH} \mid Ag$$

using TPrACl (Aldrich) as the model analyte in lithium chloride solution (LiCl, ≥ 99%, Sigma Life Science) as the aqueous electrolyte. Aliquots of TPrACl were added to the aqueous phase and gently mixed with a pipette for a homogeneous concentration during calibrations. The organic electrolyte was synthesized as described elsewhere[274] by metathesis of potassiumtetrakis(4-chlorophenyl) borate (K^+ $TPBCl^-$, Alfa Aesar) and bis(triphenylphosphoranylidene)ammoniumchloride ($BTPPA^+$ Cl^-, Alfa Aesar). Bis(triphenylphosphoranylidene)ammoniumtetrakis(4-chlorophenyl)borate (BTPPATPBCl) was used as organic electrolyte in 1,6-dichlorohexane (98%, Aldrich). All electrochemical measurements were done by using a (bi)potentiostat (CompactStat, Ivium Technologies) with Ag/AgCl quasi-reference electrodes. The electrochemical deposition of silica at the interface between water and 1,2-dichloroethane was obtained according to Poltorak et al.[275] and Herzog and co-workers[187]. A sol of 50 mM TEOS in 5 mM NaCl was adjusted to pH 3 by addition of aliquots of 1 M HCl, stirred for 90 minutes at room temperature to allow hydrolysis to occur. The ethanol produced by the hydrolysis was removed by evaporation and the pH was raised to pH 9 by the addition of aliquots of 1 M NaOH solution (unless stated otherwise). The used electrochemical cell can be described by:

$$Ag/AgCl \mid 50\ mM\ TEOS_{hydrolyzed} + 5\ mM\ NaCl_{aq} \mid\mid 14\ mM\ CTA^+\ TPBCl^-_{DCE} \mid Ag$$

The template salt in the organic phase was prepared by metathesis from K^+TPBCl^- and cetyltrimethylammonium bromide (CTAB) as described elsewhere[276]. A potential of - 0.1 V or 0 V was applied for 30 - 60 s enabling the transfer of CTA^+ from the organic to the aqueous phase, triggering the condensation reaction between silanol groups to form Si-O-Si bonds. After the electrochemical deposition step, the membrane was carefully removed from the solution and rinsed with a flow of ultrapure water to avoid any formation of silica through evaporation. The membranes were then placed in an oven at 130 °C for 16 h to ensure cross-linking.

Automated data acquisition for FIB/SEM tomography (Helios Nanolab 600, FEI, ThermoFisher Scientific) was performed with the 'slice and view' software package (FEI, ThermoFisher Scientific) with automated FIB milling (30 kV, 1.5 - 48 pA) providing a lateral resolution of 5 or 10 nm for slicing, respectively, and SEM imaging (5 kV, 86 pA) in immersion mode after each milling step. Stabilization of the silica deposits while FIB milling or TEM foil preparation was achieved by additional deposition of a thin Pt layer (3-4 nm) by sputter coating (SCD 005, BAL-TEC) and by Pt/C deposition via IBID. The 3D slices were processed by Fiji[277] using the 'linear stack alignment with SIFT'[278] and applying a FFT bandpass filter. 3D graphs were processed by Avizo 9.1.0 Lite (FEI, ThermoFisher Scientific). An overview of the different fabrication steps in FIB/SEM tomography is shown in Figure 60.

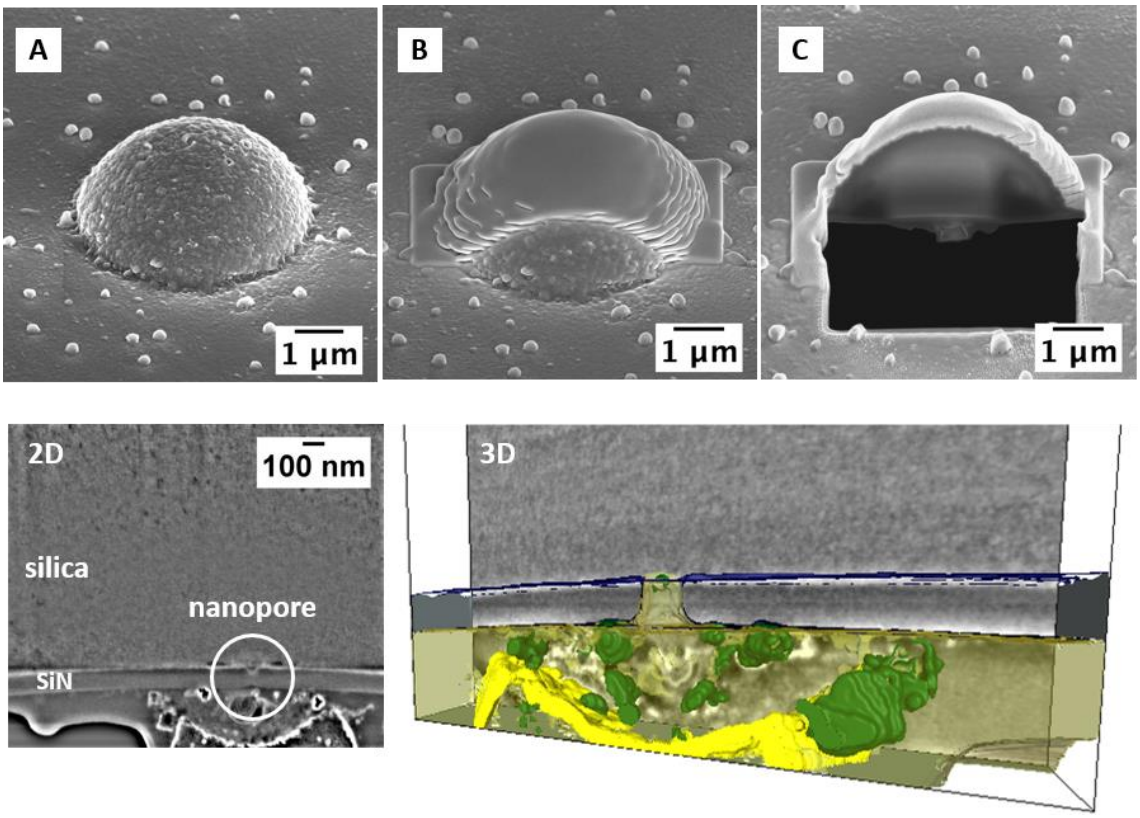

Figure 60 SEM images (5 kV/ 8 6pA) of the preparation steps for FIB/SEM tomography: A single silica deposit (A) was covered with a Pt/C protection layer by IBID (30kV, 48pA) (B) and the sample was exposed by a cross-section to localize the SiN membrane below the silica deposit (C). A different number of slices (80 – 400) with thicknesses of 5 and 10 nm, respectively, was recorded during 'Slice and View'. The slices showing the pore were then used to generate 3D projections of the sample (SEM in 2D and corresponding 3D representation are given in the

lower panel of the figure). A. Holzinger, G. Neusser, B. J. J. Austen, A. Gamero-Quijano, G. Herzog, D. W. M. Arrigan, A. Ziegler, P. Walther, and C. Kranz, *Faraday Discuss.*, 2018, **210**, 113. *Adapted from Ref.* [187]*. Distributed under the license Creative Commons Attribution-NonCommercial 3.0 Unported (CC-BY-NC 3.0),* https://creativecommons.org/licenses/by-nc/3.0/.

TEM lamellae were prepared by several successive FIB milling steps as described in detail elsewhere[279] and summarized in Figure 61. TEM (EM 912 TEM, Zeiss) images were recorded with an acceleration voltage of 120 kV. STEM and EDX measurements were done with an FE-SEM (30 kV, S-5200, Hitachi), equipped with a X-ray detector (Pheonix, EDAX) and a STEM detector (Hitachi). The images were also processed by Fiji[277].

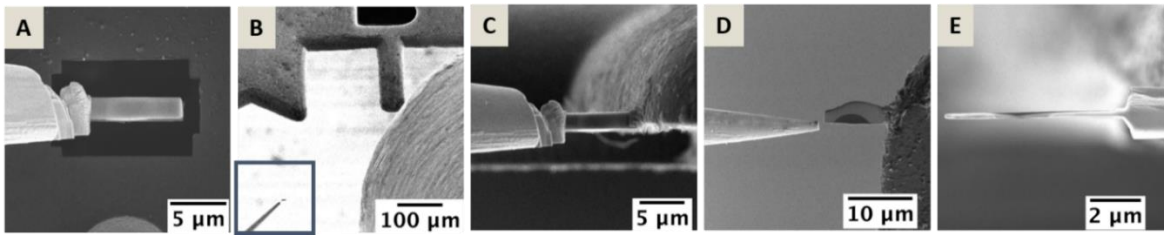

Figure 61 Overview of the preparation of TEM lamella: approx. 1 µm (in thickness) lamella is isolated from the membrane containing the silica-modified nanopore by FIB milling steps. The lamella is then attached via IBID (30 kV) to a micromanipulator needle (Omniprobe) (A), removed from the sample and transferred onto a Cu TEM grid (Omniprobe) (B, blue square marks the micromanipulation needle with the TEM sample) and fixed via IBID to the grid (C). Afterward, the micromanipulation needle is removed (D) and the lamella is thinned by FIB to a thickness of approximately 150 - 200 nm (E). A. Holzinger, G. Neusser, B. J. J. Austen, A. Gamero-Quijano, G. Herzog, D. W. M. Arrigan, A. Ziegler, P. Walther, and C. Kranz, *Faraday Discuss.*, 2018, **210**, 113. *Adapted from Ref.* [187]*. Distributed under the license Creative Commons Attribution-NonCommercial 3.0 Unported (CC-BY-NC 3.0),* https://creativecommons.org/licenses/by-nc/3.0/.

6.3 Results and discussion

6.3.1 *Diffusion at nanopore arrays*

The diffusion of a redox mediator through nanoporous arrays, driven by a concentration gradient of two reservoirs located below and above the nanoporous array (see Figure 59), is detected. The AFM-SECM probe was located in the upper compartment containing solely KCl electrolyte solution and detected the diffusion of $Ru(NH_3)_6^{3+}$ from the lower reservoir separated by the SiN membrane containing the nanopore array towards the AFM-SECM probe. In Figure 62, the results for the diffusion at nanopores with small pore-to-pore spacing are presented.

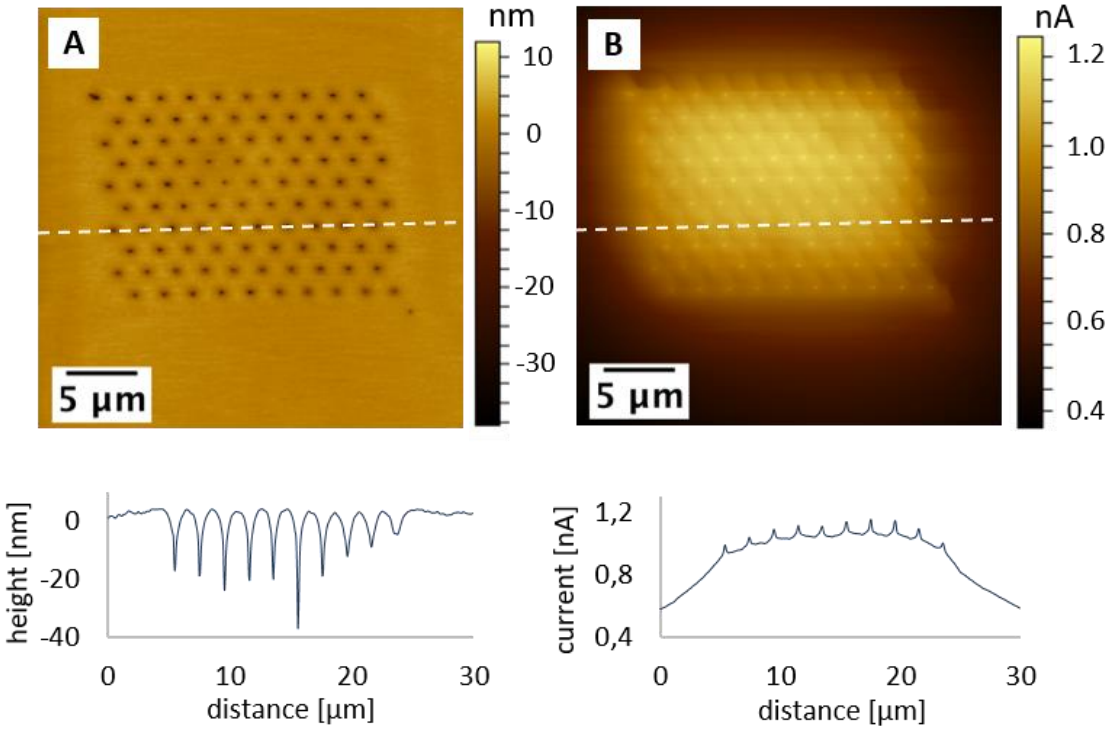

Figure 62 AFM-SECM images of a nanoporous array with 21 times separation of the individual pores in a hexagonal arrangement. Contact mode AFM topography (A) and GC mode SECM current signal (B) due to the diffusion of $[Ru(NH_3)_6]^{3+}$ through the nanopores is depicted showing an overlapped diffusion. The corresponding height and current profiles are shown below according to the marked line in (A) and (B). Original size: 35 x 35 µm², scan speed: 32.0 µm/s (0.5 ln/s), scan angle: - 14.4°. *Adapted with permission from* Y. Liu, A. Holzinger, P. Knittel, L. Poltorak, A. Gamero-Quijano, W. D.A Rickard, A. Walcarius, G. Herzog, C. Kranz, and D.W.M. Arrigan. Visualization of diffusion within nanoarrays. *Anal. Chem.* **88,** 6689–6695 (2016). *Copyright 2019 American Chemical Society*. https://pubs.acs.org/doi/10.1021/acs.analchem.6b00513.

The ratio of the distance between single pores and the radius of the pores (r_c/r_a, see equation 29) is 21 and smaller than the critical value for individual diffusion of 56 as pore-pore separation defined by Liu et al.[30] and resulting in an overlapped diffusion behavior at the nanoporous array. The AFM topography and the corresponding height profile at the marked line in the AFM image are shown in A, whereas the correlating current response with the current profile at the same location is shown in B. A clear overlapped current signal was detected with a current density of 0.64 µA/cm² above the nanoporous array. Single current peaks are visible at the location of the individual nanopores. These observations can be explained by the conductive AFM tip penetrating the nanopores and detecting the current response, which reflects the concentration in the lower compartment of $[Ru(NH_3)_6]^{3+}$. Calculations of the expected theoretical current response (based on the electrode area, diffusion coefficient, concentration, etc.) for these additional current peaks with a conical AFM tip results in a current response in the range of 0.3 – 1 nA (Table 6). Thereby, the theoretical currents I_{dif} are calculated by equation (19) (see Table 2).

	measured; peak current signal, N = 50	**calculated; for a_1 = 100 nm, h_1 = 155 nm**	**calculated; for a_2 = 40 nm, h_2 = 40 nm**	**calculated; for a_2 = 30 nm, h_2 = 30 nm**
current [nA]	0.08 ± 0.02	1.04	0.36	0.27

Table 6 Measured and calculated current for the additional current peaks as illustrated in Figure 63. The calculations were obtained with equation (19).

Only the part of the electroactive area of the AFM-SECM probe within the pore and reaching the other side of the membrane (with height h_1 and radius a_1) containing the high concentrated $[Ru(NH_3)_6]^{3+}$ solution (20 mM) is used to calculate the theoretical current response (see scheme in Figure 63).

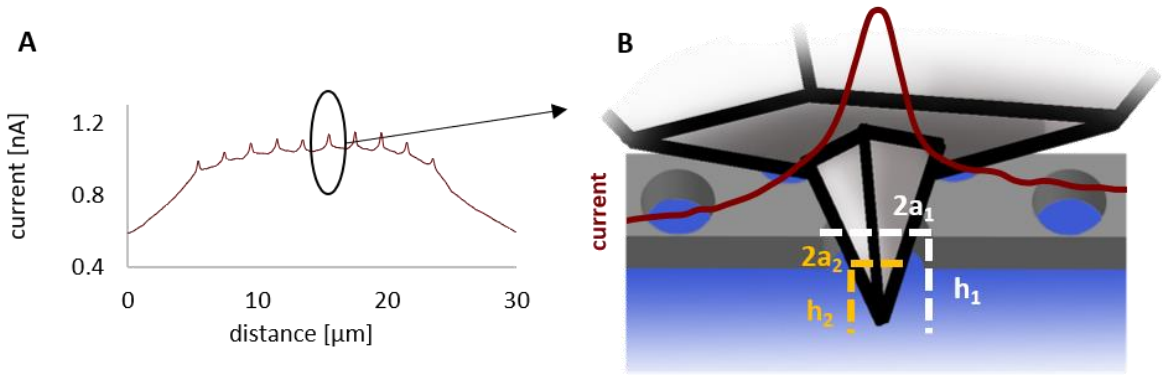

Figure 63 Current response (A) according to the AFM-SECM images shown in Figure 62 and scheme of the AFM tip penetrating a single nanopore (B). The height h and radius a, used for calculation of the theoretical current values for the observed current peak as shown in the overlaid current response (red curve), are labeled in white and yellow, respectively.

Additionally, the current is calculated for the AFM tip just immersing into the high concentrated $[Ru(NH_3)_6]^{3+}$ solution with the height h_2 and the radius a_2 according to the actual dimensions of the used AFM-SECM probe (in Table 6, two different heights and radii are compared based on the SEM images of the actual AFM-SECM probe, which are measured from two different sides of the AFM tip). The calculated currents are up to 10 times higher than the actual measured current response. Indeed, a perfect cone shape was used for the calculations, which is not the case for the actual shape of the FIB-milled AFM tip, and a maximum concentration of $Ru(NH_3)_6^{3+}$ was used as c_0. Because diffusion close to and within the pores changes the actual concentration of the redox mediator in the solution below the nanoporous array and also the penetration of the AFM tip into the pores results in additional convection in opposite direction (tip moves towards the side of the membrane facing the concentrated solution, whereas diffusion is directed from the high to less concentrated solution). Hence, the actual concentration for c_0 may be lower than the original bulk concentration of $Ru(NH_3)_6^{3+}$. Additionally, the tilt of the AFM tip towards the surface is not taken into account, which changes the actual size of the AFM tip placed within the nanopore. For an estimation of the detected current signal, the calculations used in Table 6 are sufficient and these single peaks visible for individual nanopores can be addressed by the electroactive area of the AFM-SECM actually

penetrating the nanopores. Additionally, the overall current signals are overlapped in the surrounding of the pores due to the overlapping hemispherical diffusion profiles at the individual pores. Same measurements at nanoporous arrays with a pore-to-pore separation sufficient for individual diffusion (with $r_c/r_a = 91$, see equation 29) as predicted by electrochemical investigations and theoretical calculations[30,31,97] are presented in Figure 64 and show clearly hemispherical diffusion above the single nanopores. The AFM topography with corresponding height profile is depicted in A and the correlating current image and profile at the marked line in the current image is shown in B. The current density obtained from these results is lower (0.11 µA/cm²) compared to the results shown in Figure 62 for the overlapped diffusion, but just a small section of 8 nanopores is visible within the depicted images in Figure 64 compared to the whole array with 100 nanopores in Figure 62. By calculation of the current response for solely one single nanopore within both arrays, a current density of approximately 13.3 nA/cm² for large pore/pore separation compared to 6.4 nA/cm² for small distances between single pores show the enhanced current response for single nanopores with individual hemispherical diffusion profile. The current profile in Figure 64 B also shows the current peaks with enhanced current signals at the nanopores, which is again related to the penetration of the conductive AFM tip into the pore filled with the solution of high concentration of $Ru(NH_3)_6^{3+}$.

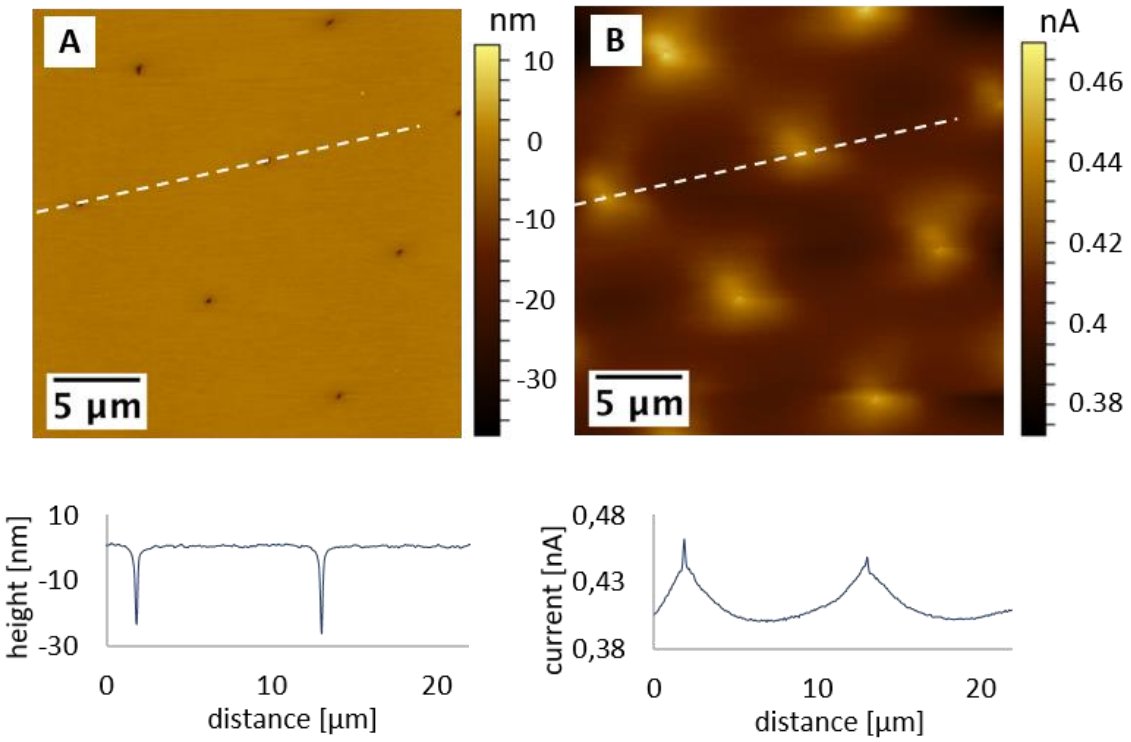

Figure 64 AFM-SECM images of a nanoporous array with 91 times separation of the individual pores in a hexagonal arrangement. Contact mode AFM topography (A) and GC mode SECM current signal (B) due to the diffusion of $[Ru(NH_3)_6]^{3+}$ through the nanopores is depicted showing individual diffusion profiles at the pores. The corresponding height and current profiles are shown beneath according to the marked line in (A) and (B). Original size: 25.3 x 25.3 µm^2, scan speed: 47.9 µm/s (1.0 ln/s), scan angle: - 34.9°. *Adapted with permission from* Y. Liu, A. Holzinger, P. Knittel, L. Poltorak, A. Gamero-Quijano, W. D.A Rickard, A. Walcarius, G. Herzog, C. Kranz, and D.W.M. Arrigan. Visualization of diffusion within nanoarrays. *Anal. Chem.* **88,** 6689–6695 (2016). *Copyright 2019 American Chemical Society*. https://pubs.acs.org/doi/10.1021/acs.analchem.6b00513.

The AFM-SECM investigations were repeated with an AFM tip-integrated recessed Au frame electrode to detect the diffusion without additional current peaks due to the penetration of a conductive AFM tip into the nanopores. Thereby, a hindered diffusion could be detected besides the pore as shown in Figure 65, with some pores seem to be blocked, indicated by an absent current signal. The results show a nanoporous array with a pore-to-pore separation of 21 in the AFM topography with the corresponding height profile (A) and the current response in B, which shows not the expected overlapped diffusion. Indeed, the current response is too low compared to calculations of the

predicted current for the diffusion of $Ru(NH_3)_6^{3+}$ and the current density (0.04 µA/cm²) is just 6 % of the current density for the results shown in Figure 62, leading to the assumption that the whole nanoporous array was blocked and not just some individual pores of the array.

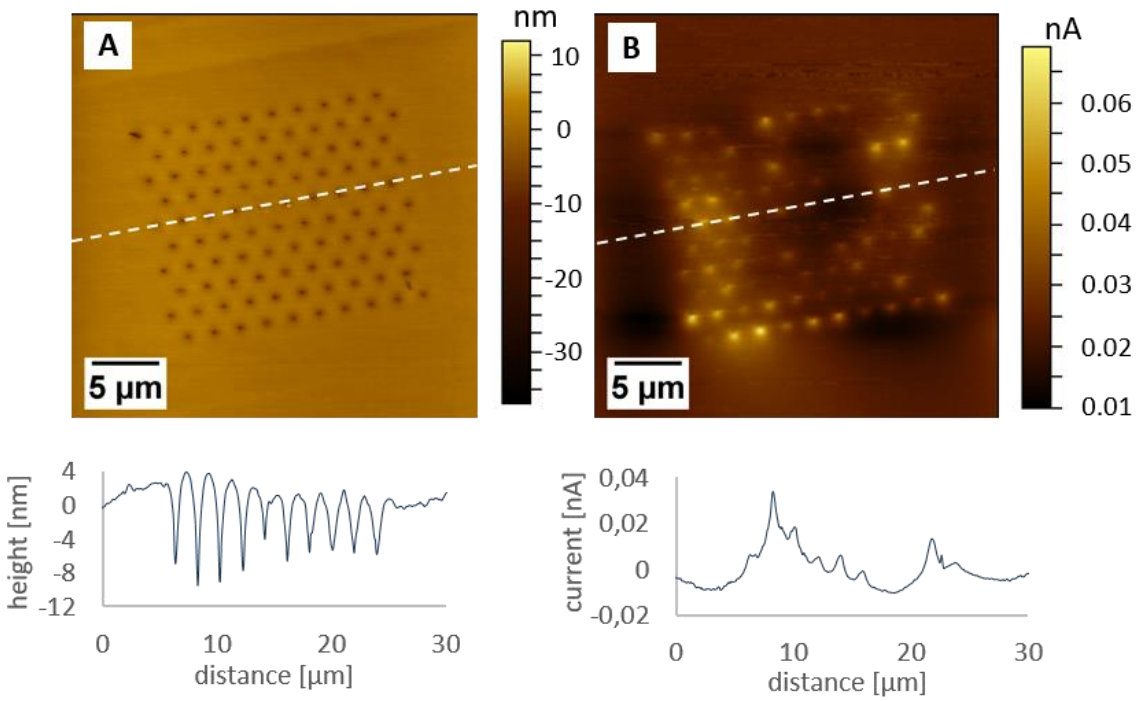

Figure 65 AFM-SECM images of a nanoporous array with 21 times separation of the individual pores in a hexagonal arrangement. Contact mode AFM topography (A) and GC mode SECM current signal (B) due to the diffusion of $[Ru(NH_3)_6]^{3+}$ through the nanopores is depicted. Some of the pores are blocked and no diffusion is detectable in (B) represented by dark region above the nanopore array. The corresponding height and current profiles are shown beneath according to the marked line in (A) and (B). Original size: 40 x 40 µm², scan speed: 47.7 µm/s (0.6 ln/s).

The observed small change in current may be explained than by the change in distance between the surface and the tip integrated electrode when the re-shaped AFM tip penetrates the pores. This behavior of blocked pores could be also observed in ITIES measurements at the nanoporous arrays. The reason for blocking has not been fully investigated and might be related either to impurities of the used solutions or to redeposited material during FIB-milling of the arrays. Additionally, small air bubbles, which may be located at the SiN membrane and may be possibly introduced during the filling of the glass tubes with one of the electrolyte solutions, might also block single pores.

For a detailed interpretation of the observed pore blocking, a detailed understanding of the location of the ITIES within the nanopores is essential. In the following section, electrochemistry at the ITIES and theoretical calculations are compared to verify the prediction of the interface being located at the aqueous facing side of the nanopores as reported for arrays produced by e-beam lithography[98,267] and also assumed for FIB-milled nanoporous arrays[31].

6.3.2 *ITIES at nanopore arrays*

For the identification of the interface within nanoporous arrays, the electrochemically driven transport of $TPrA^+$ as a model analyte at the ITIES is investigated. This was already used for characterization of porous SiN membranes and led to the conclusion that the interface at FIB-milled nanopores is comparable to nanopores fabricated by e-beam lithography[31]. Thereby, an inlaid interface facing the aqueous electrolyte solution was assumed and the calculations are based on equation (26) (see section 1.4). Because FIB-milling results in the implantation of positively charged Ga ions, which may result in a hydrophilic surface, the behavior of FIB-milled nanopores might be different for ITIES compared to nanopores obtained by e-beam lithography. Additionally, the truncated pore shape due to redeposited material during the milling process, which was already reported by several groups[32,36,37], was so far not considered.

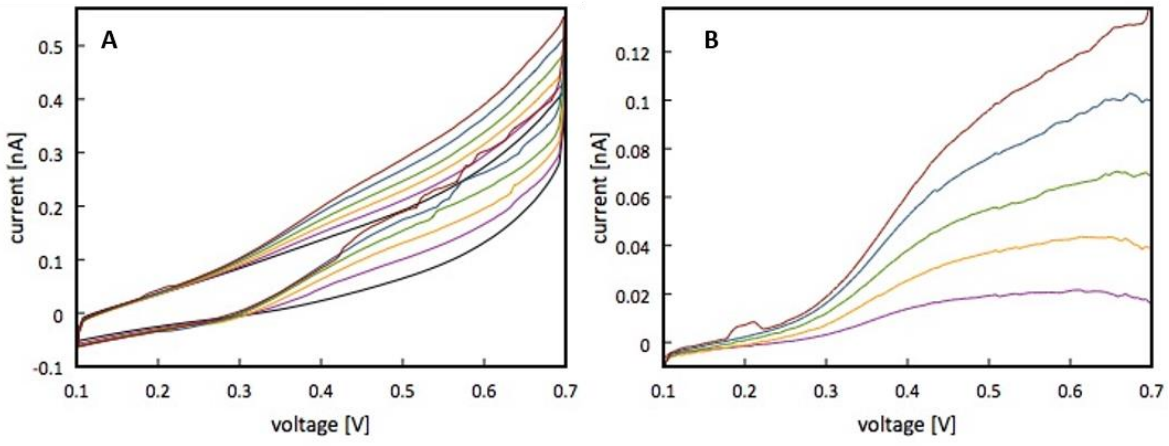

Figure 66 CV recorded at ITIES (A): black curve represents the background and colored curves represent the CV after consecutive addition of TPrACl to the aqueous phase. The current response after background subtraction is depicted in (B). Colors: 20 µM (purple), 40 µM (yellow), 60 µM (green), 80 µM (blue) and 100 µM (brown) TPrACl. Scan speed: 5 mV/s.

In Figure 66, the CV for the transport of $TPrA^+$ from the aqueous to the organic phase during the forward scans are shown within a concentration range of 20 – 100 µM $TPrA^+$, with the black CV as the background response prior to the addition of the analyte. In B, the background subtracted current response of the forward scan ($TPrA^+$ transfers from the aqueous to the organic phase) is depicted. A limiting current at 0.6 – 0.65 V is visible for the purple and the yellow curve in Figure 66 B. The current at this potential was compared to theoretical currents calculated by the different equations summarized in 1.4. Prior to the electrochemical investigations, the nanoporous array was characterized by AFM using a high-aspect ratio AFM tip, showing the pore shape and the pore orifices of the FIB-milled nanopores (see Figure 67). Whereas in prior publications, the diameters of the nanopores were evaluated by SEM[30,31], AFM provides an accurate geometry and size of the pore.

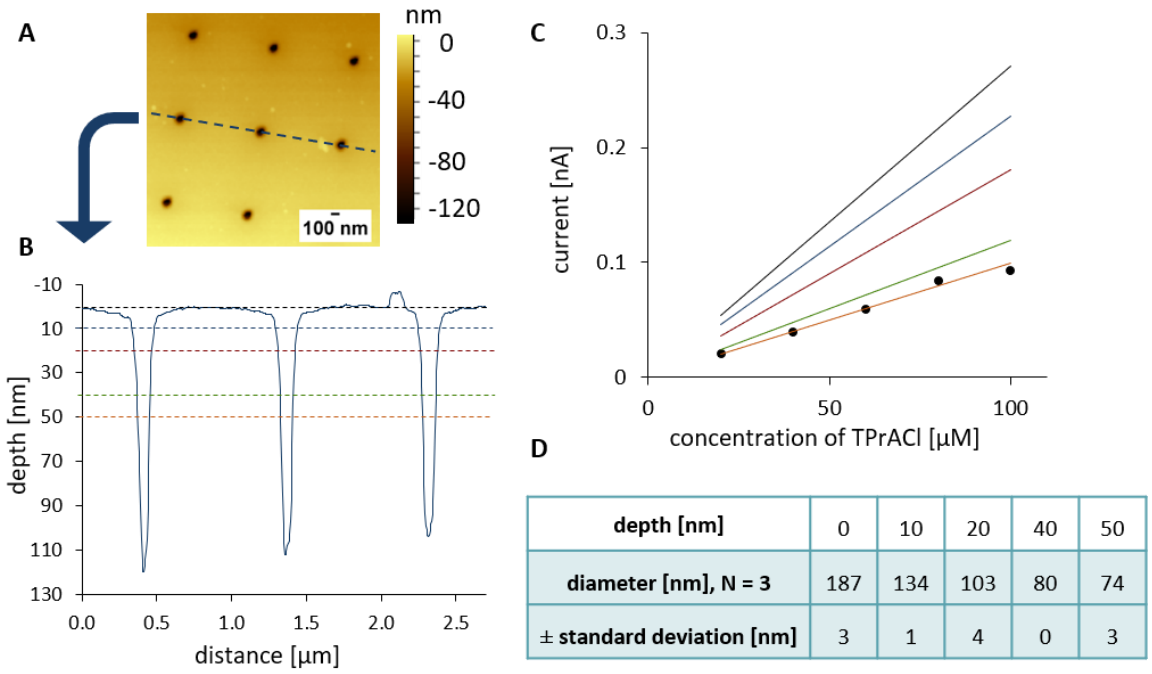

depth [nm]	0	10	20	40	50
diameter [nm], N = 3	187	134	103	80	74
± standard deviation [nm]	3	1	4	0	3

Figure 67 Dynamic mode AFM topography (A, original size: 2.75 x 2.75 µm²) of a nanopore array with height profile (B) according to the marked line in A. The results shown in Figure 66 and depicted as black points in the calibration curve in C are compared to theoretical calculations for an inlaid geometry of the interface (black line, at h= 0 nm) and a recessed interface at different locations within the nanopore as marked in the depth profile in (B). The diameters used for calculations of the theoretical currents are summarized in (D).

The measurement of the pore diameter from SEM images is suitable for pores with parallel inner walls and the same pore diameters at both sides of the membrane, whereas for a truncated pore shape, the investigation of the pore shape of nanoporous membranes with thicknesses within 50 to 100 nm via SEM will always result in mixed pore size of the truncated cone-shaped pore due to the penetration depth of the electron beam. Thereby, the calculation of the current response based on an inlaid interface, which represents the large orifice of the truncated nanopores facing the aqueous side within the reported investigations[30,31], whereas for the reported calculations the pore dimensions determined by SEM were used. These pore dimensions represent indeed an intermediate pore diameter, in between both orifices of a truncated cone-shaped pore. In Figure 67, the AFM image obtained with an ultra-sharp AFM tip (A) and the corresponding depth profile of the nanopores is depicted in B. The dashed lines within the profile represent the position of the interface used for the calculations of the theoretical current by equation (28) for truncated cone-shaped nanopores. The diameter of the nanopores at the orifice (at 0 nm in the depth profile in Figure 67 B, black dashed line) is 187 nm ± 3 nm (N = 3) and was used as r_L in the calculation of the theoretical current (based on equation (28) in 1.4) at different position of the interface within the nanopores marked by different colors in Figure 67 B. The diameters for the assumed recessed interfaces at different depths are shown in Figure 67 D and were used for r_0 in the calculations. The experimental data for the transfer of $TPrA^+$ as shown in Figure 66 are presented as black points in the calibration shown in Figure 67 C. Thereby, the data points fit well with the theoretical calibration for an interface located in the pores at a depth (or length) of L = 50 nm. The nanoporous array had a pore-to-pore separation of 10.2 ± 0.2 (N = 3) for the results shown in Figure 66 and Figure 67. This indicates an overlapped diffusion profile at this nanopore array as shown in the AFM-SECM investigations in chapter 6.3.1 (see Figure 62). Liu et al.[30,97] reported that the current response for an overlapped diffusion is up to 54 %[30] reduced to individual diffusion at the nanopores in dependence to the pore-to-pore separation. In Figure 68, two different assumptions for an overlapped diffusion are compared to the experimental data and to the theoretical current with the interface located within the truncated cone-shaped nanopores at a depth of L = 50 nm.

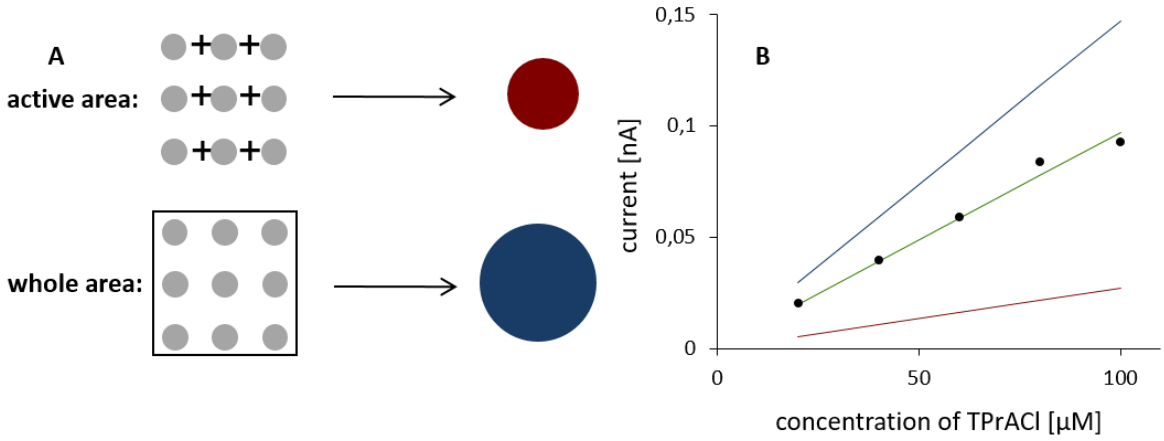

Figure 68 Schemes (A) showing the assumptions used for theoretical calculations according to an overlapped diffusion compared to the calibration curve (B, black points) of the results in Figure 66. The red and blue lines in B correspond to the theoretical assumption of one UME with the same size as the active area (red) or an UME of the same size as the whole array (blue). The green line in B corresponds to the theoretical assumption of a recessed interface located towards the organic electrolyte.

The schemes in Figure 68 A are illustrating the theoretical assumption used for the theoretical values depicted in the calibration curves in B in corresponding colors. For the approach colored in red, the active area of the single nanopores is summarized and replaced by an interface of the same area, whereas for the calculation of the whole area, the size of the array was used and replaced by a disk-shaped interface with the same area. Both approaches can be considered as the upper and lower limit of current response that can be expected for an overlapped diffusion. Another approach for the investigation of the location of the ITIES within FIB-milled nanopores is shown in Figure 69. The truncated cone shape of FIB-milled nanopores is used in the comparison of nanoporous arrays fabricated from the front or the back, so that either the small orifice is facing the aqueous electrolyte solution and vice versa, as illustrated in Figure 69 A. The used SiN membranes had a thickness of 100 nm and same parameters were used for the fabrication of the nanopore arrays by FIB milling. A similar approach was already reported by Alvarez de Eulate et al.[84] for microporous glass membranes fabricated by laser ablation with truncated cone-shaped pores. The hydrophobicity of such inner pore walls was determined by contact angle measurements and corresponding experimental and simulated data of the diffusion at the microporous array with pores oriented towards

either the aqueous or the organic electrolyte solution results in the assumption of a hemispherical shape of the interface. For the arrays reported in this publication, the pores were filled with the organic electrolyte solution[84]. For characterization of the nanopores in the experiments presented within this thesis, an ultra-sharp AFM tip was used. The sharp AFM probes were obtained by FIB milling taking into account the instrumental mounting angle (9°) of the AFM probe towards the sample surface. The AFM topography of a front and back side milled nanopore are shown in C with corresponding height profiles displayed in D.

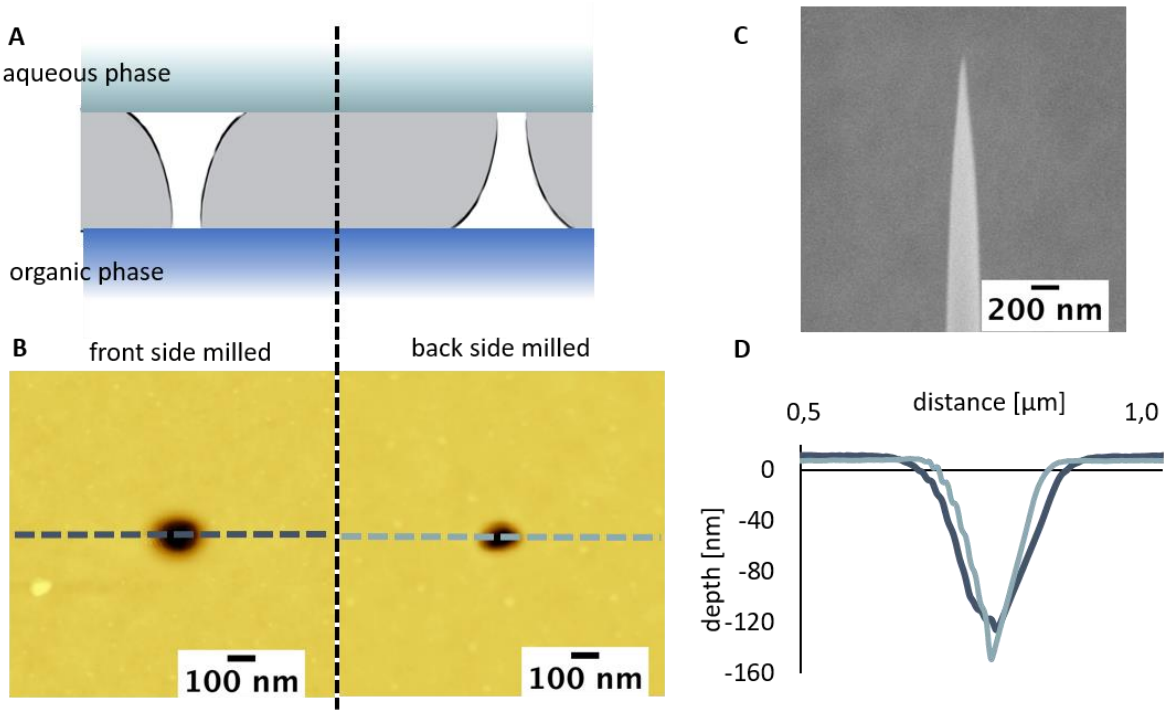

Figure 69 Comparison of front and back side milled pores: the scheme in (A) represents the orientation of the truncated cone-shaped pores towards the aqueous and organic phase, respectively, depending on the orientation of the membrane during FIB milling. AFM topography recorded in dynamic mode (B) of a front side (left) and back side (right) milled pore with corresponding height profiles as marked in (B) and depicted in (D). A high-aspect-ratio AFM tip is represented in the SEM image in (C) obtained by FIB milling. AFM parameters: 152 kHz (left)/ 169 kHz (right), scan speed: 1 ln/s (6 µm/s), original size: 3 x 3 µm². A. Holzinger, G. Neusser, B. J. J. Austen, A. Gamero-Quijano, G. Herzog, D. W. M. Arrigan, A. Ziegler, P. Walther, and C. Kranz, *Faraday Discuss.*, 2018, **210**, 113. *Adapted from Ref.* [187]*. Distributed under the license Creative Commons Attribution-NonCommercial 3.0 Unported (CC-BY-NC 3.0),* https://creativecommons.org/licenses/by-nc/3.0/.

Due to the geometry, only the pore diameter of the small orifice is accessible via AFM measurements for the back side milled nanopores. The dimensions of the nanopores are represented by the height profiles of the back side milled pore (light blue line) and the front side milled pore (dark blue line) in Figure 69 D corresponding to the topography marked by dashed lines in B in corresponding colors. The profile of the back side milled pore represents thereby the shape of the AFM tip and solely the dimension of the small orifice can be gained from these investigations. The fabricated nanoporous arrays, FIB-milled either from the front or the back of the SiN membrane, were examined in electrochemical investigations via CV for the transport of $TPrA^+$. In case that the interface is located towards the aqueous phase as assumed in previous publications[30,31], a lower current response for the back side milled nanopores is expected due to the smaller orifice facing the aqueous phase. In Figure 70 A, the background corrected forward sweep of the current response in dependence of the concentration of $TPrA^+$ in the range of 20 – 100 µM is shown and the corresponding calibration graph is represented by red points in B.

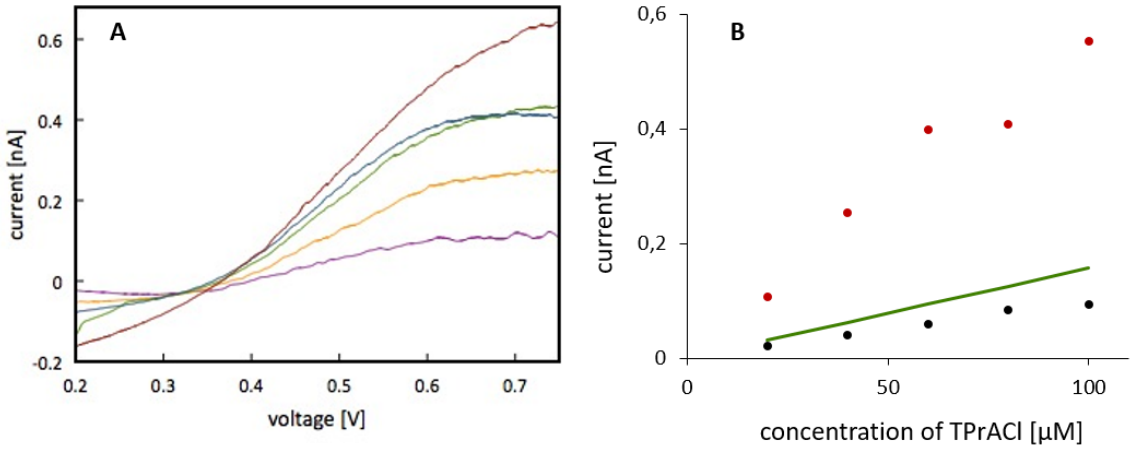

Figure 70 Current response after background subtraction (A) of consecutive addition of TPrACl at a back side milled nanopore array. Colors: 20 µM (purple), 40 µM (yellow), 60 µM (green), 80 µM (blue) and 100 µM (brown) TPrACl. Scan speed: 5 mV/s. The calibration curve (B) compares the results of A (red data) with the data obtained at ITIES at a front side milled nanopore array (black data) and the theoretical assumption (green line) of an inlaid interface facing the aqueous electrolyte.

The green line in B represents the calculated data for an inlaid interface facing the aqueous electrolyte solution and the black points represent the experimental results for a front side milled nanoporous array as already shown in Figure 66. Although the linearity for the experimental data for the nanopores FIB-milled from the back is poor, the detected current is up to 5 times higher than for the front side milled nanoporous array. The pore-to-pore separation for this array with respect to the radius of the small orifice is 17.6 ± 0.8 (N = 9) compared to 10.2 ± 0.2 (N = 3) for the results shown in Figure 66 and represented by the black data points in Figure 70 B. According to the results obtained so far[30], the diffusion at this pore array is overlapped. Either for individual or overlapped diffusion profiles, the current response has to be reduced for smaller pore diameters represented by the back side milled nanoporous array in case of an inlaid interface facing the aqueous electrolyte solution during electrochemical investigations. Of course, the influence of implanted Ga^+ ions has to be considered resulting in changes in the hydrophilicity of the membrane dependent on the orientation of the SiN membrane towards the ion beam during FIB milling. This parameter was neglected so far and has to be taken into account in future studies. Similar results showing a variation in electrochemical investigations performed at conical pores in two different orientation was already reported by Arrigan and coworkers, but for µm-sized pores in a glass membrane fabricated by laser ablation[84]. However, the hydrophilicity of these micropores was modified by an additional surface modification, which ensures the same hydrophilicity for the different orientations of these micropores. This is not the case for the FIB-milled nanopores reported within this thesis. Thereby, this is the first time that this direct comparison of nanoporous arrays in SiN membranes used for nanoITIES (see Figure 69 and Figure 70) are investigated towards the orientation of the membranes during FIB-milling. The different behavior in electrochemical investigations at nanoITIES with respect to the orientation of cone-shaped nanopores will be also considered in the following sections. The localization of the interface by AFM-SECM is difficult due to the penetration depth of the AFM tip into the nanopores and an accompanying mixture of the solutions. The diffusion behavior at nanoporous arrays was also visualized by silica deposition at the ITIES within nanoporous arrays. The size of the silica deposits formed at the interface between an aqueous phase and DCE was evaluated[181]. Within the next section, the size variation of the silica deposits is compared with respect to the actual pore diameters.

6.3.3 *Silica deposits at the ITIES for localization of the interface*

The localized deposition of silica at the ITIES is used within the following investigations to distinguish between nanopores FIB-milled either from the front or the back as shown in Figure 69. The pore-to-pore separation in both arrays is sufficient for independent pore diffusion and the diameters determined by AFM for the orifice facing the aqueous electrolyte solution are 183 nm ± 29 nm (N=3) for front side milled and 72 nm ± 12 nm (N=3) for the back side milled arrays, respectively. The SEM images of the arrays after silica deposition are depicted in Figure 71 A and the diameter of the single silica deposits for both arrays are compared in B. Thereby, a wide distribution of different deposit sizes can be seen for both approaches with larger diameters for the back side milled nanoporous array that indicates an enhanced ion transport. The size distribution within the 100 nanopores of one array is even larger than the difference between both arrays fabricated by front or back side FIB milling. A paired two-tailed t-test with a 95 % confidence level showed that the variation of the silica deposits in each array is significant and the standard deviation of the silica deposits (43 % and 57% of the mean value for diameters, respectively) within one array, which has only a small standard deviation in the original pore size, corresponding to 16 – 17 % of the mean value, is larger, than the difference between the silica depositions at both membranes. These results confirm the interpretation gained by the comparison of electrochemical results of the transfer of $TPrA^+$ at the nanoITIES as discussed in 6.3.2, showing the same trend of an enhanced diffusion for FIB-milled nanoporous arrays fabricated from the back of the SiN membrane. However, due to the broad size distribution of the results presented in Figure 71, additional investigations have been done at these modified nanopore arrays. Therefore, the silica deposits of the nanoporous array fabricated from the back are investigated in detail by FIB cross-sections and FIB/SEM tomography. During electrochemical deposition of silica at the ITIES, the template CTA^+ is transferred from the organic to the aqueous phase enabling the formation of silica by hydrolysis and condensation of TEOS.[275] Si, either as TEOS or silica, is just present in the aqueous phase, hence the location of the silica deposits is an indication for the location of the aqueous phase.

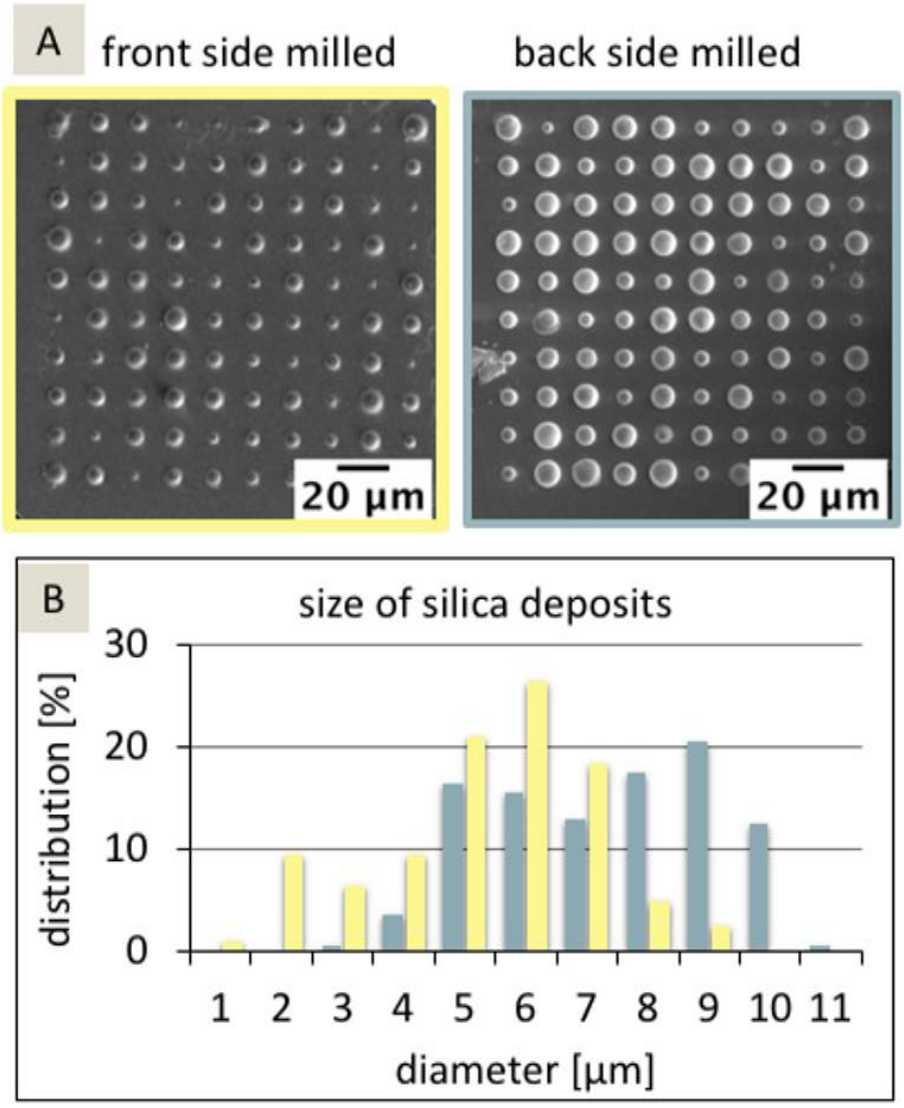

Figure 71 SEM images of the silica depositions at front (A, left) and back (A, right) side milled pore arrays, respectively. The size distribution of the arrays in A is given in B. yellow: front side, blue: back side approach. The electrochemical deposition was done at 0 V for 90 s (aqueous phase: pH 9). A. Holzinger, G. Neusser, B. J. J. Austen, A. Gamero-Quijano, G. Herzog, D. W. M. Arrigan, A. Ziegler, P. Walther, and C. Kranz, *Faraday Discuss.*, 2018, **210**, 113. *Reproduced from Ref.* [187]*. Distributed under the license Creative Commons Attribution-NonCommercial 3.0 Unported (CC-BY-NC 3.0),* https://creativecommons.org/licenses/by-nc/3.0/.

In Figure 72 A, the FIB-induced secondary electron image is shown of one silica deposit covered with a layer of Pt/C, which prevents charging effects while imaging and milling, and additionally prevents beam-induced damage of the silica deposit. In the SEM images in B-E, the cross-sections of two silica deposits with varying diameters are depicted. As shown in Figure 71, the size distribution of the silica deposits is large and both, small

(< 5 µm, in B, C) and large (> 9 µm, in D, E) deposits were investigated in detail by FIB/SEM tomography. A close-up of the silica deposits close to the nanopores is shown in C and E. Whereas for small deposits, the silica is directly attached at the SiN membrane, a gap between the silica and the SiN membrane is visible for large ones (Figure 72 E). This gap might be related to the drying step after silica formation, which might cause shrinkage of the silica deposit due to solvent loss. This effect is likely stronger for large deposits resulting in the separation of the deposit from the SiN membrane.

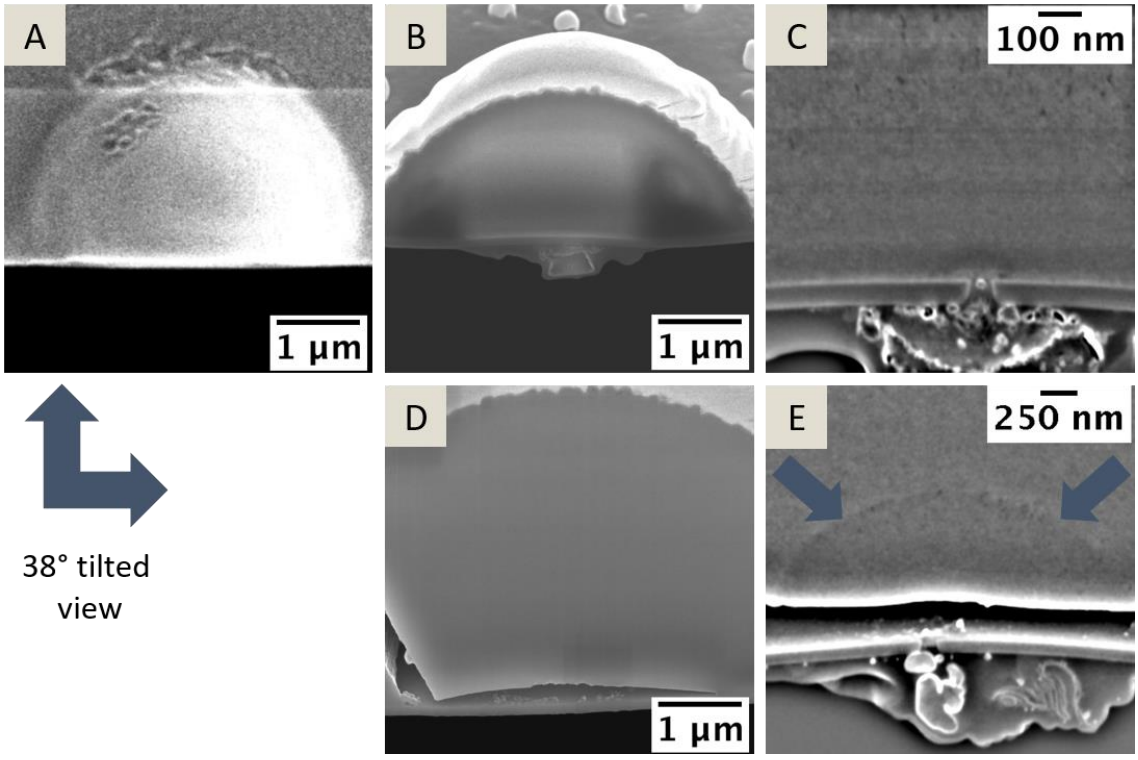

Figure 72 Differences in silica morphology: Cross-sections of silica deposits are compared for large (> 9 µm in diameter) and small (< 5 µm in diameter) deposits. The FIB-induced SE image in A shows the silica deposit partially covered with a Pt/C protection layer, whereas the SE images in B-E show the deposits in a 38° tilted perspective. The SE images shown in C and E represent a zoomed view of the samples shown in B and D, respectively, during consecutive FIB sectioning. The blue arrows in E point out an inner radial region showing different density of the deposited silica. A. Holzinger, G. Neusser, B. J. J. Austen, A. Gamero-Quijano, G. Herzog, D. W. M. Arrigan, A. Ziegler, P. Walther, and C. Kranz, *Faraday Discuss.*, 2018, **210**, 113. *Reproduced from Ref.* [187]*. Distributed under the license Creative Commons Attribution-NonCommercial 3.0 Unported (CC-BY-NC 3.0),* https://creativecommons.org/licenses/by-nc/3.0/.

Any other processes following the silica formation, such as removing the electrolyte solutions, drying, and cleaning might also have an influence on the silica deposits and with this on the investigated interface. In both examples shown in Figure 72, a dense structure of the silica deposit is visible, whereas for the large deposit in Figure 72 D and E, the dense structure shows a hemispherical region in close proximity to the nanopore (marked by arrows in E) with higher density according to the contrast in the SE image, compared to the adjacent region showing a slightly different contrast. This variation in the silica deposit can be addressed to an enhanced hemispherical diffusion near the nanopore during electrochemical deposition resulting in an enhanced formation of silica and a denser structure compared to the adjacent region. Next to the dense structure located in close proximity to the SiN membrane visible in the SE images, which correlates with the side facing the aqueous electrolyte solution during electrochemical deposition, there is an inhomogeneous structure visible below the membrane facing the organic electrolyte solution. This is recognizable for small and large silica deposits (Figure 72 C, E). This structure will be referred to as “residue” within the following discussion. In the SE image shown in C, something appearing as a ‘single particle’ is located within the nanopore. In Figure 73, several SE images of this silica deposit are shown in the FIB/SEM tomography, where the lateral distance between single SE images was 10 nm. The focus in these images was laid on the nanopore and the residue in close proximity to the nanopore. The conical shape of the nanopore is clearly visible in these images.

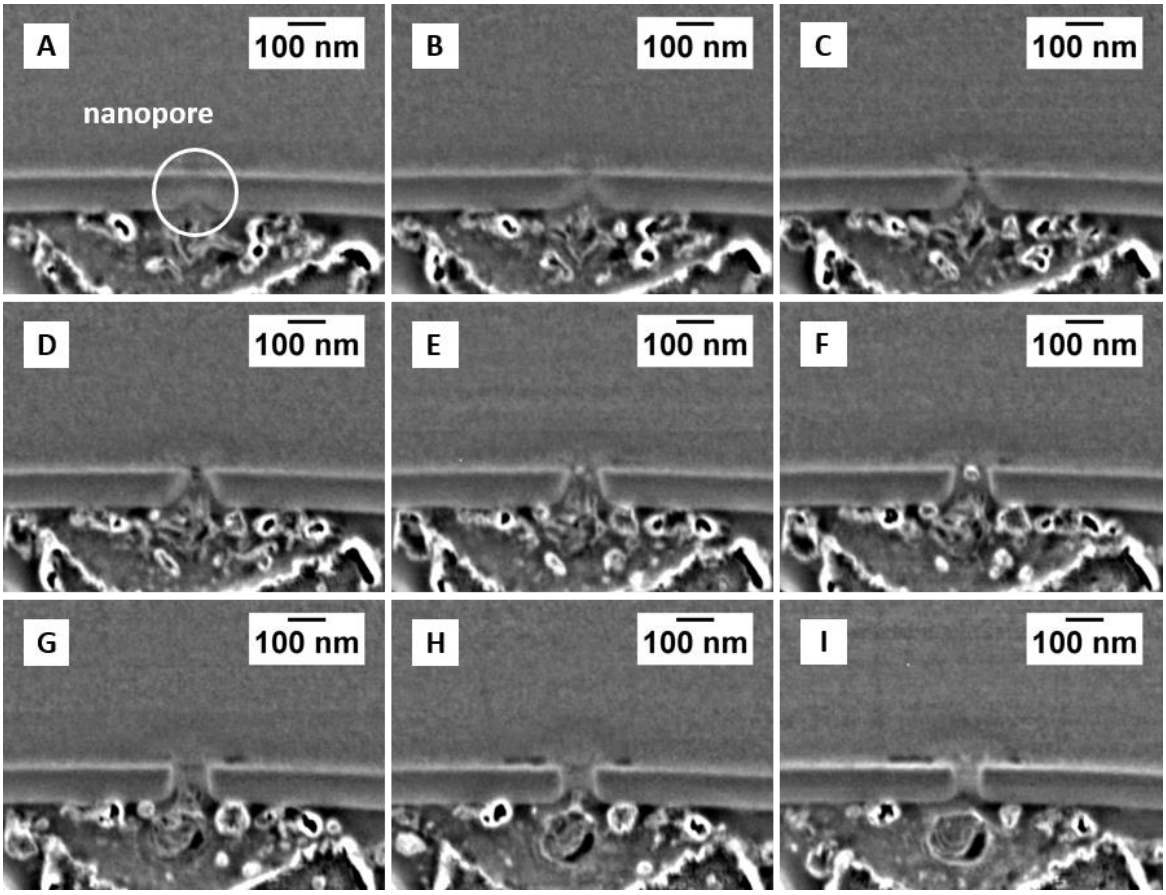

Figure 73 Processed SEM images showing a nanopore (marked area in (A)) within a series of images (A-I) with 10 nm distance between single SE images. SEM: 5 kV/ 86 pA, FIB: 30 kV/ 48 pA, 10 nm/ slice. Holzinger, G. Neusser, B. J. J. Austen, A. Gamero-Quijano, G. Herzog, D. W. M. Arrigan, A. Ziegler, P. Walther, and C. Kranz, *Faraday Discuss.*, 2018, **210**, 113. *Based on Ref.* [187]. *Distributed under the license Creative Commons Attribution-NonCommercial 3.0 Unported (CC-BY-NC 3.0), https://creativecommons.org/licenses/by-nc/3.0/.*

Additionally, the bright particle in the pore (see Figure 73 F) has a dimension of 10 – 20nm as a small variation of the contrast in the SE image in E might be part of this particle, but the particle is already no longer visible in image G. Additionally, the particle is not completely visible in image E, which might indicate that the pore is also filled with some other residue. In case that the pore is empty (except this particle) and the contrast just indicates the SiN membrane behind the nanopore, this single particle has to be also visible in the images C-E. It is difficult to discriminate between the in-plane region of the exposed area and the sample volume because the contrasts in the SE images are always a result of overlapped signals due to the penetration depth of the electron beam[184]. This is also called

'the shine through artifact' [280]. The structure of the silica deposit is homogeneous except small variation in contrast in close proximity to the nanopore, which might indicate differences in the silica formation rate due to enhanced concentrations directly at the nanopore. A detailed interpretation giving the variation in the SEM contrast is at the current state not possible. The residue at the side of the SiN membrane facing the organic electrolyte solution during ITIES measurements shows different regions given the varying, observed contrasts. The black regions are holes within this residue, whereas bright regions might be either single particles of unknown content or edges indicating the in-plane area sectioned by the ion beam. Again, it is difficult to interpret the different contrast in SE images with unknown samples and to distinguish between the in-plane area and the sample volume. Structures, which are visible in more than one SE image during FIB sectioning can be associated with the sample volume. Focusing on the nanopore, there is some connection between residue and the nanopore visible, especially in the SE images shown in Figure 73 C - G, with a single particle shown in F. A clear differentiation between the SiN membrane and this residue within the nanopore is still challenging and data have to be interpreted with care to avoid false results. The residue can be clearly addressed to the diffusion processes in close proximity to the nanopore because the residue is just located at this nanopore. These observations are more obvious in another silica deposit investigated by SEM/FIB tomography, which is presented in Figure 74. Single slices of the 3D stack are presented in A, I-IV showing the residue on the organic facing side of the SiN membrane and located close to the orifice of the nanopore. Three different regions might be differentiated within this residue. The first part seems to be some kind of encapsulating layer, followed by a porous region and a diffuse inner structure of the residue. The diffuse inner structure seems also to be within the nanopore. In total 24 SE images of the slice & view procedure are summarized in a 3D representation of the nanopore, presented by a voxel size of1.92 µm x 1.92 µm x 10 nm. The residue is shown in Figure 74 B with the inner diffuse structure marked in green and the outer layer shown in yellow. The borders of the SiN membrane are indicated in blue. The truncated cone shape of the nanopore is clearly visible in the 3D reconstruction. The drop-like residue in this example is located around the nanopore, whereas the thin layer marked in yellow seems to cover the SiN membrane over a larger region.

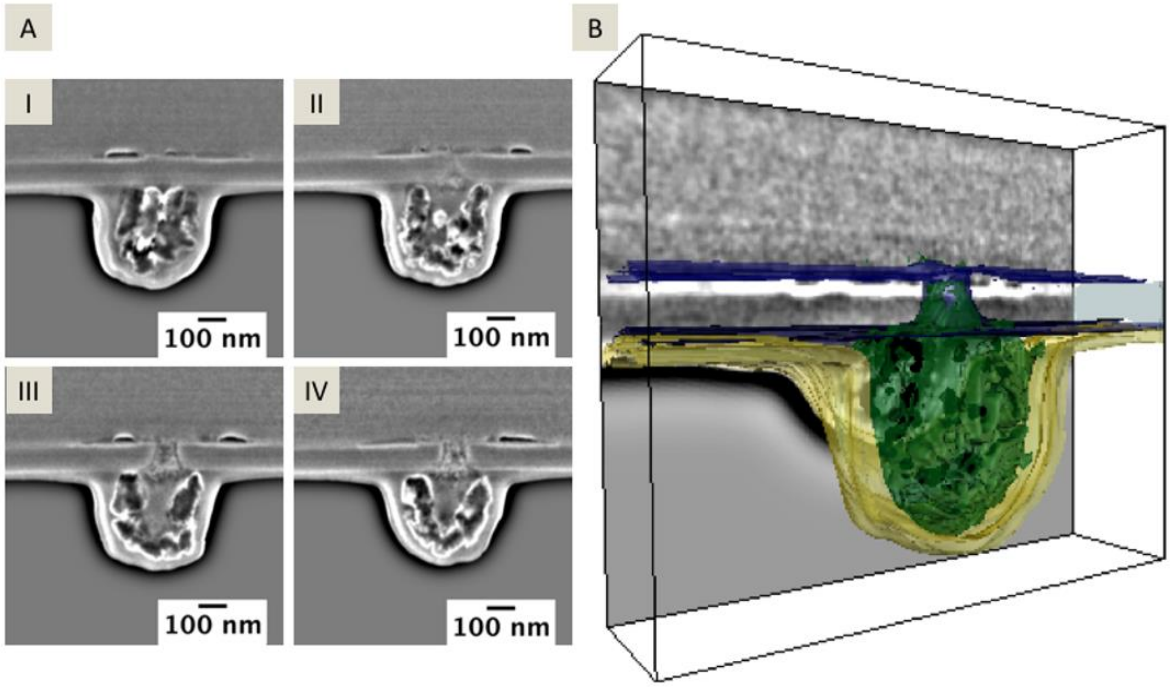

Figure 74 Processed SEM image sequence of a back side milled nanopore after silica deposition with a large residue structure located at the nanopore facing the organic electrolyte (A, I-IV). The distance between single slices is 30 nm. 3 D reconstruction of the slices and view stack is shown in B. SEM: 5 kV/ 86 pA, TLD at 38° (corrected tilt), FIB: 30 kV/ 48 pA, 10 nm/slice; in total 80 slices are imaged. A. Holzinger, G. Neusser, B. J. J. Austen, A. Gamero-Quijano, G. Herzog, D. W. M. Arrigan, A. Ziegler, P. Walther, and C. Kranz, *Faraday Discuss.*, 2018, **210**, 113. *Reproduced from Ref.* [187]*. Distributed under the license Creative Commons Attribution-NonCommercial 3.0 Unported (CC-BY-NC 3.0),* https://creativecommons.org/licenses/by-nc/3.0/.

The results shown in Figure 73 and Figure 74 indicate that the pores are filled with some residue. There is a connection between this residue and the silica deposit above the membrane facing the aqueous electrolyte solution during electrochemical investigations, however, the structure of the particles or structures within the nanopores show different contrast in the SE images compared to the silica deposits. A detailed interpretation is still difficult due to the 'shine through effect' of porous structures[280]. Additional information is gained by the investigation of the elemental composition as presented in the following section.

6.3.4 *Investigation of the elemental composition of deposited silica at nanopores*

For the determination of the elemental composition of the silica deposits and the residue at the side of the membrane facing the organic electrolyte solution during electrochemical deposition, a thin TEM lamella was prepared from a single silica deposit. The TEM lamella with a thickness smaller than 150 nm was investigated by EDX resulting in the elemental maps shown in Figure 75 (color-coded SE images in respect to the present elements on the right). The fabrication of the TEM lamella by FIB milling resulted in re-deposition of material, which is indicated by the EDX signal of Pt (light blue image). The signal has a maximum value at the edge of the diffuse residue. An enhanced signal at energies for X-rays characteristic for the other elements at this border can be also seen in the other images and is therefore negligible.

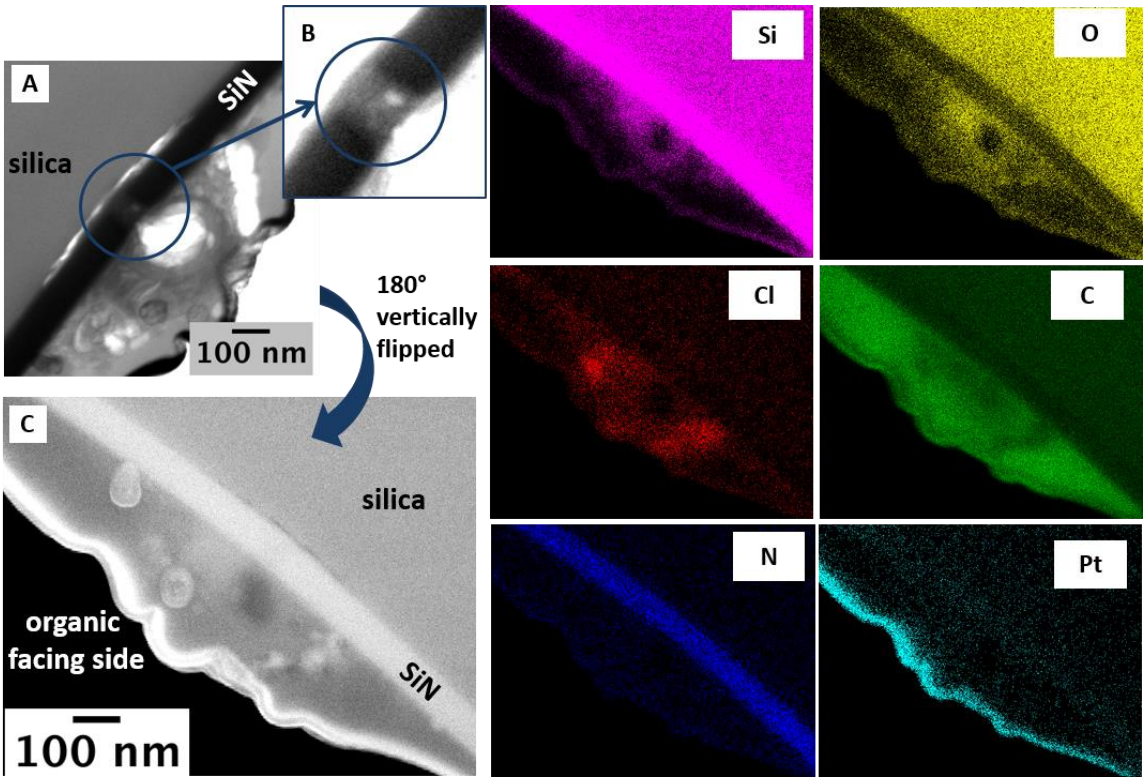

Figure 75 TEM image of a nanopore with a diameter of 80 nm (A) with a zoomed view of the pore (B) and SEM image of the same location, but vertically flipped by 180°. EDX mapping of this area is given on the right side marked by false color images according to the elemental composition given in the single images. Acceleration voltage: 10 kV. A. Holzinger, G. Neusser, B. J. J. Austen, A. Gamero-Quijano, G. Herzog, D. W. M. Arrigan, A. Ziegler, P. Walther, and C. Kranz, *Faraday Discuss.*, 2018, **210**, 113. *Adapted from Ref.* [187]. *Distributed under the license Creative Commons Attribution-NonCommercial 3.0 Unported (CC-BY-NC 3.0),* https://creativecommons.org/licenses/by-nc/3.0/.

The residue located at the nanopore shows high intensities for chloride (red), carbon (green), but also silicon (pink). Thereby, the Si signal is more pronounced and it is unlikely that this signal originates just due to redeposited material. Therefore, this residue might consist of Si, either as silica or as TEOS indicating the location of the aqueous phase during electrochemical silica deposition. For a detailed interpretation of the elemental composition of this residue, additional investigations will be necessary. The interior of the nanopore cannot be evaluated here because the signal is overlaid with the signal originating from the SiN membrane. The STEM image depicted in A shows the TEM lamella from one side, whereas the SE image in C and the corresponding EDX mapping (right side) show a vertically flipped view of the same position. From this perspective, the nanopore is not visible and the SiN membrane in this image is entirely covering the pore. For both, SEM and EDX, the penetration depth of the excitation e-beam is larger than the thickness of the TEM lamella itself[184]. For clear identification of the content within the nanopores, the pore has to be larger than the TEM lamella. Because the preparation of thin lamellas below 100 nm is challenging due to limits in the fabrication process[281,282], the nanopores prepared by FIB milling were increased to a range of 250 – 350 nm in diameter. As visualized in the schemes in Figure 76, the larger pores are accessible from both sides in lateral dimension that the contrast in SEM, TEM and the signal detected by EDX of the lamellas solely represents the inner structure within the pores avoiding the convolution of the signals with the signals originating from the SiN membrane.

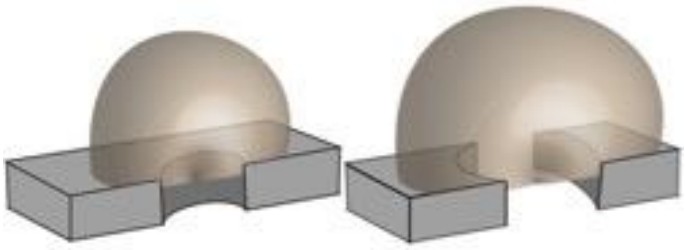

Figure 76 Scheme of two TEM lamellas with varying pore diameters, insufficient (left) and sufficient (right) for investigation of the content within the nanopores. A. Holzinger, G. Neusser, B. J. J. Austen, A. Gamero-Quijano, G. Herzog, D. W. M. Arrigan, A. Ziegler, P. Walther, and C. Kranz, *Faraday Discuss.*, 2018, **210**, 113. *Reproduced from Ref.* [187]*. Distributed under the license Creative Commons Attribution-NonCommercial 3.0 Unported (CC-BY-NC 3.0),* https://creativecommons.org/licenses/by-nc/3.0/.

For the nanoporous arrays with larger diameters ranging from 250 to 350 nm, SiN membranes with a thickness of 50 nm were used. All arrays were FIB milled from the front side facing the aqueous electrolyte solution during electrochemical silica deposition. To distinguish between Si particles located in the pore and associated with the silica deposit process, which might be moved into the pore during drying or cleaning steps after silica formation, the pH value for one silica deposition was adjusted to suppress the silica formation. Additionally, the deposition time was altered, and its influence is analyzed towards the silica deposits and the remaining residue in or below the nanopore facing the organic electrolyte solution during electrochemical deposition. An overview of silica deposits fabricated at different deposition conditions are shown in Figure 77.

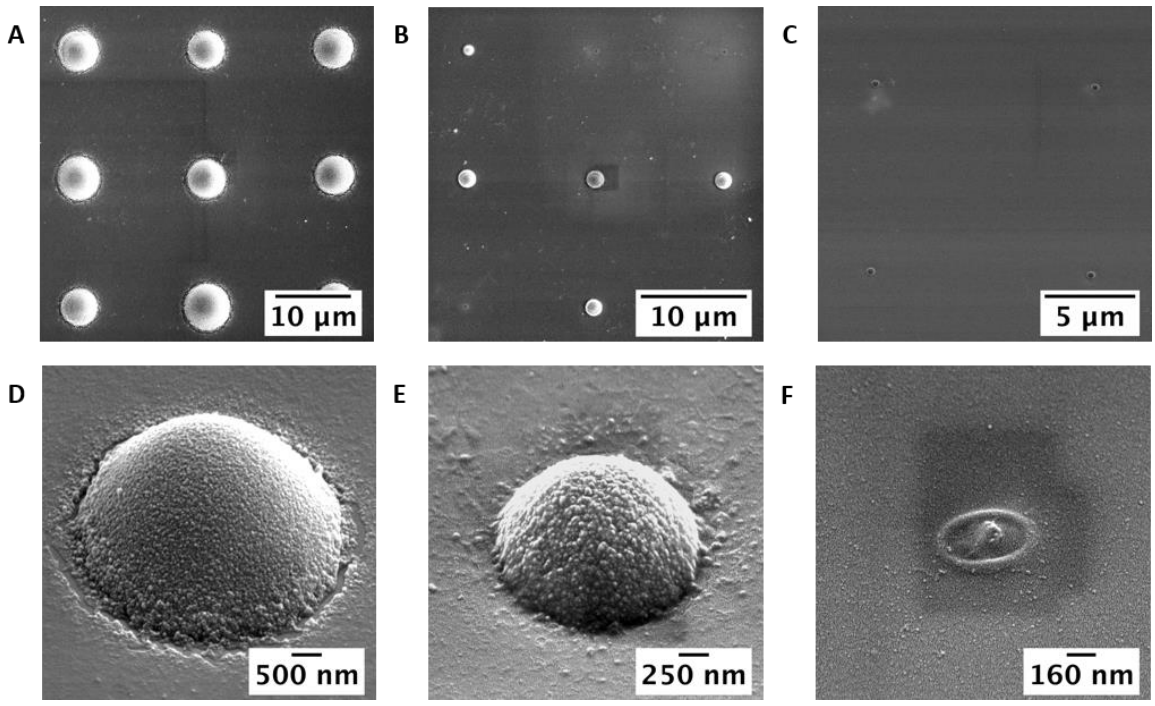

Figure 77 SEM images of different silica deposits with varying deposition parameters: array with 9 (A, B) and 4 (C) pores and silica deposits (D-F) corresponding to the arrays above. Parameters: applied potential: - 0.1 V for all arrays; for 60 s at pH 9 (A, D), for 5 s at pH 9 (B,E), for 10 s (3 times) at pH 3 (C,F). The pH value corresponds to the aqueous phase. 5 kV, 86 pA, tilt: 0° (A-C) and 52° (D-F). *Adapted from Ref.* [187]*. Distributed under the license Creative Commons Attribution-NonCommercial 3.0 Unported (CC-BY-NC 3.0),* https://creativecommons.org/licenses/by-nc/3.0/.

Thereby, the SE images in A and B show a varying size of the silica deposits with changes in deposition time at pH 9. In C, the results for the deposition at pH 3, insufficient for the silica formation, is shown. At acidic pH values, the mononuclear species of TEOS is dominant in the aqueous phase, which doesn't facilitate the transfer of the template from the organic to the aqueous phase and no condensation reaction of the TEOS occurs[276]. It is clearly visible that no silica deposits were formed above the individual pores at the aqueous facing side during electrochemical deposition. However, some particulate material was located within the nanopores in absence of silica deposits, which are embedded within the residue that was already observed for nanoporous arrays with smaller pore diameters (see Figure 72 to Figure 75). With increasing deposition times, the diameters of the silica deposits increased with 1.4 ± 0.3 µm (N = 27) for 5 s compared to 3.7 ± 0.5 µm (N = 27) for 60 s, whereas in both examples shown in Figure 77 A and B, slightly different sizes for single deposits in one array can be seen in accordance to the results presented in section 6.3.3. For short deposition times of 5 s, the silica deposits were just formed at some pores and 5 of 27 nanopores of this investigated nanoporous array showed no silica formation. For the nanoporous array used in ITIES measurements with insufficient pH values of the aqueous phase, no silica deposits were obtained (Figure 77 C, F), but some nanopores showed residue within the pores as shown in F. In Figure 78, the cross-sections of a silica deposit formed at pH 9 (A and B) are compared to the cross-section of a nanopore without silica formation due to an insufficient pH value (pH 3, C). The cross-sections shown in A and B, as well as the 3D reconstruction in D, show a dense silica deposit as already reported for the nanopores with smaller dimensions and a diffuse residue (marked yellow) within the pores with a few single particles (marked in green) and some holes (black). In the SE image in C, a large particle is visible within the nanopore embedded in the so-called residue.

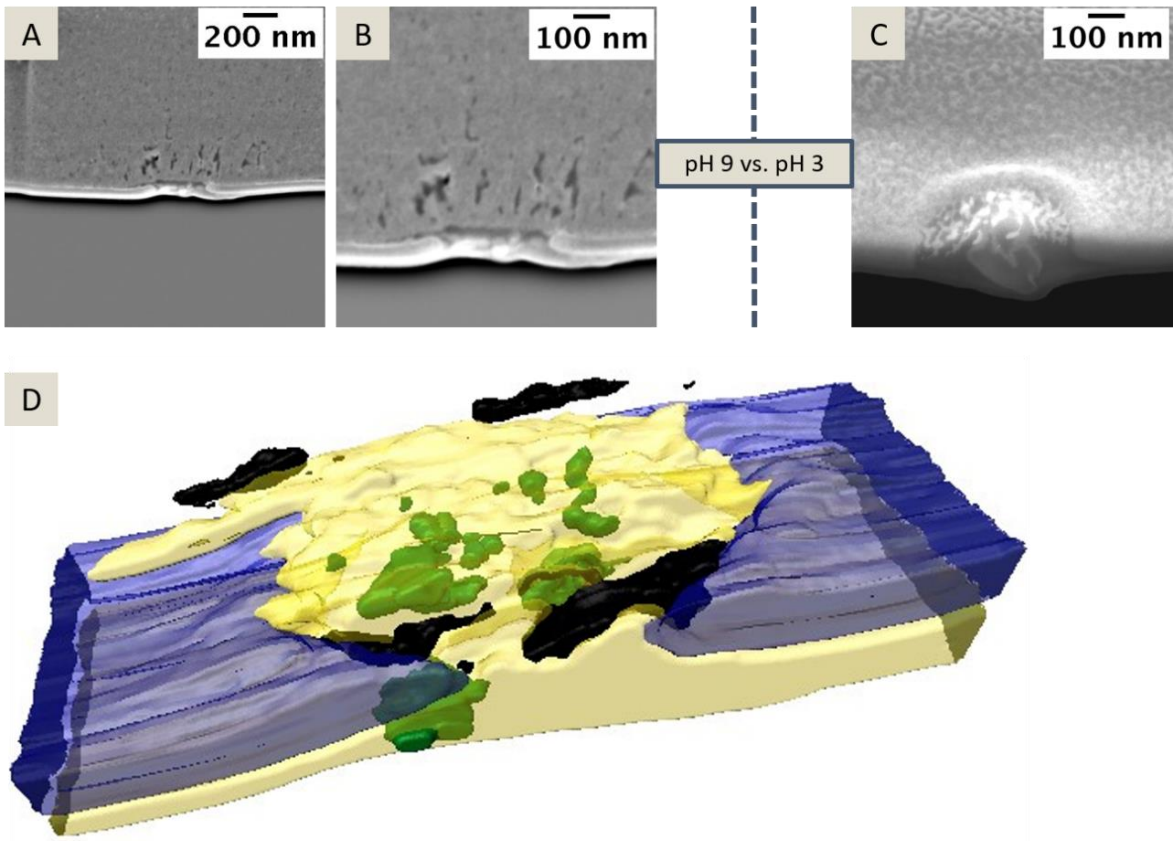

Figure 78 Influence of the pH in the aqueous phase on silica formation: A processed SEM image of a silica deposit formed at pH 9 shown at two different magnifications (A, B) and no silica formation at pH 3 (C), 38° tilted view. The residue formed at large nanopores is shown in detail in the 3D representation (D, according to the nanopore shown in A, B) with: SiN membrane (blue), single particles (green), holes (black) and the diffuse residue (yellow). SEM: 5 kV/ 86 pA, TLD at 38° (corrected tilt), FIB: 30 kV/ 48 pA, 5 nm/slice and in sum 300 slices. A. Holzinger, G. Neusser, B. J. J. Austen, A. Gamero-Quijano, G. Herzog, D. W. M. Arrigan, A. Ziegler, P. Walther, and C. Kranz, *Faraday Discuss.*, 2018, **210**, 113. *Reproduced from Ref.* [187]*. Distributed under the license Creative Commons Attribution-NonCommercial 3.0 Unported (CC-BY-NC 3.0),* https://creativecommons.org/licenses/by-nc/3.0/.

Because there is no silica condensation at the acidic aqueous solution in accordance to literature[276], detailed investigations of these particles or residues might give further information on the residues located on the side of the SiN membrane facing the organic electrolyte solution during electrochemical silica deposition. Therefore, a TEM lamella was prepared by FIB milling and the elemental composition of the residue within the nanopore was investigated. In Figure 79, SE images of a nanopore (A), the cross-section of a nanopore (B) and the preparation of a TEM lamella (C) of the nanoporous array without

silica formation is shown. The EDX spectra of two regions within the nanopore, located in a TEM lamella thinner than the actual pore diameter (STEM image in D), are compared showing a clear difference between the region of a bright particle and the residue surrounding this particle. The bright particle consists of Si as marked in blue in the EDX spectra, whereas the other residue shows almost no Si signal (marked in yellow). The Cu signal in both EDX spectra is associated with the copper TEM grid. No silica is formed at the nanopore shown in Figure 79 according to insufficient pH value.

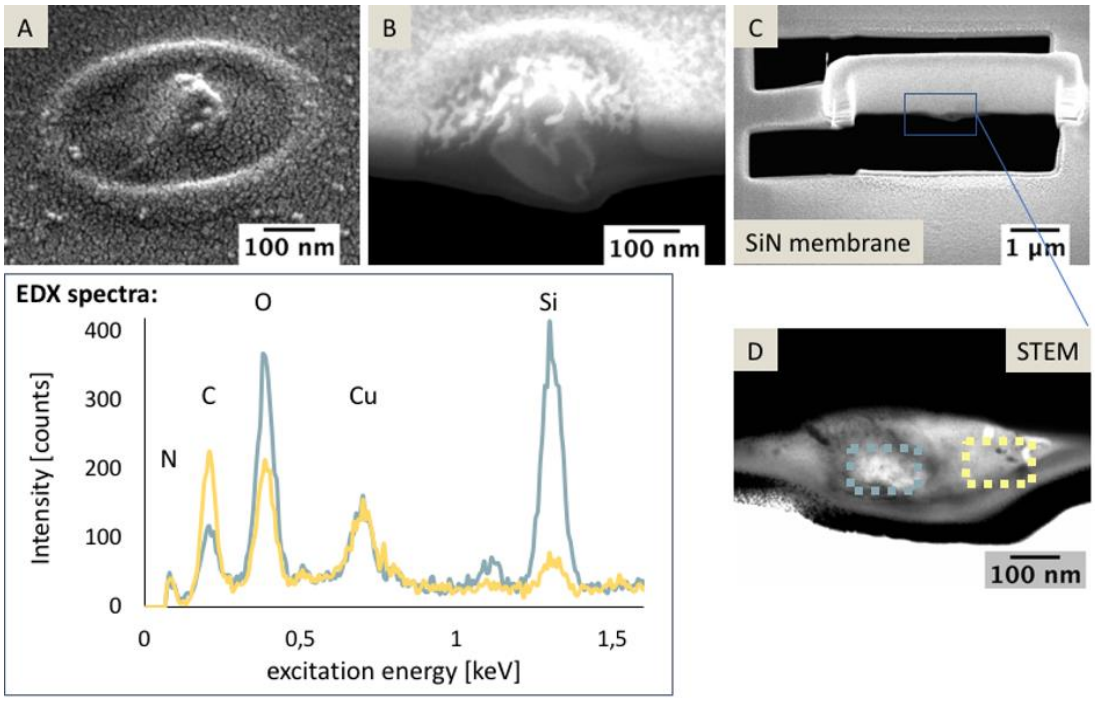

Figure 79 SE images of nanopores after electrochemical investigations with no silica deposits due to pH 3 insufficient for the silica formation at the ITIES (A - C). SE image after cross-sectioning of a nanopore filled with a bright particle (B) and SE image during the preparation of a TEM lamella by FIB milling with additional Pt/C as a protection layer (C) and STEM image of a TEM lamella (D). EDX spectra represent the marked regions in (D) in corresponding colors. SEM (A-C): 5 kV/ 86 pA, 38° tilted, STEM (D): 30 kV. A. Holzinger, G. Neusser, B. J. J. Austen, A. Gamero-Quijano, G. Herzog, D. W. M. Arrigan, A. Ziegler, P. Walther, and C. Kranz, *Faraday Discuss.*, 2018, **210**, 113. *Reproduced from Ref.* [187]*. Distributed under the license Creative Commons Attribution-NonCommercial 3.0 Unported (CC-BY-NC 3.0),* https://creativecommons.org/licenses/by-nc/3.0/.

The observed particulate material within the nanopore might be the result of a pre-concentration of non-condensed $Si(OH)_4$ of the aqueous phase during removal of the electrolyte solutions while cleaning the sample. Because Si is just located in the aqueous phase, this silica-rich particle in the nanopore was either due to the presence of the aqueous phase within the nanopore during ITIES investigations or had to be moved into the nanopore during cleaning and drying steps. Both effects may be also associated with the results obtained at nanoporous arrays under electrochemical conditions sufficient for silica formation. In Figure 80, different cross-sections of silica deposits either formed at small nanopores with pore diameters of 72 nm ± 12 nm (N=3) (A, B) and for large with nanopore diameters of 322 nm ± 84 nm (C). In all SE images shown in Figure 80, there are particles located in the residue at the side of the membrane facing the organic electrolyte solution during ITIES measurements. In case of a large pore as shown in C, these particles may have been moved to this side of the membrane due to cleaning and drying steps, whereas for the examples shown in A and B for small nanopores, the dimensions of the particles are too large to be accidentally moved to this side of the SiN membrane.

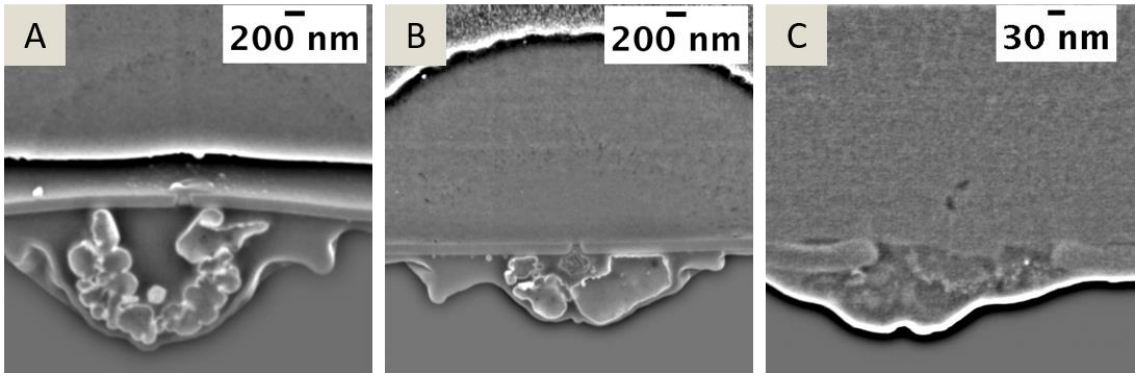

Figure 80 Differences in the residue: silica formation at nanoporous arrays with small nanopores (72 nm ± 12 nm, A, B) with particles within the residue for large (A) and small (B) silica deposits, compared to silica formation and the characteristic residue at the organic electrolyte facing side of the membrane at nanopores with large pore diameters (322 nm ± 84 nm, C). SEM: 5 kV / 86 pA, 38° tilted view. A. Holzinger, G. Neusser, B. J. J. Austen, A. Gamero-Quijano, G. Herzog, D. W. M. Arrigan, A. Ziegler, P. Walther, and C. Kranz, *Faraday Discuss.*, 2018, **210**, 113. *Reproduced from Ref.* [187]*. Distributed under the license Creative Commons Attribution-NonCommercial 3.0 Unported (CC-BY-NC 3.0),* https://creativecommons.org/licenses/by-nc/3.0/.

Therefore, it is most likely that these particles indicating the location of the aqueous phase and with this the interface between both electrolyte solutions. All SE images and EDX mappings shown within this section reveal that these particles visible within single nanopores or in the residue at the side of the SiN membrane, which face the organic phase contained Si-related species. At this point, it is not possible to distinguish between silica or TEOS. Based on the results shown in Figure 80, it is highly unlikely that these large particles are part of the silica formed at the side of the membrane facing the aqueous electrolyte solution during deposition. Either these particles indicate the location of the aqueous phase during electrochemical silica deposition at the ITIES, or the residue represents some kind of mixed phase close to the nanopores. Indeed, ethanol is formed during the hydrolysis of TEOS to silica[283], which is soluble in the aqueous electrolyte solution, but also in DCE. Although ethanol was removed prior to electrochemical deposition at the ITIES, the residue may still be related to mixed layer when ethanol was not completely removed. It has been shown that the ion transfer at truncated pores is influenced by osmotic pressures or double layers within the nanopores, even for miscible solutions. This leads to an ion current rectification with the electroosmotic flow depending on the ion flow direction within the truncated cone-shaped geometry[284]. This might also be a reason for some kind of mixed phase forming the observed residue. Hence, the observed particles may be the result of a combination of the discussed effects.

6.4 Conclusion and outlook

The advantages of FIB milling for prototyping nanoporous arrays within SiN membranes were shown in detail as already reported in previous publications[30,31,97]. The importance of the pore-to-pore separation with respect to the current response for nanoporous arrays at the liquid/liquid interface could be visualized by AFM-SECM. Additionally, the position of the liquid/liquid interface within the nanopores plays a crucial role in the application of such nanosized interfaces in electroanalysis, which was investigated by the transport of $TPrA^+$ between both electrolyte solutions and by electrochemical silica formation directly at the water/DCE interface. For the first time, 3D FIB/SEM investigations were used to visualize the silica formation in detail, enabling a close look into the nanopores and into the silica deposition at the side of the SiN membrane facing

the aqueous electrolyte solution during electrochemical deposition. Additionally, some kind of residue was observed at the side facing the organic electrolyte solution, which was characterized by SEM and by EDX measurements performed at TEM lamellas. The results obtained here indicate that the nanopores are filled with the aqueous phase, whereas additional cleaning or heating procedures during sample preparation might change the actual situation/location during electrochemical ITIES measurements dramatically. Equally reasonable and conceivable explanations would be some kind of mixed phase within the nanopores, which changes during the electrochemical investigation at the ITIES and results in a mixed, diffuse residue in close proximity to the nanopores. Hence, the assumption that the interface is located inlaid towards the aqueous electrolyte solution and that the nanopores are filled with the organic electrolyte solution as reported previously[31,267], might be doubted in case of FIB-milled arrays based on the studies presented here. The direct characterization of ITIES within nanoporous membranes is still challenging, and the approach presented here is highly interesting according to the obtained results. In future studies, different analytes should be investigated by FIB/SEM tomography, forming a solid phase directly at the interface between two liquids and showing a sufficient contrast in SE images, such as metal ions or conductive materials. To prevent changes of the deposition due to additional cleaning and drying steps and to avoid artifacts due to the removal of the electrolyte solutions, cryogenic FIB/SEM tomography might be a valuable approach for the investigations of the interface between two liquids[285].

VII. Final remarks

In this thesis, the modification of AFM tip-integrated electrodes is presented evaluating the suitability of integrated electrochemical sensors for localized detection of H_2O_2 release (see chapter 4) or pH changes (see chapter 5) in close proximity to a sample surface. The results presented within this thesis are facing the essential challenges of integrated miniaturized sensors. The fabrication of AFM-SECM probes involves several additional steps before being used in an AFM-SECM measurement, namely FIB/SEM (vacuum conditions) to expose the electrode area, to reshape a sharp AFM tip and to image the modifications, or heating and UV light exposure during mounting of AFM-SECM probes and insulation of the electrical contact. These additional treatments might change or influence the performance of integrated sensors. In the case of PB/NiHCF as H_2O_2-active material, these additional influences were investigated showing improved stability of the sensing layers in consecutive H_2O_2 calibrations (see 4.3.1).

For AFM-SECM investigations, it is essential to use electrodes with fast response times in order to observe local changes in the electrochemical signal during scans of the sample surface. The H_2O_2 sensors, as well as the pH sensors integrated into AFM-SECM probes, have been tested towards their stability in long-term measurements showing stable behavior in external calibrations. For PB/NiHCF-modified sensors, a change in morphology was detected by consecutive SEM imaging of modified UMEs after being exposed to H_2O_2 (Figure 20), by AFM in the presence of relatively high H_2O_2 concentrations of 1 mM (Figure 21), and by AFM-SECM generating H_2O_2 at the AFM tip-integrated microelectrode (Figure 19). These morphology changes might result in some kind of distortion of the detected signals, either by a change of the detected current correlated to the reduced amount of H_2O_2-sensitive PB material or by AFM tip artifacts due to the dissolution of the sensor material during scanning. Although, changes of electrochemically deposited PB/NiHCF can be investigated by SEM prior and after AFM/SECM measurements, changes occurring during ongoing measurements may remain undetected but might play a crucial limitation of these integrated H_2O_2 sensors. In section 4.3.2, modifications of AFM tip-integrated microelectrodes with optimized deposition parameters for localized deposition using

diluted solutions were presented, which showed, however, a poor reproducibility in several consecutive calibrations. No clear correlation between the amount of PB as indicated by the redox signal of PB in the film activation via CV in HCl/KCl and the sensitivity in H_2O_2 detection could be drawn. This might be also related to the separation of parts of the PB/NiHCF film resulting in a reduced amount of active PB actually in contact with the underlying microelectrode and, thus, being detected in electrochemical measurements. Especially for PB/NiHCF-modified sensors, the modification of an AFM tip-integrated electrode is challenging because the exact composition of these mixed layers is unknown. The EDX mapping presented in Figure 18 indicates a homogeneous distribution of PB and NiHCF, though, a laterally resolved determination of the distribution between both salts is difficult due to the given resolution of the method and the penetration depth of the acceleration e-beam, which is larger than the actual thickness of the bilayers. The dissolution of the PB/NiHCF bilayers deposited on UMEs, detected either by AFM or by consecutive SEM imaging, showed individual regions of the material being predominantly removed under H_2O_2 exposure. This indicates a variation in the local composition of these mixed layers. A detailed investigation of the mixed PB/NiHCF layers with respect to the composition of the material seems to be essential for these miniaturized H_2O_2 sensors, enabling a targeted optimization of deposition parameters for the modification of AFM-SECM probes.

For the results presented in chapter 5, just a limited number of AFM-SECM probes with integrated Sb or Ir metal layer suitable for imaging experiments have been available as these probes have been fabricated by former co-workers of Kranz and Mizaikoff. The presented investigations are focused on the evaluation of the most suitable material for AFM tip-integrated pH sensors facilitating future optimization of the fabrication procedure of these pH sensors. Thereby, Sb/SbO_2, AIROF, and EIROF-modified AFM-SECM probes were investigated in terms of pH sensitivity and stability. Although the number of available sensors was limited, the presented results reveal trends about the most promising material for modification of AFM-SECM probes. For all investigated materials, a broad distribution in pH sensitivity was detected ranging from 37 to 91 mV/pH for EIROF (see 5.3.3), 31 to 54 mV/pH detected in consecutive calibrations of one individual AIROF-modified AFM-SECM probe (see Figure 44), and 50 and 56 mV/pH for two investigated

AFM tip-integrated Sb/SbO_2 sensors (see Figure 46). A significant advantage of AIROF electrodes in comparison to Sb is the possibility of regeneration of the sensor by anodic oxidation in H_2SO_4. In first AFM-SECM investigations with tip-integrated pH sensors, the dissolution of calcite crystals was mapped resulting in a changed morphology of the crystals with adjoining changes in pH to more alkaline pH values. However, all investigations presented in section 5.3.2 were lacking a lateral resolution for the detected OCP signal of the Sb/SbO_2 or AIROF sensors in x-direction, but a good resolution in the scan direction (y-direction), which is also comparable to results detected by SECM-SICM[253]. Changes in the OCP signal during measurement could be correlated to the location of the actual calcite crystal but lacking sufficient lateral resolution. Therefore, further investigations should focus on optimization of response times of AFM tip-integrated pH sensors.

In chapter 6, arrays of nanopores fabricated by FIB milling in solid-state SiN membranes were presented and investigated in terms of diffusion behavior and location of the interface of two immiscible solutions within nanopores. AFM-SECM measurements revealed the change in diffusional profiles with respect to the pore-to-pore separation of individual pores in an array and showed an overlapped diffusion for closely spaced pores and individual diffusion for pores being separated by a ratio of $r_c/r_a = 91$ (see equation (29)). Further investigations of the potential-driven ion transport of $TPrA^+$ at ITIES and localized deposition of silica particles at the ITES within nanoporous arrays, addresses the question of the location of the interface. In previous publications, it was postulated that the nanopores are filled with the organic electrolyte solution, which is the case for nanoporous arrays fabricated by e-beam lithography. The assumption that FIB-milled nanoporous arrays show the same behavior may be questionable due to the known implantation of positively charged Ga ions and a conical-shaped geometry of the nanopores. Further investigations were presented in chapter 6 and FIB/SEM tomography, used for the first time for the investigation of micro- and nanointerfaces located in solid-state materials, is presented in section 6.3.3 and 6.3.4. The nanopores investigated throughout this thesis are most likely filled with the aqueous phase forming some kind of mixed phase within the nanopores during the presented electrochemical silica deposition at the nanoITIES. It should be noted that the presented results obtained for the localized

silica deposition at the interface between two immiscible liquids requires post-treatments, namely rinsing and drying, prior to being investigated by 3D FIB/SEM, which may influence the location of the interface. To circumvent this, investigations of the liquid/liquid interface could be performed under cryogenic conditions. Cryo-FIB/SEM tomography offers a new perspective on nanoporous materials visualizing interfaces or the composition of mixed electrolyte solutions within nanopores and, thus, enabling further optimization and understanding of such devices.

VIII. References

1. Galler, K., Bräutigam, K., Große, C., Popp, J. & Neugebauer, U. Making a big thing of a small cell-recent advances in single cell analysis. *Analyst* **139,** 1237–1273 (2014).

2. Sarvghad-Moghaddam, M., Parvizi, R., Davoodi, A., Haddad-Sabzevar, M. & Imani, A. Establishing a correlation between interfacial microstructures and corrosion initiation sites in Al / Cu joints by SEM – EDS and AFM – SKPFM. *Corros. Sci.* **79,** 148–158 (2014).

3. Phelan, R., Holmes, J. D. & Petkov, N. Application of serial sectioning FIB/SEM tomography in the comprehensive analysis of arrays of metal nanotubes. *J. Microsc.* **246,** 33–42 (2012).

4. Deshpande, A. & LeRoy, B. J. Scanning probe microscopy of graphene. *Phys. E* **44,** 743–759 (2012).

5. Soliman, M., Ding, Y. & Tetard, L. Nanoscale subsurface imaging. *J. Phys. Condens. Matter* **29,** 173001–24pp (2017).

6. Kang, M., Momotenko, D., Page, A., Perry, D. & Unwin, P. R. Frontiers in nanoscale electrochemical imaging: faster, multifunctional, and ultrasensitive. *Langmuir* **32,** 7993–8008 (2016).

7. Amemiya, S., Wang, Y. & Mirkin, M. V. in *Electrochemistry* **12,** 1–43 (The Royal Society of Chemistry, 2013).

8. Kueng, A., Kranz, C. & Mizaikoff, B. Scanning probe microscopy with integrated biosensors. *Sens. Lett.* **1,** 2–15 (2003).

9. Eifert, A. & Kranz, C. Hyphenating atomic force microscopy. *Anal. Chem.* **86,** 5190–5200 (2014).

10. Peddie, C. J. & Collinson, L. M. Exploring the third dimension: Volume electron microscopy comes of age. *Micron* **61,** 9–19 (2014).

11. Dryfe, R. A. W. in *Advances in Chemical Physics* (ed. Rice, S. A.) **141,** 153–215 (John Wiley & Sons, Inc., 2009).

12. Neusser, G. *et al.* FIB and MIP: understanding nanoscale porosity in molecularly imprinted polymers via 3D FIB/SEM tomography. *Nanoscale* **9,** 14327–14334 (2017).

13. Vierrath, S. *et al.* Enhancing the quality of the tomography of nanoporous materials for better understanding of polymer electrolyte fuel cell materials. *J. Power Sources* **285,** 413–417 (2015).

14. Wollschläger, N. *et al.* Characterization of the inner structure of porous TiO2 nanoparticle films in dye sensitive solar cells (DSSC) by focused ion beam (FIB) tomography and transmission Kikuchi diffraction (TKD) in the scanning electron microscope (SEM). *Mater. Charact.* **131,** 39–48 (2017).

15. Villinger, C., Neusser, G., Kranz, C., Walther, P. & Mertens, T. 3D analysis of HCMV induced-nuclear membrane structures by FIB/SEM tomography: Insight into an unprecedented membrane morphology. *Viruses* **7,** 5686–5704 (2015).

16. de Winter, D. A. *et al.* Tomography of insulating biological and geological materials using focused ion beam (FIB) sectioning and low kV BSE imaging. *J. Microsc.* **233,** 372–383 (2009).

17. Hickling, A. & Wilson, W. H. The anodic decomposition of hydrogen peroxide. *J. Electrochem. Soc.* **98,** 425–433 (1951).

18. Itaya, K., Shoji, N. & Uchida, I. Catalysis of the reduction of molecular oxygen to water at Prussian blue modified electrodes. *J. Am. Chem. Soc.* **106,** 3423–3429 (1984).

19. Karyakin, A. A. Prussian blue and its analogues: Electrochemistry and analytical applications. *Electroanalysis* **13,** 813–819 (2001).

20. Komkova, M. A. *et al.* Ultramicrosensors based on transition metal hexacyanoferrates for scanning electrochemical microscopy. *Beilstein J. Nanotechnol.* **4,** 649–654 (2013).

21. Ng, S. R. & O'Hare, D. An iridium oxide microelectrode for monitoring acute local pH changes of endothelial cells. *Analyst* **140,** 4224–4231 (2015).

22. Izquierdo, J. *et al.* Spatially resolved measurement of electrochemical activity and pH distributions in corrosion processes by scanning electrochemical microscopy using antimony microelectrode tips. *Electrochim. Acta* **56,** 8846–8850 (2011).

23. Roberts, E. J. & Fenwick, F. The Antimony-antimony trioxide electrode and its use as a measure of acidity. *J. Am. Chem. Soc.* **50,** 2125–2147 (1928).

24. Pitman, A. L., Pourbaix, M. & de Zoubov, N. Potential-pH diagram of the antimony-water system. *J. Electrochem. Soc.* **104,** 594–600 (1957).

25. Gottesfeld, S., McIntyre, J. D. E., Beni, G. & Shay, J. L. Electrochromism in anodic iridium oxide films. *Appl. Phys. Lett.* **33,** 208–210 (1978).

26. Gottesfeld, S. & McIntyre, J. D. E. Electrochromism in anodic iridium oxide films. *J Electrochem Soc Electrochem. Sci. Technol.* **126,** 742–750 (1979).

27. Steegstra, P. & Ahlberg, E. Influence of oxidation state on the pH dependence of hydrous iridium oxide films. *Electrochim. Acta* **76,** 26–33 (2012).

28. Renard, F. *et al.* Interactions of arsenic with calcite surfaces revealed by in situ nanoscale imaging. *Geochim. Cosmochim. Acta* **159,** 61–79 (2015).

29. Kaufmann, G. & Dreybrodt, W. Calcite dissolution kinetics in the system CaCO3 – H2O – CO2 at high undersaturation. *Geochim. Cosmochim. Acta* **71,** 1398–1410 (2007).

30. Liu, Y., Sairi, M., Neusser, G., Kranz, C. & Arrigan, D. W. M. Achievement of diffusional independence at nanoscale liquid−liquid interfaces within arrays. *Anal. Chem.* **87,** 5486–5490 (2015).

31. Sairi, M., Chen-Tan, N., Neusser, G., Kranz, C. & Arrigan, D. W. M. Electrochemical characterisation of nanoscale liquid/liquid interfaces located at focused ion beam-milled silicon nitride membranes. *ChemElectroChem* **2,** 98–105 (2015).

32. Li, J. *et al.* Ion-beam sculpting at nanometre length scales. *Nature* **412,** 166–169 (2001).

33. Yang, J. *et al.* Rapid and precise scanning helium ion microscope milling of solid-state nanopores for biomolecule detection. *Nanotechnology* **22,** 1–6 (2011).

34. Kuan, A. T. & Golovchenko, J. A. Nanometer-thin solid-state nanopores by cold ion beam sculpting. *Appl. Phys. Lett.* **100,** 1–4 (2012).

35. Hofmann, F. *et al.* 3D lattice distortions and defect structures in ion-implanted nano-crystals. *Sci. Rep.* **7,** 1–10 (2017).

36. Liu, S., Yuzvinsky, T. D. & Schmidt, H. Effect of fabrication-dependent shape and composition of solid-state nanopores on single nanoparticle detection. *ACS Nano* **7,** 5621–5627 (2013).

37. Lanyon, Y. H. *et al.* Fabrication of nanopore array electrodes by focused ion beam milling. *Anal. Chem.* **79,** 3048–3055 (2007).

38. J. Bard, A. & R. Faulkner, L. *Electrochemical methods : fundamentals and applications*. (John Wiley & Sons, Inc., 1980).

39. Hamann, C. H., Hamnett, A. & Vielstich, W. *Electrochemistry*. (WILEY-VCH Verlag GmbH & Co. KGaA, 2007).

40. Ciobanu, M., Wilburn, J. P., Krim, M. L. & Cliffel, D. E. in *Handbook of Electrochemistry* (ed. Zoski, C. G.) 3–29 (Elsevier, 2007).

41. Amemiya, S. in *Handbook of Electrochemistry* (ed. Zoski, C. G.) 261–294 (Elsevier, 2007).

42. Bobacka, J., Ivaska, A. & Lewenstam, A. Potentiometric ion sensors. *Chem. Rev.* **108,** 329–351 (2008).

43. Bratov, A., Abramova, N. & Ipatov, A. Recent trends in potentiometric sensor arrays- a review. *Anal. Chim. Acta* **678,** 149–159 (2010).

44. Glab, S., Maj-Żurawska, M. & Hulanicki, A. in *Reference Module in Chemistry, Molecular Sciences and Chemical Engineering* (Elsevier Inc., 2013).

45. Glab, S., Hulanicki, A., Edwall, G. & Ingman, F. Metal-metal oxide and metal oxide electrodes as pH sensors. *Crit. Rev. Anal. Chem.* **21,** 29–47 (1989).

46. Gill, E., Arshak, K., Arshak, A. & Korostynska, O. Mixed metal oxide films as pH sensing materials. *Microsyst. Technol.* **14,** 499–507 (2008).

47. Slowinska, K. & Majda, M. Measurements of the capacitance and the response time of solid-state potentiometric sensors by an electrochemical time-of-flight method. *J Solid State Electrochem* **8,** 763–771 (2004).

48. Liu, C.-C., Bocchicchio, B. C., Overmyer, P. A. & Neuman, M. R. A palladium-palladium oxide miniature pH electrode. *Science* **207,** 188–189 (1980).

49. Kinoshita, K. & Madou, M. J. Electrochemical measurements on Pt, Ir, and Ti oxides as pH probes. *J. Electrochem. Soc. Electrochem. Sci. Technol.* **131,** 1089–1094 (1984).

50. Kinoshita, E., Ingman, F., Edwall, G., Thulin, S. & Glab, S. Polycrystalline and monocrystalline antimony, iridium and palladium as electrode material for pH-sensing electrodes. *Talanta* **33,** 125–134 (1986).

51. Edwall, G. Improved antimony-antimony (111) oxide pH electrodes. *Med. Biol. Eng. Comput.* **16,** 661–669 (1978).

52. Edwall, G. & Jöngren, P.-A. Evaluation of the influence of impurities on the oxygen sensitivity of monocrystalline antimony electrodes. *Electrochim. Acta* **25,** 1585–1590 (1980).

53. Wang, M., Yao, S. & Madou, M. A long-term stable iridium oxide pH electrode. *Sensors Actuators, B Chem.* **81,** 313–315 (2002).

54. Bishop, E. & Short, G. D. Some observations on the zero-current behaviour of antimony indicator electrodes. *Talanta* **11,** 393–403 (1964).

55. Fog, A. & Buck, R. P. Electronic semiconducting oxides as pH sensors. *Sensors and Actuators* **5,** 137–146 (1984).

56. Tarlov, M. J., Semancik, S. & Kreider, K. G. Mechanistic and response studies of iridium oxide pH sensors. *Sensors Actuators B. Chem.* **1,** 293–297 (1990).

57. Katsube, T., Lauks, I. & Zemel, J. N. pH-sensitive sputtered iridium oxide films. *Sensors and Actuators* **2,** 399–410 (1982).

58. Boodts, J. C. F. & Trasatti, S. Hydrogen evolution on iridium oxide cathodes. *J. Appl. Electrochem.* **19,** 255–262 (1989).

59. Pauporté, T., Andolfatto, F. & Durand, R. Some electrocatalytic properties of anodic iridium oxide nanoparticles in acidic solution. *Electrochim. Acta* **45,** 431–439 (1999).

60. Hitchman, M. L. & Ramanathan, S. Evaluation of iridium oxide electrodes formed by potential cycling as pH probes. *Analyst* **113,** 35–39 (1988).

61. Olthuis, W., Robben, M. A. M., Bergveld, P., Bos, M. & van der Linden, W. E. pH sensor properties of electrochemically grown iridium oxide. *Sensors Actuators B. Chem.* **2,** 247–256 (1990).

62. VanHoudt, P., Lewandowski, Z. & Little, B. Iridium oxide pH microelectrode. *Biotechnol. Bioeng.* **40,** 601–608 (1992).

63. Marzouk, S. A. M. Improved electrodeposited iridium oxide pH sensor fabricated on etched titanium substrates. *Anal. Chem.* **75,** 52–60 (2002).

64. Shoup, D. & Szabo, A. Chronoamperometric current at finite disk electrodes. *J Electroanal Chem* **140,** 237–245 (1982).

65. Zoski, C. G. Ultramicroelectrodes: design, fabrication, and characterization. *Electroanalysis* **14,** 1041–1051 (2002).

66. Zoski, C. G. & Mirkin, M. V. Steady-state limiting currents at finite conical microelectrodes. *Anal. Chem.* **74,** 1986–1992 (2002).

67. Mirkin, M. V & Bard, A. J. Multidimensional integral equations: a new approach solving microelectrode diffusion problems, Part 2: applications to microband electrodes and the scanning electrochemical microscope. *J Electroanal Chem* **323,** 29–51 (1992).

68. Peljo, P. & Girault, H. H. in *Encyclopedia of Analytical Chemistry* 1–28 (John Wiley & Sons, Ltd, 2012).

69. Samec, Z. Electrochemistry at the interface between two immiscible electrolyte solutions. *Pure Appl. Chem.* **76,** 2147–2180 (2004).

70. Verwey, E. J. W. & Niessen, K. F. XL. The electrical double layer at the interface of two liquids. *Philos. Mag. Ser. 7* **28,** 435–446 (1939).

71. Gavach, C., Seta, P. & D'Epenoux, B. The double layer and ion adsorption at the interface between two non miscible solutions. Part I. Interfacial tension measurements for the water-nitrobenzene tetraalkylammonium bromide systems. *J. Electroanal. Chem.* **83,** 225–235 (1977).

72. Kakiuchi, T. & Senda, M. Structure of the electrical double layer at the interface between nitrobenzene solution of tetrabutylammonium tetraphenylborate and aqueous solution of lithium chloride. *Bull Chem Soc Jpn* **56,** 1753–1760 (1983).

73. Samec, Z., Marecek, V. & Homolka, D. The double layer at the interface between two immiscible electrolyte solutions Part II. Structure of the water/nitrobenzene interface in

the presence of 1: 1 and 2:2 electrolytes. *J Electroanal Chem* **187,** 31–51 (1985).

74. Girault, H. in *Modern Aspects of Electrochemistry* (ed. Bockris, J. O.) 1–62 (Plenum Press, 1993).

75. Girault, H. H. J. & Schiffrin, D. J. Thermodynamics of a polarised interface between two immiscible electrolyte solutions. *J Electroanal Chem* **170,** 127–141 (1984).

76. Valent, O., Koryta, J. & Panoch, M. Voltammetric study of ion transfer across the water/o-nitrophenyloctyl ether interface. Part I. Reversible process. *J. Electroanal. Chem.* **226,** 21–25 (1987).

77. Schurhammer, R. & Wipff, G. About the TATB assumption: Effect of charge reversal on transfer of large spherical ions from aqueous to non-aqueous solvents and on their interfacial behaviour. *J. Mol. Struct. THEOCHEM* **500,** 139–155 (2000).

78. Shao, Y. & Mirkin, M. V. Fast kinetic measurements with nanometer-sized pipets. Transfer of potassium ion from water into dichloroethane facilitated by dibenzo-18-crown-6. *J. Am. Chem. Soc.* **119,** 8103–8104 (1997).

79. Rodgers, P. J., Amemiya, S., Wang, Y. & Mirkin, M. V. Nanopipet voltammetry of common ions across the liquid-liquid interface. Theory and limitations in kinetic analysis of nanoelectrode voltammograms. *Anal. Chem.* **82,** 84–90 (2010).

80. Campbell, J. A. & Girault, H. H. Steady state current for ion transfer reactions at a micro liquid/liquid interface. *J. Electroanal. Chem.* **266,** 465–469 (1989).

81. Stephenson, M. J., Holmes, S. M. & Dryfe, R. A. W. A novel approach to the elucidation of facilitated ion transfer mechanisms at the liquid/liquid interface. *Electrochem. Commun.* **6,** 294–298 (2004).

82. Dryfe, R. A. W. Modifying the liquid / liquid interface : pores, particles and deposition. *Phys. Chem. Chem. Phys.* **8,** 1869–1883 (2006).

83. Zazpe, R., Hibert, C., O'Brien, J., Lanyon, Y. H. & Arrigan, D. W. M. Ion-transfer voltammetry at silicon membrane-based arrays of micro-liquid–liquid interfaces. *Lab Chip* **7,** 1732–1737 (2007).

84. Alvarez De Eulate, E., Strutwolf, J. J., Liu, Y., O'Donnell, K. & Arrigan, D. W. M. An electrochemical sensing platform based on liquid-liquid microinterface arrays formed in laser-ablated glass membranes. *Anal. Chem.* **88,** 2596–2604 (2016).

85. Huang, X., Xie, L., Lin, X. & Su, B. Permselective ion transport across the nanoscopic liquid/liquid interface array. *Anal. Chem.* **88,** 6563–6569 (2016).

86. Platt, M., Dryfe, R. A. W. & Roberts, E. P. L. Electrodeposition of palladium nanoparticles at the liquid-liquid interface using porous alumina templates. *Electrochim. Acta* **48,** 3037–3046 (2003).

87. Tsionsky, M., Bard, A. J. & Mirkin, M. V. Long-range electron transfer through a lipid monolayer at the liquid/liquid interface. *J. Am. Chem. Soc.* **119,** 10785–10792 (1997).

88. Liu, B. & Mirkin, M. V. Electrochemistry at microscopic liquid-liquid interfaces. *Electroanalysis* **12,** 1433–1446 (2000).

89. Beattie, P. D., Delay, A. & Girault, H. H. Investigation of the kinetics of assisted potassium ion transfer by dibenzo-18-crown-6 at the micro-ITIES by means of steady-state voltammetry. *J. Electroanal. Chem.* **380,** 167–175 (1995).

90. Beattie, P. D., Delay, A. & Girault, H. H. Investigation of the kinetics of ion and assisted ion transfer by the technique of AC impedance of the micro-ITIES. *Electrochim. Acta* **40,** 2961–2969 (1995).

91. Solomon, T. & Bard, A. J. Scanning electrochemical microscopy. 30. application of glass micropipet tips and electron transfer at the interface between two immiscible electrolyte solutions for SECM imaging. *Anal. Chem.* **67,** 2787–2790 (1995).

92. Molina, A., Laborda, E. & Compton, R. G. Cyclic and square-wave voltammetry at diffusionally asymmetric microscopic and nanoscopic liquid−liquid interfaces: a simple theoretical approach. *J. Phys. Chem. C* **118,** 18249–18256 (2014).

93. Braga, C., Galindo, A. & Müller, E. A. Nonequilibrium molecular dynamics simulation of diffusion at the liquid-liquid interface. *J. Chem. Phys.* **141,** 1–9 (2014).

94. Bond, A. M., Luscombe, D., Oldham, K. D. & Zoski, C. G. a comparison of the chronoamperometric response at inlaid and recessed disc microelectrodes. *J Electroanal Chem* **249,** 1–14 (1988).

95. Josserand, J., Morandini, J., Lee, H. J., Ferrigno, R. & Girault, H. H. Finite element simulation of ion transfer reactions at a single micro-liquid|liquid interface supported on a thin polymer film. *J. Electroanal. Chem.* **468,** 42–52 (1999).

96. Ellis, J. S., Strutwolf, J. & Arrigan, D. W. M. Finite-element simulations of the influence of pore wall adsorption on cyclic voltammetry of ion transfer across a liquid–liquid interface formed at a micropore. *Phys. Chem. Chem. Phys.* **14,** 2494–2500 (2012).

97. Liu, Y., Strutwolf, J. & Arrigan, D. W. M. Ion-transfer voltammetric behavior of propranolol at nanoscale liquid−liquid interface arrays. *Anal. Chem.* **87,** 4487–4494 (2015).

98. Scanlon, M. D. *et al.* Ion-transfer electrochemistry at arrays of nanointerfaces between immiscible electrolyte solutions confined within silicon nitride nanopore. *Anal. Chem.* **82,** 6115–6123 (2010).

99. Kralj, B. & Dryfe, R. A. W. Membrane voltammetry: The interface between two immiscible electrolyte solutions. *Phys. Chem. Chem. Phys.* **3,** 5274–5282 (2001).

100. Gadaleta, A. *et al.* Sub-additive ionic transport across arrays of solid-state nanopores. *Phys. Fluids* **26,** 1–11 (2014).

101. Binnig, G., Quate, C. F. & Gerber, C. Atomic force microscope. *Phys. Rev. Lett.* **56,** 930–933 (1986).

102. Müller, D. J. & Dufrêne, Y. F. Atomic force microscopy as a multifunctional molecular toolbox in nanobiotechnology. *Nat. Nanotechnol.* **3,** 261–269 (2008).

103. Dai, H., Hafner, J. H., Rinzler, A. G., Colbert, D. T. & Smalley, R. E. Nanotubes as nanoprobes in scanning probe microscopy. *Nature* **384,** 147–150 (1996).

104. Ma, X. *et al.* Sharp-tip silver nanowires mounted on cantilevers for high-aspect-ratio high-resolution imaging. *Nano Lett.* **16,** 6896–6902 (2016).

105. Kato, N., Kawashima, T., Shibata, T., Mineta, T. & Makino, E. Micromachining of a newly designed AFM probe integrated with hollow microneedle for cellular function analysis. *Microelectron. Eng.* **87,** 1185–1189 (2010).

106. Ducker, W. a., Senden, T. J. & Pashley, R. M. Direct measurement of colloidal forces using an atomic force microscope. *Nature* **353,** 239–241 (1991).

107. Weymouth, A. J., Hofmann, T. & Giessibl, F. J. Quantifying molecular stiffness and interaction with lateral force microscopy. *Science* **343,** 1120–1122 (2014).

108. Pérez, R., García, R., Pe, Â., Garcõ, R. & García, R. Dynamic atomic force microscopy methods. *Surf. Sci. Rep.* **47,** 197–301 (2002).

109. Zhong, Q., Inniss, D., Kjoller, K. & Elings, V. B. Fractured polymer/silica fiber surface studied by tapping mode atomic force microscopy. *Surf. Sci. Lett.* **290,** L688–L692 (1993).

110. Gross, L. *et al.* Atomic force microscopy for molecular structure elucidation. *Angew. Chemie - Int. Ed.* **57,** 3888–3908 (2018).

111. Minne, S. C., Hu, Y., Hu, S., Pittenger, B. & Su, C. Nanoscale quantitative mechanical property mapping using peak force tapping atomic force microscopy. *Microsc. Microanal.* **16,** 464–465 (2010).

112. Radmacher, M., Cleveland, J. P., Fritz, M., Hansma, H. G. & Hansma, P. K. Mapping interaction forces with the atomic force microscope. *Biophys. J.* **66,** 2159–2165 (1994).

113. Nonnenmacher, M., O'Boyle, M. P. & Wickramasinghe, H. K. Kelvin probe force microscopy. *Appl. Phys. Lett.* **58,** 2921–2923 (1991).

114. Bard, A. J., Fan, F. F., Kwak, J. & Lev, O. Scanning electrochemical microscopy. Introduction and principles. *Anal. Chem.* **61,** 132–138 (1989).

115. Holzinger, A., Steinbach, C. & Kranz, C. in *Electrochemical Strategies in Detection Science* (ed. Arrigan, D. W. M.) 125–169 (2016).

116. Luo, H. *et al.* Sensing application in the precursor region of localized corrosion by scanning electrochemical microscopy. *RSC Adv.* **4,** 56582–56595 (2014).

117. Bard, A. & Mirkin, M. *Scanning electrochemical microscopy*. (CRC Press, 2012).

118. Ludwig, M., Kranz, C., Schuhmann, W. & Gaub, H. E. Topography microscope feedback mechanism for the scanning electrochemical based on hydrodynamic forces between tip and sample. *Rev. Sci. Instrum.* **66,** 2857–2860 (1995).

119. Ballesteros Katemann, B., Schulte, A. & Schuhmann, W. Constant-distance mode scanning electrochemical microscopy (SECM)-Part I: Adaptation of a non-optical shear-force-based positioning mode for SECM tips. *Chem Eur J* **9,** 2025–2033 (2003).

120. James, P. I., Garfias-Mesias, L. F., Moyer, P. J. & Smyrl, W. H. Scanning electrochemical microscopy with simultaneous independent topography. *J Electrochem Soc* **145,** L64–L66 (1998).

121. Wipf, D. O., Bard, A. J. & Tallman, D. E. Scanning electrochemical microscopy. 21. constant-current imaging with an autoswitching controller. *Anal. Chem.* **65,** 1373–1377 (1993).

122. Alpuche-Aviles, M. A. & Wipf, D. O. Impedance feedback control for scanning electrochemical microscopy. *Anal. Chem.* **73,** 4873–4881 (2001).

123. Cortes-Salazar, F. *et al.* Soft stylus probes for scanning electrochemical microscopy. *Anal. Chem.* **81,** 6889–6896 (2009).

124. Lee, C., Kwak, J. & Anson, F. C. Application of scanning electrochemical microscopy to generation/collection experiments with high collection efficiency. *Anal. Chem.* **63,** 1501–1504 (1991).

125. Eckhard, K., Chen, X., Turcu, F. & Schuhmann, W. Redox competition mode of scanning

electrochemical microscopy (RC-SECM) for visualisation of local catalytic activity. *Phys. Chem. Chem. Phys.* **8,** 5359 (2006).

126. Kranz, C., Ludwig, M. M., Gaub, H. E. & Schuhmann, W. Lateral deposition of polypyrrole lines by means of the scanning electrochemical microscope. *Adv. Mater.* **7,** 38–40 (1995).

127. Eckhard, K., Etienne, M., Schulte, A. & Schuhmann, W. Constant-distance mode AC-SECM for the visualisation of corrosion pits. *Electrochem. Commun.* **9,** 1793–1797 (2007).

128. Lee, Y., Ding, Z. & Bard, A. J. Combined scanning electrochemical/optical microscopy with shear force and current feedback. *Anal. Chem.* **74,** 3634–43 (2002).

129. Wang, L., Kowalik, J., Mizaikoff, B. & Kranz, C. Combining scanning electrochemical microscopy with infrared attenuated total reflection spectroscopy for in situ studies of electrochemically induced processes. *Anal. Chem.* **82,** 3139–3145 (2010).

130. Szunerits, S., Knorr, N., Calemczuk, R. & Livache, T. New approach to writing and simultaneous reading of micropatterns: combining surface plasmon resonance imaging with scanning electrochemical microscopy (SECM). *Langmuir:* **20,** 9236–41 (2004).

131. Hansma, P. K., Drake, B., Marti, O., Gould, S. a & Prater, C. B. The scanning ion-conductance microscope. *Science* **243,** 641–643 (1989).

132. Macpherson, J. V. & Unwin, P. R. Combined scanning electrochemical-atomic force microscopy. *Anal. Chem.* **72,** 276–285 (2000).

133. Kranz, C. *et al.* Integrating an ultramicroelectrode in an AFM cantilever: combined technology for enhanced information. *Anal. Chem.* **73,** 2491–500 (2001).

134. Kueng, A., Kranz, C., Lugstein, A., Bertagnolli, E. & Mizaikoff, B. Integrated AFM-SECM in tapping mode: simultaneous topographical and electrochemical imaging of enzyme activity. *Angew. Chem. Int. Ed. Engl.* **42,** 3238–40 (2003).

135. Kranz, C., Kueng, A., Lugstein, A., Bertagnolli, E. & Mizaikoff, B. Mapping of enzyme activity by detection of enzymatic products during AFM imaging with integrated SECM–AFM probes. *Ultramicroscopy* **100,** 127–134 (2004).

136. Anne, A., Demaille, C. & Goyer, C. Electrochemical atomic-force microscopy using a tip-attached redox mediator. Proof-of-concept and perspectives for functional probing of nanosystems. *ACS Nano* **3,** 819–827 (2009).

137. Wang, K., Goyer, C., Anne, A. & Demaille, C. Exploring the motional dynamics of end-grafted DNA oligonucleotides by in situ electrochemical atomic force microscopy. *J. Phys. Chem. B* **111,** 6051–8 (2007).

138. Anne, A., Chovin, A., Demaille, C. & Lafouresse, M. High-resolution mapping of redox-immunomarked proteins using electrochemical-atomic force microscopy in molecule touching mode. *Anal. Chem.* **83,** 7924–32 (2011).

139. dos Santos Riccardi, C. *et al.* Label-free DNA detection of hepatitis C virus based on modified conducting polypyrrole films at microelectrodes and atomic force microscopy tip-integrated electrodes. *Anal. Chem.* **80,** 237–45 (2008).

140. Hirata, Y., Yabuki, S. & Mizutani, F. Application of integrated SECM ultra-micro-electrode and AFM force probe to biosensor surfaces. *Bioelectrochemistry* **63,** 217–24 (2004).

141. Kueng, A., Kranz, C., Lugstein, A., Bertagnolli, E. & Mizaikoff, B. AFM-tip-integrated amperometric microbiosensors: high-resolution imaging of membrane transport. *Angew.*

Chem. Int. Ed. Engl. **44,** 3419–22 (2005).

142. Gueneau de Mussy, J.-P., Macpherson, J. V & Delplancke, J.-L. Characterisation and behaviour of Ti/TiO2/noble metal anodes. *Electrochim. Acta* **48,** 1131–1141 (2003).

143. Davoodi, A., Pan, J., Leygraf, C. & Norgren, S. Integrated AFM and SECM for in situ studies of localized corrosion of Al alloys. *Electrochim. Acta* **52,** 7697–7705 (2007).

144. Davoodi, A., Farzadi, A., Pan, J., Leygraf, C. & Zhu, Y. Developing an AFM-based SECM system; instrumental setup, SECM simulation, characterization, and calibration. *J. Electrochem. Soc.* **155,** C474–C485 (2008).

145. Davoodi, A., Pan, J., Leygraf, C. & Norgren, S. Probing of local dissolution of Al-alloys in chloride solutions by AFM and SECM. *Appl. Surf. Sci.* **252,** 5499–5503 (2006).

146. Izquierdo, J., Fernández-Pérez, B. M., Eifert, A., Souto, R. M. & Kranz, C. Simultaneous atomic force - scanning electrochemical microscopy (AFM-SECM) imaging of copper dissolution. *Electrochim. Acta* **201,** 320–332 (2016).

147. Izquierdo, J., Eifert, A., Kranz, C. & Souto, R. M. In situ investigation of copper corrosion in acidic chloride solution using atomic force—scanning electrochemical microscopy. *Electrochim. Acta* **247,** 588–599 (2017).

148. Jones, C. E., Unwin, P. R. & Macpherson, J. V. In situ observation of the surface processes involved in dissolution from the cleavage surface of calcite in aqueous solution using combined scanning electrochemical-atomic force microscopy (SECM-AFM). *ChemPhysChem* **4,** 139–146 (2003).

149. Kueng, A., Kranz, C. & Mizaikoff, B. Imaging of ATP membrane transport with dual micro-disk electrodes and scanning electrochemical microscopy. *Biosens. Bioelectron.* **21,** 346–53 (2005).

150. Macpherson, J. V., Jones, C. E., Barker, A. L. & Unwin, P. R. Electrochemical imaging of diffusion through single nanoscale pores. *Anal. Chem.* **74,** 1841–1848 (2002).

151. Eckhard, K., Shin, H., Mizaikoff, B., Schuhmann, W. & Kranz, C. Alternating current (AC) impedance imaging with combined atomic force scanning electrochemical microscopy (AFM-SECM). *Electrochem. Commun.* **9,** 1311–1315 (2007).

152. Huang, K., Anne, A., Bahri, M. A. & Demaille, C. Probing individual redox PEGylated gold nanoparticles by electrochemical–atomic force microscopy. *ACS Nano* **7,** 4151–4163 (2013).

153. Dobson, P. S., Weaver, J. M. R., Holder, M. N., Unwin, P. R. & Macpherson, J. V. Characterization of batch-microfabricated scanning electrochemical-atomic force microscopy probes. *Anal. Chem.* **77,** 424–434 (2005).

154. Eifert, A. *et al.* Atomic force microscopy probes with integrated boron doped diamond electrodes: Fabrication and application. *Electrochem. Commun.* **25,** 30–34 (2012).

155. Gardner, C. E., Unwin, P. R. & Macpherson, J. V. Correlation of membrane structure and transport activity using combined scanning electrochemical–atomic force microscopy. *Electrochem. Commun.* **7,** 612–618 (2005).

156. Rodriguez, R. D., Anne, A., Cambril, E. & Demaille, C. Optimized hand fabricated AFM probes for simultaneous topographical and electrochemical tapping mode imaging. *Ultramicroscopy* **111,** 973–81 (2011).

157. Fasching, R. J., Tao, Y. & Prinz, F. B. Cantilever tip probe arrays for simultaneous SECM and AFM analysis. *Sensors Actuators B Chem.* **108,** 964–972 (2005).

158. Shin, H., Hesketh, P. J., Mizaikoff, B. & Kranz, C. Batch fabrication of atomic force microscopy probes with recessed integrated ring microelectrodes at a wafer level. *Anal. Chem.* **79,** 4769–4777 (2007).

159. Lee, E., Kim, M., Seong, J., Shin, H. & Lim, G. An L-shaped nanoprobe for scanning electrochemical microscopy-atomic force microscopy. *Phys Status Solidi RRL* **7,** 406–409 (2013).

160. Knittel, P., Higgins, M. J. & Kranz, C. Nanoscopic polypyrrole AFM–SECM probes enabling force measurements under potential control. *Nanoscale* **6,** 2255–2260 (2014).

161. Eifert, A., Mizaikoff, B. & Kranz, C. Advanced fabrication process for combined atomic force-scanning electrochemical microscopy (AFM-SECM) probes. *Micron* **68,** 27–35 (2015).

162. Lugstein, A., Bertagnolli, E., Kranz, C. & Mizaikoff, B. Fabrication of a ring nanoelectrode in an AFM tip: Novel approach towards simultaneous electrochemical and topographical imaging. *Surf. Interface Anal.* **33,** 146–150 (2002).

163. Knittel, P., Bibikova, O. & Kranz, C. Challenges in nanoelectrochemical and nanomechanical studies of individual anisotropic gold nanoparticles. *Faraday Discuss.* **193,** 353–369 (2016).

164. Burt, D. P., Wilson, N. R., Weaver, J. M. R., Dobson, P. S. & Macpherson, J. V. Nanowire probes for high resolution combined scanning electrochemical microscopy - atomic force microscopy. *Nano Lett.* **5,** 639–643 (2005).

165. Knittel, P., Zhang, H., Kranz, C., Wallace, G. G. & Higgins, M. J. Probing the PEDOT:PSS/cell interface with conductive colloidal probe AFM-SECM. *Nanoscale* **8,** 4475–4481 (2016).

166. Moon, J., Shin, H., Mizaikoff, B. & Kranz, C. Bitmap-assisted focused ion beam fabrication of combined atomic force scanning electrochemical microscopy probes. *Journal-Korean Phys. Soc.* **51,** 920 (2007).

167. Leonhardt, K. *et al.* Atomic force microscopy-scanning electrochemical microscopy: Influence of tip geometry and insulation defects on diffusion controlled currents at conical electrodes. *Anal. Chem.* **83,** 2971–2977 (2011).

168. Gullo, M. R. *et al.* Characterization of microfabricated probes for combined atomic force and high-resolution scanning electrochemical microscopy. *Anal. Chem.* **78,** 5436–5442 (2006).

169. Kottke, P. a. & Fedorov, A. G. Advective and transient effects in combined AFM/SECM operation. *J. Electroanal. Chem.* **583,** 221–231 (2005).

170. Ghorbal, A. *et al.* Localized electrografting of vinylic monomers on a conducting substrate by means of an integrated electrochemical AFM probe. *ChemPhysChem* **10,** 1053–1057 (2009).

171. Abbou, J., Anne, A. & Demaille, C. Probing the structure and dynamics of end-grafted flexible polymer chain layers by combined atomic force-electrochemical microscopy. Cyclic voltammetry within nanometer-thick macromolecular poly(ethylene glycol) layers. *J. Am. Chem. Soc.* **126,** 10095–10108 (2004).

172. Smirnov, W. *et al.* Diamond-modified AFM probes: from diamond nanowires to atomic force microscopy-integrated boron-doped diamond electrodes. *Anal. Chem.* **83,** 4936–4941 (2011).

173. Wiedemair, J., Moon, J. S., Eaton, D. E., Mizaikoff, B. & Kranz, C. Combined AFM-SECM: Towards a novel platform for imaging microbiosensors. *IFMBE Proc.* **25,** 372–375 (2009).

174. Wiedemair, J., Moon, J. S., Reinauer, F., Mizaikoff, B. & Kranz, C. Ion beam induced deposition of platinum carbon composite electrodes for combined atomic force microscopy-scanning electrochemical microscopy. *Electrochem. Commun.* **12,** 989–991 (2010).

175. Goldstein, J. I. *et al. Scanning electron microscopy and X-ray microanalysis*. (Kluwer Academic/Plenum Publisher, 2003).

176. Demers, H. *et al.* Three-dimensional electron microscopy simulation with the CASINO Monte Carlo software. *Scanning* **33,** 135–146 (2011).

177. Everhart, T. E. & Thornley, R. F. M. Wide-band detector for micro-microampere low-energy electron currents. *J. Sci. Instrum.* **37,** 246–248 (1960).

178. Randolph, S. J., Fowlkes, J. D. & Rack, P. D. Focused, nanoscale electron-beam-induced deposition and etching. *Crit. Rev. Solid State Mater. Sci.* **31,** 55–89 (2006).

179. Möllenstedt, G. & Speidel, R. Elektronenoptischer Mikroschreiber unter elektronenmikroskopischer Arbeitskontrolle. *Phys. Blätter* **16,** 192–198 (1960).

180. Yao, N. *Focused ion beam systems*. *Science And Technology* (Cambridge University Press, 2007).

181. Liu, Y. *et al.* Visualization of diffusion within nanoarrays. *Anal. Chem.* **88,** 6689–6695 (2016).

182. Sudraud, P. Focused-ion-beam milling, scanning-electron microscopy, and focused-droplet deposition in a single microcircuit surgery tool. *J. Vac. Sci. Technol. B Microelectron. Nanom. Struct.* **6,** 234 (1988).

183. Holzer, L., Indutnyi, F., Gasser, P., Münch, B. & Wegmann, M. Three-dimensional analysis of porous BaTiO3 ceramics using FIB nanotomography. *J. Microsc.* **216,** 84–95 (2004).

184. Cazaux, J. Recent developments and new strategies in scanning electron microscopy. *J. Microsc.* **217,** 16–35 (2005).

185. Wargo, E. A., Kotaka, T., Tabuchi, Y. & Kumbur, E. C. Comparison of focused ion beam versus nano-scale X-ray computed tomography for resolving 3-D microstructures of porous fuel cell materials. *J. Power Sources* **241,** 608–618 (2013).

186. Lasagni, F., Lasagni, A., Engstler, M., Degischer, H. P. & Mücklich, F. Nano-characterization of cast structures by FIB-tomography. *Adv. Eng. Mater.* **10,** 62–66 (2008).

187. Holzinger, A. *et al.* Investigation of modified nanopore arrays using FIB/SEM tomography. *Faraday Discuss.* **210,** 113–130 (2018).

188. Moon, J. S. Next generation of multifunctional scanning probes. (Georgia Institute of Technology, 2010). at <http://hdl.handle.net/1853/42935>

189. Dickinson, B. C. & Chang, C. J. Chemistry and biology of reactive oxygen species in signaling or stress responses. *Nat. Chem. Biol.* **7,** 504–511 (2011).

190. Yeager, E. Electrocatalysts for O2 reduction. *Electrochim. Acta* **29,** 1527–1537 (1984).

191. Fukuzumi, S. & Yamada, Y. Hydrogen peroxide used as a solar fuel in one-compartment fuel cells. *ChemElectroChem* **3,** 1978–1989 (2016).

192. Gunz, D. W. & Hoffmann, M. R. Atmospheric chemistry of peroxides: a review. *Atmos. Environ. Part A, Gen. Top.* **24,** 1601–1633 (1990).

193. Miller, W. L. & Kester, D. R. Hydrogen peroxide measurement in seawater by (p-hydroxyphenyl)acetic acid dimerization. *Anal. Chem.* **60,** 2711–2715 (1988).

194. Matsubara, C., Kawamoto, N. & Takamura, K. Oxo[5, 10, 15, 20-tetra(4-pyridyl)porphyrinato]titanium(IV): An ultra-high sensitivity spectrophotometric reagent for hydrogen peroxide. *Analyst* **117,** 1781–1784 (1992).

195. Chen, W., Cai, S., Ren, Q., Wen, W. & Zhao, Y.-D. Recent advances in electrochemical sensing for hydrogen peroxide: a review. *Analyst* **137,** 49–58 (2012).

196. Zheng, Y., Chen, W., Zuo, X. Q., Cai, J. & Chen, Y. X. The kinetics of the oxidation and reduction of H2O2 at a Pt electrode: A differential electrochemical mass spectrometric study. *Electrochem. Commun.* **73,** 38–41 (2016).

197. Wang, J. Electrochemical glucose biosensors. *Chem. Rev.* **108,** 814–825 (2008).

198. Caruana, D. J. & Heller, A. Enzyme-amplified amperometric detection of hybridization and of a single base pair mutation in an 18-base oligonucleotide on a 7-µm-diameter microelectrode. *J. Am. Chem. Soc.* **121,** 769–774 (1999).

199. You, J. M. *et al.* Reductive determination of hydrogen peroxide with MWCNTs-Pd nanoparticles on a modified glassy carbon electrode. *Biosens. Bioelectron.* **26,** 2287–2291 (2011).

200. He, J., Yang, X., Men, B. & Wang, D. Interfacial mechanisms of heterogeneous Fenton reactions catalyzed by iron-based materials: A review. *J. Environ. Sci. (China)* **39,** 97–109 (2016).

201. Keggin, J. F. & Miles, F. D. Structures and formulae of the Prussian Blues and related compounds. *Nature* **137,** 577–578 (1936).

202. Chen, J. *et al.* Prussian blue with intrinsic heme-like structure as peroxidase mimic. *Nano Res.* **11,** 4905–4913 (2018).

203. Karyakin, A. A., Gitelmacher, O. V. & Karyakina, E. E. A high-sensitive glucose amperometric biosensor based on Prussian blue modified electrodes. *Anal. Lett.* **27,** 2861–2869 (1994).

204. Sitnikova, N. A., Komkova, M. A., Khomyakova, I. V., Karyakina, E. E. & Karyakin, A. A. Transition metal hexacyanoferrates in electrocatalysis of H 2O2 reduction: An exclusive property of Prussian blue. *Anal. Chem.* **86,** 4131–4134 (2014).

205. Duncan, J. F. & Wigley, P. W. R. The electronic structure of the iron atoms in complex iron cyanides. *J. Chem. Soc.* **0,** 1120–1125 (1963).

206. Crumblis, A. L., Lug, P. S. & Morosoff, N. Alkali metal cation effects in a Prussian blue surface-modified electrode. *Inorg. Chem.* **23,** 4701–4708 (1984).

207. Zhang, D., Wang, K., Sun, D. C., Xia, X. H. & Chen, H. Y. Ultrathin layers of densely packed Prussian blue nanoclusters prepared from a ferricyanide solution. *Chem. Mater.* **15,** 4163–4165 (2003).

208. Wu, X., Jian, Z., Li, Z. & Ji, X. Prussian white analogues as promising cathode for non-aqueous potassium-ion batteries. *Electrochem. Commun.* **77,** 54–57 (2017).

209. Padigi, P. *et al.* Prussian green: A high rate capacity cathode for potassium ion batteries.

Electrochim. Acta **166,** 32–39 (2015).

210. Karyakin, A. A., Karyakina, E. E. & Gorton, L. Amperometric biosensor for glutamate using Prussian Blue-based 'artificial peroxidase' as a transducer for hydrogen peroxide. *Anal. Chem.* **72,** 1720–1723 (2000).

211. Neff, V. D. Electrochemical oxidation and reduction of thin films of Prussian Blue. *J. Electrochem. Soc.* **125,** 886 (1978).

212. Itaya, K., Shibayama, K., Akahoshi, H. & Toshima, S. Prussian-blue-modified electrodes: An application for a stable electrochromic display device. *J. Appl. Phys.* **53,** 804–805 (1982).

213. Itaya, K., Ataka, T. & Toshima, S. Spectroelectrochemistry and electrochemical preparation method of Prussian blue modified electrodes. *J. Am. Chem. Soc.* **104,** 4767–4772 (1982).

214. Nakanishi, S., Lu, G., Kothari, H. M., Bohannan, E. W. & Switzer, J. A. Epitaxial electrodeposition of Prussian blue thin films on single-crystal Au(110). *J. Am. Chem. Soc.* **125,** 14998–14999 (2003).

215. Jia, F., Yu, C., Gong, J. & Zhang, L. Deposition of Prussian blue on nanoporous gold film electrode and its electrocatalytic reduction of H2O2. *J. Solid State Electrochem.* **12,** 1567–1571 (2008).

216. Kumar, S. S., Joseph, J. & Phani, K. L. Novel method for deposition of gold - Prussian blue nanocomposite films induced by electrochemically formed gold nanoparticles : characterization and application to electrocatalysis. *Chem. Mater.* **19,** 4722–4730 (2007).

217. Abbaspour, A. & Kamyabi, M. A. Electrochemical formation of Prussian blue films with a single ferricyanide solution on gold electrode. *J. Electroanal. Chem.* **584,** 117–123 (2005).

218. Voronin, O. G. *et al.* Prussian blue-modified ultramicroelectrodes for mapping hydrogen peroxide in scanning electrochemical microscopy (SECM). *Electrochem. Commun.* **23,** 102–105 (2012).

219. Salazar, P. *et al.* Prussian blue and analogues: biosensing applications in health care. *Adv. Biomater. Biodevices* 0–35 (2014).

220. Karyakin, A. A., Karyakina, E. E. & Gorton, L. On the mechanism of H2O2 reduction at Prussian Blue modified electrodes. *Electrochem. Commun.* **1,** 78–82 (1999).

221. Derwinska, K. *et al.* Application of Prussian Blue based composite film with functionalized organic polymer to construction of enzymatic glucose biosensor. *Electroanalysis* **15,** 1843–1849 (2003).

222. Sitnikova, N. A., Borisova, A. V., Komkova, M. A. & Karyakin, A. A. Superstable advanced hydrogen peroxide transducer based on transition metal hexacyanoferrates. *Anal. Chem.* **83,** 2359–2363 (2011).

223. Pribil, M. M. *et al.* Rapid optimization of a lactate biosensor design using soft probes scanning electrochemical microscopy. *J. Electroanal. Chem.* **731,** 112–118 (2014).

224. Komkova, M. A., Maljusch, A., Sliozberg, K., Schuhmann, W. & Karyakin, A. A. Scanning electrochemical microscopy: Visualization of local electrocatalytic activity of transition metals hexacyanoferrates. *Russ. J. Electrochem.* **52,** 1159–1165 (2016).

225. Nečas, D. & Klapetek, P. Gwyddion: an open-source software for SPM data analysis. *Cent. Eur. J. Phys.* **10,** 181–188 (2012).

226. Wightman, R. M. Microvoltammetric electrodes. *Anal. Chem.* **53,** 1125A–1134A (1981).

227. Feldman, B. J. & Melroy, O. R. Ion flux during electrochemical charging of Prussian Blue films. *J. Electroanal. Chem.* **234,** 213–227 (1987).

228. Zamponi, S. *et al.* Influence of experimental conditions on electrochemical behavior of Prussian blue type nickel hexacyanoferrate film. *Electrochim. Acta* **48,** 4261–4269 (2003).

229. Gerber, S. J. & Erasmus, E. Electronic effects of metal hexacyanoferrates: An XPS and FTIR study. *Mater. Chem. Phys.* **203,** 73–81 (2018).

230. Herren, F., Ludi, A., Fischer, P. & Halg, W. Neutron diffraction study of Prussian Blue. Location of water molecules and long-range magnetic order. *Inorg. Chem.* **19,** 956–959 (1980).

231. Ganguli, S. & Bhattacharya, M. Studies of different hydrated forms of Prussian Blue. *J. Chem. Soc. Faraday Trans. 1 Phys. Chem. Condens. Phases* **79,** 1513–1522 (1983).

232. Gimenes, D. T. & Nossol, E. Effect of light source and applied potential in the electrochemical synthesis of Prussian blue on carbon nanotubes. *Electrochim. Acta* **251,** 513–521 (2017).

233. Hu, Y. L., Yuan, J. H., Chen, W., Wang, K. & Xia, X. H. Photochemical synthesis of Prussian blue film from an acidic ferricyanide solution and application. *Electrochem. Commun.* **7,** 1252–1256 (2005).

234. Pletcher, D. & Sotiropoulos, S. A study of cathodic oxygen reduction at platinum using microelectrodes. *J. Electroanal. Chem.* **356,** 109–119 (1993).

235. Carter, N. W., Rector, F. C., Campion, D. S. & Seldin, D. W. Measurement of intracellular pH with glass microelectrodes. *Fed. Proc.* **26,** 1322–1326 (1967).

236. Caldwell, P. C. An investigation of the intracellular pH of crab muscle fibres by means of micro-glass and micro-tungsten electrodes. *J. Physiol.* **126,** 169–180 (1954).

237. Caldwell, P. C. Studies on the internal pH of large muscle and nerve fibres. *J. Physiol.* **142,** 22–62 (1958).

238. Vonau, W. & Guth, U. pH monitoring: a review. *J. Solid State Electrochem.* **10,** 746–752 (2006).

239. Sardarinejad, A., Maurya, D. K. & Alameh, K. The effects of sensing electrode thickness on ruthenium oxide thin-film pH sensor. *Sensors Actuators, A Phys.* **214,** 15–19 (2014).

240. Santos, L. *et al.* WO3 nanoparticle-based conformable pH sensor. *ACS Appl. Mater. Interfaces* **6,** 12226–12234 (2014).

241. Bicher, H. I. & Ohki, S. Intracellular pH electrode; experiments on the giant squid axon. *Biochim. Biophys. Acta* **255,** 900–904 (1972).

242. Yamamoto, K. *et al.* Solid-state pH ultramicrosensor based on a tungstic oxide film fabricated on a tungsten nanoelectrode and its application to the study of endothelial cells. *Anal. Chim. Acta* **480,** 109–117 (2003).

243. Chen, J. C. & Chesler, M. pH transients evoked by excitatory synaptic transmission are increased by inhibition of extracellular carbonic anhydrase. *Proc. Natl. Acad. Sci. U. S. A.* **89,** 7786–7790 (1992).

244. Denuault, G., Frank, M H.T. & Peter, L.M. Scanning electrochemical microscopy:

potentiometric probing of ion fluxes. *Faraday Discuss.* **94,** 23–35 (1992).

245. Horrocks, B. R. R. *et al.* Scanning electrochemical microscopy. 19. Ion-selective potentiometric microscopy. *Anal. Chem.* **65,** 1213–1224 (1993).

246. Schulte, A., Belger, S. & Schuhmann, W. Corrosion of NiTi shape-memory alloys: Visualization by means of potentiometric '"constant-distance"' scanning electrochemical microscopy. *Mater. Sci. Forum* **394–395,** 145–148 (2002).

247. Liu, B., Cheng, W., Rotenberg, S. A. & Mirkin, M. V. Scanning electrochemical microscopy of living cells Part 2. Imaging redox and acid/basic reactivities. *J. Electroanal. Chem.* **500,** 590–597 (2001).

248. Niu, L. *et al.* Application of scanning electrochemical microscope in the study of corrosion of metals. *J. Mater. Sci.* **44,** 4511–4521 (2009).

249. El-Giar, E. E.-D. M. & Wipf, D. O. Microparticle-based iridium oxide ultramicroelectrodes for pH sensing and imaging. *J. Electroanal. Chem.* **609,** 147–154 (2007).

250. Etienne, M., Dierkes, P., Erichsen, T., Schuhmann, W. & Fritsch, I. Constant-distance mode scanning potentiometry. High resolution pH measurements in three-dimensions. *Electroanalysis* **19,** 318–323 (2007).

251. Izquierdo, J., Nagy, L., Santana, J. J., Nagy, G. & Souto, R. M. A novel microelectrochemical strategy for the study of corrosion inhibitors employing the scanning vibrating electrode technique and dual potentiometric/amperometric operation in scanning electrochemical microscopy: Application to the study of the cathodi. *Electrochim. Acta* **58,** 707–716 (2011).

252. Bastos, A. C., Karavai, O. V., Zheludkevich, M. L., Yasakau, K. A. & Ferreira, M. G. S. Localised measurements of pH and dissolved oxygen as complements to SVET in the investigation of corrosion at defects in coated aluminum alloy. *Electroanalysis* **22,** 2009–2016 (2010).

253. Nadappuram, B. P., McKelvey, K., Al Botros, R., Colburn, A. W. & Unwin, P. R. Fabrication and characterization of dual function nanoscale pH-scanning ion conductance microscopy (SICM) probes for high resolution pH mapping. *Anal. Chem.* **85,** 8070–8084 (2013).

254. Shin, H. Fabrication of Atomic Force Microscope Probes Integrated with Electrodes for Micro Four-Point Probe and SECM-AFM. (Georgia Institute of Technology, 2006). at <http://hdl.handle.net/1853/10428>

255. Yamanaka, K. Anodically electrodeposited iridium oxide films (AEIROF) from alkaline solutions for electrochromic display devices. *Jpn. J. Appl. Phys.* **28,** 632–637 (1989).

256. Ihli, J., Bots, P., Kulak, A., Benning, L. G. & Meldrum, F. C. Elucidating mechanisms of diffusion-based calcium carbonate synthesis leads to controlled mesocrystal formation. *Adv Funkt Mater* **23,** 1965–1973 (2013).

257. Wipf, D. O., Ge, F., Spaine, T. W. & Baur, J. E. Microscopic measurement of pH with iridium oxide microelectrodes. *Anal. Chem.* **72,** 4921–4927 (2000).

258. Elsen, H. A., Monson, C. F. & Majda, M. Effects of electrodeposition conditions and protocol on the properties of iridium oxide pH sensor electrodes. *J. Electrochem. Soc.* **156,** 6–11 (2009).

259. Herzog, G. Recent developments in electrochemistry at the interface between two immiscible electrolyte solutions for ion sensing. *Analyst* **140,** 3888–3896 (2015).

260. Lillo, M. & Losic, D. Ion-beam pore opening of porous anodic alumina: The formation of

single nanopore and nanopore arrays. *Mater. Lett.* **63,** 457–460 (2009).

261. Tong, H. D. *et al.* Silicon nitride nanosieve membrane. *Nano Lett.* **4,** 283–287 (2004).

262. Shen, M., Ishimatsu, R., Kim, J. & Amemiya, S. Quantitative imaging of ion transport through single nanopores by high-resolution scanning electrochemical microscopy. *J. Am. Chem. Soc.* **134,** 9856–9 (2012).

263. Chen, C.-C., Derylo, M. A. & Baker, L. A. Measurement of ion currents through porous membranes with scanning ion conductance microscopy. *Anal. Chem.* **81,** 4742–4751 (2009).

264. Chen, C.-C., Zhou, Y. & Baker, L. A. Single-Nanopore Investigations with Ion Conductance Microscopy. *ACS Nano* **5,** 8404–8411 (2011).

265. Morris, C. A., Chen, C.-C. & Baker, L. A. Transport of redox probes through single pores measured by scanning electrochemical-scanning ion conductance microscopy (SECM-SICM). *Analyst* **137,** 2933–2938 (2012).

266. Zhou, Y., Chen, C.-C. & Baker, L. A. Heterogeneity of multiple-pore membranes investigated with ion conductance microscopy. *Anal. Chem.* **84,** 3003–3009 (2012).

267. Rimboud, M., Hart, R. D., Becker, T. & Arrigan, D. W. M. Electrochemical behaviour and voltammetric sensitivity at arrays of nanoscale interfaces between immiscible liquids. *Analyst* **136,** 4674–4681 (2011).

268. Lillie, G. C., Dryfe, R. A. W. & Holmes, S. M. Zeolite-membrane modulation of simple and facilitated ion transfer. *Analyst* **126,** 1857–1860 (2001).

269. Izquierdo, D. *et al.* Spatial scanning spectroelectrochemistry. Study of the electrodeposition of Pd nanoparticles at the liquid/liquid interface. *Anal. Chem.* **84,** 5723–5730 (2012).

270. Booth, S. G. *et al.* Gold deposition at a free-standing liquid/liquid interface: evidence for the formation of Au(I) by microfocus X-ray spectroscopy (μXRF and μXAFS) and cyclic voltammetry. *J. Phys. Chem. C* **119,** 16785–16792 (2015).

271. Poltorak, L., Dossot, M., Herzog, G. & Walcarius, A. Interfacial processes studied by coupling electrochemistry at the polarised liquid-liquid interface with in situ confocal Raman spectroscopy. *Phys. Chem. Chem. Phys.* **16,** 26955–26962 (2014).

272. Kim, M. J., McNally, B., Murata, K. & Meller, A. Characteristics of solid-state nanometre pores fabricated using a transmission electron microscope. *Nanotechnology* **18,** 1–5 (2007).

273. Qian, H. & Egerton, R. F. Solid-state nanopores of controlled geometry fabricated in a transmission electron microscope. *Appl. Phys. Lett.* **111,** 1–4 (2017).

274. Shao, Y., Stewart, A. A. & Girault, H. H. Determination of the half-wave potential of the species limiting the potential window. *J Chem Soc Faraday Trans* **87,** 2593–2597 (1991).

275. Poltorak, L., Herzog, G. & Walcarius, A. Electrochemically assisted generation of silica deposits using a surfactant template at liquid/liquid microinterfaces. *Langmuir* **30,** 11453–11463 (2014).

276. Poltorak, L., Herzog, G. & Walcarius, A. In-situ formation of mesoporous silica films controlled by ion transfer voltammetry at the polarized liquid-liquid interface. *Electrochem. Commun.* **37,** 76–79 (2013).

277. Schindelin, J. *et al.* Fiji: An open-source platform for biological-image analysis. *Nat. Methods* **9,** 676–682 (2012).

278. Lowe, D. G. Distinctive image features from scale-invariant keypoints. *Int. J. Comput. Vis.* **60,** 91–110 (2004).

279. Overwijk, M. H. F., van den Heuvel, F. C. & Bulle-Lieuwma, C. W. T. Novel scheme for the preparation of transmission electron microscopy specimens with a focused ion beam. *J. Vac. Sci. Technol. B Microelectron. Nanom. Struct.* **11,** 2021–2024 (1993).

280. Prill, T., Schladitz, K., Jeulin, D., Faessel, M. & Wieser, C. Morphological segmentation of FIB-SEM data of highly porous media. *J. Microsc.* **250,** 77–87 (2013).

281. Tomus, D. & Ng, H. P. In situ lift-out dedicated techniques using FIB-SEM system for TEM specimen preparation. *Micron* **44,** 115–119 (2013).

282. Mayer, J., Giannuzzi, L. A., Kamino, T. & Michael, J. TEM sample preparation and damage. *MRS Bull.* **32,** 400–407 (2007).

283. Schubert, U. S. & Hüsing, N. *Synthesis of Inorganic Materials*. (WILEY-VDH, 2000).

284. Lan, W. J. *et al.* Voltage-rectified current and fluid flow in conical nanopores. *Acc. Chem. Res.* **49,** 2605–2613 (2016).

285. Saha, A., John, V. T. & Bose, A. In situ assembly of hydrophilic and hydrophobic nanoparticles at oil-water interfaces as a versatile strategy to form stable emulsions. *ACS Appl. Mater. Interfaces* **7,** 21010–21014 (2015).

IX. Appendix

IX.a. Used chemicals and materials

- 1,1'-Ferrocenedimethanole, 98 %, Acros Organics
- 1,6-Dichlorohexane, DCH, 98%, Aldrich
- 10 µm (diameter) Au wire, Goodfellows
- 18.2 MΩ, ELGA LabWater, Veolia Water Solutions & Technologies
- Ag and Pt wire, Goodfellows
- Ag/AgCl reference electrode in saturated KCl, RE-1CP, ALS Co.
- Al_2O_3 suspension, 50 nm, MasterPrep, Buehler
- Ammoniumcarbonate, $(NH_4)_2CO_3$, Merck KGaA
- Bis(triphenylphosphoranylidene)ammoniumchloride ($BTPPA^+Cl^-$) Alfa Aesar)
- Calciumchloride, $CaCl_2$, 95 %, Carl Roth
- Connecting Pt wire, insulated with Teflon, Science Products
- Crystalbond, 509, Plano
- Cu TEM grid, Omniprobe
- Disodiumhydrogenphosphate, $Na_2HPO_4 \cdot 12H_2O$, NORMAPUR, VWR Chemicals
- Dymax 9001-E-V3.1 and DYMAX 425, Dymax Europe GmbH
- Ethanol, 96 %, VWR Chemicals
- Hg/$HgSO_4$ reference electrode, sat. K_2SO_4, CH Instruments
- Hydrochloric acid, HCl, 32%, Normapure, VWR Chemicals
- Hydrogen peroxide, H_2O_2, 30%, EMSURE, Merck KGaA
- Insulating varnish, RS Components
- Iridium(IV) chloride, $IrCl_4$, Alfa Aesar GmbH & Co. KG
- Iron chloride, $FeCl_3$ x 6 H_2O, pro analysi, Merck KGaA
- Lithiumchloride, LiCl, ≥ 99%, Sigma Life Science
- Nickelchloride, $NiCl_2$, pro analysi, Merck KGaA
- Non-conductive silicon nitride tips, Veeco Instruments Inc.

- Non-metallized silicon nitride probes, OTR-P, Olympus
- Oxalic acid, C_2H_2O, Fluka Chemie GmbH
- Potassium carbonate, KCO_3, Merck KGaA
- Potassium hexacyanoferrate, $K_3[Fe(CN)_6]$, Honeywell, Fluka
- Potassiumchloride, KCl, pro analysi, Merck KGaA
- Potassiumtetrakis(4-chlorophenyl)borate (K^+ $TPBCl^-$), Alfa Aesar
- Rutheniumhexaaminechloride, $[Ru(NH_3)_6]^{3+}Cl_3$, 98 %, Aldrich
- Sharpened NCL probe (k = 48 N/m, 190 kHz, Nano World)
- SiN membranes (50/100 nm), SIMPore Inc. and DuraSiN Films, Protochips
- Sodium hydroxide, NaOH, Merck KGaA
- Sodium-di-hydrogenphosphate, NaH_2PO_4 x H_2O, pro analysi, Merck KGaA
- Stainless steel wire, insulated with Teflon, A-M Systems, Inc.
- Sulfuric acid, H_2SO_4, 98 % VWR Chemicals
- Tetrapropylammoniumchloride (TPrACl), Aldrich
- Tris(hydroxymethyl)aminomethane (TRIS), Merck KGaA

IX.b. Used instruments

- 5500 AFM/SPM microscope, Keysight Technologies
- AXIO Imager.M1m, Zeiss
- Bipotentiostat, CompactStat, Ivium Technologies
- CHI potentiostat (CHI potentiostat 660A or bipotentiostat 660C and 842B, CH Instrument)
- Dual beam FIB/SEM FEI Helios Nanolab 600, ThermoFisher Scientific
- Dual beam FIB/SEM FEI Quanta 3D FEG, ThermoFisher Scientific
- Dymax UV lamp 75 Blue Wave, Dymax Corp, λ= 320 - 395 nm and 9 W/cm^2
- EM 912 TEM, Zeiss
- FE-SEM 30 kV, S-5200, Hitachi, with a STEM detector
- Gas injection needle (IBID, precursor: methyl-cyclopentadienyl-trimethyl platinum), FEI, ThermoFisher
- InLab® Expert pro pH electrode, Mettler-Toledo Intl. Inc.
- Micromanipulation needle, Omniprobe
- Pt sputter coater: SCD 005, BAL-TEC
- X-ray detector: Pheonix, EDAX
- Zeiss Neon 40EsB, Carl Zeiss Nano Technology Systems

IX.c. Table of Tables

IX.d. Table of Figures

X. Acknowledgment

First, I want to thank my supervisor, apl. Prof. Dr. Christine Kranz, for providing the topic of my thesis. Many thanks for the helpful discussions and motivation, and especially for her patience and support throughout the whole thesis.

I want to thank Prof. Dr. Boris Mizaikoff for the opportunity to work on my thesis at the Institute of Analytical and Bioanalytical Chemistry, Ulm University.

Special thanks to Prof. Dr. Jürgen Behm for serving as the second reviewer of this thesis.

I would like to thank Prof. Dr. Mika Lindén and Prof. Dr. Paul Walther for taking the position as the additional examiners.

Maria Komkova and Prof. Dr. Arkady Karyakin, as well as my colleague Dr. Andreas Hartmann, are acknowledged for the cooperation in PB/NiHCF-modified sensors. Thanks to Jelena Kneer for her experimental support in the research towards the influence of UV light on PB/NiHCF-modified UMEs.

Many thanks to Tom Philipp and Stefan Repp for the experimental support towards the EIROF modification of UMEs and AFM-SECM probes during their Bachelor thesis.

Many thanks to all collaborators involved in the investigations of nanoITIES, namely Prof. Dr. Damien Arrigan, Benjamin Austen and Dr. Yang Liu, Dr. Alonso Gamero-Quijano and Dr. Gregoire Herzog, Prof. Dr. Paul Walther and Dr. Andreas Ziegler, as well as my colleagues Dr. Gregor Neusser and Dr. Peter Knittel.

Last but not least, many thanks to all members and former members of the IABC, especially Sandra, Margit, Marie, Sven, Alex, Javier, Robert, Kadda, Tanja and Gregor.

XI. Curriculum Vitae

Die Inhalte dieser Seite wurden aus Gründen des Datenschutzes entfernt.

Die Inhalte dieser Seite wurden aus Gründen des Datenschutzes entfernt.

XII. Publications

Book chapter:

A. Holzinger, C. Steinbach, C. Kranz, „Chapter 4: Scanning Electrochemical Microscopy (SECM): Fundamentals and Applications in Life Sciences“, in Electrochemical Strategies in Detection Science (Ed. Damien W. M. Arrigan), RSC Detection Science, 2015.

DOI: 10.1039/9781782622529-00125

Peer-reviewed articles:

M. A. Komkova, A. Holzinger, A. Hartmann, A.R. Khokhlov, C. Kranz, A. A. Karyakin, O. G. Voronin, “Ultramicrosensors Based on Transition Metal Hexacyanoferrates for Scanning Electrochemical Microscopy” *Beilstein J. Nanotechnol.,* 2013, *4*, 649–654.

DOI: 10.3762/bjnano.4.72

Y. Liu, A. Holzinger, P. Knittel, L. Poltorak, A. Gamero-Quijano, W. D. A. Rickard, A. Walcarius, G. Herzog, C. Kranz, D. W. M. Arrigan, “Visualization of Diffusion within Nanoarrays” *Anal. Chem,* 2016, *88* (13), 6689-6695.

DOI: 10.1021/acs.analchem.6b00513

A. Holzinger, G. Neusser, B. J. J. Austen, A. Gamero-Quijano, G. Herzog, D. W. M. Arrigan, A. Ziegler, P. Walther, C. Kranz, “Investigation of modified nanopore arrays using FIB/SEM tomography” *Faraday Discuss.*, **2018**, *210*, 113-130.

DOI: 10.1039/C8FD00019K

Front Cover of Electrochemistry at nano-interfaces, *Faraday Discuss.*, **2018**, *210.*

Oral presentation:

A. Holzinger, P. Knittel, J.-S. Moon, C. Kranz, “AFM Tip-integrated Antimony Electrodes for pH Detection“, the 66th Annual Meeting of the International Society of Electrochemistry 2015, Taipei, Taiwan.

A. Holzinger, P. Knittel, Y. Liu, D.W.M. Arrigan, C. Kranz, “Investigations of Nanopore Arrays for Liquid/Liquid Interfaces by Scanning Probe Techniques”, the 67th Annual Meeting of the International Society of Electrochemistry 2016, The Hague, the Netherlands.

A. Holzinger, C. Kranz, “Scanning Electrochemical Microscopy towards the Investigations of Catalytically Active Surfaces”, 1st Ulm Symposium on Solar-Driven Chemistry - SOLCHEM 2017, Ulm, Germany.

Poster presentation:

A. Holzinger, A. Hartmann, M. A. Komkova, A. A. Karyakin, B. Mizaikoff, C. Kranz, "AFM-SECM probes modified with Prussian Blue/nickel-hexacyanoferrate films for H_2O_2 detection", XVI. Annual Linz Winter Workshop 2014, Linz, Austria.

A. Holzinger, M. A. Komkova, A. A. Karyakin, C. Kranz, "AFM Tip-Integrated Prussian Blue/Nickel-Hexacyanoferrate Electrodes for H_2O_2 Detection", the 65th Annual Meeting of the International Society of Electrochemistry 2014, Lausanne, Switzerland.

A. Holzinger, M. A. Komkova, A. A. Karyakin, C. Kranz, "Untersuchung von Preußisch Blau/ Ni-Hexacyanoferrat Elektroden mittels AFM-SECM", 9. Deutsches BioSensor Symposium 2015, Munich, Germany.

A. Holzinger, J.-S. Moon, C. Kranz, „AFM Tip-integrated Electrodes and Modification Strategies“, the 8th international workshop on Scanning Electrochemical Microscopy (SECM-8), 2015, Xiamen China.

Award: 2nd prize for best poster presentation

A. Holzinger, P. Knittel, Y. Liu, D.W.M. Arrigan, C. Kranz, “Investigations of Nanopore Arrays using Scanning Probe Techniques”, Faraday Discussion: Single Entity Electrochemistry, 2016, York, UK.

XIII. Eidesstattliche Erklärung

Hiermit erkläre ich, dass ich die vorliegende Arbeit selbständig angefertigt habe und ich keine anderen als die angegebenen Quellen und Hilfsmittel benutzt, sowie wörtlich oder inhaltlich übernommene Stellen als solche gekennzeichnet habe. Keine weiteren Personen, sofern nicht in der Danksagung erwähnt, waren an der Fertigstellung der vorliegenden Arbeit beteiligt.

Ulm, den

Unterschrift